Luminescence dating of heated silex – Potential to improve accuracy and precision and application to Paleolithic sites

Inaugural-Dissertation

zur

Erlangung des Doktorgrades

der Mathematisch-Naturwissenschaftlichen Fakultät

der Universität zu Köln

vorgelegt von

Christoph Schmidt

aus Hof

Köln 2013

Erstellt mit LaTeX

Berichterstatter:	Prof. Dr. Ulrich Radtke
(Gutachter)	Prof. Dr. Ludwig Zöller
	Prof. Dr. Jörg Grunert
Tag der letzten mündlichen Prüfung:	09. 10. 2012

Contents

List of Figures

List of Tables

1 Introduction

Paleolithic archeological research has to rely on finds that endure thousands of years, and mostly the only relicts found during excavations are of lithic nature. Based exclusively on information derived from lithic artefact collections, archeological periods (technocomplexes) are distinguished for which a distinct type of artefact morphology is characteristic (Hahn 1991; Trachsel 2008). Excavations yielding human fossils along with stone tools in the same layer suggest that the artefacts were indeed produced by these people, and this allows a direct linkage of a certain artefact inventory to a certain species of human beings. For instance, Mousterian finds are associated with the presence of Neanderthals (*homo sapiens neanderthalensis*) in Western and Central Europe, based on the find situation at the sites Zafarraya in Spain (Hublin et al. 1995) or Pech-de-l'Azé I in France (Soressi et al. 2007), and Aurignacian assemblages are assumed to have been produced by anatomically modern humans (AMH, *homo sapiens sapiens*), as deduced from the excavations at the site Les Cottés in France (Talamo et al. 2012). It is further assumed that this direct correlation holds true not only for the type locality, but is applicable to wider areas as well. Although such correlated fossil and lithic finds are necessary to evidence an affiliation of technocomplexes to any form of hominids, information (1) on the age of the lithics and (2) on spatial diffusion or disappearance of certain artefact types and thus species of hominids is bound to numerical dating that provides age constraints of archeological deposits. Chronological information, however, is often difficult to obtain with the most commonly applied radiocarbon dating method, especially in Lower and Middle Paleolithic contexts, which are beyond the range of radiocarbon dating. Furthermore, organic material required for radiocarbon dating is often absent in arid or semi-arid environments. Dating methods making use of radiation damages are suitable not only to provide age information on certain parts of animals and human beings (e.g. corals and tooth enamel) by electron spin resonance (ESR), but also on lithic material by luminescence techniques. While optically stimulated luminescence (OSL) can be used to date underlying and overlying sedimentary deposits and sometimes deposition of the find layer itself, thermoluminescence (TL) allows determining the time of the firing event of heated lithic materials. In contrast to radiocarbon dating or the bracketing dates of a find layer obtained with OSL, the TL method applied on heated artefacts (or rocks in general) is considered to yield direct dates of events caused by prehistoric humans, e.g. lighting of a campfire.

Whereas accidental use of natural fire by humans goes back farther than 1 Mio. years in Africa (James 1989), evidence and chronological constraint of first intentional use of fire is difficult to adduce (Richter 2007b). Especially in Europe, the adoption of controlled use of fire seems to have taken place considerably late ($\sim$300–400 ka ago) (Roebroeks & Villa 2011). The importance of fire for mankind becomes clear as it not just provides warmth and light, but also enables the cooking of food which is seen as playing a major role in human evolution (Clark & Harris 1985; Carmody & Wrangham 2009). To directly link an event dated by TL – e.g. the heating of a lithic fragment – to human agency, the basic assumption is the frequent and intentional use of fire. Otherwise, the determined age could be that of an accidentally occurring natural fire as well, e.g. induced by a lightning. While in cave sites a lack of inflammable materials suggests a human cause of fire, open-air sites should preferably show an undisturbed and confined hearth to be able to exclude the impact of natural fires. However, the presence of heated along with unheated artefacts within the same strata or a clustering of heated ones can also be seen as a strong indication of anthropogenic campfires. With good reasons, the last heating of artefacts in most archeological contexts may thus be attributed to contemporary human occupancy of the site.

The oldest fossils of AMH, the species which we are part of, were found in Ethiopia and date back to $\sim$190 ka using the $^{40}Ar/^{39}Ar$ method (McDougall et al. 2005; Fleagle et al. 2008). These finds strengthen the "Out of Africa II" theory whose principle is the dispersal of modern humans from its origin in Eastern Africa all over the world (Eswaran 2002), in contrast to the "multi-regional" model according to which – in simple terms – AMH evolved simultaneously from several regional branches of preceding hominid forms (Wolpoff et al. 2000). The "Out of Africa II" hypothesis forms the basis of the Collaborative Research Center (CRC) 806 ("Our Way to Europe – Culture-Environment Interaction and Human Mobility in the Late Quaternary"). This project investigates the dispersal of AMH out of Africa into Europe along two corridors from which one – the Eastern trajectory via the Near East and the Balkan – is evidenced, while the other route – the Western trajectory, comprising a transition of the Sahara and the Street of Gibraltar – is still a matter of debate. Climatic conditions and their impact on environment, resources and habitats are thought to be a driving factor influencing the spread or retreat of AMH. To combine environmental and archeological data and thus elucidate any correlations between them, numerical dates of both records are indispensable. For the reasons quoted above, thermoluminescence dating of heated artefacts takes an important position to provide such information and to contribute to a crucial question of mankind. In the context of the CRC 806, the present work is concerned with methodological aspects of TL dating of heated siliceous rocks and aims to make this method feasible also in complex archeological contexts, especially in the event of "problematic" silex samples. Representing the regional focus of the CRC 806, several sites along the Eastern and Western trajectory or adjacent regions yielded heated artefacts to be dated in the course of case studies.

1.1 Aims of this study

Several TL dating studies from Paleolithic sites yielded data sets from the same archeological layer with large variability of obtained ages of individual artefacts (Mercier et al. 2007b; Richter et al. 2007; Valladas et al. 2008). This scatter of individual TL data is partly attributed to differing internal dose rates between samples, but also seen as caused by heterogeneities in environmental radiation fields. It is because of radiation hot spots present in the dated samples that Tribolo et al. (2006) had to deal with an increased uncertainty range of obtained ages. These and other studies suggest that the correct assessment of the internal dose rate and allowance for non-uniformity may play a significant role in overcoming part of the considerable scatter and uncertainty levels of TL dates (Malik et al. 1973; Valladas 1985; Selo et al. 2009). Indeed, taking into account the difference of uranium, thorium and potassium contents by factors of 10 or more (Mercier et al. 2007a) between single samples which are supposed to originate from the same raw material source, there is *a priori* no reason to assume radioisotopes to be uniformly spread in one sample. In contrast to the environmental radiation field that cannot be fully preserved during excavation, the internal configuration of radiative emitters remains intact until the specimen reaches the laboratory and is subjected to mechanical preparation. Consequently, internal dosimetric effects can be studied in detail. Therefore, a notable part of this work is concerned with the issue of the homogeneity of the internally induced radiation field of various silex samples and the resulting influence on TL ages. Especially if the luminescence sensitivity of the material changes with the local radioelement concentration, ages derived from average dose estimates and average dose rates of mixed sample material are expected to comprise systematic errors. In order to recognize difficulties associated with internal dosimetry, it is further aimed for developing a test method in the course of single-aliquot regenerative-dose measurement protocols.

Apart from issues related to the internal radiation field of silex samples, this thesis focusses on further potential sources of error and scatter. In the early years of TL dating, possible contributions of the sample holders to the detected luminescence signal were investigated – often termed "spurious" or "parasite" TL (Berger et al. 1982; Aitken 1985b) –, but have fallen into oblivion during the past decades so that most laboratories are unaware of that problem. A study of thermally and optically stimulated luminescence of a variety of sample holders thus serves to estimate the degree of interference of parasite signals and those of the sample itself. By selecting appropriate cleaning procedures and sample holders with negligible luminescence emission, it is expected to reduce both systematic and random errors of the determined radiation dose.

While OSL is routinely applied in luminescence dating of sediments, the potential of this method for heated silex has been poorly studied up to present (Poolton et al. 1995; Richter & Temming 2006). Signal resetting by heating instead of bleaching may have the potential to also take advantage of so-called *slow*-components from which some

are characterized by high saturation dose levels, enabling the dating of older samples. The parallel determination of several dates by different luminescence stimulation modes (TL and OSL) and various detection wavelengths (e.g. UV-OSL and red or blue TL) further opens up the possibility to generate multiple ages per silex specimen. This allows conclusions to be drawn on the signal stability of used emissions and the general reliability of the dating results. The present work thus contains basic investigations on OSL signal composition of silex, the components' thermal stabilities and their suitability for dating.

Since the method of artefact dating by TL has not been applied before at the Cologne luminescence laboratory, one has to make sure that systematic errors introduced during sample preparation and measurement can be ruled out. This will be tested by recovering known radiation doses given to zeroed geological as well as archeological silex samples and applying the routine sample preparation and measurement procedures. A cross-check of TL data with an independent method (radiocarbon dating) will be carried out for samples from a Gravettian find layer. Furthermore, in a second step, the findings from the dosimetric investigations will then be applied to heated silex samples from different archeological contexts.

In summary, the main focus of the present study is a methodological one. As a central aim, it focusses on the reduction of systematic and random errors in the TL dating process of heated silex. Based on the previous considerations, this work addresses the following questions:

1. Do spurious luminescence signals contribute significantly to the uncertainty of luminescence data?

2. Are omnipresent impurities in silex related to gradients in the internal radiation field?

3. Is it possible to recognize and quantify internal heterogeneity and to account for it to improve accuracy and precision of TL ages?

4. Are single-aliquot procedures suitable for providing information on malign influence of non-uniform dose rate and for discrimination between affected samples and those yielding valid ages?

5. How is the composition of the OSL signal of silex and can *slow*-components increase the dating limit?

The following part of the introduction summarizes specific luminescence-related features of silex, and the basic principles and mechanisms of luminescence dating are presented. Here, focus is set on issues being of particular relevance for TL of silex, e.g. α-radiation and its efficiency in luminescence production. The detailed information on this item is presented with having in mind its significance for evaluating internal dose rate properties. Since fundamental processes of luminescence generation (Section 1.3.2.2) and the mathematical

description of TL and OSL curve shapes (Section 1.3.2.4) provide the background for the comprehension of the OSL study or aspects of applied dating (e.g. Chapters 5 and 6), these topics are given detailed attention. The main luminescence emissions of silex (respectively quartz) are also introduced, because ages based on several TL emissions will be compared in the course of the applied dating studies.

1.2 General characteristics of silex

Predictable knapping properties of the raw material are a prerequiste for the production of high-quality stone-tools. These features are particularly provided by rocks showing conchoidal fracture which goes along with isotropy of working properties. Due to their directional cleavage, macrocrystalline rocks are far less suitable for tool processing than amorphous or microcrystalline materials. The compactness and the resistance to weathering are characteristic of silex and, accordingly, most of the stone artefacts excavated from Paleolithic sites consist of any type of silex. The general features and diagenesis of silex will be shortly described in the following.

1.2.1 Terminology

The terminology associated with the types of raw materials used for tool production is obfuscating and follows different criteria and local variations. An international or standardized system, either from the archeological or from a mineralogical or geological point of view, does not exist. Expressions appearing in this context comprise flint, chert, hornstone, jasper, agate, chalcedony, opal, quartzite, radiolarite, silcrete and many more. Distinction can be made with respect to the rock's composition, how it was formed or when it was formed. Referring to the latter possibility, chemically and petrographically identical material is termed differently according to its geological origin. For instance, this is the case for flint (Cretaceous) and hornstone (Jurassic) (Floss 2003; Graetsch & Grünberg 2012). Mercier et al. (1995) and Aitken (1985b) see flint as a form of chert found in chalk layers, whereas chert is defined as made up mainly of chalcedony. However, unequivocal subdivision in terms of mineralogical composition is hampered by smooth transitions between constitutive phases. Unambiguous identification of mineral phases is related to considerable analytical efforts and thus mostly not feasible in the context of archeological research. The conditions of formation may also play a role in nomenclature as is the case for radiolarite. While some scholars often subsume all varieties of amorphous/microcrystalline siliceous rocks under the expression "flint", Americans prefer the term "chert" and French the name "silex" (Richter et al. 1999). In this work, the latter term – *silex* – is chosen to summarize all forms and varieties of silica studied, also because this expression involves literally the main component of all these materials, i.e. silica (SiO_2).

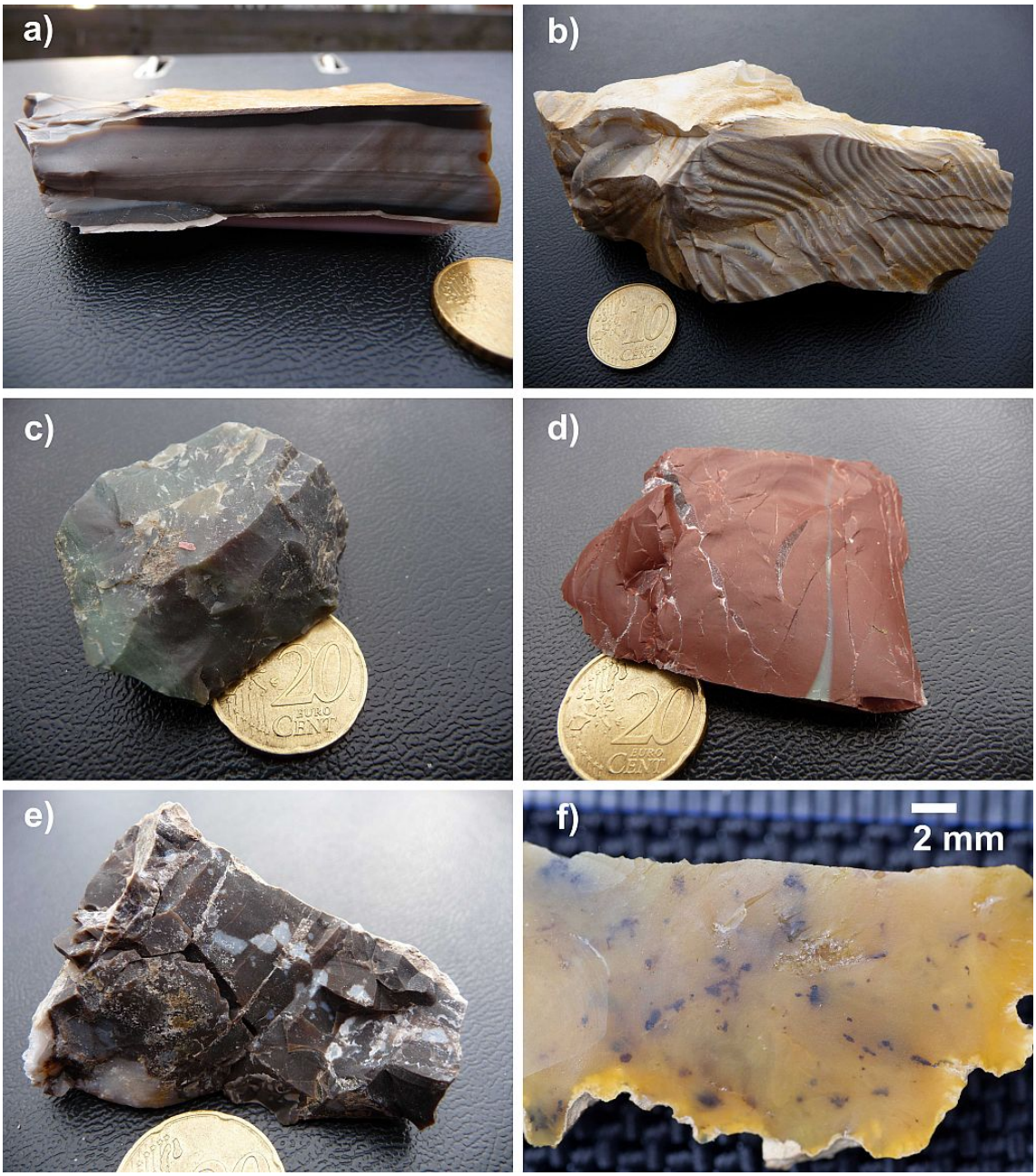

Figure 1.1: Compilation of various silex raw materials. (a) Tabular hornstone (Upper Jurassic) from Abensberg-Arnhofen, Germany; (b) Banded flint (Jurassic) from the Holy Cross Mountains, Poland; (c) Radiolarite from Gemsteltal-Widderstein (Kleinwalsertal), Austria; (d) Radiolarite from Gemsteltal-Widderstein/Bärenkopf, Kleinwalsertal, Austria; (e) Trigonodus hornstone (Middle Triassic) from Dinkelberg, Germany; (f) Close-up of chalcedony from Romania, showing Fe-Mn-oxy-hydroxide inclusions (see Section 4.3.5).

1.2.2 Constituents and diagenesis

Composition and formation regimes of silex may considerably determine the luminescence characteristics and thus the value of the age information. As will be evident in the following chapters, impurities play an important role in this respect. Therefore, basic information on constituents and diagenesis of silex will be given here.

Silex can either occur as nodules or as (banded) layers of several centimeters thickness. Main components of siliceous rocks are SiO_2, water and $CaCO_3$, while further contributions come from minor and trace elements, foreign phases in cracks, inclusions and organic matter, summarized as impurities (Micheelsen 1966). Infrared-spectroscopy has shown that water in silex may be present as molecular water or in form of hydroxyl groups and is quoted to amount to $\sim$0.5–2 wt.% in chalcedony (Graetsch et al. 1985; Okrusch & Matthes 2005), but can reach concentrations up to 20 wt.% in opal (Okrusch & Matthes 2005). As suspected by Andersen (1982), water penetrating through cracks in the rock is able to carry impurities into the rock or, vice versa, may leach out considerable amounts of trace elements. Trace elements account for the colors observed for various silices, including all shades of grey, red, yellow, ochre, brown and dark green to almost black. Some specimens illustrating the huge variety of textures and colors are shown in Fig 1.1. A striking characteristic of most silices is a white coating or rind which is either *cortex* or *patina*. The cortex is the boundary layer of silex and host rock and of similar composition as the silex. Patina, however, forms by weathering of silex without cortex: Silica is leached from the outer part of the rock and leaves cavities which may subsequently be filled by precipitation of siliceous solutions, causing the white appearance (Rottländer 1975; Graetsch & Grünberg 2012).

Going into detail, the siliceous components of silex can be divided into amorphous opal ($SiO_2 \cdot n\,H_2O$) and fibrous or grainy microcrystalline SiO_2 (chalcedony, jasper) (Floss 2003; Okrusch & Matthes 2005). Empirical studies on the grain size of the microcrystalline phase quote values of 2–30 µm for Danish flint, while these grains are composed of piles of plates with a thickness of $\sim$59 nm (Micheelsen 1966), and a range of crystallite sizes of $\sim$30–55 nm for various flints and $\sim$30–200 nm for diverse chert samples, derived by X-ray diffractometry (Graetsch & Grünberg 2012). Based on the resolution of a specific X-ray diffraction peak, Murata & Norman (1976) proposed a crystallinity index which is seen as a function of crystal size and ranges from <1 up to >10. On this scale, silex samples mostly yield values of <1 up to 3, while also values of >8 are reported for American chert samples. Macrocrystalline quartz always has a crystallinity index value of >8.5. The broadening of reflection peaks in X-ray diffractometry is generally attributed to small crystallite size or microstrain induced by lattice imperfections (Markl 2008; Graetsch & Grünberg 2012). Thus, the relatively larger the amorphous component of a silex sample, the more diffuse will the quartz reflection peak be (see Fig. 1.3).

Silices may form in various environments and thus exhibit different diagenetic pathways. Chemical disequilibrium in chalk deposits leads to redistribution of silica delivered

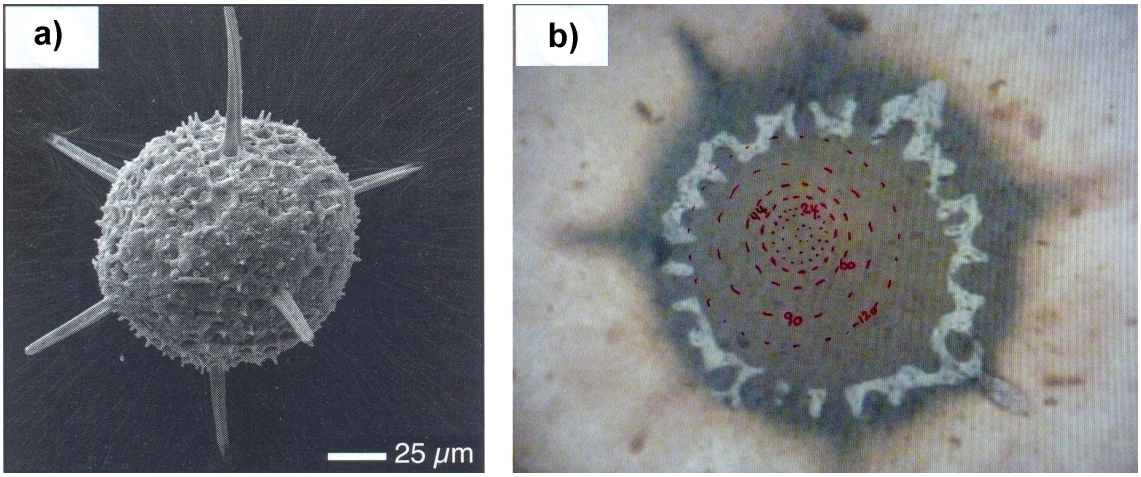

Figure 1.2: SEM and optical microscope images of radiolaria. (a) SEM image taken from Markl (2008). (b) cross-section of a fossilized radiolaria found in sample O4 during LA-ICP-MS analysis (see Chapter 4). The red circles on the photo visualize the beam diameters (in µm) of the laser and serve here as a scale. Both images have approximately the same scaling.

by skeletons of marine organisms and to the formation of silica gel concretions (pers. comm. Dr. Rolf Hollerbach, Institute of Geology and Mineralogy, University of Cologne, 2011). In marine milieus of the Paleozoic, siliceous matter was provided by diatoms and radiolaria, whose skeletons are made up of amorphous silica (opal-A). Their accumulation and decay forms the basis of diatomite and radiolarite (Markl 2008). Opal may also be formed by precipitation from hydrothermal solutions or in volcanic settings as a decay product of young volcanic rocks (Okrusch & Matthes 2005). The initial stages of biogenic amorphous SiO_2 are not in thermodynamic equilibrium and marine silica then undergo the following transition path (Markl 2008; Graetsch & Grünberg 2012):

$$\text{opal-A} \rightarrow \text{opal-CT} \rightarrow \text{opal-C} \rightarrow \text{quartz}$$

Opal-CT shows initial signs of a long-range order and thus microcrystallinity, whereas CT stands for the cristobalite-tridymite structure. Further cristallization yields opal-C and finally quartz with macroscopical crystal structure. At least theoretically, during this process the water content decreases and the crystal size increases and so does the crystallinity index. Hence, the degree of crystallinity should be an indicator of geological age. However, since the transition from amorphous to macrocrystalline SiO_2 is dependent not only on time, but also on burial depth (pressure), chemical environment and impurities and since it may take different paths of diagenesis and involve various precurser phases, this relationship does not hold true in all cases, as exposed in Graetsch & Grünberg (2012) and references therein. Non-marine forms of silices may have undergone different processes of formation, e.g. metamorphism in the case of Devonian quartzite (Floss 2003). Due to the simultaneity of transformation processes (see also Fig. 1.3), most siliceous rocks are made up of multiple phases, including mostly microcrystalline constituents (e.g. chalcedony) and amorphous components (opal-A) (Markl 2008).

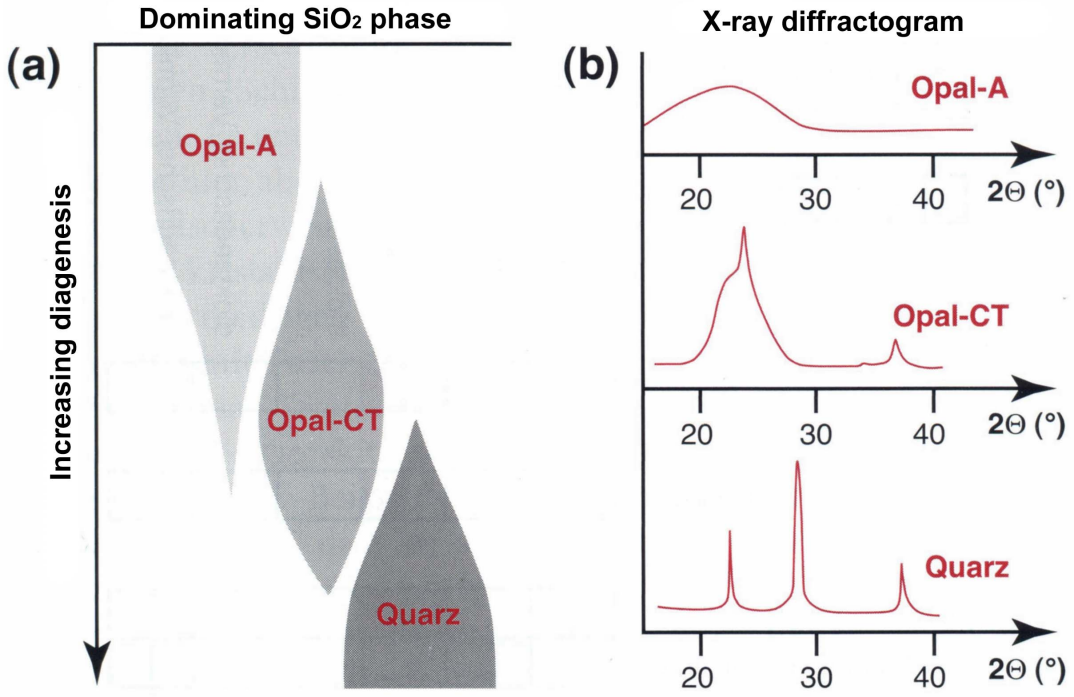

Figure 1.3: Recrystallization of amorphous opal-A to macrocrystalline quartz. (a) Transition from opal-A via opal-CT to quartz. These processes go along with increasing crystal size what affects the shape of the peaks observed in X-ray diffractograms (b). Modified from Markl (2008).

1.2.3 Heat alteration

Thermoluminescence dating is only applicable to sufficiently heated silex ($> \sim 350$–$400\,^{\circ}\mathrm{C}$). Therefore, recognition of heating of a sample by visual indicators is of great importance for the selection of potential candidates for dating. According to Purdy & Brooks (1971), Mercier et al. (1995), Richter (2007b) and Richter et al. (2011), optical signs of heat treatment include

1. **Crazing, cracking or craquelation**. These patterns of cracks at the surface are probably caused by thermal expansion and contraction. Severe and rapid heating might result in fragmentation, shattering or even explosion of the sample due to internal water evaporation.

2. **Vitreous luster**

3. **Characteristic uneven planes of fracture** which differ from weathered surfaces or cleavage faces caused by knapping.

4. **Potlids**, i.e. hollow moulds of a size of several mm. According to Weymouth & Williamson (1951), as cited in Richter et al. (2011), they occur during heating rather than cooling due to evaporation of molecular (at $\sim 100\,^{\circ}\mathrm{C}$) and hydroxyl water (at $\sim 365\,^{\circ}\mathrm{C}$).

5. **Color change** to red or reddish. This process has been attributed to the oxidation of $Fe_{(II)}$ to $Fe_{(III)}$ and occurs at temperatures above $\sim 250\,^{\circ}C$ (Purdy & Brooks 1971). Black coloration due to carbonization of organic impurities has been reported by Rottländer (1989), as cited in Richter et al. (2011).

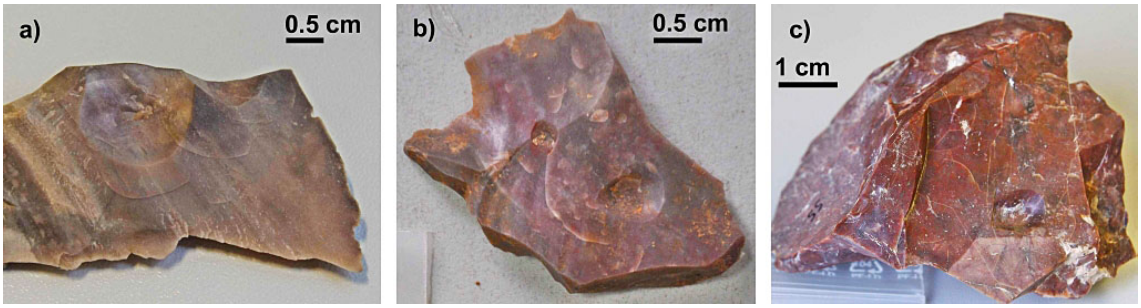

Figure 1.4: Signs of heat alteration of archeological silex samples. (a) Sample PRC3 from Praia Rei Cortiço, Portugal: potlids, slight craquelation and dark discoloration. (b) Sample LP4 from Las Palomas, Spain: potlids and slight reddish/pinkish discoloration. (c) Sample Rom27 from Românești-Dumbrăviţa I, Romania: Potlids, craquelation and prominent color change from ochre/brown (raw material) to dark red.

The presence of one of the listed indicators provides not necessarily evidence of heating, as weathering or freezing may cause these features as well (Richter et al. 2011). In the event that more of these attributes are observed for a sample, however, this is a strong indication that it has been heated. Furthermore, the temperature reached during heating cannot be deduced from external signs, except for the color change that seems to occur at certain temperatures for some specific raw materials (see Section 6.2.2). Corresponding to the huge variety of siliceous materials, the "response" to heating differs from sample to sample. Whether or not certain signs of heat treatment are present is further dependent on the heating rate and the duration of heating. Additionally, the temperatures necessary to reset the TL signal and to cause signs of heat alteration can be provided by direct exposure to fire only. Even small sediment layers of a thickness of a few centimeters are sufficient to shield the heat of a hearth from the buried lithics, which in turn strengthens the direct correlation between heating of the artefacts and occupation of the site (Campbell et al. 1995; Werts & Jahren 2007).

As far as the heating of lithic material is related to human activities, the way they were fired – by accident or intentionally – is not crucial for the pure dating application. Richter (2007b) argues for accidental fire impact in most cases. This did not change until the Solutrean in which period regular signs of heat alteration have been related to the technique of tempering. Other sources, however, already attributed Neanderthals a fire-management comparable to that of AMH (Roebroeks & Villa 2011). Tempering includes controlled and slow heating of raw material what is said to improve the chipping properties to enable the use of medium- or bad-quality materials for elaborated tools, as is characteristic e.g. for the Solutrean (Hahn 1991). A study of Purdy & Brooks (1971) on

Florida cherts suggests that temperatures of 350–400 °C maintained for "sustained periods" result in melting of impurity phases which are seen as a flux for the SiO_2 microcrystals. Thus, the microcrystals are bound closer together after heating, accompagnied by an improvement of knapping properties.

1.3 Luminescence dating of heated silex

Luminescence dating is based on time-dependent storage of energy in insulators. Imparting ionizing radiation causes a separation of charge – and thus an overall increase of potential energy – that can be maintained over periods of time sufficient to date Middle and Upper Paleolithic events. Here, naturally occurring radionuclides (mainly those from uranium, thorium and potassium) play a major role: they supply energy/ionizing radiation via their radiative decay. The longer a sample, for instance a silex artefact, is exposed to environmental radiation of surrounding sediment, the higher will the accrued radiation dose be, which is proportional to the age of the dated event. The sample thus acts as dosimeter. Considering silex in particular, radiation coming from the sample itself has to be accounted for as well, due to non-negligible amounts of radioactive elements within the specimen. The stored energy can be released in the form of light (*luminescence*) by stimulation with either light or heat. The luminescence signal is hence set to zero. Knowing the rate with which dose is delivered (*dose rate*) and the functional relationship between dose and luminescence output allows calculating the time elapsed since storage began.

This explanation requires a close relation of processes which reset the accumulated dose (or, in other words, the "luminescence clock") and the event of interest actually to be dated (see Fig. 1.5). Several mechanisms are capable of zeroing the luminescence signal: Heat (volcanic events, fire exposure, frictional heat), light (sunlight exposure) and pressure/shock (e.g. earthquakes). In addition, the time of mineral formation is inherently connected with the absence of any latent luminescence signal (Wagner 1995). Of special interest for the scope of this work is signal erasure by heat, since fired siliceous material is often found in the context of archeological sites, especially in hearths. From the distribution of these finds and various signs of heat impact (e.g. the spatial correlation of heated lithics with fire-related discoloration of underlying sediments) it may be inferred that the heating is closely connected to human use of fire and is unlikely to have happened during natural fires (Richter 2007a; Richter et al. 2009). Thermoluminescence thus facilitates a means to directly date past human actvitity and the occupation of Paleolithic sites.

1.3.1 History, trends and applications of silex dating

The use of minerals as radiation dosimeters for dating purposes was first suggested by Daniels et al. (1953) in their path-breaking publication dealing with "Thermoluminescence as a research tool". At this time, only signal resetting by heat was known and it was seen as possible to estimate "the dates at which limestones and ancient pottery were

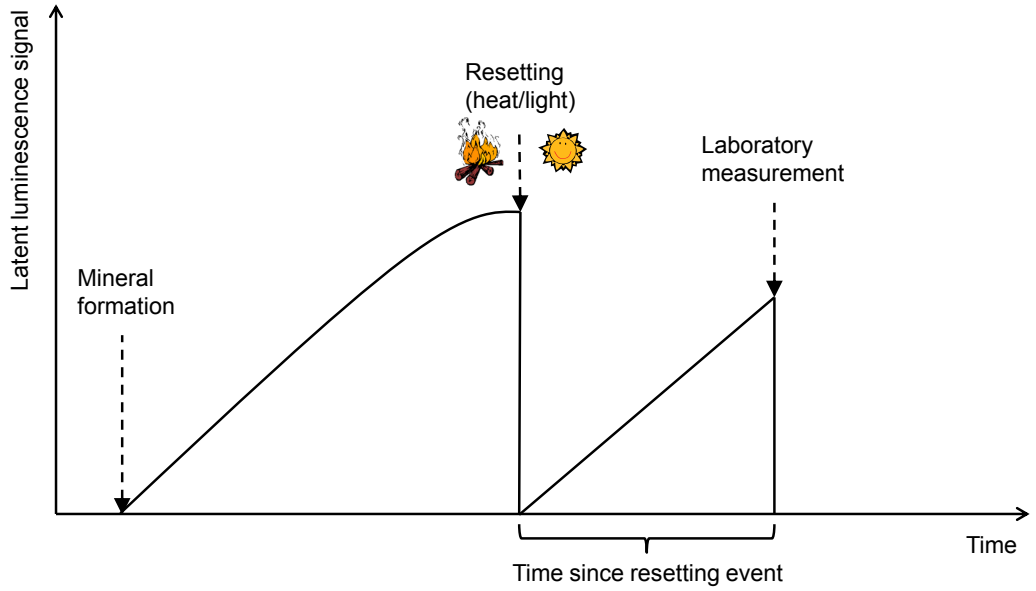

Figure 1.5: Growth and resetting of the latent luminescence signal. Modified from Richter (2007a).

heated to high temperatures" (Daniels et al. 1953: 349). The authors further highlight the potential of TL for correlating sediment strata by comparing their TL fingerprints, i.e. their specific TL glow curves (recorded luminescence versus heating temperature). The use of luminescence as a dosimetric means has only been possible with the development of highly sensitive measurement devices that are able to register very low amounts of light, e.g. the photomultiplier (Aitken 1985b). First measurements of TL from burnt ceramics were made in the early 1960s by Kennedy & Knopff (1960) and at the University of Bern by Grögler et al. (1960).

Basic research on "regenerated TL" (Göksu & Fremlin 1972), which is here used to describe the spurious TL recorded after annealing the sample, prepared the ground for the first application of TL in dating of heated silex artefacts. The method and dates presented in the *Science* publication of Göksu et al. (1974) demonstrated the applicability of the approach which yielded ages for heated silex from Middle and Upper Paleolithic sites and the Bronze Age compatible with radiocarbon ages, stratigraphy and cultural attribution. Besides success in application, the authors illustrated and discussed general considerations and difficulties in regard to material properties, sample preparation, measurement procedures as well as main sources of error. Initial TL measurements on heated silex artefacts were conducted using thin slices of the interior parts of the specimen (Göksu & Fremlin 1972; Göksu et al. 1974; Aitken & Wintle 1977; Melcher & Zimmerman 1977). One of the reasons for utilizing slices (mostly of 1 mm thickness or less) is explained by Göksu & Fremlin (1972): grinding or crushing of the sample could at first result in tri-

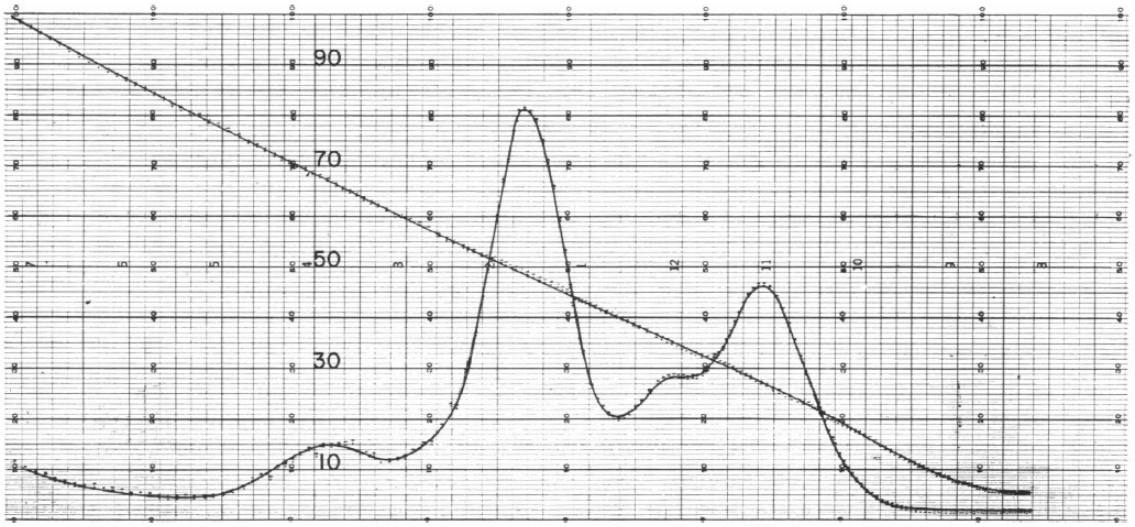

Figure 1.6: TL glow curve of a γ-irradiated limestone sample. The temperature-axis is inverted (see the plotted heating ramp), 0 = 0 °C, 100 = 500 °C, heating rate 0.8 K s^{-1}. From Daniels et al. (1953).

boluminescence and, secondly, in an increase of surface having contact to the environment (air, water), leading to the unwanted effect of spurious TL. Disadvantages, however, were related to the heterogeneity of the slices in terms of opacity and dosimetry (e.g. determination of the α-efficiency) (Aitken & Wintle 1977). Valladas (1978) found out that the spurious TL, obviously generated by residual carbonates within the sample, can be eliminated by acid treatment of the crushed sample with diluted HCl. Since then, exclusively crushed or ground samples have been used for measurements. Effects of mechanical treatments (grinding, crushing) on the luminescence signals of the samples have not been detected so far (Huxtable 1982; Aitken 1985b).

Melcher & Zimmerman (1977) approached the question of sufficient TL signal depletion through ancient heating by comparing the TL of heated silex with that of raw material. As visual appearance and optical indication of firing are (mostly) only qualitative features, this article introduced a numerical assessment of the ancient temperature reached. Other methods to estimate the heating temperature were presented by Valladas (1981), Göksu et al. (1989) and Michab et al. (1998). Göksu et al. (1989) consider the 110 °C TL peak and its temperature-induced sensitization to be an appropriate means for this test. During the 1990s, two papers on TL emission spectra of silex were published (Martini et al. 1999; Richter et al. 1999), amending early investigations of Bailiff et al. (1977) and Wintle & Aitken (1977) and confirming a strong orange-red emission for most silex samples. This emission, however, has been disregarded until recently (see below). Further methodological aspects such as TL signal saturation effects, fitting of dose response data (Mercier 1991; Mercier et al. 1992) or determination of the α-efficiency (Valladas 1988; Tribolo et al. 2001) were published by the members of the French silex dating group in Gif-sur-Yvette.

A crucial point in the evolution of luminescence dating was the discovery that light can also be used for stimulation (optically stimulated luminescence, OSL). This opened up the possibility of sediments being dated more precisely, as a direct measurement of the optically sensitive luminescence signal was now feasible (Huntley et al. 1985). In principal, it should be possible to use OSL for silex dating as well, because heat (>350–$400\,^{\circ}C$) is expected to erase all bleachable signal components. Only two studies have so far dealt with OSL properties of silex: Poolton et al. (1995) carried out spectrometric measurements and presented the fundamental differences between OSL from silex and from macro-crystalline quartz, but concluded from pulse annealing experiments that the thermal stability of the OSL signal is insufficient to be used for dating; Richter & Temming (2006) found poor reproducibility of a given laboratory dose in dose recovery tests using OSL. Nevertheless, OSL was applied to heated quartzite fragments to determine both the equivalent dose and the α-efficiency (Tribolo et al. 2001; Tribolo et al. 2003). The authors found, however, discrepancies between TL reference ages and the OSL ages which they attributed to accidental bleaching of the stones during sampling.

For determination of the equivalent dose (D_e) – the laboratory dose that induces the same luminescence output as the natural dose –, usually the multiple-aliquot additive-dose approach (see Section 1.3.4.1) has been used, in order to circumvent influences of sensitivity changes occurring during repeated heating and/or irradiation. Non-linear increase of the first (additive) dose response curve at low doses is accounted for by constructing a second (regenerated) glow curve (Aitken 1985b; Valladas 1985; Mercier et al. 1995). Given the development of single-aliquot regenerative-dose (SAR) protocols in OSL dating of sediments since the early 1990s (Duller 1991; Mejdahl & Bøtter-Jensen 1994; Murray et al. 1997; Murray & Wintle 2000), only quite recently SAR procedures have been applied to silex as well (Richter & Krbetschek 2006). The authors made use of low sensitivity changes observed for the red TL (RTL) emission of silex during repeated heating and irradiation and presented a protocol with a reduced number of regeneration points. More details on D_e determination will be given in Section 1.3.4.

A first overall summary of the state of the art of TL dating in general is given by the book of Aitken (1985b). The knowledge of TL dating of heated silex in particular was summarized first in a paper by Valladas (1985); other publications followed a few years later by Valladas (1992), Mercier et al. (1995) and, most recently, by Richter et al. (2000), Richter (2007a) and Wintle (2008).

Numerous case studies have proven the importance and prominence of TL dates of heated artefacts. Particularly in the Levant, TL chronologies shed light on Middle Paleolithic occupational sequences and the question of simultaneous occurrence of AMH and Neanderthals. Among the most important dates collected in this region are those concerned with Quafzeh Cave (Israel, $\sim$90–100 ka) (Valladas et al. 1988) and Es-Skhul (Israel, $\sim$120 ka) (Mercier et al. 1993) which provide age estimates of heated lithics associated with AMH. The youngest ages related to the presence of Neanderthals were

determined at Kebara and Amud Cave (Israel, ∼50–60 ka) (Valladas et al. 1987; Valladas et al. 1999), giving a temporal overlap with the presence of AMH of several 10 ka. Going back further in time, Mercier et al. (2007a) dated 77 single artefacts excavated at Hayonim Cave (Israel) and could establish a detailed chronology reaching from ∼125–230 ka. Other TL dating studies of Mediterranean sites include those of Sodmein Cave (Egypt, Middle Paleolithic, ∼120 ka) (Mercier et al. 1999), Theopetra Cave (Greece, Middle Paleolithic, ∼130 ka) (Valladas et al. 2007) and Rhafas Cave (Morocco, Middle Paleolithic, ∼60–90 ka) (Mercier et al. 2007b), to name just a few. Indications for the antiquity of modern human behaviour were brought about by TL dating of heated Middle Stone Age quartzite and silcrete remains at Blombos Cave (South Africa) to about 74 ka by Tribolo et al. (2006).

However, not just Mediterranean sites provided heated lithics suitable for TL dating. Direct age estimates for the occupation of sites yielded important information on the temporal and spatial distribution of Neanderthals and the invasion of AMH into Europe. Important TL-dated Lower and Middle Paleolithic sites in France are e.g. Combe Grenal (∼44–113 ka) (Bowman & Seeley 1978; Bowman & Sieveking 1983), Les Forêts and Jiboui (∼93 and 52 ka, respectively; in combination with ESR) (Duttine et al. 2005) and Bérigoule (∼54–111 ka) (Richter et al. 2007). Huxtable & Jacobi (1982) dated the Mesolithic site at Longmoor Inclosure (East Hampshire, UK) to ∼8–10 ka, in agreement with radiocarbon ages (obtained in the early 1980s) and showing the applicability of the method to comparatively young sites. A comprehensive study of ^{14}C, ESR and TL dating was presented by Richter et al. (2000) for Upper Paleolithic layers in the Geißenklösterle Cave (Germany). Disagreement of TL and radiocarbon ages for the Aurignacian level are explained by the lack of appropriate ^{14}C calibration. Furthermore, TL dates of heated artefacts were obtained for the Eastern European sites of Piekary IIa (Poland, ∼39 ka) (Mercier et al. 2003) which are compatible with OSL ages of well-bleached grains from the same layer, and for the site of Brno-Bohunice (Czech Republic) (Richter et al. 2009). Here, the occupation layer was dated both by TL of heated artefacts and OSL of sediments to 48 ± 2 ka and 59 ± 6 ka, respectively.

The case studies given here represent, however, just a small selection; more examples for the application of the TL method can be found in the reviews by Valladas (1992), Mercier et al. (1995), Richter (2007a) and Wintle (2008).

1.3.2 Physical basics of luminescence in crystalline and amorphous SiO_2

Luminescence as a mineralogical and biological phenomenon has been known for several thousands of years (Harvey 1957). By heating certain minerals, light of different colors is emitted, which cannot be attributed to incandescence and is thus referred to as “cold light”. However, only with the development of solid state physics a plausible explanation of the processes “behind the scenes” could be found; a full and all-encompassing theory is nevertheless still outstanding. The basic principles of charge transfer responsible for luminescence emissions in minerals will be outlined in the following sections.

1.3.2.1 The energy band model

In isolated atoms, electronic states have clearly defined energies. If many atoms are brought together to form a crystal lattice, the vicinity of the atoms causes the electrons to tunnel from one atom to the other. Thus, the duration of stay of a valence electron "in" its mother atom is limited and according to Heisenberg's uncertainty principle for energy and time, the originally sharp energy states broaden. The probability of tunneling for electrons in the inner shells of an atom is much lower, and hence is also the broadening of the energy states. In view of the entire crystal, defined energy states emerge into quasi-continuous energy bands where each band contains a number of electronic states equal to the number of lattice constituents (therefore "quasi-continuous"). At $T = 0\,\mathrm{K}$, all energy states with $E < E_F$ are filled, and all states with $E > E_F$ are empty, with E_F being the Fermi energy or Fermi level. This sharp edge of the distribution of filled states is smoothened at higher temperatures and the product of state density and Fermi-Dirac distribution (applicable for electrons as they are fermions) governs the occupation of states (Meschede & Vogel 2006).

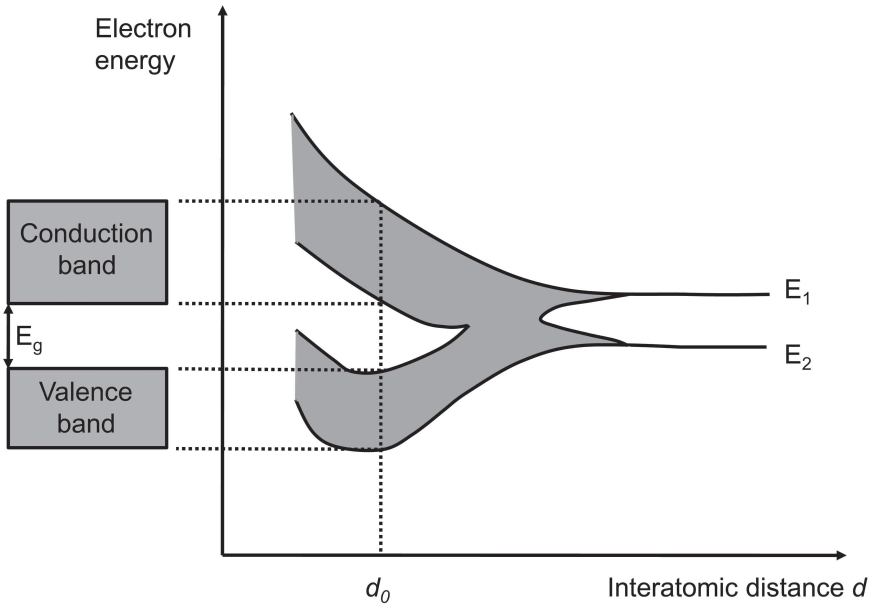

Figure 1.7: Formation of energy bands. Discrete electronic energy states (E_1, E_2) emerge into quasi-continuous energy bands as the atomic distance is reduced. At the equilibrium distance (d_0), the resulting energy bands are separated by a forbidden zone of size E_g. Modified and redrawn from Ibach & Lüth (2009).

As quantum-mechanical calculations (Demtröder 2005; Kittel 2006) and the above considerations show, there is a band gap or energy gap E_g between the energy bands which results directly from the periodicity of the lattice and its potential (Fig. 1.7). The location of E_F within the system of energy bands determines the electric conductivity and divides materials into conductors, semi-conductors and insulators. In case of conductors,

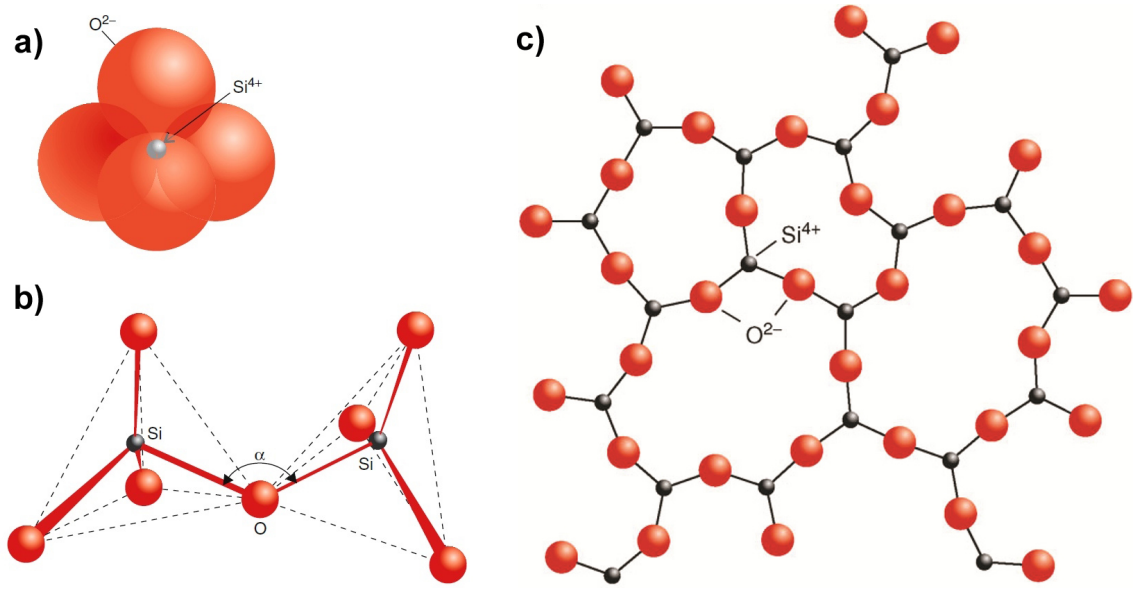

Figure 1.8: Molecular structure of amorphous SiO_2. SiO_4 tetrahedra (a) are connected to each other by shared O atoms with bonding angles α (b). Due to the lacking long-range order of amorphous materials, the bonding angles vary in between connected molecules (c). From Demtröder (2005).

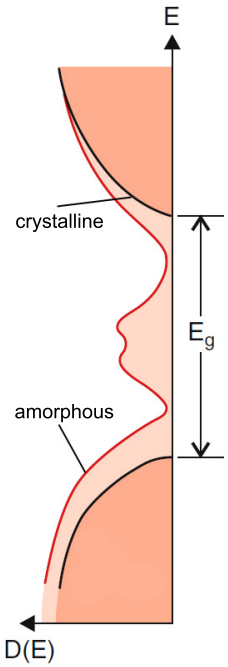

Figure 1.9: Distribution of electronic states in crystalline and amorphous solids, here shown for silicon. Clearly defined band edges separate valence and conduction band in case of crystalline Si, while varying bonding angles lead to band tails reaching into the band gap for amorphous Si. Dangling bonds are responsible for the creation of electronic states in the band gap. The situation may be similar for amorphous and microcrystalline SiO_2, except for dangling bonds which are expected to be saturated by O atoms. $D(E)$ describes the density of states as a function of energy. Modified from Demtröder (2005).

E_F lies within an energy band (which is then only partly filled with electrons), whereas it is located in the band gap for semi-conductors ($E_g \sim 1$–$2.5\,\mathrm{eV}$) and insulators ($E_g > 2.5\,\mathrm{eV}$) (Yukihara & McKeever 2011). The energy gap of quartz is $\sim 8.5\,\mathrm{eV}$ (Bailey & McKeever in prep.). Of interest for the luminescence process are only the highest band filled with electrons (*valence band*) and the lowest empty band (*conduction band*).

In ideal crystals, the edges of valence and conduction band are sharply defined and for electrons it is forbidden to enter the band gap (zero probability of finding an electron there since there is no solution of the Schrödinger equation in this energy interval). In contrast, amorphous and to a certain extent microcrystalline SiO_2 misses a long-range order of atoms, while a short-range order (next neighbors) is still given by the configuration of SiO_4 tetrahedra (Fig. 1.8). The amorphous character is related to varying bonding angles of the molecules and local shifts in energy what finally leads to valence and conduction band tails reaching into the band gap (Poolton et al. 1995; Demtröder 2005).

Deviations from the perfect crystal structure are prerequisites for the occurrence of luminescence. In fact, the regular and well-ordered configuration of atoms in crystals is always disturbed to a certain extent. These aberrations from the ideal lattice structure (termed as *defects*) occur at concentrations in the range 10^{-8}–10^{-7} and can form due to chemical or physical treatments, exposure to ionizing radiation or already at time of mineral growth (Wagner 1995). In general, there are three groups of defects to be distinguished (Mahesh et al. 1989; Kittel 2006):

- **Vacancies** (Schottky defects): An atom is removed from its place and leaves a vacant lattice position. Even in a perfect crystal, there is always a certain number of vacancies at thermal equilibrium (for $T > 0\,\mathrm{K}$). Common vacancies in quartz are E' centers, i.e. types of oxygen vacancies (Preusser et al. 2009).

- **Interstitials** (Frenkel defects): An atom is removed from its place and occupies an interstitial site. As for Schottky defects, interstitial atoms occur always at $T > 0\,\mathrm{K}$.

- **Substitutions**: An atom of the regular lattice structure is replaced by an atom of similar atomic radius, e.g. substitution of Si^{4+} by Al^{3+} in quartz. Apart from Al^{3+}, only a limited range of ions (Ga^{3+}, Fe^{3+}, Ge^{4+}, Ti^{4+} and P^{5+}) is capable of subsituting Si^{4+}, owing to its small ionic radius. For charge compensation, alkali ions such as H^+, Li^+ or Na^+ are incorporated along the channels of the *c*-axis in the quartz lattice. The concentration of substitutional atoms in minerals is closely related to the conditions of mineral formation (Krbetschek et al. 1997; Preusser et al. 2009).

The types of defects listed here are point defects, i.e. are restricted to singular displacements only. These defects are most relevant for the occurrence of luminescence (Krbetschek et al. 1997). Other lattice defects can be of larger dimensions, such as lattice

translations, edge dislocations or the inclusion of foreign minerals (impurities). Furthermore, the crystal surface itself can also be regarded as an extensive defect. Gradients in concentrations of point defects lead to temperature-dependent diffusion of defects within the crystal (Demtröder 2005; Kittel 2006). All types of defects have in common that their presence is connected to a region of net charge within the crystal that is capable of attracting free charge carriers (electrons or defect electrons). For instance, an oxygen vacancy in quartz causes a positive net charge, and charge compensation is achieved by trapping a negatively charged electron.

With respect to the energy band model, defects account for the creation of discrete energy levels within the forbidden zone that can be occupied by electrons or defect electrons (holes). Whether defect sites are occupied by electrons or holes is determined by the position of the Fermi level E_F which lies in between the valence and conduction band for quartz. Below E_F, electrons are abundant (all electronic states are filled) and losing an electron – being equal to attracting a hole – is more likely than gaining another electron. Therefore, near the valence band edge defect sites act as hole trapping sites (Fig 1.10). Inversely, trapping sites above E_F and near the conduction band edge attract electrons, thus termed as electron traps (Bailey & McKeever in prep.).

Naturally occurring amorphous SiO_2 phases, such as silex materials being of concern for this study, are often found in combination with fibrous or grainy microcrystalline structures. Moreover, silex is known to be a very impure mineral, influenced by additional organic impurities and crystal water (see Section 1.2), for which reasons the exact band configuration and the luminescence behavior are difficult to predict and presumably prone to large variations between samples.

The basic mechanisms of charge transfer underlying the generation of luminescence can be illustrated in idealized form using the energy band model. While the system of charge movements is understandable either by electrons or holes as mobile charge carriers, focus will be set on electrons here for the ease of explanation. Initially, none of the trapping sites is occupied and all valence electrons are bound to atoms, i.e. are located in the valence band. Ionizing radiation (e.g. α-, β- or γ-radiation, X-rays) is able to detach valence electrons from the atomic union, and they may gain enough energy to be lifted into the delocalized band (conduction band) where they can move freely through the compound. The missing electron leaves a hole that can similarly propagate through the valence band. Most of the electrons immediately return to the valence band and recombine with holes. Through interactions and collisions with atoms and impurities, the electrons in the conduction band gradually slow down, lose energy, and some of them become trapped, if the potential energy of Coulombic attraction of the defect exceeds the kinetic energy of the electron. The energy needed to overcome this potential determines the thermal lifetime of the trap which is defined as the average time τ an electron is expected to be caught in the trap. Assuming first-order kinetics (no retrapping of electrons after their release), the basic charge rate equations give (Aitken 1985b; Bailey & McKeever in prep.):

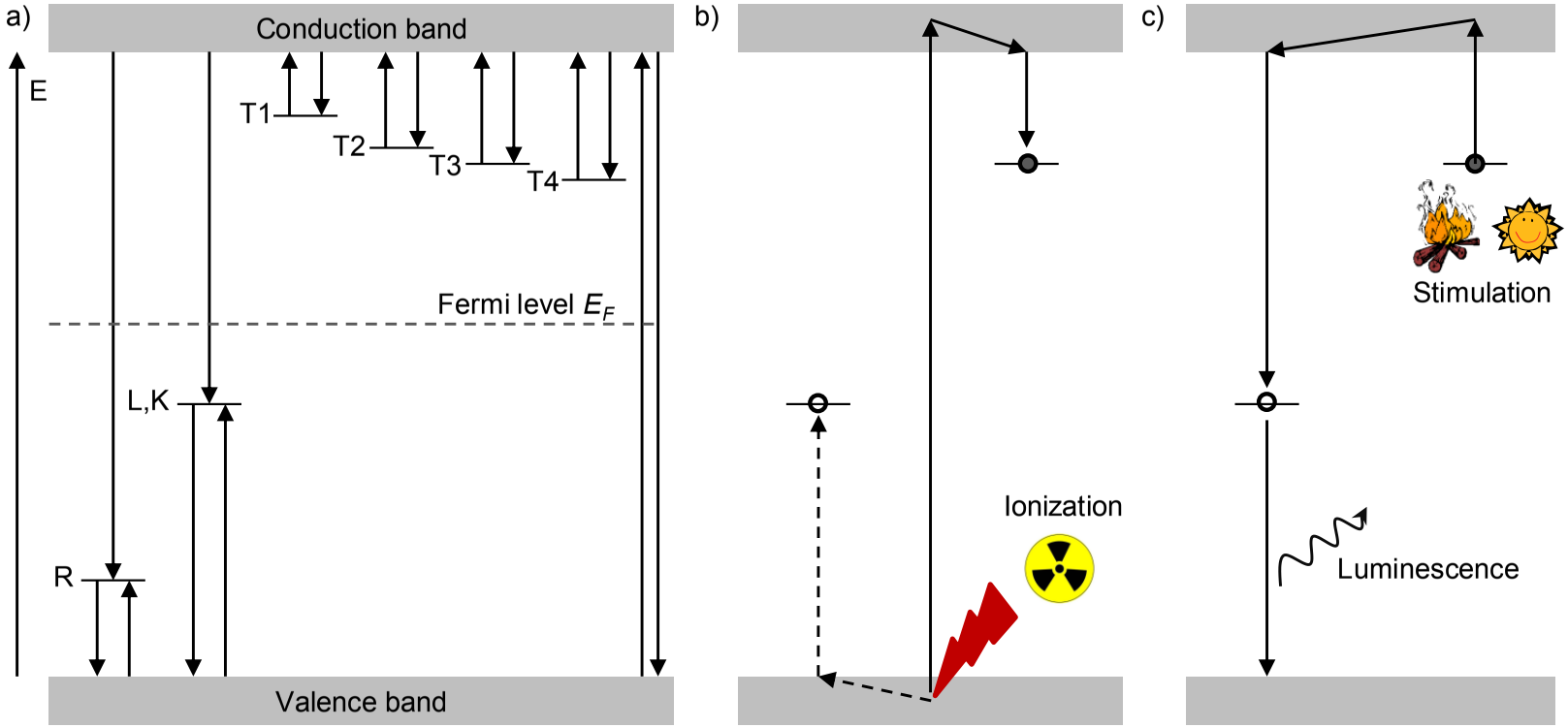

Figure 1.10: Energy band diagram with traps and recombination centers showing charge transfer processes. In figure (a), the Fermi level E_F separates electron traps from hole traps. Furthermore, the distance of electron traps from the conduction band edge corresponds to their trap depths, i.e. T1 illustrates shallow and thermally instable traps (e.g. the 110 °C TL trap), whereas deeper traps (T2 – T4) are thermally stable over Paleolithic time scales. The recombination centers, denoted as L and K, represent luminescence and "killer" centers, the latter being characterized by radiationless recombination. Absolute and relative concentrations of L- and K-centers thus control the luminescence output for a given amount of released electrons. Reservoir centers (R-centers) are located closer to the valence band edge and are hence less thermally stable. They can store holes temporarily and play a role in modelling of dose quenching and sensitization. Although only one type of L-, K- and R-center is shown here, there may be several types of each center in a sample, similar to the depicted electron traps. Possible routes of electron transfer are shown as arrows. The filling of electron traps and hole traps (called "centers" if occupied) due to interaction with ionizing radiation is displayed in figure (b) (open circle = hole, filled circle = electron). The captured electron can be freed and lifted to the conduction band by external stimulation (heat, light) and a small percentage recombines at L-centers, whose relaxation from an excited state to the ground state is related to the emission of light (luminescence), as shown in (c). The processes sketched in this figure are, however, idealized mechanisms for crystalline solids and may be far more complicated in heterogeneous materials such as silex. Modified from Aitken (1985b), Bailey (2001) and Bailey & McKeever (in prep.).

$$\tau = s^{-1} \cdot \mathrm{e}^{\frac{E}{kT}} \tag{1.1}$$

where s (in s^{-1}) is a frequency factor (describing the interaction of lattice and electron), E (in eV) the thermal activation energy needed to release the electron from the trap to the conduction band (also called "trap depth"), k Boltzmann's constant and T (in K) the temperature. The lifetime τ at the estimated burial temperature has to be at least ten times the period to be dated for the thermal loss of electrons to be $< 5\,\%$ (Aitken 1985b). The decisive parameters for the lifetime are therefore the trap depth E, indicated in the energy band diagram by the distance of the trap to the conduction band edge, and the frequency factor s. Wintle & Aitken (1977) reported a lifetime of $\sim 50\,\mathrm{Ma}$ for the $\sim 370\,^{\circ}\mathrm{C}$ peak in flint which is sufficient to allow dating back to the beginning of the Middle Paleolithic. Correspondingly, holes can be trapped at defects with negative net charge – then referred to as hole traps – with equal conditions for their lifetimes. With supply of sufficient external energy (stimulation with heat or light), the trapped electrons may escape to the conduction band and recombine either with holes in the valence band or with trapped holes. However, thermal eviction applies to trapped holes in the same way as to trapped electrons; therefore hole traps suited for recombination (then called recombination sites or centers) have to exhibit sufficient thermal stability and are thus located towards the mid-gap region in the energy band scheme (Yukihara & McKeever 2011). The transition of an electron from an excited state of the recombination site to the ground state yields the luminescence (see Section 1.3.2.2). There is also the possibility of electrons to become retrapped; in this case second-order kinetics must be considered. Finally, with all electrons having recombined with holes either in the valence band or at recombination sites, the initial state is restored.

Apart from recombination centers giving luminescence (L-centers), thermally stable so-called "killer centers" or K-centers lead to radiationless recombination (see Fig. 1.10). In addition, Zimmerman (1971b) postulated thermally unstable reservoir centers (R-centers) which compete for holes with L-centers. It is obvious that the amount of recorded luminescence not just depends on the number of released electrons, but to a high degree also on absolute concentration and relative abundance of activated (i.e. occupied by a hole) L-, R- and K-centers and their individual properties. Accordingly, each variation in population density of both traps and the various kinds of centers, e.g. in the course of light or heat exposure or irradiation, affects the light output per administered unit dose of radiation. These sensitivity changes of the dosimeter have to be monitored throughout the measurement procedure to avoid errors in the estimate of D_e. Based on the work of Zimmerman (1971b), subsequent empirical studies and models (Wintle & Murray 1999; Li 2001; Bailey 2001) made use of R-centers to explain sensitivity changes induced by irradiation and thermal treatment. Following this theory, R-centers compete for holes with L-centers during irradiation, thus reducing luminescence sensitivity compared to the state of com-

plete absence of R-centers. This effect is referred to as *dose quenching* and its magnitude is related to the relative abundance of L- and R-centers and their hole trapping probabilities. Bailey et al. (2005) suggested to frequently interrupt prolonged artificial irradiation by preheat steps (pulsed irradiation) to empty the R-centers and avoid pronounced dose quenching at high doses. In a more general way, heating the sample is thought to release holes from R-centers and to transfer them into L-centers which are then activated, causing an increase of sensitivity (*thermal activation*).

In summary, the basic scheme of the energy band model, as illustrated in Fig. 1.10, is able to explain some essential features of TL and OSL (e.g. the glow curve shape), but fails to account for the entire variety of luminescence characteristics observed for SiO_2. Extension of the model may help to increase the field of explicable phenomena, such as the inclusion of reservoir centers to model sensitivity changes. Another approach adds deep, thermally disconnected electron traps to the band model which serve to explain supralinear dose response at low doses via trap competition effects (Faïn et al. 1994). Although the energy band model is by far the most widely used one, it should not be omitted that there are other approaches/models seeking to explain the luminescence phenomenon in insulators, such as the defect pair model (Itoh et al. 2002; Preusser et al. 2009).

1.3.2.2 The process of luminescence production – a more detailed view

Phenomena such as luminescence emission of recombination centers, Stokes shift and thermal quenching can be explained qualitatively by the *configurational coordinate diagram* (Mahesh et al. 1989; Gaft et al. 2005; Bailey & McKeever in prep.). This model takes into account the adaption of the potential energy of ground state and excited state of the center considering its next neighbors, in comparison to the case of the perfect mineral structure (i.e. the absence of the center).

The presence of a defect means a change in the charge configuration, to which the direct neighbors and the respective ion itself adjust and take a new position of equilibrium. The equilibrium positions of ground and excited states may differ and are indicated by the configurational coordinates Q_0 and Q_1 in Fig. 1.11. Exemplarily, this figure shows the potential energy (approximated by parabolic functions) of the ground and one excited state of the entire molecule. Excited states are characterized by more extended electronic wave functions, corresponding to less curvature of the potential curve. The recombination process includes at first the trapping of a delocalized electron to an excited state of the center (A). Since the probability of losing energy by generation of phonons is four orders of magnitude larger than by emitting photons (Gaft et al. 2005), the electron relaxes nonradiative to the lowest vibrational energy level of the excited state (transition $A \rightarrow B$). The quantized vibrational energy levels of each state are drawn as horizontal lines. From B, further vibrational loss of energy is not possible and the electron undergoes a transition to C, yielding a photon (luminescence). Due to the comparatively low mass of the electron, the electronic relaxation is very fast in relation to the reaction of the ionic configuration;

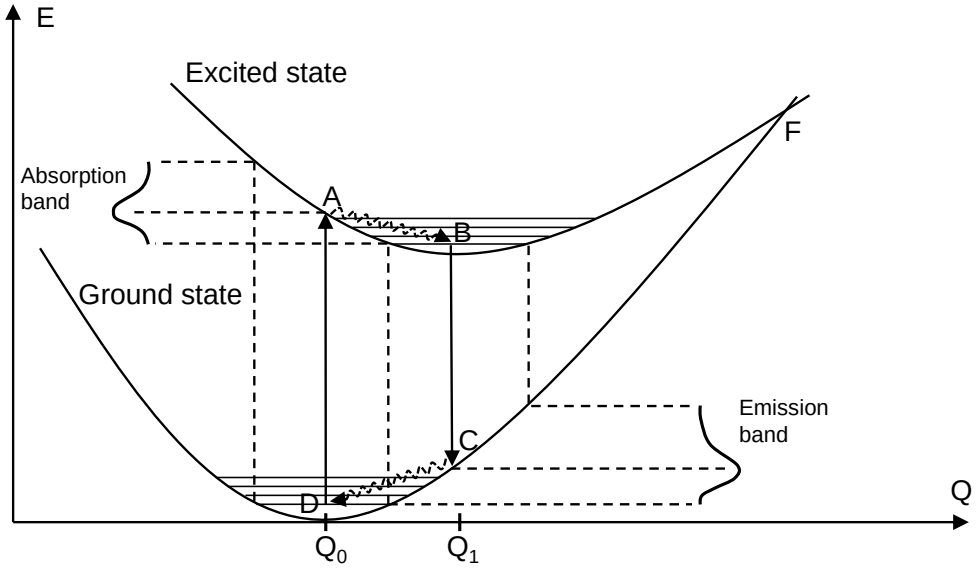

Figure 1.11: Configurational coordinate diagram. Electronic transitions related to photon absorption or emission are depicted as solid arrows, nonradiative transitions as dashed and oscillating arrows. See main text for further details. Modified from Gaft et al. (2005).

that is why the transition $B \rightarrow C$ may be indicated as a vertical arrow (Frank-Condon principle). Finally, the pathway $C \rightarrow D$, accompanied by phonon emission, brings the electron to the lowest energy level of the ground state. From there, it can be excited back to A by light absorption, and the cycle is repeated. Prompt luminescence emission during optical stimulation – termed as *photoluminescence* – is characterized by the emission energy being lower than the excitation energy (Yukihara & McKeever 2011). This effect is known as Stokes shift and can be directly deduced from the different lengths of absorption and emission arrows in Fig. 1.11 (Krbetschek et al. 1997; Gaft et al. 2005; Bailey & McKeever in prep.).

The configurational coordinate diagram further illustrates the existence and width of absorption and emission bands. In the lowest vibrational energy level of each state, the electron can be found anywhere along the horizontal line between the potential walls and, consequently, undergo the luminescence-emitting transition from different horizontal positions. The probability of finding an electron at a certain location at a certain time is given by the respective wave function of the state, with the highest probability in the middle (i.e. Q_0 and Q_1 in Fig. 1.11). Transitions from different points on the lowest levels result in different energies of absorbed and emitted photons, providing an explanation for the spectral width of absorption and emission bands (Mahesh et al. 1989; Gaft et al. 2005).

Wintle (1975) first decribed the effect of *thermal quenching* in quartz, which is in general defined as the decrease of luminescence efficiency with rising temperature, caused by increase of nonradiative transitions. Picking up the configurational coordinate diagram,

increasing thermal stimulation energy causes an electron in an excited state to take higher energetic levels. With sufficiently high temperature, it can finally reach the level of point F where both potential curves intersect. It is now possible for the electron to relax to the ground state nonradiatively, i.e. by exclusive emission of phonons. The factor η expressing the luminescence efficiency is exponentially dependent on temperature, as far as only one type of center is regarded (Wintle 1975):

$$\eta(T) = \frac{1}{1 + K \cdot \exp\left(-\frac{W}{kT}\right)}, \tag{1.2}$$

with K being a dimensionless factor and W the thermal activation energy. By inspection of Fig. 1.11, it is further clear that the likelyhood for thermal quenching changes with the distance Q_0 – Q_1: A small distance correlates with low thermal quenching and a large lateral displacement results in increased thermal quenching. The physical background of differences in horizontal offset of ground and excited state is the "strength of the coupling", describing the degree to which the defect ion is bound to its neighbors and is able to relax after photon absorption or emission. With final reference to Fig. 1.11, it is obvious that samples of the weak coupling case will also show small Stokes shift and less thermal quenching (Gaft et al. 2005; Yukihara & McKeever 2011; Bailey & McKeever in prep.).

An alternative model for the explanantion of thermal quenching to the one outlined above (Mott-Seitz model) is the Schön-Klasens model. According to that, thermal instability of recombination centers causes a temperature-dependent decrease of luminescence intensity (Yukihara & McKeever 2011).

When it comes to applied dating, sensitivity changes are the main obstacle to apply regenerative-dose measurements (see Section 1.3.4 and Chapter 7). If not adequately corrected, sensitivity changes due to heating, bleaching or irradiation lead to dose over- or underestimation, as sketched in Fig. 1.12. Usually, sensitivity changes are monitored and accounted for by the response to a constant test dose in the course of the measurement procedure (Murray et al. 1997; Murray & Wintle 2000). As a temperature-dependent process, thermal quenching affects high-temperature TL peaks, and this may be problematic for samples yielding low signal levels on the one hand or measurement conditions entailing increased background levels on the other hand (e.g. red TL). To increase the signal-to-noise ratio, it may thus be advantageous to shift the signal of interest towards lower temperatures, for instance by using low heating rates (see Section B.2.2 and Fig. B.5).

1.3.2.3 Overview of luminescence emissions of silex and associated defects

From the preceding sections, it follows that the type of recombination center controls the energy of the emitted photon (and thus the wavelength and color of luminescence). Spectral measurements thus serve to identify the causative defects. Beside early investigations

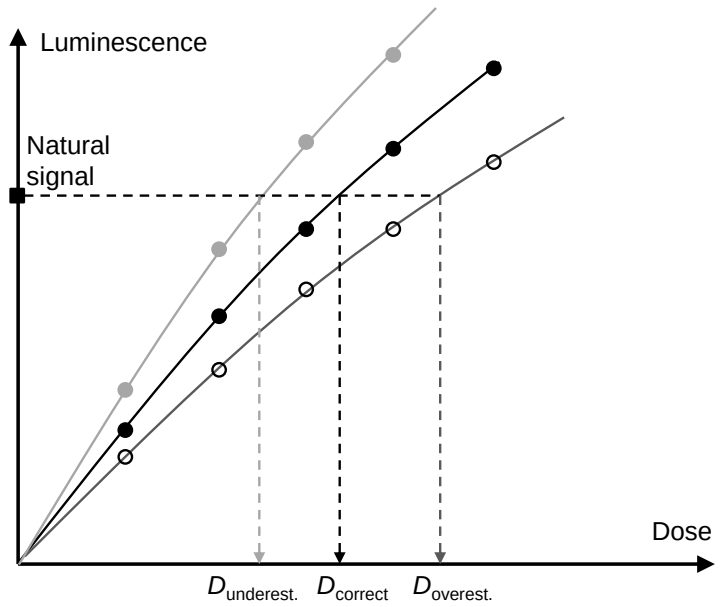

Figure 1.12: Influence of sensitivity changes on dose determination. Using the single-aliquot regenerative-dose (SAR) protocol, a dose response curve is constructed, on which the natural luminescence signal is projected to give the equivalent dose (D_e). Black circles and the fitted dose response curve represent the case of zero sensitivity changes, leading to the correct dose D_{correct}. If, however, the sensitivity of the sample increases (grey circles) or decreases (black rings) during the measurement sequence, the dose is either under- or overestimated, respectively.

using different filter combinations (Wintle & Aitken 1977; Huxtable 1982), only few studies concerned with spectrally resolved luminescence measurements of silex have been published up to now (Bailiff et al. 1977; Martini et al. 1999; Richter et al. 1999). Furthermore, the attribution of observed emission bands to distinct defects in silex has not been attempted so far. The similarities between the emission patterns of silex and quartz, however, gives rise to the hypothesis that close analogies may be found between the type of defects involved in both materials (Rink et al. 1993). The main emissions of TL and OSL and their associated defects will be listed in the following.

Thermoluminescence

Ultraviolet emission ($\sim$320–380 nm). This band is recorded in all types of investigated samples; Martini et al. (1999) further detected an ultraviolet (UV) emission at $\sim$260–330 nm in Italian flint. The corresponding glow curves were observed to peak at $\sim$100 °C and $\sim$360 °C, however strongly depending on the samples and the heating rate used (Martini et al. 1999; Richter et al. 1999). The electrons released from traps of increasing depths during heating are supposed to recombine all at the same center. While Richter et al. (1999) doubted the suitability of this emission for dating due to measured athermal signal loss (*fading*) and its light sensitivity (also at red light laboratory

conditions), a series of TL ages from various Paleolithic sites was obtained using a filter with maximum transmission at 380 nm (Mercier et al. 1999; Mercier et al. 2007a; Valladas et al. 1999; Valladas et al. 2008). Combined electron spin resonance (ESR) and TL measurements of quartz suggested the UV emission at ∼380 nm to come from recombination at $[H_3O_4]^0$ or $[AlO_4/M^+]^0$ centers, while for emission with slightly higher energies also oxygen vacancies are discussed as possible origin (Alonso et al. 1983; Yang & McKeever 1990; Rink et al. 1993; Itoh et al. 2002).

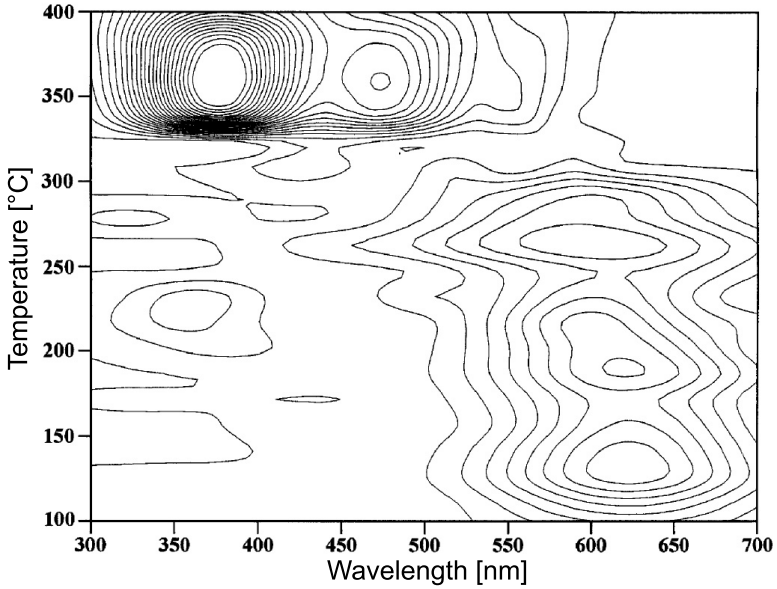

Figure 1.13: TL spectrum of a Cretaceous flint sample. The contour plot shows the three main TL emissions (UV, blue and orange-red). The sample was annealed and irradiated with 2 kGy prior to the spectral measurement. The spectrum itself is not corrected for instrumental response, that is why the red emissions appear to be of lower intensity than those in the UV and blue. From Richter et al. (1999).

Blue emission (∼ 430–500 nm). Being a common emission in silex, its peak positions in the glow curve are roughly similar to those of the UV band for the samples investigated. However, for a few samples additional peaks in the temperature range 200–320 °C or overlapping peaks with variable intensities between samples are reported (Martini et al. 1999; Richter et al. 1999). The centers proposed for giving rise to the broad blue emission in quartz include a self-trapped exciton emission at ∼450 nm (Stevens Kalceff & Phillips 1995) and the $[AlO_4]^0$ center in the range 470–500 nm (McKeever 1991).

Orange-red emission (∼ 580–640 nm). Orange-red TL (henceforth RTL) was recorded for all samples under study in Martini et al. (1999) and Richter et al. (1999), but was completely lacking for silex samples from Romania investigated in the frame of this work (see Section 6.3.2.2). While the samples in the aforementioned studies show RTL peak positions in the range 100–300 °C, a peak at ∼380 °C was observed for Baltic flint and

various other samples at ∼630 nm (pers. observation). Richter et al. (1999) proposed the orange-red emissions at ∼250 °C for dating of "low heated silex". Usually, the orange-red signal is the dominant one in the spectrum, but is mostly "quenched" during regular TL measurements if no red-sensitive photomultiplier is used, due to the low quantum efficiency (in the order of 1 % at 600 nm) at high wavelengths of conventional photomultipliers attached to the luminescence readers (Fattahi & Stokes 2000b). Furthermore, the orange-red band is known to have saturation dose levels far exceeding those of the UV and blue bands: Fattahi & Stokes (2000a) report values for the characteristic saturation dose D_0 of 6.3 kGy and continued signal growth was observed for doses up to 20 kGy for volcanic quartz (Ganzawa & Maeda 2009) and up to 50 kGy for xenolithic quartz (Miallier et al. 1991). The value D_0 describes the dose for which the luminescence signal reaches $1 - e^{-1}$ (∼63 %) of its saturation level, assuming a single saturating exponential form of the dose response curve. Own experiments on Baltic flint veryfied the findings of high saturation dose, yielding a D_0 value of ∼7 kGy. Little sensitivity changes following repeated irradiation and TL measurements led Richter & Krbetschek (2006) to introduce a RTL single-aliquot regeneration (SAR) protocol for equivalent dose estimation without the need of test dose correction. In fact, RTL sensitivity changes seem to be sample-dependent (cf. TL samples from Sodmein Cave as illustrating examples, Section 7.3) and their correction during the measurement procedure was applied for most of the samples dated in the context of this study (see Chapter 7). Possible candidates for the recombination center causing the orange-red emission in quartz are the non-bridging oxygen hole center (NBOHC) and various precursors (Götze et al. 2001) as well as oxygen vacancies (E' centers) (Luff & Townsend 1990). Hashimoto (2008) attributes the formation of NBOHC to two closely incorporated Al impurities whose attractive potential breaks a Si–O–Si bond, finally causing an RTL center. This proposition correlates with his observation of a functional relationship between Al content of quartz samples and their RTL intensity.

Optically stimulated luminescence

Only one study was so far concerned with OSL properties of different silex materials (Poolton et al. 1995). The authors show that the OSL emission of silex is more complex than in the case of macrocrystalline SiO_2, comprising both dose- and time-dependent and dose- and time-independent parts. The anti-Stokes shifted dose-dependent signals are attributed to the microcrystalline phase, while the dose-independent Stokes and anti-Stokes shifted emission are supposed to arise from the amorphous phase (see also Section 1.3.2.2). The difference of OSL features between silex and quartz is underlined by the fact that continuous absorption and emission spectra are observed rather than separate emission bands, respectively (Fig. 1.14). Poolton et al. (1995) further observed a more rapid signal decay of the dose-dependent component than expected for quartz and found the saturation dose

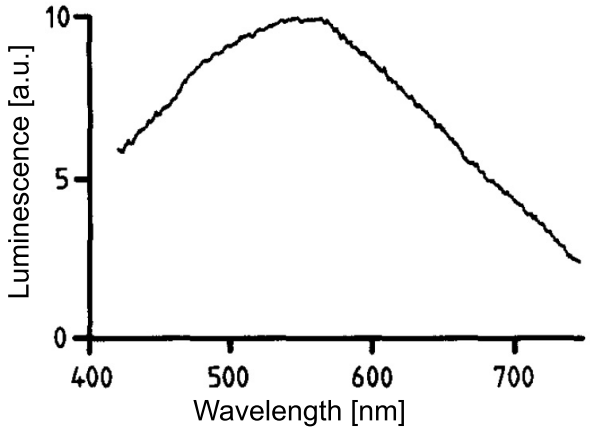

Figure 1.14: Photo-stimulated emission spectrum of flint. Shown is the dose-independent Stokes shifted signal component of a flint sample from Laugerie Haute (France). Excitation wavelength is 340 nm, the spectrum was corrected for instrumental response. From Poolton et al. (1995).

level D_0 to lie far beyond 300 Gy. Unfortunately, the paper contains no information about the signal integrals used for data analyses. From pulse annealing experiments, it is finally concluded that the dose-dependent signal is related to a TL peak at $\sim 180\,^{\circ}\mathrm{C}$ and is hence not thermally stable enough for dating of Paleolithic events.

In contrast to recombination centers, information on the defects associated with certain electron traps is much more difficult to obtain. Whilst spectrometric data recorded under certain conditions can be used for identifying correlations between emission bands and recombination centers, the only measurable property of a TL trap is its peak temperature in the glow curve. The peak temperature, however, does not provide any information on the type of defect involved (McKeever 1984; Preusser et al. 2009). Only in combination with other methods (e.g. ESR), assignment of certain traps to specific defects is possible. For instance, McKeever et al. (1985) attributed the mechanism responsible for the 100 °C TL peak (usually "110 °C peak") to a $[GeO_4]^0$ site which turns into $[GeO_4]^-$ when capturing an electron. For OSL measurements, suitable traps are selected by appropriate preheat procedures, but the general problem of scarce information on the trap-related defects remains. For more detailed information on emissions and associated defects, the reader is referred to e.g. Rink et al. (1993), Krbetschek et al. (1997), Götze et al. (2001), Preusser et al. (2009), King et al. (2011a) and King et al. (2011b).

1.3.2.4 Mathematical description of TL and OSL curves

In general, formula describing the luminescence intensity versus temperature (TL) or time (OSL) can be obtained by solving the differential equations which represent the charge flow between traps, centers and the delocalized bands during stimulation. For the sake of simplicity, we regard one type of trap and one type of recombination center only ("one

trap/one center model"), as first introduced by Randall & Wilkins (1945). Furthermore, the shape of TL and OSL curves depends on the kinetic order, i.e. the retrapping probability of freed electrons, and the mode of stimulation.

Thermoluminescence

Thermal stimulation is usually carried out by increasing the temperature linearly (constant heating rate), but can also occur at a fixed temperature (isothermal TL). With respect to the measurements made in the course of this study, only linearly ramped TL stimulation will be considered in the following.

The change of the density of occupied electron traps n with time t is seen as controlling the temporal course of luminescence. Provided that no retrapping occurs (*first-order kinetics*), the differential $\frac{\mathrm{d}n}{\mathrm{d}t}$ is proportional to the density of remaining occupied traps and to the probability of thermal eviction which is reciprocal to the electronic lifetime τ in a trap at the current temperature (Randall & Wilkins 1945; Mahesh et al. 1989):

$$-\frac{\mathrm{d}n}{\mathrm{d}t} = \frac{n}{\tau} = ns \cdot \mathrm{e}^{-\frac{E}{kT}} \tag{1.3}$$

Parameters are defined as in Section 1.3.2.1. The minus sign at the beginning is inserted because the differential is negative (decreasing n with time) what is, however, impossible for the right hand side of the equation. The sample is warmed with a constant heating rate $q = \frac{\mathrm{d}T}{\mathrm{d}t}$ what allows elimination of t. Rearrangement and separation of variables give:

$$\frac{\mathrm{d}n}{n} = -\frac{s}{q} \cdot \mathrm{e}^{-\frac{E}{kT}} \mathrm{d}T \tag{1.4}$$

With initial conditions $T = T_0$ and $n = n_0$ at the start of heating and integration we obtain (whereas the integral of the right hand side is not solvable analytically) (Kitis et al. 1998):

$$n = n_0 \cdot \exp\left(-\frac{s}{q}\int_{T_0}^{T} \mathrm{e}^{-\frac{E}{kT'}} \mathrm{d}T'\right) \tag{1.5}$$

The emitted luminescence intensity I is seen as proportional to the change of the density of occupied electron traps, i.e. $I = c\,\frac{\mathrm{d}n}{\mathrm{d}t}$ (c = const.). We can combine Eq. 1.3 and 1.5, hence:

$$I(T) = c\,s\,n_0 \cdot \mathrm{e}^{-\frac{E}{kT}} \cdot \exp\left(-\frac{s}{q}\int_{T_0}^{T} \mathrm{e}^{-\frac{E}{kT'}} \mathrm{d}T'\right) \tag{1.6}$$

This equation describes the shape of a TL peak, generated by electrons released from a single trap type that recombine at a single type of center. The probability of electron

retrapping is assumed to be negligible, or in other words, there are much more recombination centers than traps. If, however, the concentration of traps and centers is similar, the likelihood of a liberated electron to become retrapped is approximately equal to its recombination, giving rise to *second-order kinetics*. The derivation of the formula is similar to that shown above, and according to Garlick & Gibson (1948) one obtains for the intensity of a second-order TL peak:

$$I(T) = \frac{c\,s\,n_0^2}{N} \cdot \mathrm{e}^{-\frac{E}{kT}} \left(1 + \frac{sn_0}{qN} \int_{T_0}^{T} \mathrm{e}^{-\frac{E}{kT'}} \mathrm{d}T' \right)^{-2} \tag{1.7}$$

where N is the concentration of all electron traps of a single type. As can be seen from this equation, the initial trapped charge concentration n_0 influences the shape of the TL peak, not just its magnitude as in the first-order case. Therefore, peak positions that shift with increasing n_0 and hence increasing dose, are indicative of non-first-order processes. A comparison of simulated first- and second-order TL peaks is shown in Fig. 1.16a. In practice, estimating the order of kinetics is often hampered by closely overlapping peaks that appear as one broad peak in the glow curve. Furthermore, there may be samples showing TL behavior somewhere in between the two cases outlined above, i.e. neither the conditions for first-order nor those for second-order kinetics apply. Then, general-order kinetics must be taken into account.

It is obvious that two parameters are essential to describe the properties of an electron trap, namely the trap depth E and the frequency factor s. Several methods have been proposed to derive E and s from measured glow curves, e.g. the method of two heating rates (Hoogenstraaten 1958), the initial rise method (Mahesh et al. 1989), the half-width method (Halperin & Braner 1960), the isothermal decay method (Spooner & Questiaux 2000) or glow curve deconvolution (Kitis et al. 1998; Subedi et al. 2012). However, it is important to note that recently, Subedi et al. (2012) found out that thermal quenching of glow curves may lead to erroneous results for all methods except the isothermal decay method, since thermal quenching alters the shape of glow curves in the high temperature region (above $\sim$100–150 °C). Glow curve reconstruction – i.e. correction for thermal quenching – circumvents this problem (Subedi et al. 2010; Subedi et al. 2012). An example of a reconstructed TL curve of a flint sample and the influence of thermal quenching on glow curve shape is depicted in Fig. 1.15.

Optically Stimulated Luminescence

During optical stimulation, similar conditions apply as for TL to set up the charge rate equations. For first-order kinetics and constant stimulation intensity the “one trap/one center model” gives (Yukihara & McKeever 2011)

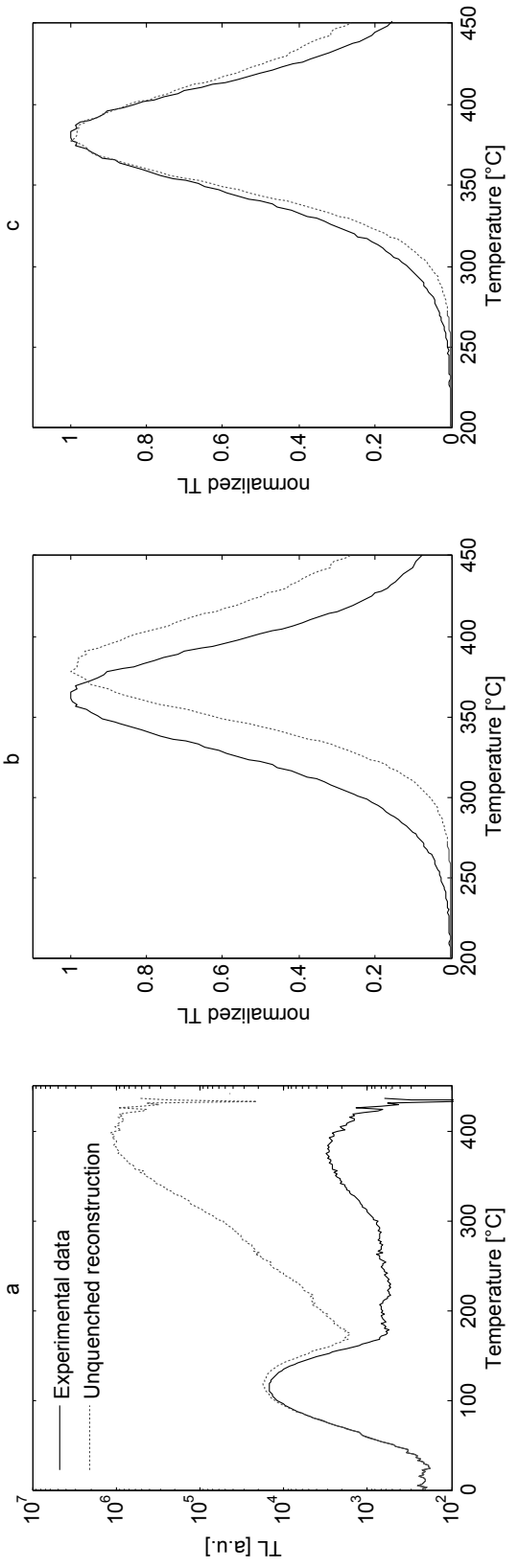

Figure 1.15: Influence of thermal quenching on glow curve position and shape. (a) Experimental and reconstructed (corrected for thermal quenching) glow curves of an artificially dosed Baltic flint sample, measured with a heating rate of $2\,\mathrm{K\,s^{-1}}$ in the orange-red detection window ($630\,\Delta\,60\,\mathrm{nm}$ interference filter). The activation energy W and the constant K of Eq. 1.2 were taken from Wintle (1975) as these parameters have not been determined for silex and seem to be universally valid for quartz (Subedi et al. 2012). (b) Peak shift caused by thermal quenching for the high temperature TL peak of the same Baltic flint sample. Measurement conditions were equal except for a blue-transmitting interference filter ($475\,\Delta\,50\,\mathrm{nm}$) used here to record the curve. To enable direct comparison, the maximum of both peaks was normalized to unity. (c) The same curves as in (b), however shifted for the peak maxima to coincide to illustrate the differing peak shapes of experimental and reconstructed glow curves.

$$-\frac{\mathrm{d}n}{\mathrm{d}t} = n\,p \tag{1.8}$$

with $p = \sigma\,\Phi$ being the probability per unit time for an electron to be optically released from the trap. The photoionization cross-section σ (in cm^2) describes the likelihood of optical detrapping of a captured electron as a function of stimulation energy and Φ is the stimulation intensity. Using the relation $I = c\,\frac{\mathrm{d}n}{\mathrm{d}t}$ and the exponential solution for $n(t)$ of Eq. 1.8, the intensity I of OSL with stimulation time t is

$$I(t) = c\,p\,n_0 \cdot \mathrm{e}^{-pt} \tag{1.9}$$

In case of non-first-order kinetics, Eq. 1.8 must be expanded to account for retrapping of freed electrons back into empty traps (Bøtter-Jensen et al. 2003):

$$-\frac{\mathrm{d}n}{\mathrm{d}t} = n\,p - n_c\,A(N-n) \tag{1.10}$$

All parameter definitions are as before; n_c denotes the momentary concentration of electrons in the conduction band. From the right hand side of the equation, the proportion of electrons is subtracted that is retrapped with the probability A per unit time. With A_m being the probability of an electron to recombine with a hole in a center, and some simplifying assumptions ($N \gg n$, $R = A/A_m \gg n/(N-n)$) the OSL decay curve of general-order kinetics can be written as

$$I(t) = \frac{p\,n_0^2}{NR}\left(1 - \frac{p\,n_0\,t}{NR}\right)^{\frac{b}{1-b}} \tag{1.11}$$

Here, $b > 1$ is the parameter indicating the order of kinetics (e.g. $b = 2$ for second-order). Experimental shine-down curves of natural quartz never show strict single exponential decay, as would be expected if the system followed first-order kinetics. Either non-first-order processes or a linear combination of first-order curves provide possible explanations for this observation. Bulur (1996) introduced a method of optical stimulation that enables a more intuitive separation of involved signal components (*deconvolution*). Analogous to linearly ramped TL stimulation, he suggested to linearly increase the stimulation light intensity (linearly modulated OSL, LM-OSL), with the consequence of a successive release of electrons from traps with increasing optical stability during measurement. Accordingly, the resulting LM-OSL curve looks similar to a TL curve, revealing several separate or overlapping peaks.

The initial charge rate equation for the differential change of the concentration of trapped electrons n in case of linearly increasing stimulation light intensity is (Bulur 1996; Bøtter-Jensen et al. 2003; Yukihara & McKeever 2011)

$$-\frac{\mathrm{d}n}{\mathrm{d}t} = n\,\sigma\,\frac{\Phi_{max}}{P}\,t \tag{1.12}$$

where Φ_{max} is the maximum stimulation intensity at the end of the measurement and P is the total measurement time. The solution for this differential equation is a Gaussian function. Assuming a composite signal consisting of κ first-order components, then the resulting sum curve can be written as

$$I(t) = c\,\frac{\Phi_{max}}{P}\,t\sum_{i=1}^{\kappa} n_{0,i}\,\sigma_i \cdot \exp\left(-\frac{1}{2}\sigma_i\frac{\Phi_{max}}{P}\,t^2\right) \tag{1.13}$$

Setting the derivative of this equation equal to zero gives the position of the peaks in the LM-OSL curve:

$$t_{max,i} = \sqrt{\frac{P}{\sigma_i \Phi_{max}}} \tag{1.14}$$

This implies that t_{max} only depends on the photoionization cross-section of the respective first-order component. For a non-negligible and unknown retrapping rate, time-dependent LM-OSL intensity of a signal composed of κ general-order components reads (Bulur 1996; Bøtter-Jensen et al. 2003)

$$I(t) = \frac{\Phi_{max}}{P}\,t\sum_{i=1}^{\kappa} n_{0,i}\,\sigma_i\left((b-1)\frac{\sigma_i\,\Phi_{max}}{2\,P}t^2+1\right)^{\frac{b}{1-b}} \tag{1.15}$$

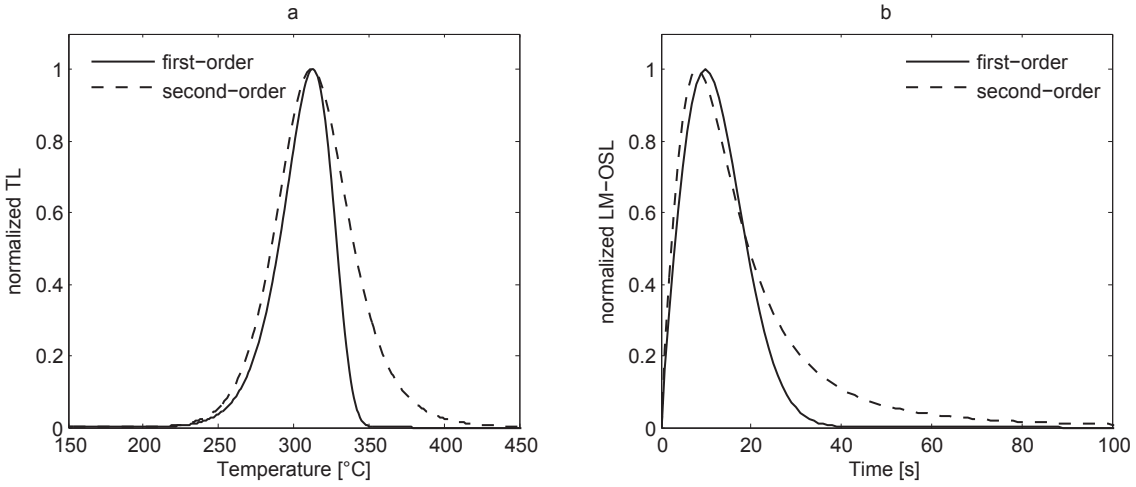

Figure 1.16: Simulated TL and LM-OSL curves of first- and second-order kinetics. The peak maxima in (a) were normalized to unity. The parameters chosen for the simulation were: $E = 1.78\,\mathrm{eV}$, $s = 6.7\cdot10^{14}\,\mathrm{s}^{-1}$, $n_0 = N$, $q = 5\,\mathrm{K\,s}^{-1}$ and $c = 1$. Glow curves were calculated with Matlab by solving numerically the integral in the exponent of Eq. 1.6 and 1.7. (b) Simulated LM-OSL curves of a single component according to Eq. 1.13 and 1.15 with parameters $\sigma = 2.5\cdot10^{-17}\,\mathrm{cm}^2$ and $\gamma = 0.01\,\sigma^{-1}$, where $\gamma t = (\sigma\tau)^{-1}$.

It must be noted that Eq. 1.15 holds true for the condition $n_0 = N$ (saturated traps) only (Bulur & Göksu 1999). Simulated LM-OSL curves for first- and second-order kinetics are shown in Fig. 1.16. Deconvolution by curve fitting has shown the presence of 3–7

LM-OSL components in quartz samples, named *fast*-, *medium*- and *slow*-components, whereas the latter is further subdivided into *slow1*-, *slow2*-, ... components. The optically most sensitive *fast*-component is characterized by $\sigma \sim 2.5 \cdot 10^{-17}\,\mathrm{cm}^2$, the optically most resistent one by $\sigma \sim 2 \cdot 10^{-21}\,\mathrm{cm}^2$ (Jain et al. 2003; Singarayer & Bailey 2003). Goble & Rittenour (2006) refer to a thermally unstable *ultrafast*-component which seems to be a rare observation though. Furthermore, the photoionization cross-section is wavelength- and temperature-dependent (Bailey 2002; Singarayer & Bailey 2003). Variations of σ with stimulation energy can be used to selectively bleach certain components, as done e.g. by Bailey (2010) for the *fast*-component which has proven to have the most suitable properties for optical dating. Since at least one component has shown insufficient thermal stability (Jain et al. 2003; Singarayer & Bailey 2003), careful choice of the signal part used for dose estimation is crucial. Investigations on the components involved in the OSL signal of silex have not been attempted so far.

1.3.3 The dose rate, its constituents and determination

The stability of a nuclide is determined by the numbers of protons (Z) and neutrons (N) it is composed of. A quite narrow range of the numerical relation N/Z is characteristic for stable nuclides, all others (N too large or N too small) undergo radioactive decay to approach the stability zone. Moreover, nuclei with even numbers of Z and N are more stable than those with uneven Z and N. Radioactive decay may change Z and N of a nucleus, and since the number of protons is characteristic for an element, it may also lead to a transition from one element to another. This process is non-deterministic (spontaneous) and follows Poisson statistics. However, for macroscopical quantities, the law of exponential decay applies. An important parameter in this context is the half-life $t_{1/2}$ after which only half on the initial mass of a nuclide remains (Demtröder 2010). Since radioactive decay is a solely time-dependent process and independent of other state variables (e.g. temperature or pressure), it is the underlying mechanism not just of luminescence dating but also of other radiometric dating methods such as the α-recoil method or those based on mother and daughter abundance of nuclides (e.g. $^{39}\mathrm{Ar}/^{40}\mathrm{Ar}$) or radioactive disequilibria (e.g. $^{230}\mathrm{Th}/\mathrm{U}$ method) (Geyh 2005; Demtröder 2010).

If the decay product (often called daughter) itself is instable, it will undergo another decay. This process continues until a stable end product, characterized by a maximum of negative binding energy of the nucleons, impedes further decay. Such a sequence of stepwise decay and transformation of elements is referred to as a *decay chain* (see Fig. 1.17). Almost all naturally occurring radionuclides are part of one of three decay chains which are named after their mother nuclides ($^{238}\mathrm{U}$, $^{235}\mathrm{U}$ and $^{232}\mathrm{Th}$). The latter are, however, also daughters of nuclides with a much shorter half-life (e.g. $^{239}\mathrm{Pu}$, $^{240}\mathrm{Pu}$ or $^{239}\mathrm{U}$), so that the original heads of the decay chains are practically absent today (Demtröder 2010).

Since negative binding energies of nucleons increase along the decay chains, it is clear that radioactive decay is related to the emission of energy, either as α-, β- or γ-radiation.

U	Pa	Th	Ac	Ra	Fr	Rn	As	Po	Bi	Pb	Tl
92	91	90	89	88	87	86	85	84	83	82	81

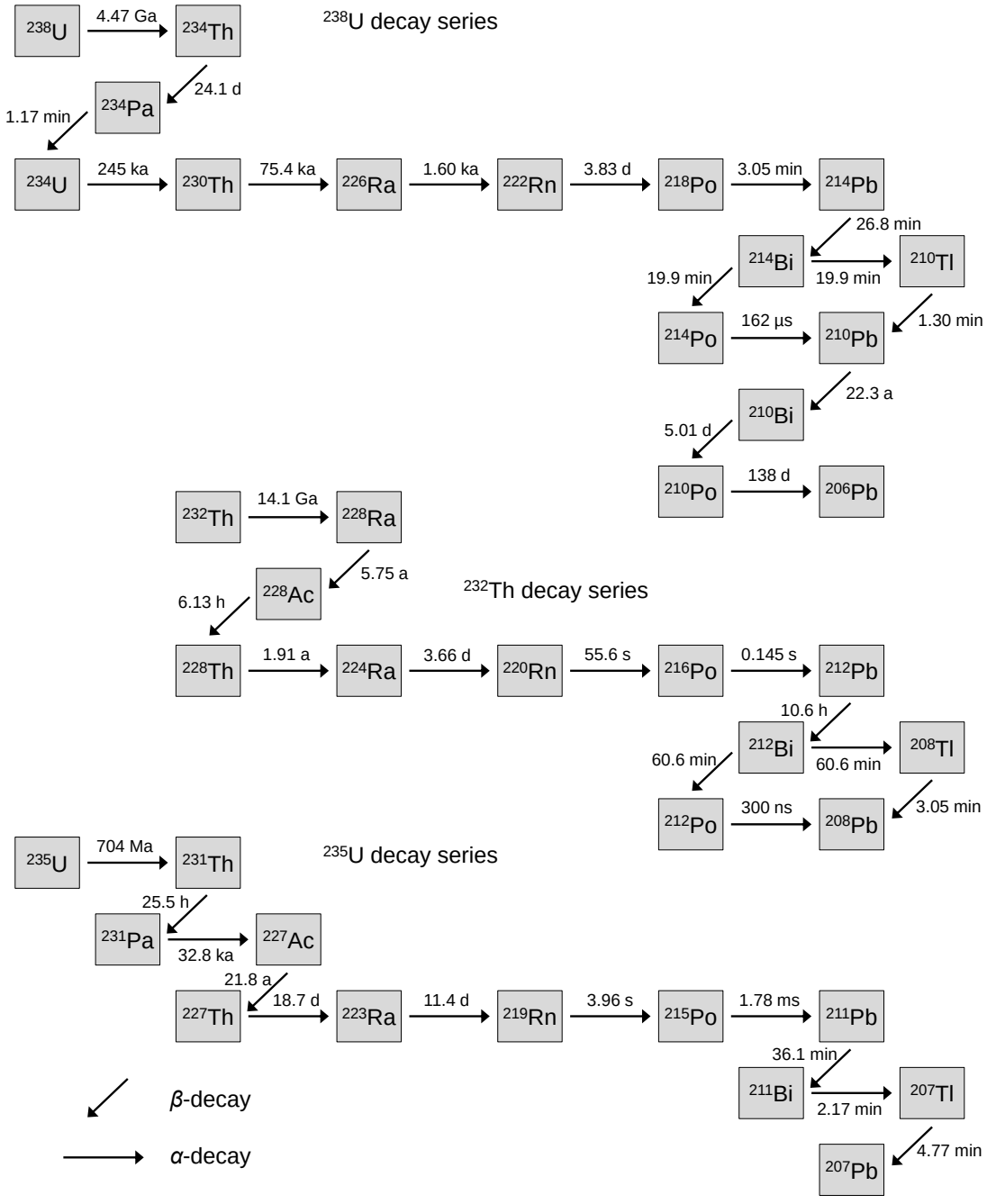

Figure 1.17: Decay series of ^{232}Th, ^{235}U and ^{238}U. This chart was modified from Geyh (2005) and the half-lives taken from there and Aitken (1998).

All of these radiation types are capable of detaching electrons from the atomic shell, leaving an ionized atom, for which reason they are called *ionizing radiation*. The energy needed to induce a latent luminescence signal is thus on the one hand derived from radiative decay of naturally occurring U and Th (with their radionuclides ^{235}U, ^{238}U and ^{232}Th) and, additionally, from the radioactive isotopes ^{40}K and ^{87}Rb which are not part of a decay chain. On the other hand, cosmic radiation contributes to the imparted energy (dose rate) as well. Recent values of the energy release per disintegration of ^{40}K and ^{87}Rb isotopes and of those of the U and Th decay chains are given in Guérin et al. (2011). The stopping power, i.e. the energy lost per unit length of path, can be used to describe the interaction characteristics of radiation with matter in regard to the efficiency of luminescence production.

1.3.3.1 Low stopping power radiation

Radiation types with comparatively low stopping power are, for instance, β- or γ-radiation and X-rays or cosmic rays, i.e. streams of charged particles and of high-energetic photons or, alternatively, electromagnetic waves. The most important decay and conversion processes will be described below.

Beta-decay and beta-radiation

Beta radiation consists of electrons or positrons, characterized by a continuous energy spectrum reaching from zero to $E_{\max}$ (several keV to several MeV, depending on the β-emitting nuclide). A nucleus emits an electron when a neutron is transformed into a proton. The reaction equation is as follows:

$$^{A}_{Z}\mathrm{X} \longrightarrow {}^{A}_{Z+1}\mathrm{Y} + \mathrm{e}^{-} + \overline{\nu} \tag{1.16}$$

Here, X and Y are different elements, it is $A = Z + N$, e^{-} represents an electron and $\overline{\nu}$ an antineutrino. The continuous energy spectrum of β-particles and observations of certain decay properties require the antineutrino as additional reactant to maintain conservation of energy and impetus. The average travel range of β-radiation depends on the density of traversed matter and is about 2 mm in rocks with a density of $2.5\,\mathrm{g\,cm^{-3}}$ (Wagner 1995; Aitken 1998). Due to the small rest mass of electrons, their ionization density is lower than e.g. that of α-particles (Geyh 2005).

A symmetrical process yields positrons (e^{+}), which are equal to electrons, but positively charged:

$$^{A}_{Z}\mathrm{X} \longrightarrow {}^{A}_{Z-1}\mathrm{Y} + \mathrm{e}^{+} + \nu \tag{1.17}$$

where ν is a neutrino. However, the lifetime of positrons in matter is short since they annihilate with electrons by expelling two γ-quanta (Krieger 2007; Demtröder 2010).

Electron capture decay

Conversion of a proton into a neutron within the nucleus may also happen by capturing an electron from the atomic shell (mostly the K-shell):

$$ {}^{A}_{Z}\mathrm{X} + \mathrm{e}^{-} \longrightarrow {}^{A}_{Z-1}\mathrm{Y} + \nu \tag{1.18} $$

Electron capture does not lead to β-radiation, but yields characteristic X-rays caused by electrons succeeding from outer shells to the empty state of one of the inner shells. Furthermore, γ-radiation is emitted when the converted nucleus relaxes from an excited into the ground state (Meschede & Vogel 2006; Krieger 2007; Demtröder 2010).

Gamma-radiation

This type of radiation occurs in combination with α- and β-decay and consists of photons with energies in the range 10^4–10^7 eV (Demtröder 2010). A previous decay may have left the nucleons in excited rotational and vibrational states from which they relax by emitting characteristic γ-radiation/photons. Due to the intricacy of excited state configurations of the nucleus, γ-emissions can show a high degree of complexity (Krieger 2007; Demtröder 2010). During this process, Z and N do not change, because no charged particles are emitted. Having a rest mass of zero and thus low ionization density, the range of γ-radiation in siliceous rocks (mass density as above) is about 30 cm (Aitken 1998).

Cosmic radiation

Through interaction of primary, galactic radiation (e.g. protons, α-particles, electrons) with the earth's atmosphere, secondary radiation (e.g. pions, neutrons, protons, myons, electrons) is generated in form of cascades. The composition of the secondary radiation changes with altitude, with mainly myons remaining at sea level due to absorption and interaction of most particles in higher parts of the atmosphere (Krieger 2007). Considering further the influence of the earth's magnetic field, the cosmic contribution to the dose rate is consequently a function of altitude above sea level and geographic coordinates. Long-term variations of cosmic dose rate over the period of interest (Middle and Upper Paleolithic) are unlikely to exceed $\sim 3\,\%$ und can thus be neglected in most circumstances. With increasing depth below surface, the cosmic radiation rapidly falls off (Prescott & Hutton 1988; Prescott & Hutton 1994). The "weak" component of cosmic radiation (electrons, photons) is absorbed in the first tens of cm of the substrate, so that for deeper buried samples only the hard component (mainly myons) contributes to the dose rate (Aitken 1985b). Difficulties of cosmic dose rate calculation may arise in archeological

cave sites where the shape and thickness of the roof/abris significantly influences the myon flux at the sampling position (Smith et al. 1997).

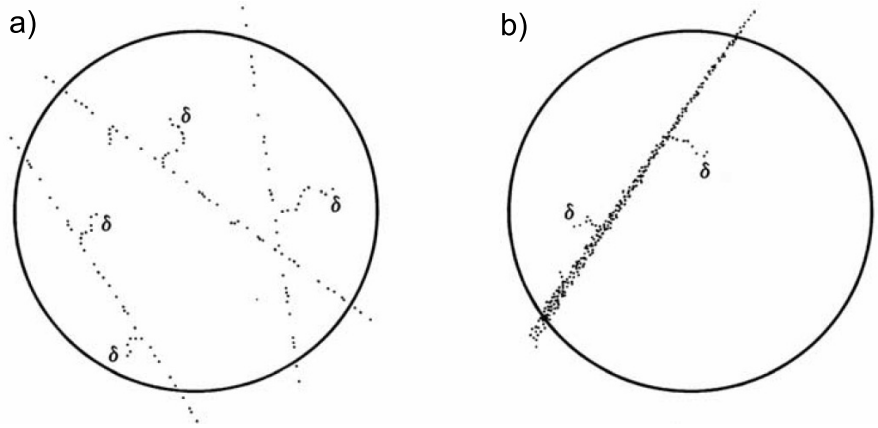

Figure 1.18: Illustration of radiation with different ionization densities. (a) Imparting slightly ionizing radiation (e.g. γ-radiation). (b) Track of an imparting particle of higher mass (e.g. α-particle). The total number of ionizing events in each circle and thus the mean deposited dose is equal in both figures. The small lateral tracks are caused by so-called δ-electrons which are the result of singular events with high energy transfer. From Krieger (2007).

The types of radiation described in this section have in common that they produce secondary electrons while traversing solid matter, and these, in turn, may cause further ionizing events. The scattering of these electrons and the overall slightly ionizing character of β- and γ-radiation gives rise to a roughly uniform distribution of ionizing events over the irradiated volume (Fig. 1.18). In other words, the simultaneous ionization of microscopically adjacent regions is very unlikely (Krieger 2007). By contrast, the ionization density – defined as generated charge of one algebraic sign per volume – of radiation with high stopping power is greater, as will be discussed in the following.

1.3.3.2 High stopping power radiation

Of all forms of radiation with high stopping power (e.g. protons, fission products), only α-radiation delivers significant contributions in terms of dosimetry for luminescence dating. In contrast to the quartz inclusion technique applied to sediments (Fleming 1978; Aitken 1998), the α-radiation may play a considerable role in determination of the internal dose rate of silex. Therefore, and with regard to the dosimetry investigations in Chapters 3 and 4, the interaction characteristics of α-particles with matter and the calculation of the effective dose rate will be outlined in more detail below.

Alpha-decay

During α-decay, a particle consisting of two protons and two neutrons ($^4_2$He) is emitted from a nuclei, leading to the reaction equation

$$^{A}_{Z}\mathrm{X} \longrightarrow {}^{A-4}_{Z-2}\mathrm{Y} + {}^{4}_{2}\mathrm{He} \tag{1.19}$$

The energy spectrum of α-radiation is discrete and energy and impetus conservation are fulfilled without an additional reactant (Demtröder 2010).

The interaction of alpha-radiation with matter

Having a comparatively large mass and ionization density, α-particles deposit high amounts of energy along the tracks they generate during impact. The rapid energy loss along a relatively short track classifies α-radiation as high stopping power radiation and is responsible for locally very high doses, in the order of 10^5 Gy in the core of the track (Waligórski et al. 1986). Those α-tracks are approximately 0.1 µm in diameter and a few tens of µm long in solids such as quartz (Zimmerman 1972; Aitken 1985b), depending on the energy of the α-particles (Fig. 1.19). Therefore, the ionizing energy is confined to a very small sample volume, in contrast to β- and γ-radiation. Within this cylindric volume around the α-track, much more free charge carriers (electrons) are generated than high energetic states (traps) are available. The bigger part of the absorbed energy can hence not be stored in such states and is lost for subsequent luminescence emissions. In fact, many other explanations of the limited ability of α-particles to induce luminescence were suggested, such as "thermal release" (the heat in the α-track causes a release of electrons from the traps) or "dead zones" (difference of luminescence efficiency of surface and sample interior). Zimmerman (1972) summarizes alternative models, however the approach given here ("high ionization/energy density") has proven to be the most stringent one. Nevertheless, this means the efficiency of α-radiation in luminescence production is lower than for slightly ionizing β- and γ-radiation. Consequently, a factor expressing the α-efficiency is considered in the age equation which will be discussed below.

On the other hand, the α-induced luminescence grows linearly up to doses for which the luminescence after β- or γ-irradiation is long in the non-linear (saturating) part of the growth curve (Zimmerman 1972; Aitken 1984). We can explain this with the small sizes of the α-tracks in comparison to the sample volume. Saturation effects (and thus the flattening of the dose response curve) begin not until the integrated α-flux is high enough for the α-tracks to overlap. Then, the α-efficiency further decreases. In the context of luminescence dating, very high doses must be applied to cause track overlap; Zimmerman (1972) reports doses of 1 kGy or more for Norwegian quartz. At even higher α-doses the energy density throughout the sample will be uniform and α- and β-induced luminescence will grow equally (Zimmerman 1972; Mauz et al. 2006). Furthermore, it should be noted here that Zimmerman (1972) found varying α-sensitivities for different TL peaks and a relationship between the β-saturation dose (D_0) and the α-efficiency: The higher D_0 – and thus the trap concentration – the higher will also the α-efficiency be, what can be directly deduced from the "high energy density" concept.

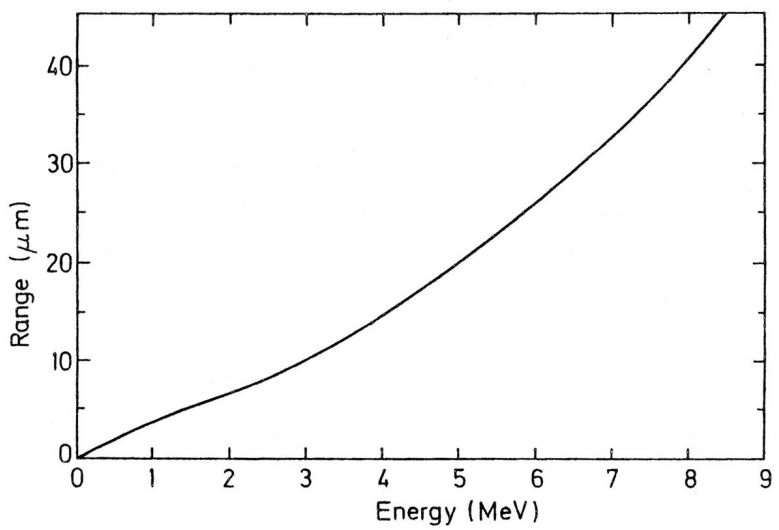

Figure 1.19: Alpha-particle attenuation. The range R of α-particles as a function of α-energy, calculated here for pottery (density $\rho = 2.6\,\mathrm{g\,cm^{-3}}$). From AITKEN (1985b).

The systems used for alpha-efficiency determination

Generally speaking, the α-efficiency is determined by comparing the luminescence signals after laboratory α- and β-irradiation. Most laboratories use ^{241}Am for α-irradiation, though there are radioistopes that emit α-particles with higher energies (e.g. ^{242}Cm, its disadvantages such as a short half-life are discussed in SINGHVI & AITKEN (1978)). Having a half-life of 432 a and α-particle energies of ~ 5.5 MeV, ^{241}Am is appropriate for controlled and convenient irradiation. This isotope also shows a weak γ-emission (0.06 MeV), but it is considered negligible in terms of deposited dose in α-thin sample layers (AITKEN 1985b).

Commercially available ^{241}Am-foils (Amersham, UK) are ~ 1 µm thick and protected by a 2 µm covering of Au-Pd alloy. This protective layer absorbs part of the α-energy, whereas the absorbed energy fraction is strongly dependent on the angle with which the particle passes through the protective layer. The longer the pathway through the covering, the more energy is lost there. For perpendicular incidence, the α-energy is reduced to ~ 4 MeV. Determination of α-efficiency requires that the α-particles have enough remaining energy to fully penetrate the sample layer. Otherwise, the luminescence recorded after β-irradiation is received from a larger sample volume than after α-irradiation, with the consequence of systematic errors of α-efficiency. This condition requires that only α-particles reach the sample which hit the covering layer perpendicular or within a tolerable angle. Therefore, in practice the distance of the source to the sample is increased with the drawback of reduced α-flux on the sample (AITKEN 1985b). For a common six position irradiation facility (Littlemoore), SINGHVI & AITKEN (1978) experimentally determined this distance to be at least 10 mm to cross the whole thickness of a "standard fine grain sample layer" (~ 8 µm). In order to prevent unnecessary energy loss, α-irradiation should always be carried out evacuated (the α-range in air is about 25 mm for ~ 4 MeV particles) (AITKEN 1985b).

Over the past four decades different concepts have evolved that account for the different luminescence efficiencies of α-particles in comparison to β- and γ-radiation. These approaches will be shortly outlined below. An overview of the various concepts and their interdependencies is also given by Aitken (1985a).

The *k*-value system

In this system, the amount of luminescence recorded after α-irradiation with 3.7 MeV particles with that recorded after β-irradiation is compared, giving as definition (Zimmerman 1971b; Aitken 1985a):

$$k_{3.7} = \frac{\text{Luminescence per Gy for 3.7 MeV } \alpha\text{-particles}}{\text{Luminescence per Gy for } \beta\text{-irradiation}} \tag{1.20}$$

For α-efficiency determination, it is important to use monoenergetic particles for the following reason: As the particle slows down, the energy loss $\frac{\mathrm{d}E}{\mathrm{d}x}$ in the sample is not linear, but increases, eventually reaches a maximum (the Bragg peak) shortly before decreasing sharply to zero when the particle comes to rest (Fig. 1.20) (Demtröder 2010; Krieger 2011). With reduced energy, an α-particle spends more time in a unit volume along the track which results in a higher interaction cross-section of particle and traversed matter. Since the dose in units of Gy is defined as $\mathrm{J\,kg^{-1}}$, the deposited dose is not constant throughout the pathway of the α-particle. This, however, also means that the α-efficiency (in terms of luminescence per deposited dose) varies with depth within the sample if a whole spectrum of α-energies is used for irradiation. Furthermore, the exact sample thickness is usually not known. Therefore, the only way of getting around those difficulties is to use monoenergetic α-radiation in order to 'crowd' the Bragg peak out of the sample and to be in the flat or moderately rising part of the Bragg curve (Fig. 1.20) (Krieger 2007).

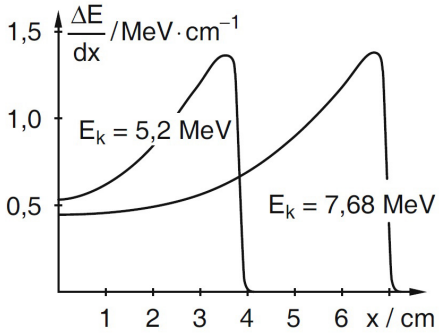

Figure 1.20: Energie loss of α-particles with covered distance. The Bragg curves show the energy loss $\frac{\mathrm{d}E}{\mathrm{d}x}$ in units $\mathrm{MeV\,cm^{-1}}$ of α-particles per unit track length in air (atmospheric pressure, 1 bar) for different α-energies E_k. From Demtröder (2010).

The α-energy of 3.7 MeV was the one used by Zimmerman (1972) in his basic experiments, but is somehow arbitrary as long as the energy is sufficiently high for guaranteed complete penetration of the sample layer. Clearly, in antiquity the sample received α-radiation not monoenergetically, but as a whole spectrum reaching from 0 to 8.8 MeV,

originating from the decay of U and Th and their daughter products. Consequently, correction is needed for the $k_{3.7}$-value to be adapted to the natural spectrum, resulting in the k_{eff}-value. The ratio $k_{\text{eff}}/k_{3.7}$ is 0.80 for the U series and 0.86 for the Th series. For equal U and Th activities, $k_{3.7}$ has thus to be multiplied by 0.83 to give the corrected value for insertion into the age equation (Zimmerman 1971a).

The *a*-value system

As described above, there are substantial difficulties in using the k-value system, such as the energy dependence of the α-efficiency. Zimmerman (1971a) and Aitken & Bowman (1975) found that the luminescence induced per unit track length is nearly independent of α-energy as far as the particle still has more than $\sim 2\,\text{MeV}$ on leaving the sample, and used this fact to introduce a new value expressing the α-efficiency, the a-value. The definition is (according to the nomenclature of Aitken (1985a)):

$$a = \frac{x}{13S} \tag{1.21}$$

where x is the dose in Gy required to produce the same amount of luminescence as 1 minute of irradiation with an α-source of strength S. Source strength S is now expressed in μm^{-2} min^{-1}, i.e. in generated track length per unit time. The numerical factor 13 can be deduced as follows (Aitken 1985b; Aitken 1985a): The energy loss of a 3.7 MeV α-particle is $0.21\,\text{MeV}\,\mu\text{m}^{-1}$ for a density of $2.6\,\text{g}\,\text{cm}^{-3}$. Therefore, a source of strength S generates per minute S µm track length per μm^3 sample volume, and thus deposits $0.21\,S\,\text{MeV}$ of energy per minute within the sample (produced track length multiplied by energy loss per track length). It is thus possible to calculate the absorbed dose per minute (i.e. the dose rate) by applying that the dose $D = E/m = E/(\rho \cdot V)$ and converting all units in SI units:

$$\frac{0.21 \cdot S \cdot MeV}{m \cdot \rho} = \frac{0.21 \cdot S \cdot 10^6 \cdot 1.6 \cdot 10^{-19} \cdot 10^6}{10^{-6} \cdot 2.6 \cdot 10^{-3}} = \frac{0.21 \cdot S \cdot 1.6 \cdot 10^2}{2.6} \approx 13 \cdot S \tag{1.22}$$

For quartz $a = k_{3.7}$, as can be seen from the above calculation. When the α-efficiency of other materials than quartz is to be determined, the ratio r of α-stopping powers of the investigated material and quartz have to be multiplied by the k-value, whereas the stopping power is given by $\rho^{-1} \cdot \frac{\text{d}E}{\text{d}x}$:

$$a = r \cdot k_{3.7} \tag{1.23}$$

The *b*-value system

As we have seen in the last section, the a-value is confusing in terms of physical units. That is why Bowman & Huntley (1984) proposed the b-value system which is more consistent and intuitive. It also operates with the track length concept instead of deposited dose:

$$b = \frac{\text{Luminescence per unit } \alpha\text{-track length per unit volume}}{\text{Luminescence per unit of absorbed } \beta\text{-dose}} \tag{1.24}$$

The unit of b is $\mathrm{Gy\,m^2}$. Although the a-value is, technically speaking, dimensionless, we can relate it numerically to the b-value if the latter is expressed in units $\mathrm{Gy\,\mu m^2}$:

$$b = 13a \tag{1.25}$$

Following the calculation of Bowman & Huntley (1984), an a-value of 0.03 would correspond to a b-value of $0.39\ \mathrm{Gy\,\mu m^2}$, or in other words, the TL induced by a β-dose of 0.39 Gy is the same as that induced by one incident α-particle per $\mu\mathrm{m}^2$.

The S_α-system

This system, proposed and applied by the French flint dating group (Valladas & Valladas 1982; Mercier et al. 1995), operates with the flux of α-particles instead of deposited dose. The definition is (according to the original nomenclature):

$$S_\alpha = \frac{L_\alpha \cdot D_\beta}{\phi_\alpha \cdot L_\beta} \tag{1.26}$$

with L_α being the luminescence after the integrated laboratory α-flux ϕ_α and L_β the luminescence after the laboratory β-dose D_β. The SI unit of S_α is $\mathrm{Gy\,m^2}$. In fact, for constant thickness of the sample layer between aliquots, each incident α-particle produces the same amount of track length. The S_α-system is thus equivalent to the a-value and b-value system.

Depending on the system to be used, the α-source has to be calibrated in different manners. The k-value system requires calibration in terms of deposited energy per unit mass (Gy), the a-value and b-value systems in terms of generated track length per unit volume per unit time ($\mathrm{m^{-2}\,s^{-1}}$) and the S_α concept in incident α-particles per unit area per unit time, i.e. the α-flux ($\mathrm{m^{-2}\,s^{-1}}$). However, great care has to be taken to produce fine grain sample layers of reproducible thickness for the purpose of source calibration and subsequent α-efficiency measurements when using one of the track length systems (a-value, b-value, S_α).

Until the advent of an α-source at the Cologne luminescence laboratory, α-irradiation was performed with a Littlemoore facility (^{241}Am-foils, ~ 200 MBq) at the University of Bayreuth. According to their calibration in terms of deposited dose in a fine grain layer of quartz, the correspondence of the k-value and the a-value system was used to determine the α-efficiency for the sample series from Românești-Dumbrăviţa I (Chapter 6). Calibration of the ^{241}Am-source in Cologne was carried out against the Littlemore source at the Heidelberg luminescence laboratory which, in turn, has been calibrated against an α-source in Oxford. The latter has been calibrated absolutely in terms of deposited track length as described in Aitken (1985b). The used reference material ("calibration quartz") was a fine grain quartz separate from Inden near Cologne (sample code IN7), which shows

excellent reproducibility. Using comparative regenerative-dose measurements, the Cologne α-source could thus be calibrated and gave a source strength of $0.813 \pm 0.026\,\mu m^{-2}\,min^{-1}$. This allowed using the b-value system for α-efficiency determination for subsequent silex samples.

1.3.3.3 Methods for dose rate determination

Using buried silex artefacts as radiation dosimeter, the overall dose rate can be subdivided into *internal dose rate*, generated by the sample itself, and *external dose rate* from the surrounding (sediment, cave walls, cosmos). The common sample preparation technique includes the discard of the outer 2 mm shell which is influenced by external α- and β-radiation. Therefore, only external γ- and cosmic dose rate contributions have to be taken into account which are further assumed to be spatially homogeneous within the sample, given the small dimension of most artefacts (a few cm) in relation to the range of γ- and cosmic radiation. Moreover, considering internal β-emitters to be uniformly distributed, the use of the interior part of the sample allows to assume an infinite matrix β-dose rate (Brennan 2003), so that β-attenuation factors are not necessary.

Basically, the dose rate in a homogeneous medium may be determined with the following methods:

- Direct measurement of the activity of a radiation type (e.g. thick-source α-counting or β-counting) with subsequent conversion into dose rates
- Analysis of the concentration of radioactive elements (U, Th and K) in the medium with subsequent conversion into dose rates
- Placement of highly-sensitive, integrating, artificial dosimeters into the medium at the positions of interest

In this study, element concentrations of U, Th and K of surrounding sediment were derived from high-resolution γ-spectrometry of homogenized and dried samples. These were taken from a ~ 30 cm sphere around the location of the artefact or from representative layers nearby. Whenever practical, additional *in-situ* γ-dose measurements were carried out in order to best record the radiation field present at the find spot. Due to the small size of the dated artefacts, only limited amounts of sample material were available for internal dose rate calculation. Hence, inductively coupled plasma mass spectrometry (ICP-MS) served to determine the abundance of radioactive elements within the silex sample. The methods being of relevance for applied dating in this work will be briefly described below. Additional information about how dose rates were obtained for individual samples will also be given in Chapter 7.

Gamma-spectrometry

To register γ-photons emitted by the sample, a γ-spectrometer with a lead-shielded high-purity Ge detector is used which facilitates energy dispersive and quantitative measurements. Incident photons are able to detach an electron from the atomic union which, in turn, produces further electron-hole pairs along the way through the detector, and by means of an applied voltage the generated charge is collected. The resulting current pulse is recorded and represents one photon impact event. Energy calibration making use of characteristic γ-quanta of known energy is necessary to relate the current pulse to the energy of the incident photon; efficiency calibration provides a function relating the number of recorded events to the concentration of radionuclides in the sample. For this purpose, a standard is measured that contains well-known amounts of U, Th and K (Preusser & Kasper 2001). Thus, the position of a recorded signal (photo-peak) on the energy axis allows a conclusion to be drawn about the emitting isotope (daughter nuclides of the U and Th decay chains) via their known and characteristic energy lines. At the Cologne luminescence laboratory, the energy lines of ^{226}Ra, ^{214}Pb and ^{214}Bi (^{238}U decay chain), of ^{228}Ac, ^{212}Pb and ^{208}Tl (^{232}Th decay series) and of ^{40}K are recorded. With the assumption of secular radioactive equilibrium in the respective decay chain and hence equal activities of all members, the concentration of the heads of the decay chains (U and Th) can be determined. For analysis of the K content, a single and prominent energy line at $\sim$1.46 MeV is used (Aitken 1985b). The typical shape of a γ-spectrum (see Fig. 1.21) represents two interaction processes of the incident photon and shell electrons: (1) Transfer of the entire energy from a photon to an electron yields sharp and characteristic lines in the spectrum (photo-peaks); (2) single and multiple elastic scattering events of the photon results in the broad, underlying background (Compton-spectrum) (Aitken 1985b; Krieger 2011).

In order to account for loss of ^{222}Rn during sampling and preparation, the sample is stored in a sealed Marinelli beaker for about one month to restore equilibrium activities between ^{226}Ra and ^{214}Bi prior to analysis (Hilgers 2007). According to Preusser & Kasper (2001), the overall measurement reproducibility of the facilities at the Cologne luminescence laboratory is 3.4 % for U, 4.6 % for Th and 2.1 % for K. In a few cases, the amount of surrounding sample material was not sufficient to match the minimum mass required for analysis in Cologne. Then, low-level γ-spectrometry was carried out by Dr. Detlev Degering at the Verein für Kernverfahrenstechnik und Analytik Rossendorf e. V. in Dresden, Germany.

In-situ gamma-scintillometry

The scintillator probe "Automess 6150AD b" used for *in-situ* measurements of photon radiation was the same as described in Hilgers (2007). The light pulses induced by γ- and cosmic radiation are amplified by a photomultiplier, and an averaged dose rate (in

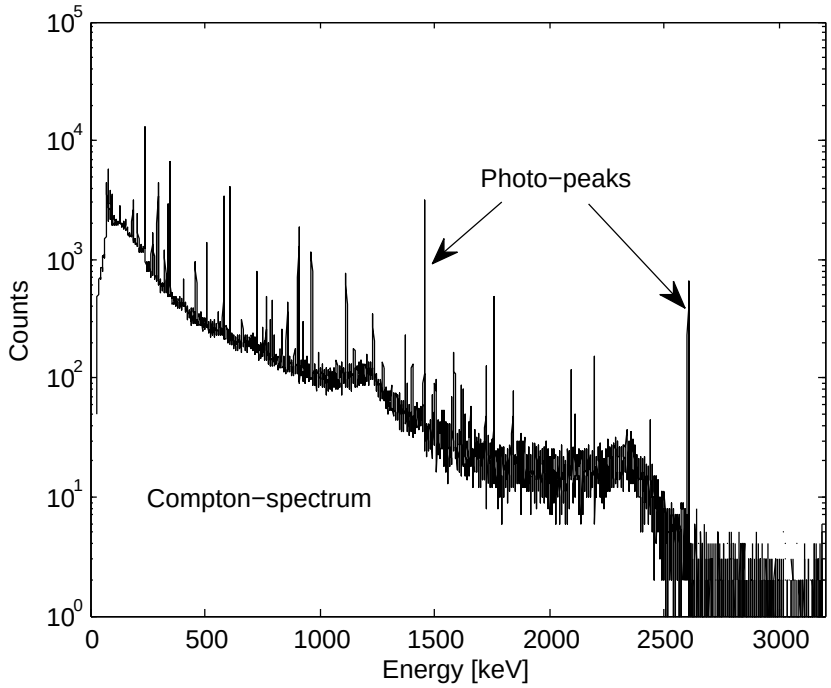

Figure 1.21: Typical γ-spectrum of a sediment sample. This one originates from a loessic sample taken from the excavation in Românești-Dumbrăviţa I, Romania, for determination of the external dose rate of heated artefacts (see Section 6.5).

µSv h^{-1}) of user-defined periods is obtained. Since a complete 4π-geometry of a radius of ~ 30 cm is covered and the actual radiation field of the undisturbed configuration of emitters and absorbing material is recorded, *in-situ* γ-scintillometry is advantageous in sampling positions where inhomogeneous dose rate distribution is expected. However, this method is not able to detect radioactive disequilibria.

Inductively coupled plasma mass spectrometry (ICP-MS)

In general, mass-spectrometry separates and counts atoms. Therefore, the atoms of the sample are firstly ionized what is done by inductive heating to high temperatures (several thousand °C) and generation of an argon plasma. An electric field then accelerates the ions, and they traverse a magnetic field in which they are deflected. According to their large inertia, atoms with a high mass are subject to weaker deflection than those of comparatively low mass, but equal net charge. However, physical laws describing the trajectories of the deflected atoms only allow for determination of the ratio charge/mass (q/m), not of the atom mass alone. Care has thus to be taken to account for interfering isobar ions, i.e. those having equal numbers of nucleons. Using a stationary ion detector, variation of the

electric and magnetic fields facilitates the registration of atoms with different ratios q/m (Demtröder 2005; Geyh 2005).

Especially for samples with low radioisotope content, mass-spectrometry overcomes the need for prolonged counting of decay events. Furthermore, comparatively low amounts of sample material (at least $\sim 250\,\mathrm{mg}$) are sufficient for analysis. In this study, ICP-MS was used to determine U, Th and K concentrations of the interior parts of silex samples in order to calculate the internal dose rate. Measurements were carried out with a Perkin Elmer/Sciex ELAN 6000 ICP-MS (ICP quadrupole mass- spectrometer) by Dr. Haino Uwe Kasper at the Institute for Geology and Mineralogy of the University of Cologne. Analysis of internal and external standards served for drift correction and as a check for the accuracy of the data, respectively. This results in an overall measurement uncertainty of less than $\pm 5\,\%$, mainly influenced by deviations from the well-known element concentrations of the standards. An intercomparison between results from γ-spectrometry and ICP-MS, both carried out in Cologne, supports the validity of the obtained data (Preusser & Kasper 2001). All details concerned with sample preparation for ICP-MS are given in Section 4.2.

Conversion of element concentrations to dose rates

Recent conversion factors to obtain dose rates from U, Th, K and Rb concentrations are given by Guérin et al. (2011). They are calculated for an infinite matrix and homogeneous absorption characteristics. The conversion factors used in this study, however, are those from Adamiec & Aitken (1998), as they are implemented in the age calculation program Age. These values are presented in Table 1.1. The deviations to the factors presented by Guérin et al. (2011) are $< 2\,\%$ (except for Rb), so that corresponding errors are seen as very small, compared to uncertainties introduced e.g. by soil moisture assessment.

Table 1.1: Conversion factors for dose rate calculation, taken from Adamiec & Aitken (1998). The values for the effective α-dose rate $\dot{D}_{\alpha,\mathrm{eff}}$ are already corrected for α-efficiency by use of the track length system, assuming an a-value of 0.1. For natural U, a mass abundance of $99.28\,\%$ ^{238}U and $0.72\,\%$ ^{235}U is assumed, and an atomic abundance of $116.7\,\mathrm{ppm}$ ^{40}K of total K. Further, a branching between β- and γ-disintegration of $89.3\,\%$ and $10.7\,\%$, respectively, is used for calculations. The cosmic dose rate contribution and the impact of moisture content are not considered in this compilation.

Element concentration	$\dot{D}_{\alpha,\mathrm{eff}}$ [Gy ka^{-1}]	$\dot{D}_{\beta}$ [Gy ka^{-1}]	$\dot{D}_{\gamma}$ [Gy ka^{-1}]	$\dot{D}_{\mathrm{total}}$ [Gy ka^{-1}]	Percentage of $\dot{D}_{\mathrm{total}}$
1 ppm U	0.218	0.146	0.113	0.477	28.8 %
1 ppm Th	0.0611	0.0273	0.0476	0.1360	8.2 %
1 % K		0.782	0.243	1.025	61.9 %
50 ppm Rb		0.019		0.019	1.1 %
Sum	0.2791	0.9743	0.4036	1.6570	

Specific α-flux rates (in SI units $m^{-2}\,s^{-1}$) can be calculated from U and Th concentrations in the sample (Valladas et al. 1988). The effective α-dose rate $\dot{D}_{\alpha,\mathrm{eff}}$ to be inserted into the denominator of the age equation is obtained by multiplying S_α with the flux rates ($19400\,cm^{-2}\,a^{-1}$ per ppm U and $5377\,cm^{-2}\,a^{-1}$ per ppm Th, respectively). This procedure and the single-aliquot determination of S_α is described in Tribolo et al. (2001).

1.3.3.4 Spatial and temporal dose rate variations

Variations of dose rate experienced by the sample over the burial period may result in erroneous age estimates. The factors potentially causing temporal dose rate changes will be briefly considered in this section, along with uncertainties which may be introduced by analyzing bulk samples for external dose rate determination.

The self-dosing of a silex sample due to its internal dose rate can be of considerable advantage when the long-term constancy of external dose rate data is doubted. Throughout the dated period, silex – at least the core of the specimen used for measurements – is regarded as geochemically stable so that the internal dose rate can be seen as constant. Consequently, the higher the percentage of the internal to the total dose rate is, the relatively smaller will the errors introduced by temporal changes of the external dose rate be. For instance, if the internal dose rate makes up 80 % of the total one, any fluctuations of the external radiation field will have considerably less impact on the resulting age than in the case of only 10 % internal contribution (Aitken 1985b; Richter 2007a). This argumentation implies the absence of any errors caused by non-uniformity of the internal dose rate. Chapters 3 and 4 provide detailed experimental data with respect to the question whether this assumption is justified or not. The following paragraphs will give an overview of sources for environmental dose rate fluctuations.

Cosmic dose rate fluctuations

Since extraterrestrically induced changes of the cosmic dose rate may be regarded as negligible for the period of interest, the parameter controlling the cosmic contribution is the overburden of the sample and its variations through time (beside altitude and geographic coordinates, which are known). Accordingly, the degree of correct cosmic dose rate assessment strongly depends on how precise the sedimentation rates, periods of surface stability and perhaps also erosional phases can be reconstructed. Several scenarios of accumulation and stagnancy of overburden were modeled by Munyikwa (2000), and Hilgers (2007) applied this concept to dune profiles. Such an approach, however, assumes accurate knowledge on sedimentation history and thus a high-resolution age-depth-model, e.g. provided by OSL. According to the findings of Hilgers (2007), significant effects of time-variant cosmic dose rate are only expected if comparatively old layers are rapidly buried by thick young layers. Needless to say that the here discussed variabilities of cosmic radiation lose

impact for dominating α-, β- and γ-dose rates and in caves where the roof shields considerable parts of the cosmic radiation.

Heterogeneous gamma-radiation fields

At archeological sites, non-uniformity of the γ-radiation fields within the ~ 30 cm sphere around the finding spot of a heated lithic is the rule rather than the exception. The find layers are mostly of heterogeneous, sometimes organic-rich composition and differ from the layers below and above, so that varying dose rates in these layers are expected. Cave sites are prone to exhibit even more complicated settings, due to weathering of the abris or roof and variable-sized blocks which have fallen down. For instance, big limestone blocks of low radioactivity in a matrix of fine sediments may considerably reduce the γ-dose rate received by a sample close to such a block. Three different sampling scenarios are shown in Fig. 1.22. Because of the small size of the dated artefacts (a few cm) in relation to the γ-range in sediment (~ 30 cm), the internal γ-dose rate can be assumed as uniform. Problems of gradients in the radiation field rather arise from dose rate determination using homogenized sample material, as done by high-resolution γ-spectrometry in the laboratory. The exact radiation geometry, caused by the specific spatial γ-emitter configuration during burial, can hence not be reproduced. To circumvent the usage of mean γ-dose rates, it is advisable to carry out *in-situ* γ-spectrometry or to employ dosimeter capsules as close as possible to the finding spot. Archeological excavations proceed horizontally from top to bottom, with the consequence that at least 2π (one hemisphere) of the irradiation geometry at the finding spot is lost, if the excavators have not stored the removed material. However, even then only mean values of the γ-dose rate can be obtained. In such cases, vertical profiles that most closely replicate the section containing the artefact may be sampled at corresponding depths and different lateral positions to get an approximation of the 4π irradiation geometry at the finding spot and its horizontal variability within the finding layer. The error of the external dose rate thus can significantly exceed the pure measurement uncertainty (Richter 2007a). In case the documentation of the excavation contains the exact position, size and shape of rocks, computerized reconstruction (Guibert et al. 1998) or modeling (Brennan et al. 1997) of the actual γ-dose rate at the sample position is possible, but complex. New approaches make use of non-invasive measurements of γ-radiation while the excavation proceeds (Guérin & Mercier 2012).

Fluctuation of moisture content

The absorption of radiation in water is more effective than in air. Hence, the strength of γ-radiation received by a buried silex sample depends on the degree to which the pores of the surrounding sediment are filled with water, or, in other words, on the moisture content

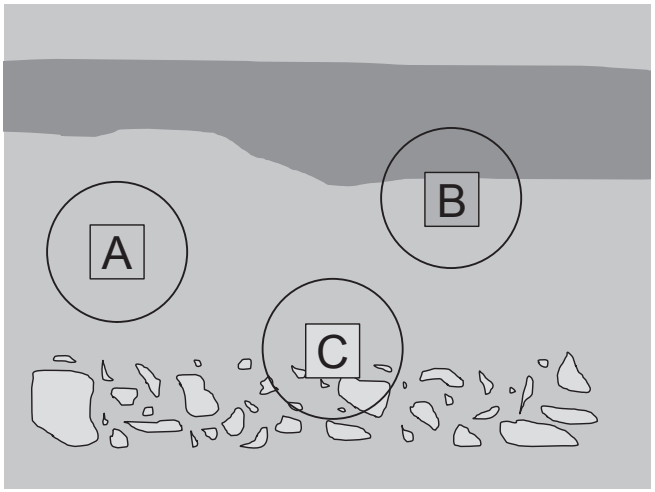

Figure 1.22: Spatial variability of γ-radiation. The γ-radiation field around the position **A** is homogeneous, whereas the influence of a layer with higher radioactivity (e.g. an organic-rich horizon, shown here with dark color) leads to a higher γ-dose rate and a non-uniform radiation field at position **B**. Big blocks of lower radionuclide content than the sediment matrix within the sphere of γ-range cause local variations of radiation and an overall lower dose rate at position **C**. Redrawn from Hilgers (2007).

of the sediment. The formula usually used to calculate the influence of moisture on the γ-dose rate includes a specific attenuation factor of 1.14 (Zimmerman 1971a) and is given by

$$\dot{D}_{\gamma,wet} = \frac{\dot{D}_{\gamma,dry}}{1 + 1.14 \cdot W \cdot F} \tag{1.27}$$

Here, W denotes the saturation water content (weight of water over dry weight) and F is the average water content during burial over saturation water content W (Aitken 1985b). The present water content of a sediment sample can easily be determined. However, this value may not reflect the mean moisture content of the burial period which is difficult to estimate. The uncertainty effects on the age are minimal in case of soils that have been water saturated over the time of burial ($F = 1$) or in arid environments which are characterized by water contents close to zero. Multiple reasons are responsible for fluctuations of the moisture content on various time-scales: Seasonally, the soil water content follows the annual changes in precipitation; on geological time-scales it is influenced by large-scale climate changes in the course of glacial–interglacial and stadial–interstadial cycles. Variation in the precipitation regime might also have influence on the rise and fall of the groundwater table, while warm periods promote soil formation which goes along with weathering, production of fine-grained material and enrichment of organic components. This again has impact on the moisture capacity. Further mechanical interaction (compacting, selective washout) and micro and macro soil biota may alter the grain size spectrum and porosity and thus contribute to variations of water content through time (Hilgers 2007). It is obvious that it is hardly possible to account for all of these factors for the period of burial.

While an upper limit can be approximated by the size distribution of porosities (Fuchs 2001), an increased uncertainty reflecting the (mostly) poorly-known moisture content must be assessed for each site and considered in the age equation (Aitken 1985b).

Radioactive disequilibria

Without external influence, a decay chain reaches radioactive equilibrium, i.e. the absolute number of decays per unit time of the daughter is the same as that of its mother. Here, the decay rate λ is related to the half-life by $\lambda = \ln 2 / t_{1/2}$. The different half-lives of the isotopes in a decay chain imply that the abundance of the isotopes must be reciprocal to their half-lives to maintain radioactive equilibrium, which is then characterized by equal activity of all members. If a fraction of a chain's constituent is removed, this balanced situation is disturbed, the overall activity of the chain decreases and hence does the associated dose rate. The opposite mechanism applies to addition of an amount of isotopes what results in excess activity. In case the disturbance is of short-term nature only, equilibrium of production and decay of the respective isotope is reached again after about five half-lives. This means that radioactive disequilibria potentially having prevailed in the past cannot be detected by analyzing the present sediment composition (Aitken 1985b). If possible, time-dependent dose rate variations introduced by radioactive disequilibria should be accounted for to avoid erroneous age results (Krbetschek et al. 1994; Olley et al. 1997; Prescott & Hutton 1995).

Due to low geochemical mobility of Th and the relatively short half-lives of the chain members, disequilibria in the Th decay series are not expected to be a serious problem. Furthermore, the relative contribution of the ^{235}U chain to the γ-radiation induced by natural U is only 1.8 % (Guérin et al. 2011). Consequently, disequilibria in the ^{238}U decay series, whose members have half-lives of up to 245 ka, will have the greatest impact on the dose rate. According to Krbetschek et al. (1994), the main reasons for radioactive disequilibria in this chain include at first the oxidation of ^{234}U to uranyl compounds which are water soluble, just as is ^{226}Ra. Secondly, ^{230}Th is readily absorbed, leading to an excess amount of this isotope. Finally, the gaseous diffusion of ^{222}Rn may also induce disequilibrium. The effect of emanation is particularly severe because $\sim$98 % of the γ-radiation of the ^{238}U decay series is emitted by this isotope and its descendants (Mercier et al. 1995; Guérin et al. 2011). Organic matter is prone to be enriched in U under wet conditions, leading to an excess amount of U in the decay chain (Geyh & Techmer 1997; Geyh et al. 1997).

From the above explanations, it can be deduced that radioactive disequilibria are more problematic in wet sedimentary environments. Whether the burying sediments of an archeological site are affected by any form of radioactive disequilibrium is thus dependent on local settings, as case studies by Feathers (2002), Valladas et al. (2008) and Mercier et al. (2007b) show. Since *in-situ* measurements of γ-radiation are not capable of revealing

radioactive disequilibria, additional analysis by high-resolution γ-spectrometry is essential. At the Cologne laboratory, γ-radiation emitted during decay of the isotopes ^{226}Ra, ^{214}Pb and ^{214}Bi (^{238}U decay chain), and of ^{228}Ac, ^{212}Pb and ^{208}Tl (^{232}Th decay chain) is measured. Deviations $> 2\,\sigma$ of the calculated activities of these members are indicative of radioactive disequilibrium in the lower part of the chain (^{226}Ra and its successors). Inconsistencies in the upper part of the ^{238}U decay chain may be revealed by use of high-resolution α-spectrometry (Krbetschek et al. 1994).

1.3.4 Evaluation of absorbed dose

Before the accumulated radiation dose of a silex sample can be measured, the sample has to be prepared. Commonly, the outer surface of the sample (> 2 mm thickness) is stripped off with a water-cooled diamond saw and the inner core is gently crushed with a hydraulic press to the final grain (better: fragment) size of $\sim$100–200 µm (Valladas 1992; Mercier et al. 1995). Alternatively, fine grain separates ($\sim$4–11 µm) may be used for dose evaluation, which are obtained by acetone settling (Zimmerman 1972). After treatment with 10 % HCl, the sample material is ready for measurement in the routinely used Risø or Lexsyg luminescence readers. Further details on measurement parameters used in this study are given in Sections 6.3.1 and 7.1 and Chapter B.

Due to the high variability of luminescence characteristics among different silex samples (or mineral samples in general), no universally valid relationship between given dose and luminescence output can be established. This necessitates to determine the sensitivity, or dose response, for each sample individually. By administering different doses D and recording the resulting TL, an empirical function TL(D) can be established, the dose response curve or growth curve. Using this relationship, an estimate of the paleodose is obtained by the artificial dose for which the recorded TL is equal to the natural TL. This dose is called the equivalent dose D_e.

The most common methods used for D_e determination will be described only in their principal functionality here. For examples of application of various measurement protocols, the reader is referred to the case studies given in Section 1.3.1 and Chapter 7. Furthermore, focus is set on TL protocols that were used to collect most of the data in this work. The OSL dating procedures applied are described in Chapter 5.

1.3.4.1 Additive-dose techniques

Since it has been known that thermal treatment and irradiation may change the luminescence sensitivity of a sample, the multiple-aliquot additive-dose (MAAD) approach is designed to reduce these influences. Increase or decrease of the sensitivity during repeated measurements of the same aliquot – if not adequately corrected – would result in errors in the determined D_e, as illustrated for regenerative-dose measurements in Fig. 1.12. To build a MAAD dose response curve, several sets of natural aliquots therefore receive in-

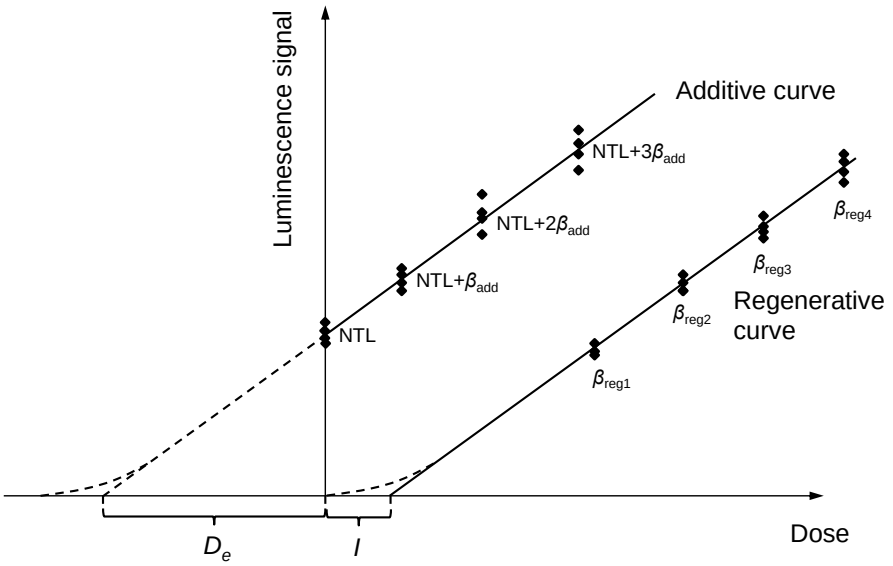

Figure 1.23: Equivalent dose determination using multple-aliquot protocols. For further details see main text.

creasing additive β-doses (e.g. β, 2β, 3β, ...) so that this irradiation is the only laboratory treatment prior to TL measurement. The integrated numbers of photomultiplier counts of a thermally stable region of the glowcurve (see Section 1.3.4.3) are then plotted against the known additive doses and the dose points fitted with an appropriate function (additive or first growth curve). This is mostly a linear, quadratic or exponentially saturating function, depending on the dose range and the dose saturation level of the sample. For equivalent dose determination, the fitted curve is extrapolated to negative dose values and the (negative) intercept with the dose axis is seen as being representative of the D_e. Since this method is based on extrapolation, the exact curvature of the dose response curve at low doses is unknown. Some samples, however, have shown supralinear signal increase at low doses which is accounted for by constructing a regenerative dose response curve (regenerative or second growth curve) (Aitken 1985b; Valladas et al. 1999; Richter et al. 2000; Mercier et al. 2007b). The regenerative curve is obtained by annealing part of the sample material and irradiating several sets of aliquots with increasing β-doses. The corrected D_e is then calculated by adding the supralinearity correction I (Fig. 1.23). Especially if non-linear curve fitting is applied, it is important that the extrapolated dose ranges of additive and regenerative curves approximately match to give valid results for the supralinearity correction (i.e. $\mathrm{NTL} \approx \mathrm{TL}(\beta_{\mathrm{reg1}})$).

The signal scatter of individual aliquots may substantially increase the uncertainty of the curve fit and thus the uncertainty of the D_e. To reduce this scatter, several normalization procedures have been proposed, such as weight normalization, second glow, zero glow or equal pre-dose normalization (Aitken 1985b; Franklin & Hornyak 1992). In case of

second glow normalization, after initial TL readout a constant dose is given to all aliquots and its response is used for normalization. In contrast, a small dose prior to the natural TL (NTL) measurement induces a signal of the highly sensitive 110 °C TL peak which is considered as proportional to the "dating" peak at higher temperatures and serves for zero glow normalization. Application of the equal pre-dose approach requires an identical thermal and dose history of all samples prior to a normalization dose measurement, so that additional irradiation and heating steps for part of the aliquots are necessary (Aitken 1985b). The sucess of different normalization techniques is likely to be sample-dependent. This topic is also discussed in Section 4.4 for silex samples.

1.3.4.2 Regenerative-dose techniques

To overcome the uncertainties introduced by extrapolation of the MAAD curve, regenerative methods may be applied. Using multiple aliquots, the D_e is estimated by projection of the NTL signal onto the regenerative curve and the corresponding dose is read from the dose axis. As mentioned in the last section, heating of the sample prior to regenerative dosing can result in changes of the sensitivity. If both additive- and regenerative-dose response curves are constructed, sensitivity changes caused by heating can be recognized by differences in their slopes.

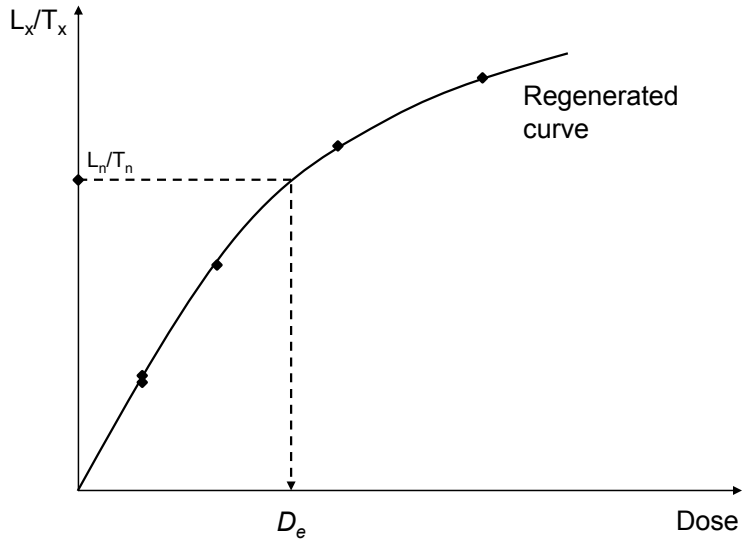

Figure 1.24: Equivalent dose determination using the SAR protocol. The dose response curve is constructed by five regeneration points, including one repeat point. The D_e is determined by projection of L_n/T_n onto the fitted growth curve and reading from the dose axis. For further details see main text.

The single-aliquot regenerative-dose (SAR) method requires in principle only one aliquot for D_e determination. Here, after readout of the natural signal (L_n), increasing regenerative

Table 1.2: Measurement sequence of the SAR protocol. The general procedure is according to Murray & Wintle (2000), but adopted to thermal instead of optical stimulation. The regeneration dose D_x is increased throughout the sequence and a repeated dose point measured at the end of the protocol.

Step	Treatment	Yield
1	TL measurement	L_n
2	Give fixed test dose D_T	
3	TL measurement	T_n
4	Give regeneration dose D_x	
5	TL measurement	L_x
6	Give fixed test dose D_T	
7	TL measurement	T_x
8	Return to step 4	

doses are given to construct a dose response curve for this aliquot. These doses have to be chosen to enclose the expected natural dose. Sensitivity changes due to repeated heating and irradiation are monitored by measuring the response to a constant test dose in between the regenerative steps. Provided that the regenerated signal L_x is directly proportional to the test dose response T_x, the growth curve can be corrected for the sensitivity changes (or better: normalized) by dividing L_x by T_x. Through fitting of the growth curve and projection of L_n/T_n onto this curve, the D_e is obtained (Fig. 1.24) (Murray & Wintle 2000). A general measurement routine of the SAR protocol is outlined in Table 1.2. If sensitivity correction works adequately, a repeated dose point at the end of the SAR cycle should yield the same L_x/T_x-value as the first one. The ratio of both, the *recycling ratio*, should ideally be unity and is used to assess the validity of the SAR procedure for a respective sample. A zero dose point, as usually measured in the course of OSL-SAR protocols to register recuperation, is not included in the TL-SAR protocol, because recuperation is not expected to be a matter when applying thermal resetting. Another check for the suitability of the regenerative method is the dose recovery test (DRT): After zeroing the signal, a known laboratory dose is administered, treated as unknown and determined by the chosen measurement protocol. The degree of coincidence of given and determined (recovered) dose within uncertainties provides a criterion for the protocol's validity (Richter & Temming 2006; Wintle & Murray 2006). Examples of DRT's performed in the course of the present thesis are given in Chapters 7 and B.

1.3.4.3 Selection of thermally stable signal parts: the plateau test

The TL glow curve usually consists of several overlapping peaks, each having a different thermal trap depth and hence thermal stability (see Section 1.3.2.1). To be confident of negligible thermally induced charge loss over the storage period, the thermal lifetime of a trap must be about one order of magnitude longer than the dated time span. In contrast

to glow curves recorded after artificial dosing, natural glow curves do not exhibit a TL signal below $\sim 200\,^{\circ}\mathrm{C}$, due to the low thermal stability of the corresponding shallow traps. The thermally stable region in the glow curve to be used for dating is usually detected by application of the plateau test (Aitken 1985b).

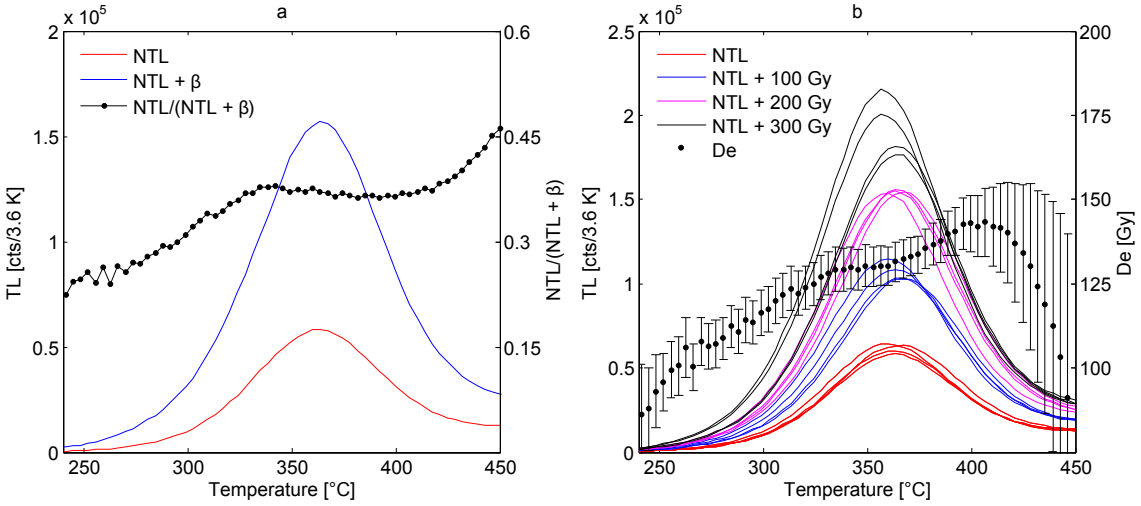

Figure 1.25: Heating and D_e-plateau test. (a) Heating plateau of a Portuguese silex sample (not part of this thesis). (b) D_e-plateau of the same sample, obtained by evaluation of MAAD data with the Analyst software (version 3.24). The measurements were conducted with a heating rate of $2\,\mathrm{K\,s^{-1}}$ and using the blue filter combination centered at 410 nm.

The ratio of natural TL (NTL) of a sample and the signal after receiving an additive β-dose (NTL + β) is plotted against temperature, which is termed *heating plateau test*. This ratio yields a plateau in the thermally stable region, as exemplarily shown in Fig. 1.25a. Assuming linear dose response and neglecting supralinearity, a first guess of the equivalent dose can be made by means of the heating plateau test: if $r = \frac{\mathrm{NTL}}{\mathrm{NTL}+\beta}$, then the equivalent dose is approximated by $\frac{r}{1-r} \cdot \beta$ (Aitken 1985b). The absence of a heating plateau in the high-temperature region ($\geq 300\,^{\circ}\mathrm{C}$) may have several reasons (Aitken 1985b; Richter 2007a):

- Presence of anomalous (athermal) fading of some signal components. This has been reported for the UV emission (around 340 nm) of silex (Richter et al. 1999).
- Contamination of the sample with spurious TL components or foreign material. The glow curve then clearly differs from that of a pure silex sample.
- Incomplete signal resetting during heating by ancient man.

The last item implies that the heating plateau test can also be applied to check sufficient signal erasure during the last heating process. Incompletely heated samples, which are useless for dating, can hence be sorted out. It must be noted that passing the plateau test is a requirement, but is not sufficient to guarantee appropriate TL resetting. Moreover,

there must be a notable signal increase after additive dosing to ensure the signal is not in saturation (geological signal, $r = 1$ in this case). Complications with the heating plateau test may further arise from altering of the glow curve shape after various heat treatments (Michab et al. 1998). Therefore, the glow curves should be checked for their symmetrical shape; any high-temperature shoulders or deviations from a Gaussian-shaped peak can be indicative of insufficient heating in the past (Richter et al. 1999; Richter et al. 2011).

In the non-linear dose range, a sample showing overlapping peaks with varying dose saturation characteristics would fail to yield a plateau, though adequately heated. The *D_e-plateau test* overcomes this pitfall while giving an individual D_e-value for each temperature interval of the glowcurve (e.g. 5 °C intervals). A D_e-plateau is thus a more reliable indication of the stable temperature region (Berger 1994; Zöller & Blanchard 2009). An example of a satisfactory heating and D_e-plateau, respectively, is shown in Fig. 1.25; further examples of passed and failed plateau tests are given in Chapter C.

Once a stable signal part is identified, an equivalent dose can be determined by multiple- or regenerative-dose procedures and integrating of this signal for dose response curve construction, or, with help of appropriate software, by averaging the invidual D_e's obtained from the D_e-plateau test over this range.

1.3.5 Calculation of the age

The age equation in its simplest form can be written as

$$\text{Age} = \frac{\text{Equivalent dose}}{\text{Dose rate}} = \frac{D_e}{\dot{D}} \tag{1.28}$$

The dose rate, however, consists of several individual parts, as shown in Section 1.3.3. Citing these separately gives

$$\text{Age} = \frac{D_e}{\dot{D}_{\alpha,\text{eff}} + \dot{D}_\beta + \dot{D}_\gamma + \dot{D}_{\text{cosmic}}} \tag{1.29}$$

Here, $\dot{D}_{\alpha,\text{eff}}$ is the effective α-dose rate (corrected for α-efficiency) and $\dot{D}_\gamma$ is the average "wet" γ-dose rate during burial according to Eq. 1.27. In case of MAAD data, the D_e may comprise a supralinearity correction I. The resulting age is usually quoted with its $1\,\sigma$ confidence interval which means that with a probability of $\sim 68\,\%$ the true age lies within the quoted uncertainty boundaries (assuming Gaussian distribution of the random terms).

When it comes to dating of allegedly contemporaneously heated artefacts – e.g. from one confined find layer or a hearth –, the age is to be quoted as the error-weighted mean of the samples' individual ages. Therefore, however, it must be veryfied within a certain level of significance (usually 5 %) that all ages originate from the same statistical distribution. The χ^2-test allows deciding whether this condition is fulfilled or not. By use of the error-weighted mean, ages with smaller standard deviations σ is given more weight than those with larger errors, leading to the following equations for the weighted mean age $\bar{A}$ and its $1\,\sigma$ confidence interval when n individual ages are averaged (Geyh 2005):

$$\bar{A} = \frac{\sum_{j=1}^{n} A_j \cdot \frac{1}{\sigma_j^2}}{\sum_{j=1}^{n} \frac{1}{\sigma_j^2}} \tag{1.30}$$

$$\bar{\sigma} = \sqrt{\frac{1}{\sum_{j=1}^{n} \frac{1}{\sigma_j^2}}} \tag{1.31}$$

Analyses and D_e calculation of multiple-aliquot additive- and regenerative-dose data sets were performed with version 3.24 of the Analyst software (Duller 2007) in this study and the obtained standard deviations used for further age calculation. Evaluation of SAR data was carried out with Matlab (version 2007b) in which the dose response curve was fitted and the D_e obtained by solving the fit equation for $y = L_n/T_n$. The $1\,\sigma$ uncertainty includes errors due to counting statistics (assuming Poisson distribution of photomultiplier counts), curve fitting, reproducibility of measurements (taken to be 1.5 %) and β-source calibration (5 %) (Aitken 1985b; Hilgers 2007). While the source calibration error is technically a systematic one, it has no distinct algebraic sign so that it has an inherent statistical nature (Kalchgruber 2002). Therefore, the error σ_{D_e} may be derived by applying the Gaussian law of error propagation to the individual errors (Geyh 2005). All dose and dose rate data with their standard deviations were inserted into the Age program from Prof. Dr. R. Grün (version 1999) to calculate individual TL ages. To sum up this chapter, the generalized procedure for TL dating of heated artefacts is shown as a flowchart in Fig. 1.26.

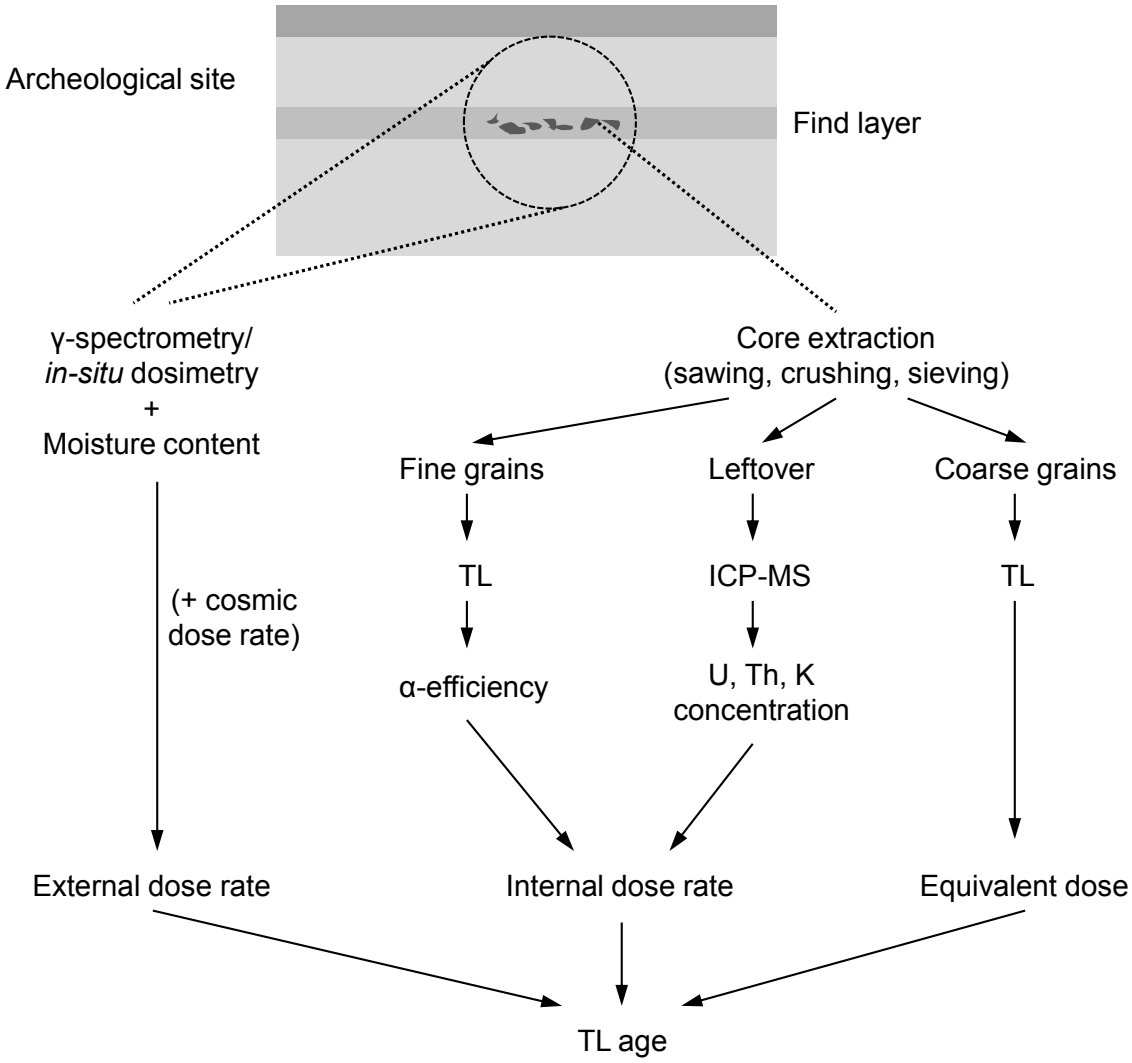

Figure 1.26: Generalized working steps for TL age determination of heated silex.

1.4 Outline of thesis

The structure and basic content of the following chapters is outlined below to provide an overview of their interrelationship.

Chapter 2 contains the study on spurious luminescence signals from sample holders. Possible reasons for these luminescence emissions are given along with cleaning methods for their elimination in order to measure a preferably pure signal of the sample and to avoid systematic or random errors caused by the spurious contributions.

Chapters 3 and **4** address the question wether or not and to what extent heterogeneous distribution of radionuclides and hence of dose rate may affect the accuray and precision of TL dates. Several qualitative and quantitative approaches (autoradiography, LA-ICP-MS) are applied to gain detailed knowledge on the amount and distribution of uranium, thorium and potassium. These extensive investigations were split into two publications with the ineluctable consequence of a partial thematic overlap of both discussion sections.

OSL properties of four silex samples are studied in detail in **Chapter 5**. LM-OSL measurements and tests on the thermal long-term stability of the detected signal components are investigated. For two archeological samples, the thermally most stable component was used for age determination, and finally OSL ages are compared to ages obtained by TL.

The logical consequence of the dose rate studies is to find appropriate means to routinely detect and circumvent malign influences of non-uniform internal dose rate, preferably in the course of the TL measurements in-house and without the need to carry out expensive analyses. In **Chapter 6**, a set of heated artefacts from Romania serves to test exemplarily the applicability of (1) a multi-protocol approach, i.e. the parallel use of various TL emissions and measurement protocols and (2) a SAR protocol-based method to check the reliability of obtained ages. Additionally, sediment OSL data of the find layer and under- and overlying deposits were generated. After selection of valid age information, the archeological implications of the TL and OSL dates are discussed.

Further case studies of applied dating of Middle and Early Upper Paleolithic sites are contained in **Chapter 7**. The investigated sites from the Iberian Peninsula and Egypt cover different depositional environments (open-air and cave sites) and face various problems related to internal as well as external dosimetry.

Chapter 8 provides a conclusive summary of the results of the previous chapters. The findings are placed in a wider context and the TL method and its benefits and shortcomings opposed to alternative chronological methods. As an outlook, possible strategies to better face internal dose rate issues are discussed (e.g. spatially resolved dose and dose rate determination).

Chapter B provides the results and a short discussion of the laboratory dose recovery tests performed to evaluate the validity of applied sample preparation and measurement procedures. Additional data and plots with respect to dated silex samples (Chapter 7) are given in **Chapter C**.

References

Adamiec, G., Aitken, M., 1998. Dose-rate conversion factors: update. Ancient TL 16, 37–50.

Aitken, M., Bowman, S., 1975. Thermoluminescence dating: Assessment of alpha particle contribution. Archaeometry 17, 132–138.

Aitken, M., Wintle, A. G., 1977. Thermoluminescence dating of calcite and burnt flint: The age relation for slices. Archaeometry 19, 100–105.

Aitken, M., 1984. Non-linear growth: Allowance for alpha particle contribution. Ancient TL 2, 2–5.

Aitken, M., 1985a. Alpha particle effectiveness: numerical relationship between systems. Ancient TL 3, 22–25.

Aitken, M., 1985b. Thermoluminescence dating. Academic Press, London.

Aitken, M., 1998. An introduction to optical dating. The dating of Quaternary sediments by the use of photon-stimulated luminescence. Oxford University Press, Oxford.

Alonso, P., Halliburton, L., Kohnke, E., Bossoli, R., 1983. X-ray-induced luminescence in crystalline SiO_2. Journal of Applied Physics 54, 5369–5375.

Andersen, H. H., 1982. A study of water uptake in flint. PACT 7, 447–458.

Bailey, R., 2001. Towards a general kinetic model for optically and thermally stimulated luminescence of quartz. Radiation Measurements 33, 17–45.

Bailey, R., 2002. Simulations of variability in the luminescence characteristics of natural quartz and its implications for estimates of absorbed dose. Radiation Protection Dosimetry 100, 33–38.

Bailey, R., Armitage, S., Stokes, S., 2005. An investigation of pulsed-irradiation regeneration of quartz OSL and its implications for the precision and accuracy of optical dating (Paper II). Radiation Measurements 39, 347–359.

Bailey, R., 2010. Direct measurement of the fast component of quartz optically stimulated luminescence and implications for the accuracy of optical dating. Quaternary Geochronology 5, 559–568.

Bailey, R., McKeever, S. W. S., in prep. Theory of luminescence dating. In: Luminescence Dating: An introduction and handbook. Springer.

Bailiff, I., Morris, D., Aitken, M., 1977. A rapid-scanning interference spectrometer: application to low-level thermoluminescence emission. Journal of Physics E: Scientific Instruments 10, 1156–1160.

Berger, G. W., Brown, T. A., Huntley, D. J., Wintle, A. G., 1982. 5 spurious tidbits. Ancient TL 18, 7–10.

Berger, G. W., 1994. Thermoluminescence dating of sediments older than $\sim$ 100 ka. Quaternary Science Reviews 13, 445–455.

Bøtter-Jensen, L., McKeever, S. W. S., Wintle, A. G., 2003. Optically stimulated luminescence dosimetry. Elsevier, Amsterdam.

Bowman, S., Seeley, M., 1978. The British Museum flint dating project. PACT 2, 151–164.

Bowman, S., Sieveking, G., 1983. Thermoluminescence dating of burnt flint from Combe Grenal. PACT 9, 253–268.

Bowman, S., Huntley, D., 1984. A new proposal for the expression of alpha efficiency in TL dating. Ancient TL 2, 6–8.

Brennan, B., Schwarcz, H., Rink, W., 1997. Simulation of the gamma radiation field in lumpy environments. Radiation Measurements 27, 299–305.

Brennan, B., 2003. Beta doses to spherical grains. Radiation Measurements 37, 299–303.

Bulur, E., 1996. An alternative technique for optically stimulated luminescence (OSL) experiment. Radiation Measurements 26, 701–709.

Bulur, E., Göksu, H. Y., 1999. Infrared (IR) stimulated luminescence from feldspars with linearly increasing excitation light intensity. Radiation Measurements 30, 505–512.

Campbell, G., Jungbauer, J., Bristow, K., Hungerford, R., 1995. Soil temperature and water content beneath a surface fire. Soil Science 159, 363–374.

Carmody, R. N., Wrangham, R. W., 2009. The energetic significance of cooking. Journal of Human Evolution 57, 379–391.

Clark, J., Harris, J., 1985. Fire and its roles in early hominid lifeways. The African Archaeological Review 3, 3–27.

Daniels, F., Boyd, C. A., Saunders, D. F., 1953. Thermoluminescence as a Research Tool. Science 117, 343–349.

Demtröder, W., 2005. Experimentalphysik 3. Atome, Moleküle und Festkörper. Springer, Berlin and Heidelberg.

Demtröder, W., 2010. Experimentalphysik 4. Kern-, Teilchen- und Astrophysik. Springer, Berlin and Heidelberg.

Duller, G. A. T., 1991. Equivalent dose determination using single aliquots. Nuclear Tracks and Radiation Measurements 18, 371–378.

Duller, G. A. T., 2007. *Analyst Version 3.24*. Institute of Geography and Earth Sciences, University of Wales, Aberystwyth. United Kingdom.

Duttine, M., Guibert, P., Perraut, A., Lahaye, C., Bechtel, F., Villeneuve, G., 2005. Effects of thermal treatment on TL and EPR of flints and their importance in TL-dating: application to French Mousterian sites of Les Forêts (Dordogne) and Jiboui (Drôme). Radiation Measurements 39, 375–385.

Eswaran, V., 2002. A diffusion wave out of Africa. Current Antropology 43, 749–774.

Faïn, J., Sanzelle, S., Miallier, D., Montret, M., Pilleyre, T., 1994. A TL model based on deep traps competition. Radiation Measurements 23, 287–291.

Fattahi, M., Stokes, S., 2000a. Extending the time range of luminescence dating using red TL (RTL) from volcanic quartz. Radiation Measurements 32, 479–485.

Fattahi, M., Stokes, S., 2000b. Red thermoluminescence (RTL) in volcanic quartz: development of a high sensitivity detection system and some preliminary findings. Ancient TL 18, 35–44.

Feathers, J. K., 2002. Luminescence dating in less than ideal conditions: case studies from Klasies River Main Site and Duinefontein, South Africa. Journal of Archaeological Science 29, 177–194.

Fleagle, J. G., Assefa, Z., Brown, F. H., Shea, J. J., 2008. Paleoanthropology of the Kibish Formation, southern Ethiopia: Introduction. Journal of Human Evolution 55, 360–365.

Fleming, S., 1978. The quartz inclusion method. PACT 2, 125–130.

Floss, H., 2003. Quarz, Quarzit und Feuerstein - Rheinablagerungen als Rohmaterialquelle der altsteinzeitlichen Sammler und Jäger. In: Schirmer, W. (Ed.), GeoArchaeoRhein 4. Münster, 327–347.

Franklin, A. D., Hornyak, W. F., 1992. Normalization of inclusion size quartz TL data. Ancient TL 10, 1–6.

Fuchs, M., 2001. Die OSL-Datierung von Archäosedimenten zur Rekonstruktion anthropogen bedingter Sedimentumlagerung. PhD thesis, Universität Heidelberg.

Gaft, M., Reisfeld, R., Panczer, G., 2005. Luminescence Spectroscopy of Minerals and Materials. Springer, Berlin and Heidelberg.

Ganzawa, Y., Maeda, M., 2009. 390–410 °C isothermal red thermoluminescence (IRTL) dating of volcanic quartz using the SAR method. Radiation Measurements 44, 517–522.

Garlick, G., Gibson, A., 1948. The electron trap mechanism of luminescence in sulphide and silicate phosphors. Proceedings of the Physical Society 60, 574–590.

Geyh, M., Hennig, G., Oezen, D., 1997. U/Th-Datierung interglazialer und interstadialer Niedermoortorfe and Lignite – Stand und Zukunft. In: Freund, H., Caspers, G. (Eds.), Vegetation und Paläoklima der Weichsel-Kaltzeit im nördlichen Mitteleuropa – Ergebnisse paläobotanischer, -faunistischer und geologischer Untersuchungen. Schriftenreihe der Deutschen Geologischen Gesellschaft 4, 187–199.

Geyh, M., Techmer, A., 1997. ^{230}Th/^{234}U-Datierung der organogenen Sedimente der Bohrung Groß Todtshorn (Kr. Harburg; Niedersachsen). In: Freund, H., Caspers, G. (Eds.), Vegetation und Paläoklima der Weichsel-Kaltzeit im nördlichen Mitteleuropa – Ergebnisse paläobotanischer, -faunistischer und geologischer Untersuchungen. Schriftenreihe der Deutschen Geologischen Gesellschaft 4, 103–110.

Geyh, M., 2005. Handbuch der physikalischen und chemischen Altersbestimmung. Wissenschaftliche Buchgesellschaft, Darmstadt.

Goble, R., Rittenour, T., 2006. A linear modulation OSL study of the unstable ultrafast component in samples from Glacial Lake Hitchcock, Massachusetts, USA. Ancient TL 24, 37–46.

Göksu, H. Y., Fremlin, J. H., 1972. Thermoluminescence from unirradiated flints: regeneration thermoluminescence. Archaeometry 14, 127–132.

Göksu, H. Y., Fremlin, J. H., Irwin, H. T., Fryxell, R., 1974. Age determination of burned flint by a thermoluminescent method. Science 183, 651–654.

Göksu, H. Y., Weiser, A., Regulla, D. F., 1989. 110 °C TL peak records the ancient heat treatment of flint. Ancient TL 7, 15–17.

Götze, J., Plötze, M., Habermann, D., 2001. Origin, spectral characteristics and practical applications of the cathodoluminescence (CL) of quartz – A review. Mineralogy and Petrology 71, 225–250.

Graetsch, H., Flörke, O., Miehe, G., 1985. The nature of water in chalcedony and opal-C from Brazilian agate geodes. Physics and Chemistry of Minerals 12, 300–306.

Graetsch, H., Grünberg, J., 2012. Microstructure of flint and other chert raw materials. Archaeometry 54, 18–36.

Grögler, N., Houtermans, F., Stauffer, H., 1960. Über die Datierung von Keramik und Ziegel durch Thermolumineszenz. Helvetica Physica Acta 33, 595–596.

Guérin, G., Mercier, N., Adamiec, G., 2011. Dose-rate conversion factors: update. Ancient TL 29, 5–8.

Guérin, G., Mercier, N., 2012. Field gamma spectrometry, Monte Carlo simulations and potential of non-invasive measurements. Geochronometria 39, 40–47.

Guibert, P., Bechtel, F., Schvoerer, M., Müller, P., Balescu, S., 1998. A new method for gamma dose-rate estimation of heterogeneous media in TL dating. Radiation Measurements 29, 561–572.

Hahn, J., 1991. Erkennen und Bestimmen von Stein- und Knochenartefakten: Einführung in die Artefaktmorphologie. Archaeologica Venatoria 10, Tübingen.

Halperin, A., Braner, A. A., 1960. Evaluation of thermal activation energies from glow curves. Physical Review 117, 408–415.

Harvey, E., 1957. A history of luminescence. Memoirs of the American Philosophical Society 44, 1–351.

Hashimoto, T., 2008. An overview of red-thermoluminescence (RTL) studies on heated quartz and RTL application to dosimetry and dating. Geochronometria 30, 9–16.

Hilgers, A., 2007. The chronology of Late Glacial and Holocene dune development in the northern Central European lowland reconstructed by optically stimulated luminescence (OSL) dating. PhD thesis, Universität zu Köln.

Hoogenstraaten, W., 1958. Electron traps in zinc-sulphide phosphors. Philips Research Reports 13, 515–693.

Hublin, J.-J., Barroso Ruiz, C., Medina Lara, P., Fontugne, M., Reyss, J.-L., 1995. The Mousterian site of Zafarraya (Granada, Spain): dating and implications on the palaeolithic peopling processes of Western Europe. Comptes rendus de l'Académie des Sciences 321 (IIa), 931–937.

Huntley, D. J., Godfrey-Smith, D. I., Thewalt, M. L. W., 1985. Optical dating of sediments. Nature 313, 105–107.

Huxtable, J., 1982. Fine grain thermoluminescence (TL) techniques applied to flint dating. PACT 6, 346–352.

Huxtable, J., Jacobi, R. M., 1982. Thermoluminescence dating of burned flints from a British Mesolithic site: Longmoor Inclosure, East Hampshire. Archaeometry 24, 164–169.

Ibach, H., Lüth, H., 2009. Festkörperphysik. Springer, Berlin and Heidelberg.

Itoh, N., Stoneham, D., Stoneham, A., 2002. Ionic and electronic processes in quartz: mechanisms of thermoluminescence and optically stimulated luminescence. Journal of Applied Physics 92, 5036–5044.

Jain, M., Murray, A. S., Bøtter-Jensen, L., 2003. Characterisation of blue-light stimulated luminescence components in different quartz samples: implications for dose measurement. Radiation Measurements 37, 441–449.

James, S. R., 1989. Homonid use of fire in the lower and middle Pleistocene – A review of the evidence. Current Anthropology 30, 1–26.

Kalchgruber, R., 2002. α-Al_2O_3:C als Dosimeter zur Bestimmung der Dosisleistung bei der Lumineszenzdatierung. PhD thesis, Universität Heidelberg.

Kennedy, G., Knopff, L., 1960. Dating by thermoluminescence. Archaeology 13, 147–148.

King, G., Finch, A., Robinson, R., Hole, D., 2011a. The problem of dating quartz 1: Spectroscopic ionoluminescence of dose dependence. Radiation Measurements 46, 1–9.

King, G., Finch, A., Robinson, R., Taylor, R., Mosselmans, J., 2011b. The problem of dating quartz 2: Synchrotron generated X-ray excited optical luminescence (XEOL) from quartz. Radiation Measurements 46, 1082–1089.

Kitis, G., Gomez-Ros, J., Tuyn, J., 1998. Thermoluminescence glow-curve deconvolution functions for first, second and general orders of kinetics. Journal of Physics D: Applied Physics 31, 2636–2641.

Kittel, C., 2006. Einführung in die Festkörperphysik. Oldenbourg, München and Wien.

Krbetschek, M. R., Rieser, U., Zöller, L., Heinicke, J., 1994. Radioactive disequilibria in palaeodosimetric dating of sediments. Radiation Measurements 23, 485–489.

Krbetschek, M. R., Götze, J., Dietrich, A., Trautmann, T., 1997. Spectral information from minerals relevant for luminescence dating. Radiation Measurements 27, 695–748.

Krieger, H., 2007. Grundlagen der Strahlungsphysik und des Strahlenschutzes. Teubner, Wiesbaden.

Krieger, H., 2011. Strahlungsmessung und Dosimetrie. Vieweg+Teubner, Wiesbaden.

Li, S.-H., 2001. Identification of well-bleached grains in the optical dating of quartz. Quaternary Science Reviews 20, 1365–1370.

Luff, B., Townsend, P., 1990. Cathodoluminescence of synthetic quartz. Journal of Physics: Condensed Matter 2, 8089–8097.

Mahesh, K., Weng, P., Furetta, C., 1989. Thermoluminescence in solids and its applications. Nuclear Technology Publishing, Ashford, Kent.

Malik, S. R., Durrani, S. A., Fremlin, J. H., 1973. A comparative study of the spatial distribution of uranium and of TL-producing minerals in archaeological materials. Archaeometry 15, 249–253.

Markl, G., 2008. Minerale und Gesteine. Spektrum Akademischer Verlag, Heidelberg.

Martini, M., Sibilia, E., Croci, S., 1999. Glow curves and emission spectra of burnt flints. Quaternary Geochronology 18, 287–292.

Mauz, B., Packman, S., Lang, A., 2006. The alpha effectiveness in silt-sized quartz: new data obtained by single and multiple aliquot protocols. Ancient TL 24, 47–52.

McDougall, I., Brown, F., Fleagle, J., 2005. Stratigraphic placement and age of modern humans from Kibish, Ethiopia. Nature 433, 733–736.

McKeever, S. W. S., 1984. Thermoluminescence in quartz and silica. Radiation Protection Dosimetry 8, 81–98.

McKeever, S. W. S., Chen, C. Y., Halliburton, L. E., 1985. Point defects and the pre-dose effect in natural quartz. Nuclear Tracks and Radiation Measurements 10, 489–495.

McKeever, S. W. S., 1991. Mechanisms of thermoluminescence production: Some problems and a few answers? Nuclear Tracks and Radiation Measurements 18, 5–12.

Mejdahl, V., Bøtter-Jensen, L., 1994. Luminescence dating of archaeological materials using a new technique based on single aliquot measurements. Quaternary Science Reviews 13, 551–554.

Melcher, C., Zimmerman, D., 1977. Thermoluminescent determination of prehistoric heat treatment of chert artifacts. Science 197, 1359–1362.

Mercier, N., 1991. Flint palaeodose determination at the onset of saturation. Nuclear Tracks and Radiation Measurements 18, 77–79.

Mercier, N., Valladas, H., Valladas, G., 1992. Observations on palaeodose determination with burnt flints. Ancient TL 10, 28–32.

Mercier, N., Valladas, H., Bar-Yosef, O., Vandermeersch, B., Stringer, C., Joron, J.-L., 1993. Thermoluminescence date for the Mousterian burial site of Es-Skhul, Mt. Carmel. Journal of Archaeological Science 20, 169–174.

Mercier, N., Valladas, H., Valladas, G., 1995. Flint thermoluminescence dates from the CFR laboratory at Gif: Contributions to the study of the chronology of the Middle Palaeolithic. Quaternary Science Reviews 14, 351–364.

Mercier, N., Valladas, H., Froget, L., Joron, J.-L., Vermeersch, P., Van Peer, P., Moeyersons, J., 1999. Thermoluminescence dating of a Middle Palaeolithic occupation at Sodmein Cave, Red Sea Mountains (Egypt). Journal of Archaeological Science 26, 1339–1345.

Mercier, N., Valladas, H., Froget, L., Joron, J.-L., Reyss, J.-L., Balescu, S., Escutenaire, C., Kozlowski, J., Sitlivy, V., Sobczyk, K., Zieba, A., 2003. Luminescence dates for the palaeolithic site of Piekary IIa (Poland): comparison between TL of burnt flints and OSL of a loess-like deposit. Quaternary Science Reviews 22, 1245–1249.

Mercier, N., Valladas, H., Froget, L., Joron, J.-L., Reyss, J.-L., Weiner, S., Goldberg, P., Meignen, L., Bar-Yosef, O., Belfer-Cohen, A., Chech, M., Kuhn, S., Stiner, M., Tillier, A.-M., Arensburg, B., Vandermeersch, B., 2007a. Hayonim Cave: a TL-based chronology for this Levantine Mousterian sequence. Journal of Archaeological Science 34, 1064–1077.

Mercier, N., Wengler, L., Valladas, H., Joron, J.-L., Froget, L., Reyss, J.-L., 2007b. The Rhafas Cave (Morocco): Chronology of the mousterian and aterian archaeological oc-

cupations and their implications for Quaternary geochronology based on luminescence (TL/OSL) age determinations. Quaternary Geochronology 2, 309–313.

Meschede, D., Vogel, H., 2006. Gerthsen Physik. Springer, Berlin and Heidelberg.

Miallier, D., Faïn, J., Montret, M., Pilleyre, T., Sanzelle, S., Soumana, S., 1991. Properties of the red TL peak of quartz relevant to thermoluminescence dating. Nuclear Tracks and Radiation Measurements 18, 89–94.

Michab, M., Valladas, H., Froget, L., Mercier, N., 1998. Distinguishing burnt from partly bleached unburnt quartz pebbles of Pedra Furada, Brazil. Ancient TL 16, 5–9.

Micheelsen, H., 1966. The Structure of Dark Flint from Stevns, Denmark. Dansk Geologisk Forening 16, 286–368.

Munyikwa, K., 2000. Cosmic ray contribution to environmental dose rates with varying overburden thickness. Ancient TL 18, 27–34.

Murata, K., Norman, M., 1976. An Index of Crystallinity for Quartz. American Journal of Science 276, 1120–1130.

Murray, A. S., Wintle, A. G., 2000. Luminescence dating of quartz using an improved single-aliquot regenerative-dose protocol. Radiation Measurements 32, 57–73.

Murray, A. S., Roberts, R. G., Wintle, A. G., 1997. Equivalent dose measurement using a single aliquot of quartz. Radiation Measurements 27, 171–184.

Okrusch, M., Matthes, S., 2005. Mineralogie. Springer, Berlin and Heidelberg.

Olley, J. M., Roberts, R. G., Murray, A. S., 1997. Disequilibria in the uranium decay series in sedimentary deposits at Allen's cave, nullarbor plain, Australia: Implications for dose rate determinations. Radiation Measurements 27, 433–443.

Poolton, N. R. J., Bøtter-Jensen, L., Rink, W. J., 1995. An optically stimulated luminescence study of flint related to radiation dosimetry. Radiation Measurements 24, 551–555.

Prescott, J. R., Hutton, J. T., 1988. Cosmic ray and gamma ray dosimetry for TL and ESR. Nuclear Tracks and Radiation Measurements 14, 223–227.

Prescott, J. R., Hutton, J. T., 1994. Cosmic ray contributions to dose rates for luminescence and ESR dating: Large depths and long-term time variations. Radiation Measurements 23, 497–500.

Prescott, J. R., Hutton, J. T., 1995. Environmental dose rates and radioactive disequilibrium from some Australian luminescence dating sites. Quaternary Science Reviews 14, 439–448.

Preusser, F., Kasper, H. U., 2001. Comparison of dose rate determination using high-resolution gamma spectrometry and inductively coupled plasma-mass spectrometry. Ancient TL 19, 19–23.

Preusser, F., Chithambo, M. L., Götte, T., Martini, M., Ramseyer, K., Sendezera, E. J., Susino, G. J., Wintle, A. G., 2009. Quartz as a natural luminescence dosimeter. Earth-Science Reviews 97, 184–214.

Purdy, B., Brooks, H., 1971. Thermal alteration of silica minerals: an archaeological approach. Science 173, 322–325.

Randall, J., Wilkins, M., 1945. Phosphorescence and electron traps I. The study of trap distributions. Proceedings of the Royal Society A 184, 365–389.

Richter, D., Krbetschek, M., Rieser, U., Trautmann, T., Wagner, G., 1999. Spectral investigation of the thermoluminescence of heated flint (silex). Quaternary Geochronology 18, 279–285.

Richter, D., Waiblinger, J., Rink, W. J., Wagner, G. A., 2000. Thermoluminescence, electron spin resonance and ^{14}C-dating of the Late Middle and Early Upper Palaeolithic site of Geißenklösterle Cave in southern Germany. Journal of Archaeological Science 27, 71–89.

Richter, D., Krbetschek, M., 2006. A new thermoluminescence dating technique for heated flint. Archaeometry 48, 695–705.

Richter, D., Temming, H., 2006. Testing heated flint palaeodose protocols using dose recovery procedures. Radiation Measurements 41, 819–825.

Richter, D., 2007a. Advantages and limitations of thermoluminescence dating of heated flint from Paleolithic sites. Geoarchaeology 22, 671–683.

Richter, D., 2007b. Feuer und Stein – Altersbestimmung von steinzeitlichem Feuerstein mit Thermolumineszenz. In: Wagner, G. (Ed.), Einführung in die Archäometrie. Springer, Berlin and Heidelberg. 33–49.

Richter, D., Mercier, N., Valladas, H., Jaubert, J., Texier, P.-J., Brugal, J.-P., Kervazo, B., Reyss, J.-L., Joron, J.-L., Wagner, G., 2007. Thermoluminescence dating of heated flint from the Mousterian site of Bérigoule, Murs, Vaucluse, France. Journal of Archaeological Science 34, 532–539.

Richter, D., Tostevin, G., Škrdla, P., Davies, W., 2009. New radiometric ages for the Early Upper Palaeolithic type locality of Brno-Bohunice (Czech Republic): comparison of OSL, IRSL, TL and ^{14}C dating results. Journal of Archaeological Science 36, 708–720.

Richter, D., Alperson-Afil, N., Goren-Inbar, N., 2011. Employing TL methods for the verification of macroscoplically determined heat alteration of flint artefacts from palaeolithic contexts. Archaeometry 53, 842–857.

Rink, W. J., Rendell, H., Marseglia, E. A., Luff, B. J., Townsend, P. D., 1993. Thermoluminescence spectra of igneous quartz and hydrothermal vein quartz. Physics and Chemistry of Minerals 20, 353–361.

Roebroeks, W., Villa, P., 2011. On the earliest evidence for habitual use of fire in Europe. Proceedings of the National Acadamy of Sciences 108, 5209–5214.

Rottländer, R., 1975. The formation of patina on flint. Archaeometry 17, 106–110.

Rottländer, R., 1989. Verwitterungerscheinungen an Silices und Knochen. Archaeologica Venatoria, Tübingen.

Selo, M., Valladas, H., Mercier, N., Joron, J., Bassinot, F., Person, A., Nouet, J., 2009. Investigations of uranium distribution in flints. Radiation Measurements 44, 615–619.

Singarayer, J. S., Bailey, R., 2003. Further investigations of the quartz optically stimulated luminescence components using linear modulation. Radiation Measurements 37, 451–458.

Singhvi, A. K., Aitken, M., 1978. Americium-241 for alpha-irradiations. Ancient TL 3, 2–9.

Smith, M., Prescott, J., Head, M., 1997. Comparison of ^{14}C and luminescence chronologies at puritjarra rock shelter, central Australia. Quaternary Science Reviews 16, 299–320.

Soressi, M., Jones, H. L., Rink, W. J., Maureille, B., Tillier, A.-m., 2007. The Pech-de-l'Aze´ I Neandertal child: ESR, uranium-series, and AMS ^{14}C dating of its MTA type B context. Journal of Human Evolution 52, 455–466.

Spooner, N. A., Questiaux, D. G., 2000. Kinetics of red, blue and UV thermoluminescence and optically-stimulated luminescence from quartz. Radiation Measurements 32, 659–666.

Stevens Kalceff, M. A., Phillips, M. R., 1995. Cathodoluminescence microcharacterization of the defect structure of quartz. Physical Review B 52, 3122–3132.

Subedi, B., Kitis, G., Pagonis, V., 2010. Simulation of the influence of thermal quenching in thermoluminescence glow-peaks. Physica Status Solidi A 207, 1216–1226.

Subedi, B., Polymeris, G. S., Tsirliganis, N. C., Pagonis, V., Kitis, G., 2012. Reconstruction of thermally quenched glow curves in quartz. Radiation Measurements 47, 250–257.

Talamo, S., Soressi, M., Roussel, M., Richards, M., Hublin, J.-J., 2012. A radiocarbon chronology for the complete Middle to Upper Palaeolithic transitional sequence of Les Cottés (France). Journal of Archaeological Science 39, 175–183.

Trachsel, M., 2008. Ur- und Frühgeschichte. Quellen, Methoden, Ziele. Orell Füssli, Zurich.

Tribolo, C., Mercier, N., Valladas, H., 2001. Alpha sensitivity determination in quartzite using an OSL single aliquot procedure. Ancient TL 19, 47–50.

Tribolo, C., Mercier, N., Valladas, H., 2003. Attempt at using the single-aliquot regenerative-dose procedure for the determination of equivalent doses of Upper Palaeolithic burnt stones. Quaternary Science Reviews 22, 1251–1256.

Tribolo, C., Mercier, N., Selo, M., Valladas, H., Joron, J.-L., Reyss, J.-L., Henshilwood, C., Sealy, J., Yates, R., 2006. TL dating of burnt lithics from Blombos Cave (South Africa): Further evidence for the antiquity of modern human behaviour. Archaeometry 48, 341–357.

Valladas, G., 1988. Stopping power and range for α particles in SiO_2. Ancient TL 6, 7–8.

Valladas, H., 1978. Thermoluminescence dating of burnt stones from prehistoric site. PACT 2, 180–183.

Valladas, H., 1981. Thermoluminescence de gres de foyers prehistoriques: Estimation de leur temperature de chauffe. Archaeometry 23, 221–229.

Valladas, H., Valladas, G., 1982. Effet de l'irradiation alpha sur des grains de quartz. PACT 6, 171–178.

Valladas, H., 1985. Some TL properties of burnt prehistoric flints. Nuclear Tracks and Radiation Measurements 10, 785–788.

Valladas, H., Joron, J. L., Valladas, G., Arensburg, B., Bar-Yosef, O., Belfer-Cohen, A., Goldberg, P., Laville, H., Meignen, L., Rak, Y., Tchernov, E., Tillier, A. M., Vandermeersch, B., 1987. Thermoluminescence dates for the Neanderthal burial site at Kebara in Israel. Nature 330, 159–160.

Valladas, H., Reyss, J.-L., Joron, J.-L., Valladas, G., Bar-Yosef, O., Vandermeersch, B., 1988. Thermoluminescence dating of Mousterian 'Proto-Cro-Magnon' remains from Israel and the origin of modern man. Nature 331, 614–616.

Valladas, H., 1992. Thermoluminescence dating of flint. Quaternary Science Reviews 11, 1–5.

Valladas, H., Mercier, N., Froget, L., Hovers, E., Joron, J.-L., Kimbel, W. H., Rak, Y., 1999. TL dates for the Neanderthal site of the Amud Cave, Israel. Journal of Archaeological Science 26, 259–268.

Valladas, H., Mercier, N., Froget, L., Joron, J. L., Reyss, J. L., Karkanas, P., Panagopoulou, E., Kyparissi-Apostolika, N., 2007. TL age-estimates for the Middle Palaeolithic layers at Theopetra cave (Greece). Quaternary Geochronology 2, 303–308.

Valladas, H., Mercier, N., Ayliffe, L. K., Falguères, C., Bahain, J.-J., Dolo, J.-M., Froget, L., Joron, J.-L., Masaoudi, H., Reyss, J.-L., Moncel, M.-H., 2008. Radiometric dates for the Middle Palaeolithic sequence of Payre (Ardèche, France). Quaternary Geochronology 3, 377–389.

Wagner, G. A., 1995. Altersbestimmung von jungen Gesteinen und Artefakten. Enke, Stuttgart.

Waligórski, M., Hamm, R., Katz, R., 1986. The radial distribution of dose around the path of a heavy ion in liquid water. Nuclear Tracks and Radiation Measurements 11, 309–319.

Werts, S., Jahren, A., 2007. Estimation of temperatures beneath archaeological campfires using carbon stable isotope composition of soil organic matter. Journal of Archaeological Science 34, 850–857.

Weymouth, J., Williamson, W., 1951. Some physical properties of raw and calcined flint. Mineralogical Magazine 29, 573–593.

Wintle, A. G., 1975. Thermal quenching of thermoluminescence in quartz. Geophysical Journal. Royal Astronomical Society 41, 107–113.

Wintle, A. G., Aitken, M., 1977. Thermoluminescence dating of burnt flint: application to a lower Palaeolithic site, Terra Amata. Archaeometry 19, 111–130.

Wintle, A. G., Murray, A. S., 1999. Luminescence sensitivity changes in quartz. Radiation Measurements 30, 107–118.

Wintle, A. G., Murray, A. S., 2006. A review of quartz optically stimulated luminescence characteristics and their relevance in single-aliquot regeneration dating protocols. Radiation Measurements 41, 369–391.

Wintle, A. G., 2008. Fifty years of luminescence dating. Archaeometry 50, 276–312.

Wolpoff, M., Hawks, J., Caspari, R., 2000. Multiregional, not multiple origins. American Journal of Physical Anthropology 112, 129–136.

Yang, X. H., McKeever, S. W. S., 1990. Point defects and the pre-dose effect in quartz. Radiation Protection Dosimetry 33, 27–30.

Yukihara, E. G., McKeever, S. W. S., 2011. Optically Stimulated Luminescence – Fundamentals and Applications. Wiley, West Sussex.

Zimmerman, D., 1971a. Thermoluminescence dating using fine grains from pottery. Archaeometry 13, 29–52.

Zimmerman, D., 1972. Relative thermoluminescence effects of alpha and beta radiation. Radiation Effects 14, 81–92.

Zimmerman, J., 1971b. The radiation-induced increase of the 100°C thermoluminescence sensitivity of fired quartz. Journal of Physics C: Solid State Physics 4, 3265–3276.

Zöller, L., Blanchard, H., 2009. The partial heat – longest plateau technique: Testing TL dating of Middle and Upper Quaternary volcanic eruptions in the Eifel area, Germany. Eiszeitalter und Gegenwart 58, 86–106.

2 On the luminescence signal of empty sample carriers

Christoph Schmidt[a], Sebastian Kreutzer[b], Morteza Fattahi[c], Richard Bailey[c], Anja Zander[a], Ludwig Zöller[b]

[a] Institute for Geography, University of Cologne, Otto-Fischer-Str. 4, 50674 Köln, Germany
[b] Geographical Institute, Geomorphology, University of Bayreuth, 95440 Bayreuth, Germany
[c] Oxford University Centre for the Environment, University of Oxford, South Parks Road, Oxford OX1 3QJ, United Kingdom

Ancient TL 29, 65–74 (2011)

Abstract

Luminescence dating is a leading technique for a large spectrum of Quaternary dating applications. Since the development of automated reader systems, handling great amounts of samples has become possible. A large quantity of data is produced in a short time and a detailed check of every single curve is often impractical. Therefore, it is important to be confident in excluding any kind of unwanted signal contributions, such as those from sample carriers. For commonly used types of steel and aluminium (Al) carriers from three laboratories, luminescence characteristics of spurious and radiation-induced signals are presented. TL and OSL emissions of discs show natural (Al) and regenerated thermally stable signals in the UV, UV-blue and red detection range. These signals have characteristic saturation doses of several hundred Gy. Furthermore, we demonstrate light insensitive signal components and phototransferred thermoluminescence (PTTL). Due to high scatter between discs, the proportion of unwanted disc signal contribution to the entire signal is difficult to predict, without direct measurement. The sources of these signals are possibly chemical compounds acting as luminophores or oxide layers (Al_2O_3 layers in case of Al discs).

2.1 Introduction

Since the beginning of thermoluminescence (TL) and later optically stimulated luminescence (OSL) dating much effort has been focused on avoiding unwanted signal contributions to those used for dating purposes (Aitken 1985; Aitken 1998). These contributions can originate from the sample itself or the measurement setup, e.g. the atmosphere during TL measurements or phosphorescence from the filters. The choice of the sample carrier is therefore of paramount importance for measuring a clean luminescence signal from the sample only.

The first TL measurements with relevance to recent dating applications were carried out with samples mounted on glass plates (Daniels et al. 1953). Several other materials were used as sample holders in the following decades, such as aluminium (Al), platinum, nickel, steel (Bøtter-Jensen 1997), or silver (Yawata & Hashimoto 2007). Only sparse information on the applicability of those substances is given in the literature (Berger et al. 1982; Aitken 1998). The authors report on "parasite" luminescence signals generated by Al holders. Today, most laboratories use stainless steel or Al carriers for sample placement in the commonly used Risø readers, usually termed as discs (flat plate) or cups (with depression). It should be mentioned, however, that one of the first materials used for TL dosimetric purposes was Al oxide (Al_2O_3) (Osvay & Biró 1980).

However, to our best knowledge, no systematic study has been published in the contemporary luminescence dating literature to prove the absence of parasite luminescence for commonly used sample holders. Standard measurement protocols do not check for unwanted signal contributions. Thus, the registered net luminescence (background subtracted) is routinely attributed in its entirety to the sample.

Since we found hints on spurious (i.e. non-radiation-induced) and dose-dependent luminescence signals of a variety of different disc materials during experimental measurements, we conducted a study to investigate the features of these potentially problematic signals and their expected influence on dose determination. Therefore, we measured various sample carriers (Al and steel) from the luminescence laboratories in Oxford, Cologne and Bayreuth using different stimulation methods (TL, OSL, IRSL) and detection windows (UV: $340\,\Delta\,80\,\mathrm{nm}$, UV-blue: $420\,\Delta\,30\,\mathrm{nm}$, red: $625\,\Delta\,25\,\mathrm{nm}$ and $630\,\Delta\,30\,\mathrm{nm}$). Furthermore, we examined the dose response characteristics and the bleachability of the signals as well as the phototransferred thermoluminescence (PTTL) (Furetta 2010; Kalchgruber 2002) of empty discs. An exemplary equivalent dose determination (SAR protocol, after Murray & Wintle (2000)) of a well-studied sediment sample acts as reference point for assessing signal interference. Finally, an alternative method for cleaning the discs is presented and its effectiveness is tested.

2.2 Materials and methods

2.2.1 Sample carriers

To investigate the luminescence behavior of sample carriers, three kinds of empty discs or cups commonly employed in laboratories were tested:

1. Stainless steel discs used in Oxford and Cologne (Cr-Ni steel V4A, diameter 9.8 mm, thickness 0.5 mm),
2. Al discs used in Oxford, Cologne and Bayreuth (unknown Al composition, diameter 9.8 mm or 9.6 mm, thickness 0.45 mm),
3. Al cups, manufactured in Bayreuth (Goodfellow Al foil, purity 99.0 %, diameter 12.0 mm, thickness 0.1 mm).

From each kind of discs or cups, at least five exemplars were measured. We chose all discs randomly from the "clean disc box" (for the applied cleaning procedure, see below) and measured them without further chemical and physical treatments. Regarding Al discs, we tested both used and new discs. Al cups from Bayreuth were new, because cleaning without damaging is difficult due to their low thickness.

2.2.2 Disc cleaning procedures

To test the effects of disc cleaning procedures on spurious and dose-dependent signals, two methods were applied on used discs in Cologne.

1. Steel and Al discs were cleaned in an ultrasonic bath in addition to mechanical rubbing (sponge) and washing with rinsing agent to remove remaining silicon oil. Afterwards, the discs were flushed with distilled water and purged in acetone.
2. A mechanically more severe procedure was applied to remove the oxidized layers from steel and Al discs. Several tens of discs were placed in a bottle of chalk suspension and kept on the shaking table for polishing for 24 h, or 72 h if they were scrubbed with scouring agent in advance. Washing with distilled water afterwards prevents measuring spurious signals from carbonates. The loss in mass is negligible.

2.2.3 Measurement setup

The luminescence measurements were carried out on different Risø DA-12, DA-15 and DA-20 readers in Cologne, Oxford and Bayreuth, equipped with a standard bialkali photomultiplier tube (EMI 9235QB). In addition, for the red detection a cooled trialkaline photomultiplier tube (EMI 9658B) described in Fattahi & Stokes (2005) was used in Oxford. The luminescence was measured placing the following filters consecutively between the disc and the photomultiplier:

1. Hoya U340 (7.5 mm, 340 Δ 80 nm),
2. Combination of Schott GG400 (3.0 mm), Corning 7-59 (2.0 mm), Schott BG39 (1.0 mm) and HA3 (4.0 mm): UV-blue detection centered at 420 nm,
3. Chroma D410/30x interference filter for UV-blue detection (410 Δ 30 nm) for IRSL,
4. Chroma D630/60 M (630 Δ 30 nm, Cologne) or Omega D625/DF50 (625 Δ 25 nm, Oxford) interference filters for red detection, respectively.

The heating rates were set to values of 2 or 5 $K\,s^{-1}$ and the measurement chamber was flushed with N_2 for two minutes before each measurement exceeding 160 °C, except where indicated otherwise. Maximum temperatures for UV TL (UVTL) and UV-blue TL (BTL) measurements were 500 °C and for red TL (RTL) 450 °C. The background for each measurement was recorded immediately afterwards. For OSL measurements of the UV emissions, blue LEDs (470 Δ 30 nm) and for IRSL measurements, infrared LEDs (870 Δ 40 nm) were used.

The discs received radiation doses from $^{90}Sr/^{90}Y$ β-sources delivering around 5 $Gy\,min^{-1}$ (DA-12 and DA-15) or 7 $Gy\,min^{-1}$ (DA-20). These dose rates are usually calculated for mineral grains mounted on the discs and not for the discs themselves. Therefore, the dose rates are approximations.

2.2.4 Dose response measurements

For dose response measurements, blank discs were irradiated with incremental doses up to ca. 1 or 2 kGy and subsequently TL and OSL were measured. A standardized luminescence efficiency value, with units cts $(K\,Gy)^{-1}$ for TL and cts $(s\,Gy)^{-1}$ for OSL, respectively, allows comparing measurements with differing parameters, e.g. heating rate or measurement channels (suggested by M. Krbetschek, pers. comm.). The TL signal was integrated over the thermally stable range of 300–400 °C for UVTL and BTL. To avoid the influence of increasingly noisy net signals above 350 °C, the integration interval for RTL was lowered to 250–350 °C. The OSL/IRSL decay curves were measured at 125 °C read temperature after a preheat of 260 °C (OSL) for 10 s and read temperatures of 50 °C after a preheat of 250 °C for 60 s or 270 °C for 10 s (IRSL).

2.3 Experimental details and results

2.3.1 Thermoluminescence signal

2.3.1.1 Steel discs

Steel discs from the Cologne and Oxford laboratories were heated to 500 °C (UVTL and BTL) or 450 °C (RTL) and TL was measured first without irradiation, then after incremental β-doses. Between the dose steps, a test dose was given to record potential sensitivity

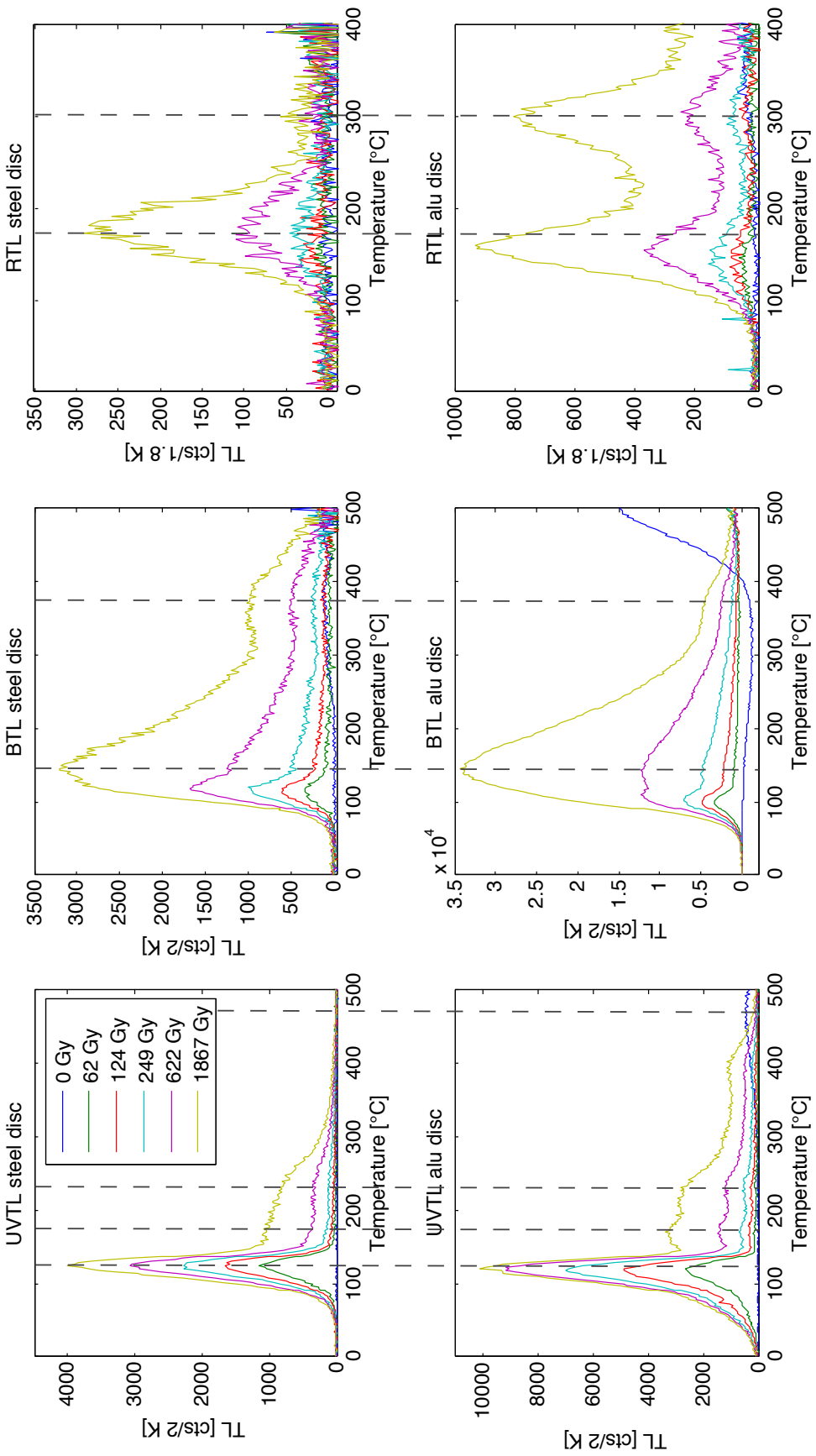

Figure 2.1: Natural and regenerated TL signals from single steel and Al discs for different detection wavelengths. All measurements were performed in Cologne and carried out at 5 K s^{-1}. For further details, see text.

changes. No signal above background could be detected for non-irradiated steel discs except for a small 380 °C peak in the blue range (Fig. 2.1). Significant TL signals resulted from exposure to ionizing radiation. UVTL and BTL showed a strong 110 °C peak, whereas for BTL this peak slightly shifts towards higher temperatures or is superposed by another peak on its high temperature shoulder for high doses (> 1 kGy). At higher temperatures, we observed at least two other peaks which form a broad continuously decreasing shoulder between 150 and 300 °C in the UV range. Little UVTL signal is detected above 300 °C. A similar shoulder occurs in the blue window, followed by a distinct peak centered at 380 °C in the high temperature region. In the red detection window, steel discs are far less sensitive to irradiation. We only observed signals above background noise for doses > 250 Gy (peak at 180 °C).

2.3.1.2 Al carriers

We applied the same measurement routine to Al discs from the Oxford and Cologne laboratories. In contrast to steel discs, Al discs yielded a notable TL signal without artificial irradiation. The peak positions for this spurious signal are 480 °C (UV) and ≥ 500 °C (UV-blue) with count rates extending from a few hundred cts K^{-1} in the UV and red (no peak observable) up to several thousand cts K^{-1} in the blue detection window. For BTL, however, difficulties with the background subtraction led to a negative net signal and the "natural" peak may also suffer from this problem. The natural UVTL and BTL signal is not depleted completely by measurements up to 500 °C. Hence, remaining trapped charge appears to cause a spurious signal also in subsequent measurements (data not shown).

Following β-irradiation, the 110 °C UVTL peak of Al discs appears at slightly lower temperatures in comparison to steel, due to the higher thermal conductivity of Al and thus reduced thermal lag between heater plate and upper disc surface. We observed three other UVTL peaks at 180, 220 and 400 °C for β-doses > ca. 250 Gy (Fig. 2.1). Similar to the BTL emission of steel, Al discs yield a 110 °C peak that is surpassed in growth by a peak at 140 °C for doses > 600 Gy. A further small BTL peak of Al is centered at 380 °C. The RTL emission of Al discs is dominated by two maxima at 150 and 300 °C. The low temperature peak seems to correspond to the RTL peak observed for steel discs, whereas steel discs only show a very weak 300 °C peak.

The positions of the TL peaks in the various detection windows for steel and Al discs are roughly the same for all measured discs. However, the intensities of the luminescence emissions and the relation of peak heights vary considerably between individual discs.

We also detected low spurious TL signals in the UV range for Al cups as a slowly growing shoulder from 200 up to 450 °C. Following β-irradiation up to ca. 1 kGy, we found UVTL peaks at 110 °C and at around 400 °C for doses > 500 Gy (see supplementary data at www.aber.ac.uk/ancient-tl, respectively in Section A.1). BTL glow curves of several Al cups exhibit a very weak peak at 110 °C after the highest regeneration dose (> 1 kGy). In general, used and cleaned Al and steel discs produce much higher spurious and regenerated signal intensities in the UV and blue detection range than new Al cups. RTL emissions of Al cups were not investigated.

Fig. 2.2 presents the results of an experiment to measure the influence of grain coverage on unwanted signal contributions of used Al discs. All signals were recorded in the UV detection window. Fig. 2.2a shows the integrated TL (300–350 °C) of the spurious signal and the regenerated signal after 50 Gy β-irradiation for 45 discs. The ratio of these signals for each disc is plotted in Fig. 2.2b. The annealed discs were then irradiated with 50 Gy and immediately covered with annealed quartz grains (BT781, loessic sample from Nussloch, Germany, unit P4-1, 100–200 µm, heated at 500 °C for 1 h) using masks of different diameter (discs 1–15: 1 mm; discs 16–30: 2 mm; discs 31–45: 8 mm). Fig. 2.2c shows the ratio of the regenerated TL signal of grain-covered discs and uncovered discs (measured after cleaning the discs individually afterwards). These measurements indicate that the effect of light shielding through grain coverage is negligible. The fact that the ratio is higher than 1 is probably a result of the cleaning procedure. Fig. 2.2d shows the ratio of the 50 Gy irradiated quartz sample (mounted on Al discs using the same order and mask diameters as in Fig. 2.2c) and the regenerated signal after the same dose of the same discs without quartz layer.

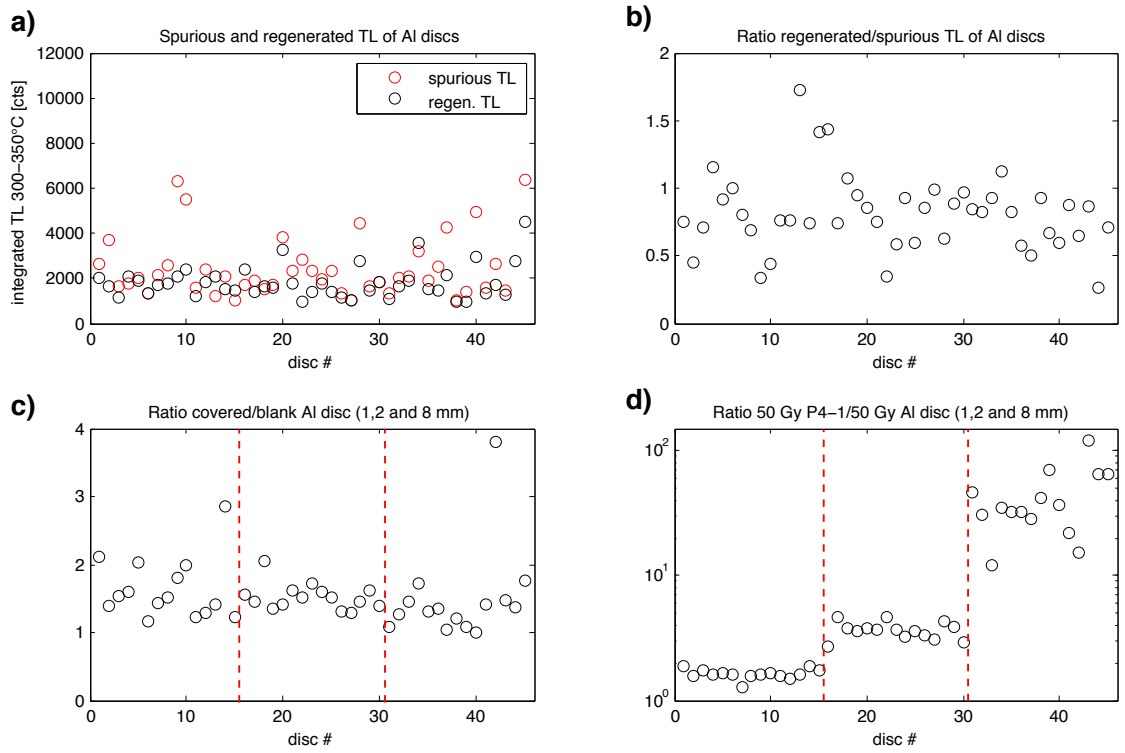

Figure 2.2: Results of the experiment to measure the influence of grain coverage on unwanted signal contributions of used Al discs (UV detection range). Experimental conditions and detailed descriptions are given in the text.

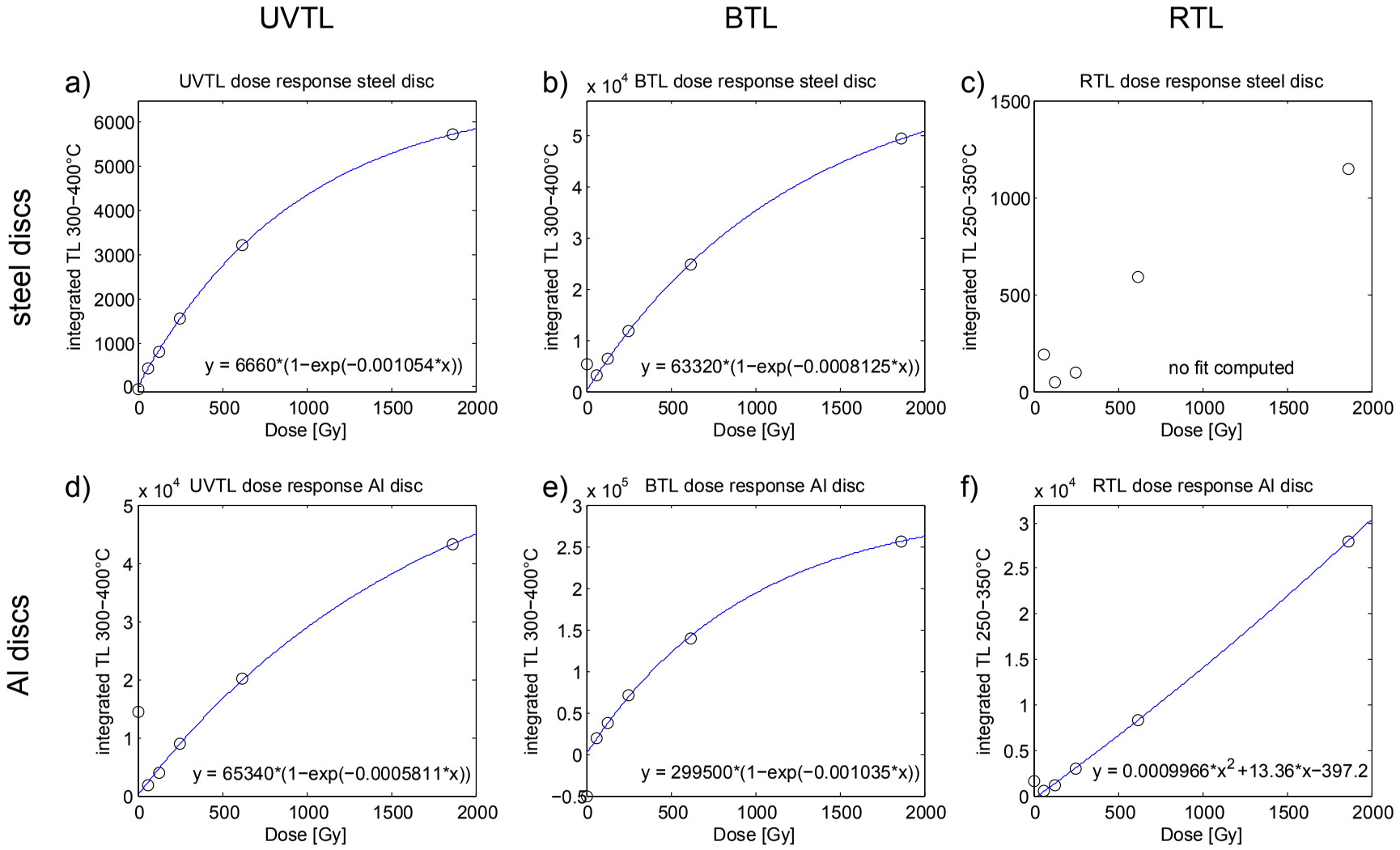

Figure 2.3: TL dose response curves of steel and Al discs for different emissions. The investigated discs are the same as shown in Fig. 2.1. Integration limits are as indicated on the ordinate. For further details, see text.

2.3.1.3 Dose response

Growth curves of UVTL and BTL emissions of steel discs can be fitted to single saturating exponentials with characteristic saturation doses (D_0) of ca. 950 Gy and 1.23 kGy, respectively (Fig. 2.3). For low β-doses (< 200 Gy), the dose response can be approximated with a linear fit. In this range, the dose response amounts to about 3 cts $(\mathrm{K\,Gy})^{-1}$ for UVTL and 24 cts $(\mathrm{K\,Gy})^{-1}$ for BTL. For higher doses, these values decrease due to saturation. The RTL signals in the thermally stable region are too low to estimate their dose response. The UVTL and BTL growth curves of Al discs show similar behavior with approximately linear growth up to doses of 500 Gy (UVTL) and 300 Gy (BTL) and characteristic saturation doses of 1.72 kGy and 970 Gy, respectively. In contrast, the RTL Al emission reveals supralinear increase for doses < 2 kGy. Up to onset of saturation, the dose response of Al discs can be expressed as ca. 20 cts $(\mathrm{K\,Gy})^{-1}$ for UVTL, ca. 180 cts $(\mathrm{K\,Gy})^{-1}$ for BTL and ca. 4–6 cts $(\mathrm{K\,Gy})^{-1}$ for RTL emissions.

Test dose monitoring shows little sensitization for steel discs and Al discs and cups. The effect is most distinct for the 110 °C TL peak in the UV and blue detection window and the BTL high temperature peaks of Al discs, but not quantifiable for other high temperature peaks.

2.3.1.4 Growth rate of the spurious signal

As spurious and dose-dependent signals of Al discs may derive from oxide layers, the signal response was investigated for different durations of oxygen exposure. Fresh chalk-polished Al discs (Cologne, procedure see above) were stored in an acetone bath in a closed bottle to prevent contact with oxygen. Batches of 5 discs were successively removed at defined times. The remaining time to the UVTL measurements is then the oxygen exposure time. Those were set to 10 minutes (approximated 0 days), 2, 5, 20 and 41 days. The TL signal was integrated over the range 250–450 °C.

We observed no growth within measurement uncertainty up to oxygen exposure durations of 20 days, due to high scatter of the spurious TL signal between discs (Fig. 2.4a). For longer contact with air, the discs showed a substantially increased signal. In order to check whether there is a correlation between spurious and regenerated signal, all discs received a β-dose of 250 Gy after initial spurious signal readout (Fig. 2.4b). We calculated the ratio of both signals in the same temperature interval. The ratio values (regenerated signal/spurious signal) denote high disc-to-disc scatter and suggest that both signals are not closely correlated (data not shown). However, Fig. 2.4 indicates that longer oxygen exposure duration generates both stronger spurious and radiation-induced TL signals.

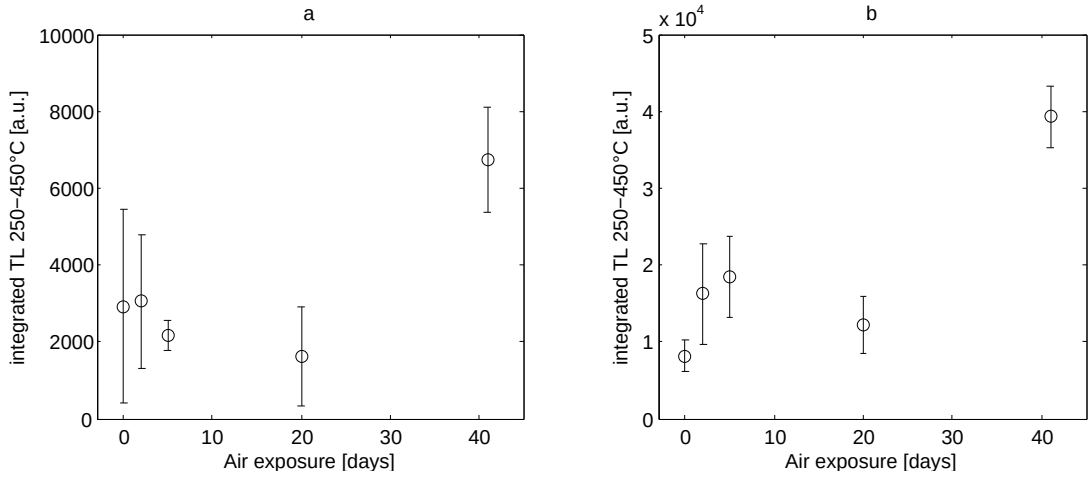

Figure 2.4: Growth of (a) spurious and (b) 250 Gy regenerated UVTL signals of Al discs with air (oxygen) exposure duration. The error bars represent the standard deviation of 5 discs each.

2.3.2 Optically and infrared stimulated signals

2.3.2.1 OSL

All steel discs were preheated to 260 °C for 10 s at a rate of $5\,\mathrm{K\,s^{-1}}$ to simulate conditions equal to routine OSL measurements. We observed negligible OSL signals without artificial irradiation, but count rates up to $20\,\mathrm{cts\,(s\,Gy)^{-1}}$ for β-doses < 100 Gy (Fig. 2.5). Pronounced scatter of signal intensity and growth between single discs is typical. Al discs show OSL signals of about $2\,\mathrm{cts\,(s\,Gy)^{-1}}$ after a 260 °C preheat for 10 s up to the highest regeneration dose. Al cups produce OSL signal above background in the range of $10\,\mathrm{cts\,(s\,Gy)^{-1}}$ in the first one or two measurement channels after irradiation, indicating a rapidly decaying signal component (supplementary data). As for steel discs, initial OSL signal intensities of Al cups differ considerably from cup to cup. Due to low signal-to-noise ratios of the test dose signals, we cannot provide any information on potential sensitivity changes for OSL of steel and Al sample carriers.

2.3.2.2 IRSL

We also checked the IRSL signals from discs during common IRSL (feldspar) measurement conditions. After a 270 °C preheat for 10 s or 250 °C for 60 s IRSL was measured at 50 °C. Steel discs as well as Al cups completely lack IRSL signals (natural and after irradiation). Al discs reveal a dose dependent, slowly decaying signal with count rates in the range of 2–5 $\mathrm{cts\,(s\,Gy)^{-1}}$, but no natural IRSL signal (supplementary data).

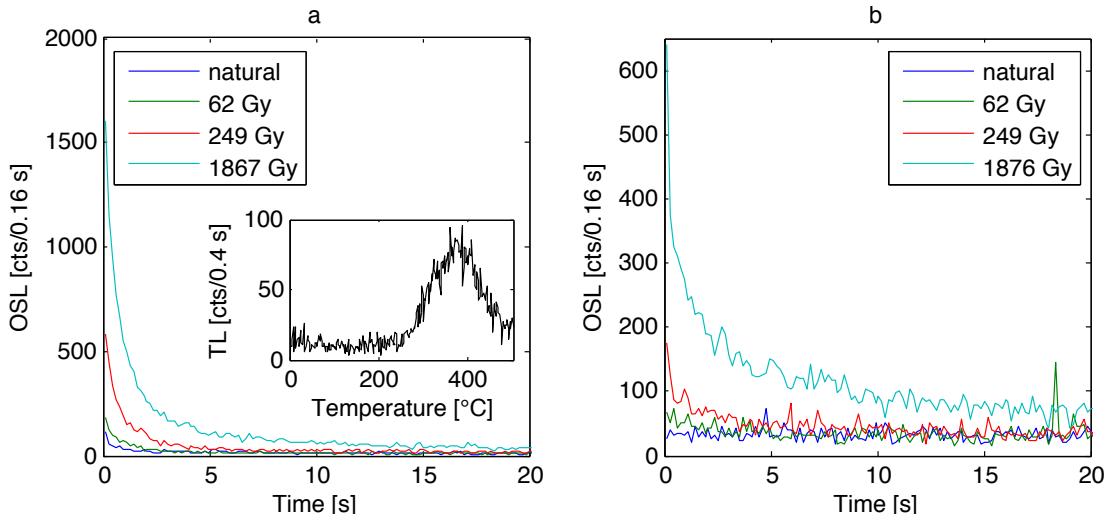

Figure 2.5: Natural (0 Gy) and regenerated OSL signals of single (a) steel and (b) Al discs after preheat (260 °C for 10 s). The inset in (a) shows the residual UVTL measured after β-irradiation of 1867 Gy and 40 s blue optical stimulation (470 Δ 30 nm). For further details, see text.

2.3.2.3 Residual TL

After OSL signal depletion and subsequent TL measurement we detected a non-bleachable or slowly bleachable signal component at high temperatures for both steel and Al discs. An example of the residual UVTL of a steel disc after 1867 Gy β-irradiation is shown in the inset of Fig. 2.5a. In general, the residual UVTL signal of Al discs shows higher count rates than that for steel discs (Fig. 2.6). Furthermore, the peak positions of natural and regenerated residual glow curves of Al discs differ significantly. As the empty discs are handled under room light conditions (and therefore light sensitive components should be removed), it is probable that the 0 Gy peak in Fig. 2.1 (lower left) is identical to the 0 Gy peak shown in Fig. 2.6. The dose response of Al residual UVTL is approximately linear up to β-doses of 500 Gy, but shows exponential saturation for higher doses ($D_0 \sim 2$ kGy, Fig. 2.6).

2.3.2.4 Photo-transferred thermoluminescence (PTTL)

For the measurement of PTTL, the discs were first irradiated with 250 Gy, twice annealed to 500 °C, and subsequently two cycles of OSL and UVTL were measured without further irradiation. The OSL signals (max. about 1500 cts s^{-1}) of the Al discs show an initial increase before decaying exponentially as expected from a typical OSL curve. This is contrary to the OSL signals observed after lower preheat temperatures. Optical stimulation induced a weak PTTL signal (ca. 60 cts K^{-1}) with a peak at 190 °C (Fig. 2.7c). The dose response of the PTTL signal was not investigated. Our results indicate that steel discs are free from PTTL signals.

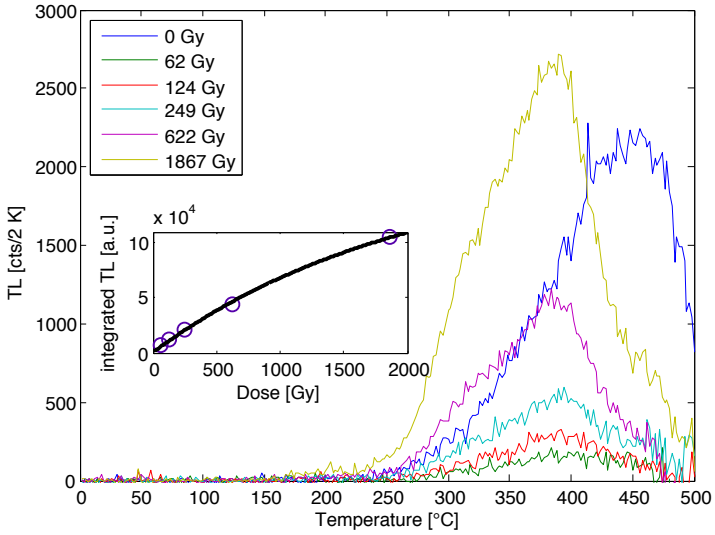

Figure 2.6: Dose response of residual UVTL after blue optical stimulation (470 Δ 30 nm) for 40 s for one Al disc. The inset displays the signal growth for integrated TL (340–440 °C) as a function of the regeneration dose, fitted to a single saturating exponential ($y = a \cdot (1 - \exp(-b \cdot x))$, where a = 1.74E+05, b = 4.95E-04 and x is dose in Gy).

2.3.3 Influence of cleaning procedures

Since the BTL emissions of both steel and Al discs showed the strongest luminescence, we used them as an indicator of signal reduction attributed to the chalk cleaning procedure. The polishing of steel discs with chalk reduced the spurious and dose-dependent BTL signals by about 40–50 % but did not suppress them completely (data not shown). Though natural signals are lacking, we still observed a prominent 110 °C peak of about 10 cts $(\mathrm{K\,Gy})^{-1}$.

Al discs showed a natural BTL signal with a peak at 450 °C (ca. 100–200 cts K^{-1}) and a regenerated emission of 1–2 cts $(\mathrm{K\,Gy})^{-1}$ after air storage of several days. Accordingly, the disturbing signal can be effectively reduced but not fully eliminated.

2.3.4 Influence of the disc signals on D_e determination

In order to test the effect of unwanted signal contributions of sample discs during an equivalent dose determination, a standard SAR protocol was carried out (Murray & Wintle 2000) using a coarse grain quartz sample (BT781) whose reliable luminescence characteristics are known (Zöller et al. 1988; Tissoux et al. 2010). Half of 10 steel and half of 10 Al discs were annealed (500 °C for 30 s), the other half remained untreated prior to grain deposition (aliquots of 2 mm diameter). A preheat temperature of 240 °C, a cutheat of 220 °C and a read temperature of 125 °C were chosen and a hot bleach (OSL at 280 °C for 40 s) was applied at the end of each SAR cycle. Excluding one outlier

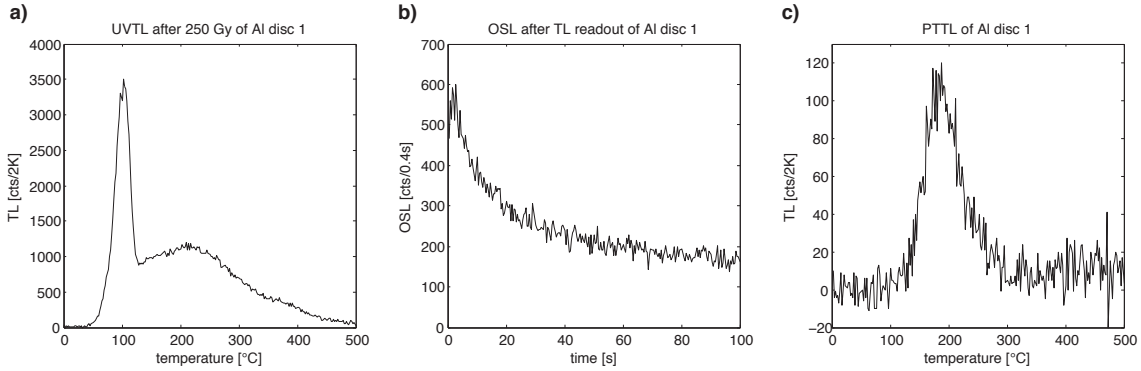

Figure 2.7: PTTL measurement in the UV of an Al disc after a β-dose of 250 Gy was given: (a) background subtracted TL measurement up to 500 °C after irradiation. (b) subsequently recorded blue stimulated OSL signal. (c) photo-transferred TL signal after optical signal depletion.

(annealed steel disc no. 4, supplementary data Fig. A.3a), the mean D_e values determined with natural discs are ca. 20 % (steel, $n = 4$) and 35 % (Al, $n = 5$) higher than those measured with annealed discs ($n = 5$ each). This indicates that the natural disc signal contributes verifiably to the initially measured geological signal of the sample. In addition, the measurement uncertainty of each single D_e value increases substantially if the discs are not annealed before the measurement. This effect is more distinct for steel than for Al discs, i.e., the mean uncertainty increases by about 90 % and 72 %, respectively, if the discs remain untreated prior to the measurement. Differences in the recycling ratio for annealed and non-annealed discs are not significant. However, statistical validity is limited by the small number of measured aliquots and further measurements are needed (supplementary data).

2.4 Discussion

The striking difference of TL peak temperatures for spurious and radiation-induced signals from Al discs (Fig. 2.1) suggests that different kinds of traps are involved in charge storage, but that potentially the same suit of recombination pathways are used owing to the common emission band (although detailed spectral measurements would be needed in order to confirm this). We observed several UVTL and BTL peaks between 100–400 °C that cannot be distinguished without curve fitting. The RTL glow curve on the other hand consists of only two visually distinguishable peaks, suggesting involvement of fewer types of charge traps. In contrast to Cr-Ni steel, the charge occupation sites connected to the spurious and the dose-dependent signal of Al both include non-bleachable (insensitive to visible light) residual TL, suggesting that full signal erasure may only be possible by heat treatment.

Due to the high affinity of Al to O, aluminium oxide layers build up within a few minutes when the (hypothetically) clean disc is exposed to oxygen. These layers reach thicknesses

of up to 30 nm on pure Al at high temperatures (> 300 °C) (Ostermann 2007). Diffusion of O is then not possible anymore and the layer protects against continuing corrosion (Bargel & Schulze 2008). Possibly, intrinsic defects of Al_2O_3 are responsible for part of the luminescence signal of the Al discs.

Similar to silicon dioxide (SiO_2), Al_2O_3 can also facilitate vacancies and interstitials (due to impurities) in its molecular structure, such as oxygen vacancies which in quartz act as hole traps (Kelly & Laubitz 1967; Preusser et al. 2009). Oxygen vacancies are described in Al_2O_3 as well, but acting as traps for electrons instead of holes (Hakanen et al. 1997). The remarkable luminescence sensitivity of Al_2O_3 is commonly used for dosimetric applications, where the dosimeters are additionally doped with e.g. C, Fe or recently with Tb and Tm (Osvay & Biró 1980; Aypar 1986; Akselrod et al. 1993; Barros et al. 2010). Luminescence properties are then, however, strongly influenced by the elements used for doping.

Stainless steel, as used for the discs, contains small amounts of carbon and silicon which might together form luminophores (carbides) (pers. comm. M. Krbetschek). It cannot be excluded that those contribute to the luminescence signal of the investigated steel discs. Furthermore, we cannot rule out that a small layer of Cr and Fe oxides (a few atom layers thick, arising from the admixture of Cr to the alloy) on Cr-Ni steel, causes part of the dose-dependent luminescence signal (Blasek & Weihert 1979; Bargel & Schulze 2008).

Although we observed minor dissimilarities between glow curves of steel and Al discs, the main peaks seem to correspond for both materials and all measured emissions (Fig. 2.1). This fact suggests that there is one common source for all disc materials.

Previous studies dealing with spurious luminescence from silicone oil revealed ambiguous findings. In combination with Al discs, considerable spurious TL signals were found, but not with steel discs (Murray 1981). Vandenberghe et al. (2008) reported that silicone oil (Willy Rüsch GmbH) potentially contributes to disturbing OSL signals. In both investigations, sample carrier materials are not described in detail. In contrast, Fuchs (2001) found silicone oil (from the same manufacturer) on Al cups to be free from spurious and radiation-induced OSL signals. The fact that Vandenberghe et al. (2008) observed disturbing signals of used and cleaned steel cups indicates that adherent silicone residues are a potential source. This would imply that conventional cleaning techniques (as described above) are not capable of removing silicone oil completely. As silicone is made up of silicon and oxygen atoms (among others), there might be chemical reactions during heat treatment or storage resulting in some kind of luminophore. Spurious signal levels of new sample holders possibly depend on the cleaning procedure prior to first use (if cleaned at all) because in some workshops lubricant oils (containing forms of silicone) might be used for disc or cup manufacturing. Beside the technique mentioned above, there are also alternative methods to remove silicone relics and to clean the discs, such as using propanol or butanone (Vandenberghe et al. 2008) or short acid treatments (e.g. 1–2 % aqua regia or diluted phosphoric acid for a few minutes).

In summary, there are two main sources potentially causing the observed disc signals: luminescent chemical compounds of the carrier material itself, or some kind of contamination resulting from grain deposition (silicone oil) that resists the cleaning procedures. Similar glow curves for both investigated materials favor contaminations as main source. However, further investigation is needed for conclusive determination of the origin of the observed signals.

For TL measurements, it is clearly advisable to use Al cups of the type described above or steel discs, despite lower thermal conductivity and higher costs for steel discs. Al discs show lower unwanted signals with regard to OSL measurements. During our investigations we applied relatively high β-doses. The majority of luminescence samples require less irradiation for D_e determination, so that the effect of the disc signal is less pronounced. However, when measuring very dim samples or for basic studies, one should always be aware of the "disc problem" and its influence on weak luminescence signals.

The contribution of the disc signal to the entire recorded signal depends only weakly on light shielding by the grain-covered area of the disc for coarse grains (Fig. 2.2), but shielding is likely to be more effective for fine grain layers. Correction for disc influence requires careful investigation of each individual disc, especially in the case of Al discs. Consequently, alternative and chemically more inert disc materials (nickel, silver, rhodium, gold etc.) should be investigated in detail.

2.5 Conclusions

Spurious and dose-dependent TL and OSL emissions from commonly used sample carriers were investigated in this study. We observed:

1. Al discs showed significant TL and OSL signals in the UV, UV-blue and red detection range.

2. Steel discs showed no significant spurious, but dose-induced signals in the UV and UV-blue windows.

3. For Al cups (from Bayreuth) we found no spurious signals for UVTL and generally low sensitivity to irradiation.

4. The provided cleaning procedures for discs (Al and steel) can reduce spurious and dose-dependent signals, but cannot eliminate them completely.

5. For most bright samples, the influence of disc signals is expected to be negligible, but further investigation for the case of single grain discs is needed.

These phenomena seem to be widespread among laboratories as they were observed in at least three luminescence dating facilities and with various kinds of sample holders. However, this paper is not a comprehensive luminescence study of specific disc materials. The

influence of spurious and dose-dependent signals on particular measurements is different for each disc and sample and difficult to assess because of highly differing characteristics between discs. In short, the résumé of this paper is to alert the reader to the problem of unwanted luminescence contributions from the sample holder and to advise careful measurement of these signals when measuring relatively young and/or dim samples (including single grains).

Acknowledgments

We thank Dr. Regina DeWitt for helpful comments and suggestions on earlier versions of this manuscript. This work was partly funded by the German Academic Exchange Service (DAAD) (project number 50022024 ARC-XXIII).

References

Aitken, M., 1985. Thermoluminescence dating. Academic Press, London.

Aitken, M., 1998. An introduction to optical dating. The dating of Quaternary sediments by the use of photon-stimulated luminescence. Oxford University Press, Oxford.

Akselrod, M. S., Kortov, V. S., Gorelova, E. A., 1993. Preparation and properties of α-Al_2O_3:C. Radiation Protection Dosimetry 47, 159–164.

Aypar, A., 1986. Thermoluminescent response of single crystal Al_2O_3:Fe. Applied Radiation and Isotopes 37, 961–963.

Bargel, H.-J., Schulze, G., 2008. Werkstoffkunde. Springer, Berlin.

Barros, V. S. M., de Azevedo, W. M., Khoury, H. J., Andrade, M. E. A., Linhares Filho, P., 2010. Thermoluminescence study of aluminum oxide doped with therbium and thulium. Radiation Measurements 45, 435–437.

Berger, G. W., Brown, T. A., Huntley, D. J., Wintle, A. G., 1982. 5 spurious tidbits. Ancient TL 18, 7–10.

Blasek, G., Weihert, M., 1979. A study of the initial oxidation of chromium-nickel-steel by SIMS. Surface Science 82, 215–227.

Bøtter-Jensen, L., 1997. Luminescence techniques: instrumentation and methods. Radiation Measurements 27, 749–768.

Daniels, F., Boyd, C. A., Saunders, D. F., 1953. Thermoluminescence as a Research Tool. Science 117, 343–349.

Fattahi, M., Stokes, S., 2005. Dating unheated quartz using a single aliquot regeneration-dose red thermoluminescence protocol (SAR RTL). Journal of Luminescence 115, 19–31.

Fuchs, M., 2001. Die OSL-Datierung von Archäosedimenten zur Rekonstruktion anthropogen bedingter Sedimentumlagerung. PhD thesis, Universität Heidelberg.

Furetta, C., 2010. Handbook of Thermoluminescence. World Scientific, Singapore.

Hakanen, A., Laine, E., Haapakka, K., 1997. Physical origin of the intrinsic cathodic luminescence of an oxide-covered aluminium electrode. Europhysics Letters 39, 311–316.

Kalchgruber, R., 2002. α-Al_2O_3:C als Dosimeter zur Bestimmung der Dosisleistung bei der Lumineszenzdatierung. PhD thesis, Universität Heidelberg.

Kelly, P., Laubitz, M., 1967. Thermoluminescence of alumina. Journal of The American Ceramic Society 50, 540–542.

Murray, A. S., 1981. Environmental radioactivity studies relevant to thermoluminescence dating. DPhil thesis, University of Oxford.

Murray, A. S., Wintle, A. G., 2000. Luminescence dating of quartz using an improved single-aliquot regenerative-dose protocol. Radiation Measurements 32, 57–73.

Ostermann, F., 2007. Anwendungstechnologie Aluminium. Springer, Berlin.

Osvay, M., Biró, T., 1980. Aluminium oxide in TL dosimetry. Nuclear Instruments and Methods 175, 60–61.

Preusser, F., Chithambo, M. L., Götte, T., Martini, M., Ramseyer, K., Sendezera, E. J., Susino, G. J., Wintle, A. G., 2009. Quartz as a natural luminescence dosimeter. Earth-Science Reviews 97, 184–214.

Tissoux, H., Valladas, H., Voinchet, P., Reyss, J., Mercier, N., Falguères, C., Bahain, J.-J., Zöller, L., Antoine, P., 2010. OSL and ESR studies of aeolian quartz from the Upper Pleistocene loess sequence of Nussloch (Germany). Quaternary Geochronology 5, 131–136.

Vandenberghe, D., Jain, M., Murray, A. S., 2008. A note on spurious luminescence from silicone oil. Ancient TL 26, 29–32.

Yawata, T., Hashimoto, T., 2007. Development of a red TL detection system for a single grain of quartz. Radiation Measurements 42, 1460–1468.

Zöller, L., Stremme, H., Wagner, G. A., 1988. Thermolumineszenz-Datierung an Löss-Paläoboden-Sequenzen von Nieder-, Mittel- und Oberrhein/Bundesrepublik Deutschland. Chemical Geology (Isotope Geoscience Section) 73, 39–62.

3 The assessment of radionuclide distribution in silex by autoradiography in the context of dose rate determination for thermoluminescence dating

Christoph Schmidt[a], Daniel Rufer[b], Frank Preusser[c], Matthias Krbetschek[d,e], Alexandra Hilgers[a]

[a] Institute for Geography, University of Cologne, Otto-Fischer-Str. 4, 50674 Köln, Germany
[b] Institute of Geological Sciences, University of Bern, Baltzerstr. 1+3, 3012 Bern, Switzerland
[c] Department of Physical Geography and Quaternary Geology, Stockholm University, 10691 Stockholm, Sweden
[d] Saxon Academy of Sciences, Institute for Applied Physics, TU Freiberg, Leipziger Str. 23, 09596 Freiberg, Germany
[e] Freiberg Instruments, Am St. Niclas Schacht 13, 09599 Freiberg, Germany

Archaeometry 55, 407-422 (2013)

Abstract

A combination of two autoradiography methods was applied to investigate the radionuclide distribution patterns in a range of different silices. We obtained greyscale images (β-radiation) and α-track patterns for qualitative assessment, and used a statistical approach to quantify the degree of uniformity of the radiation fields. It was found that almost all samples are poor in potassium, thorium and uranium, and that locally high concentrations are present only in dark-colored veins and inclusions. Statistical analyses reveal evidence of radionuclide clustering in more than half of the 21 specimens. Concerning thermoluminescence dating of burnt lithics, such gradients should be taken into account to improve precision and accuracy in cases where the external radiation is not strongly dominating for the sample under consideration.

3.1 Introduction

Since many rocks used for tool-making by ancient humans consist of amorphous or cryptocrystalline siliceous material, most of them yield a thermoluminescence (TL) signal after exposure to ionizing radiation. Such TL signals are used to determine the last heating of the artefact above about 400 °C caused by intentional or accidental firing. The complete zeroing of the TL signal – and therefore the previously absorbed dose – by heating is the prerequisite for obtaining an equivalent dose representative for the time elapsed since the heating event. Numerous studies have shown the applicability of the TL dating method to provide age information far beyond the age range of the radiocarbon technique (Bowman & Sieveking 1983; Mercier et al. 2003; Mercier et al. 2007a; Mercier et al. 2007b; Valladas et al. 2007).

The range of raw materials with appropriate properties for tool-making is huge including, for example, flint, opal, radiolarite, quartzite and hornstone. However, the terminology is not internationally standardized and is thus often quite confusing (Floss 1994; Richter et al. 1999). While some nomenclature is based solely on material properties, other terminology also discriminates with regard to geological origin. Hence, petrographically identical material is often called "flint" when it is of Cretaceous origin and "hornstone" when it is assigned to the Jurassic. In this study, the more general term "silex" is used when not referring to a specific sample. Whilst the knapping features of rocks for tool-making have to fulfil certain conditions, the visual appearance can differ considerably in form, color (of the bulk material as well as of irregularities), opacity and uniformity.

In contrast to most sediment samples used for luminescence dating, silex samples are present in consolidated form. The first TL investigations of flint were carried out on thin slices cut from the interior part of the specimen (Göksu et al. 1974) in order to avoid unwanted triboluminescence and so-called spurious TL, both effects arising from milling or crushing the bulk sample to powder (Göksu & Fremlin 1972). Valladas (1978) showed that spurious TL is related to carbonates and can be suppressed by etching with dilute HCl. Since then, only crushed samples have been used for TL measurements.

A great deal of effort has been put into the correct determination of the equivalent dose (Valladas & Gillot 1978; Aitken 1985; Mercier 1991), whereas the calculation of the dose rate (the absorbed dose per unit time) has mostly been based on the premise of a simple dosimetric model. This model is predicated on the assumption of negligible spatial differences in the internal dose rate, cf. the case studies of Valladas et al. (2007) and Mercier et al. (2007b). However, using the crushing method, over-dispersed data often result if the internal dose rate is spatially inhomogeneous (Mayya et al. 2006). Tribolo et al. (2006) modeled and quantified the influence of microdosimetric effects and calculated differences in age of about 10–30 % for uniform U distribution on the one side and U concentration in so-called "hot spots" on the other side. Up to the present time, several studies have dealt with the internal radionuclide content and its distribution within

silex using different methods (e.g., fission track mapping and neutron activation analyses – Aspinall & Feather (1972) and Valladas (1985a)), but have shown rather ambiguous findings. Only slight differences in radionuclide content have been determined comparing different parts of the same silex specimen (Aspinall & Feather 1972; Bowman & Sieveking 1983; Valladas 1985b), but more severe heterogeneity is reported when the scale is refined (Malik et al. 1973; Selo et al. 2009).

Since information about the degree of spatial homogeneity of radionuclides is of crucial importance in order to further increase the precision of TL dating, this study is aimed at approaching this topic by using two complementary autoradiography methods. In addition to visual assessment by radiation-induced greyscale and track images, statistical procedures are used to quantify the degree of uniform radionuclide distribution. The routine applied for statistical analysis is capable of covering any user-defined spatial resolution. In summary, we will present a comprehensive overview of internal radiation patterns of a variety of 21 different silices.

3.2 Materials and methods

3.2.1 Samples and sample preparation

The samples for this study have been selected to reflect the variety of materials of relevance for tool-making purposes. On the one hand, we attempted to cover different provenances/geological origin of the raw material. On the other hand, we have covered the diversity of differently termed siliceous materials. As a consequence, this study comprises 21 specimens from Middle and Eastern Europe (Belgium, Germany, Poland, Austria, Italy, Hungary and Romania), Jordan and Morocco, mostly of Cretaceous or Jurassic origin. In order to study compositional differences of several samples from the same provenance, multiple specimens from the Banat region (Romania) were investigated. A list of all the samples is given in Table 3.1. The greater part of the samples originates from raw material collections of archeologists, thus ensuring the archeological relevance of the samples.

The rock samples had to fulfil certain conditions for autoradiography investigations. In order to obtain plane surfaces for accurate contact between the sample and the detection unit (image plate or track detector) for a maximum of sharpness, samples were cut with a water-cooled diamond saw (Buehler Isomet 1000). Cortex and carbonate remains were not removed, in order to enable examination of their radiation characteristics. After conducting β-autoradiography, the thick sections were polished with silicon carbide for α-autoradiography exposure.

3.2.2 Beta-autoradiography

Beta-autoradiographs of cut sections of the samples were obtained using commercially available BAS–MS imaging plates (Fuji Photo Film Co. Ltd) and a BAS-1800 bio-imaging

Table 3.1: A list of the investigated samples. All samples are geological samples collected by archeologists to trace the origin of the raw material used for artefacts. Exceptions are specimens N1 and O4—O8, which were found during archeological surveys and excavations.

Internal code	Denomination	Provenance	Geological origin
A1R	Chalcedony	Ain Zora, Morocco	Tertiary
A2R	Chalcedony	Ain Zora, Morocco	Tertiary
M1R	Tabular hornstone	Abensberg-Arnhofen, Franconia, Germany	Upper Jurassic
M4R	Flint	Orsbach, North Rhine–Westphalia, Germany	Upper Cretaceous
M5R	Flint	Lousberg, North Rhine–Westphalia, Germany	Upper Cretaceous
M9RII	Flint	Rullen, Belgium	Upper Cretaceous
M11R	Quartzite	Lenderscheid, Hessia, Germany	Tertiary
M12R	Flint	Holy Cross Mountains, Poland	Jurassic
M13R	Chalcedony	Salzkammergut, Austria	Unknown
M15R	Flint	Rijckholt, St Geertruid, Belgium	Upper Cretaceous
M16R	Trigonodus hornstone	Dinkelberg, Baden-Württemberg, Germany	Middle Triassic
M17R	Banded hornstone	Kleinkems, Baden-Württemberg, Germany	Upper Jurassic
M20R	Flint	Caredo, Lessinian Mountains, Italy	Unknown
M26R	Flint	Fehmarn, Baltic Sea, Germany	Cretaceous
N1	Flint	Petra region, southern Jordan	Cretaceous
O2R	Radiolarite	Szentgál, Bakony Mountains, Balaton, Hungary	Middle Jurassic
O4	Jasper or chalcedony	Coşava, Banat, Romania	Unknown
O5	Cornelian	Coşava, Banat, Romania	Unknown
O6	Cornelian	Coşava, Banat, Romania	Unknown
O7	Cornelian	Coşava, Banat, Romania	Unknown
O8	Chalcedony	Românești, Banat, Romania	Unknown

analyzer system (Fujifilm Life Science Corporation), according to the technical and procedural details given in Rufer & Preusser (2009) and summarized below.

The sample was placed in direct surface contact to a radiation sensor (the imaging plate, "IP"), in which the natural radiation emitted from the specimen gives rise to a latent luminescence signal within the IP's phosphor layer (Miyahara 1989; Schweizer 2001). Accumulation over time leads to a signal distribution within the IP that most closely represents the distribution of radiation intensity of the sample's contact surface, similar to a photographic contact copy. Exposure of the IPs was achieved by encasing the sample in a combination of 1 mm copper, 1 cm wood and a shielding of 5 cm radionuclide-free lead, in order to suppress signal generation by ambient background radiation during exposure. Due to weak signals, the exposure times were increased to 245, 263 and 456 h, respectively, for the three batches to enhance the signal-to-noise ratio. Sample N1 was the only specimen for which an exposure time of 123 h was sufficient. Additionally, a color scan of each silex surface was made for direct comparison with the autoradiography results.

After removal of the samples from the IP under strongly subdued light, such as not to impair the recorded signal, the IPs were read out by stimulation with a focused laser light that causes a luminescence emission (photostimulated luminescence, "PSL") of a part of the stored signal. By linescanning over the IP, this time-variant emission can be digitized into a greyscale image (Miyahara 1989; Rowlands 2002).

Readout was performed three times and the obtained images were aligned and stacked in order to improve the signal-to-noise ratio (Rufer & Preusser 2009). The resulting greyscale image is a representation of the spatially resolved β-radiation intensity along the contact surface, as the short-range α-radiation is mostly blocked by the IP's protective Mylar layer. The highly penetrative γ-radiation will cause a largely uniform signal increase (Rufer & Preusser 2009). Because point sources are being imaged with decreasing focus with distance to the contact surface and because of the β-attenuation by the sample itself, only β-emitters lying within a thin layer of less than 2 mm from the contact surface contribute to the texturally resolvable part of the autoradiographic image. For visualization and qualitative analysis, the obtained image can then be treated in any suitable way (e.g. by enhancing the contrast, changing its dynamic range or color inversion).

3.2.3 Alpha-autoradiography

Alpha-autoradiography is based on α-track detection. Polycarbonate plates CR-39 from TASL (Bristol, UK) were used as detection medium and tightly fixed with tape on the thick sections to avoid relative movements of the sample and the polycarbonate plate. On the basis of previous experience (Haustein 2002), the duration of exposure was set to 26 weeks. Too short or too long exposure will result in subsequent data analyses being impeded by patterns of very low α-track density or strongly interfering tracks, respectively. A plastic-laminated wooden box was encased in several layers of plastic foil and sealed. This casing was assumed to be airtight and sheltered the samples during storage in order

to avoid continuous contamination by ^{222}Rn. Additionally, the interior of the box was filled with radioactively inert styrofoam plates to a maximum degree for the purpose of replacing as much air as possible. The samples with the mounted CR-39 sheets were then placed on top of the styrofoam plates. An additional detector sheet without a mounted sample thick section was positioned in the box as well, to monitor the influence of remaining or potentially trespassing ^{222}Rn. Due to its high density, radon tends to accumulate at the bottom of the remaining air volume in the box; that is, on top of the styrofoam plates. The recorded α-track density of the empty detector has thus to be regarded as a measure of the maximum local concentration of enclosed ^{222}Rn. However, the background relevant for the track pattern induced by the silex samples is much lower, because it is assumed that almost all air is displaced between the CR-39 sheet and the plane level that is formed by the thick section and its surrounding glue rim (Fig. 3.1). Consequently, an estimate of the actual background is recorded in those parts of the detector that are in contact with the glue rim, provided that the glue is free of any α-emitting radionuclides. If this is not the case, the background must be considered as a maximum value in respect of the silex samples (see also Fig. 3.1). After exposure, the CR-39 plates were developed in 7.25 N sodium hydroxide solution at 71 °C for 6 h (Haustein 2002).

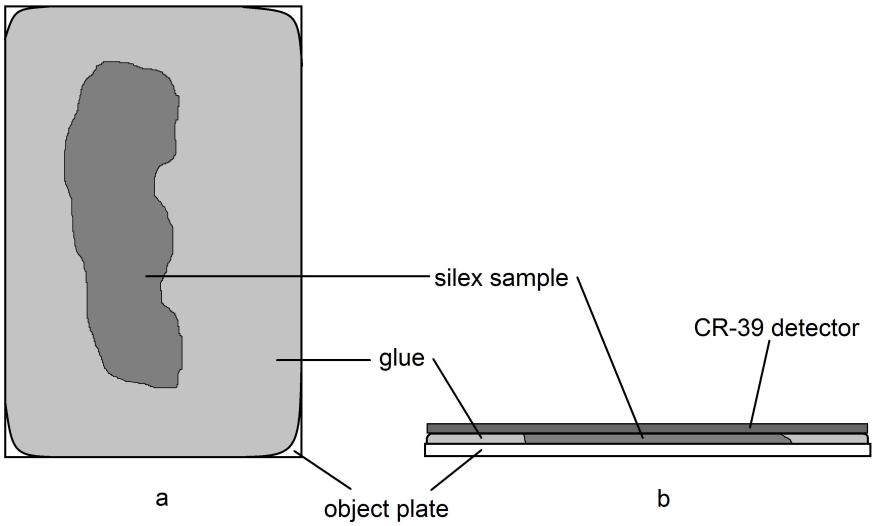

Figure 3.1: A sketch of the prepared silex thick sections and the mounted polycarbonate detector, showing (a) the top view and (b) the profile of the experimental configuration, including the mounted CR-39 plate.

Subsequently, the etched CR-39 plates were photographed section-wise with a camera attached to an optical microscope at magnifications of 50 ×, and 100 × for selected plates.

The single images were then digitally stitched to an image displaying the whole detector sheet. A MATLAB code was developed, which includes the *CircularHough_Grd* function for detection of circles in greyscale images using the Circular Hough transform (PENG 2005). This function allows identification of elliptical and circular shapes (i.e., the etched α-tracks) and their locations, and features separate counting of overlapping tracks.

The etched α-tracks are visible on the microscope scans as black circles with different sizes and hues, ranging continuously from intense to pale and barely observable. As the *CircularHough_Grd* function features thresholding of gradient magnitudes of the input image to identify circle boundaries, very pale α-tracks not exceeding this threshold are not recognized. Lowering of the threshold, however, leads to an increased level of counting artefacts/miscounting. Ignoring pale tracks leads to a slight (but not quantifiable) reduction of the thickness of the sample layer from which α-radiation is recorded. Since the silex samples were cut at random positions, this fact is not considered to have any influence on the validity of the results. Oblique incidence of α-particles on the detector yields conical-shaped and pointed tracks. In the event that their shapes differ too much from the ideal circular shape, they are not identified by the routine. Manual counting of missed cones shows that they amount to $< 1\,\%$ of correctly recognized tracks, so that the associated error is considered as negligible. Additionally, severe track overlapping ("hot spots") sometimes leads to the "loss" of tracks in automatic counting, so that the track numbers have to be corrected manually. Whereas a few samples (M1R, M9RII and M12R) are free of such hot spots and miscounting is close to 0 %, other samples require additional manual counting of tracks that are located in regions with high track density (e.g. M11, O6 and O8). One of the most extreme cases of (locally constrained) miscounting is a hot spot in sample N1, in which only about 44 % (35 out of ~ 80) of the α-tracks are identified. As a consequence of intense track overlapping and interference, it is only possible to provide an estimate of the track number, even by manual counting. All in all, 12 out of the 21 samples needed manual correction of track numbers.

Moreover, the MATLAB routine can superimpose a variable-sized grid on the image and automatically count the number of tracks in each square. Thus, analysis based on counting statistics at different scales is facilitated. The unit used in image processing is pixels; it can, however, be converted into absolute scales (µm or mm) for a given magnification.

3.2.4 "Homogeneity" of point distributions

With reference to previous investigations, the term "homogeneous" or "uniform" is often used to characterize the distribution of radionuclides within rock samples (ASPINALL & FEATHER 1972; MALIK et al. 1973; VALLADAS 1985b; SELO et al. 2009). These expressions may be applied to non-discrete – that is, spatially continuous – features such as the U distribution. When assessing continuous features by autoradiography, continuous distributions are converted into point fields, in which the spatial point density is representative of the concentration of the original quantity (e.g. the U concentration). Taking

into account the random process of radioactive decay, a spatially uniform concentration of a specific radionuclide thus generates a two-dimensional random field of points; that is, a Poisson field. Accordingly, inhomogeneous radionuclide concentrations result in more or less clustered point fields.

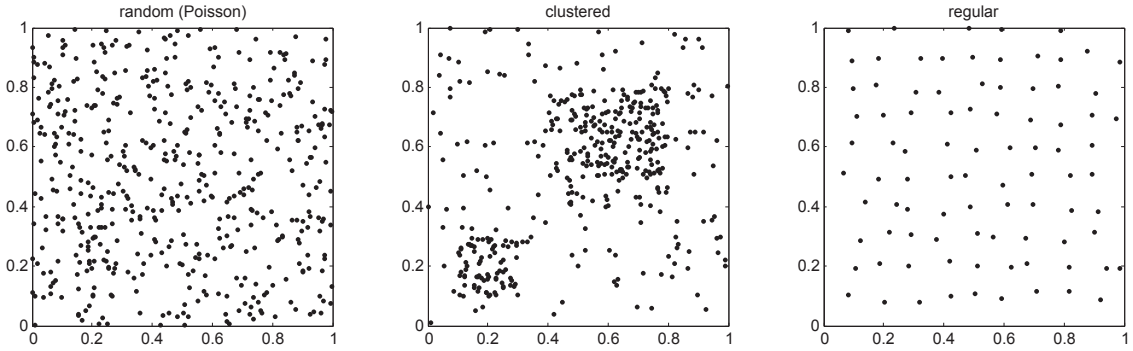

Figure 3.2: Simulations of three types of point fields. Left: the expected distribution for random processes (Poisson field), such as the α-track distribution generated by spatially homogeneous radionuclide concentrations; middle: a point field with strong clustering, as is expected for a spatially heterogeneous radionuclide distribution; right: a regular distribution of points.

In general, three major kinds of point fields are to be distinguished: random (Poisson), clustered and regular. Examples of the latter are the centers of atoms in a crystal lattice or a point field derived from a hardcore process; that is, a point field with certain minimum distances between all points (Stoyan & Stoyan 1994). Simulations of the mentioned classes of point fields are shown in Fig. 3.2. Through the use of statistical parameters, a given field can be categorized in one of the three classes – as is done, for example, in animal or vegetation ecology (e.g. King (1969) and references therein; Orlóci (1978)). In a case, in which several subpopulations are being analyzed (counted tracks in equal-sized areas), the decisive parameter is the index of dispersion, which is defined as $D = \sigma^2/\mu$, where σ^2 is the variation of count numbers in the subpopulations (variance) and μ is the mean count number per area. For Poisson distributions, σ^2 is equal to μ, and thus $D = 1$. Over-dispersed (clustered) point fields yield $D > 1$ and under-dispersed fields $D < 1$, whereas in the latter case the distribution is more regular than expected for Poisson processes. Assignment of a given point field to a certain distribution model requires extension of D, so that the extended index of dispersion is now $I = (n-1) \cdot \sigma^2/\mu$, where n is the number of subpopulations (sub-areas). The two-sided χ^2 test of goodness of fit can then be applied with the assumption of random distribution (null hypothesis), where the number of degrees of freedom is $k = n - 1$ (Stoyan & Stoyan 1994). On the basis of decision criteria, the given distribution can hence be classified as random, clustered or regular for certain levels of significance. However, regular distributions of α-tracks are not expected to be observed here because of the genesis of the material, and hence this case is not discussed further.

3.3 Results

3.3.1 Beta-autoradiography

The images indicate that most of the siliceous materials yield only low levels of activity, with some specimens not giving a signal above background (eight out of the 21 specimens; Fig. 3.3 and supplementary data Figs. A.9, A.10 and A.11). For these samples (M1R, M5R, M9RII, M11R, M12R, M15R, M17R and M20R), no statement can be made about the radionuclide's spatial configuration. The other sample surfaces showed mostly weak signals slightly above background, with hardly visible internal differences in greyscale values. An exception is sample N1: this yields by far the strongest PSL signal, which is homogeneous and clearly traces the shape of the specimen. The background is defined here as the recorded PSL intensity of IP regions that were not in contact to sample surfaces (see also Fig. 3.3). Since three different exposure times were used, the background intensities are not the same for all samples. Owing to the relatively high levels of background random noise and the expected limited benefit, we did not perform a background subtraction in this qualitative part of the study.

Comparing the IP images with the surface scans, we observed that variations in bulk material color are not reflected in the β-autoradiography results for the majority of the samples. Differences in the bulk material color are usually attributed to changes in trace element concentrations, and the bulk color might also reflect variability in the concentration of radioactive elements (K, U and Th). We can now show that this is obviously not the case within the sensitivity of the method. In contrast to bulk color changes, secondary phases and inclusions could often be recognized very well on the greyscale pictures. Inclusions are incorporated during formation of the siliceous material, whereas secondary phases are the result of intrusion of foreign material into fissures and fractures of the silex (veins). Samples O6 and O7, for example, exhibit clearly visible, elevated PSL signals in their autoradiography images, which can be associated with the black or brownish veins on the corresponding rock surface, see also Schmidt et al. (2012). Punctual inclusions were not represented on the greyscale images in most of the cases. In addition, very fine components such as the dark veins of O6 were not traced in original fine detail on the autoradiograph due to limitations in terms of imaging resolution. However, our observations imply, for veins and inclusions, that dark regions represent high and light or transparent zones rather low levels of ionizing radiation in the samples investigated here. Thus, there appear to be parallels between the radiation pattern and the visual appearance.

The outer parts and rims, often consisting of the host rock such as limestone, and the cortices of the investigated samples often show differing chemical compositions (e.g. a lower content of SiO_2) compared to the interior part, due to water loss, impregnation and weathering (Floss 1994). These regions could not be identified on the β-autoradiographs of most of the silices. If there were differences in β-radiation intensity between cortex and interior part, the method is too insensitive to show them. Only one piece (M13R) showed a substantially increased blackening of the rim (Section A.2, Fig. A.10).

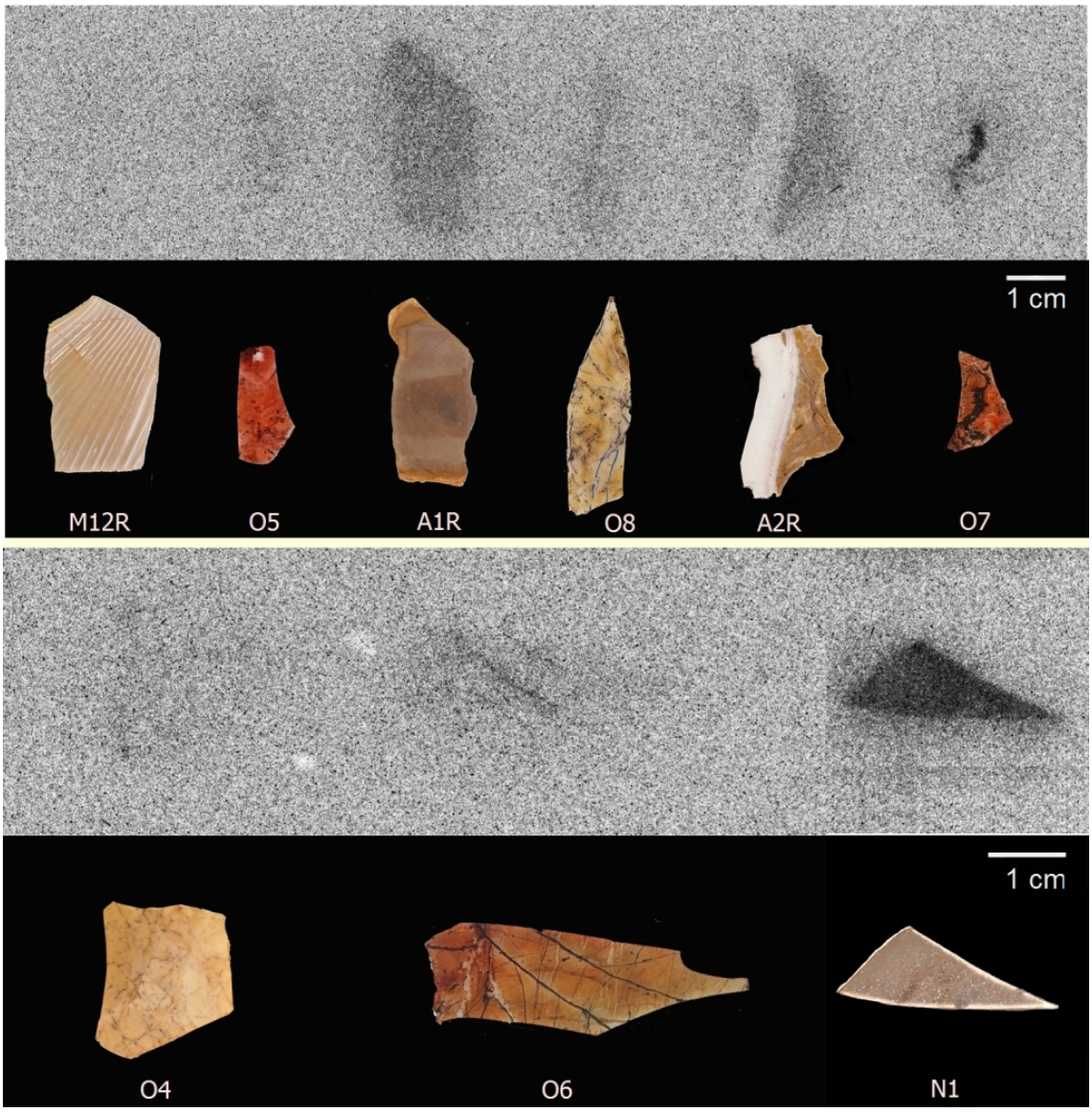

Figure 3.3: Beta-autoradiography images and color scans of nine selected silex samples. The exposure duration was 263 h, except for sample N1 (123 h). The light dots between the autoradiographs of samples O4 and O6 are due to defects in the IP. As a result of different exposure times, slightly different background levels appear as edges on the stitched autoradiography images (e.g. on the left-hand side of N1). On the upper left-hand side of A2R, a small dark area is observed on the greyscale image, which can be attributed to cortex remains (barely visible on the scan). Furthermore, the IP signal of N1 covers a larger area than the silhouette of the rock (like a halo). This known effect is called "bleeding" (Rufer & Preusser 2009) and affects strongly radiating samples, as the β-radiation from inside the samples influences areas of the IP beyond the covered surface as well.

3.3.2 Alpha-autoradiography: statistical processing

From the entire sample surface, only those regions that are usually employed for TL measurements were used for the statistical analyses. Thus, the outer 2 mm rim of each sample was digitally discarded – except for sample A2R, where the transparent silex generated almost no tracks. Hence, the statistical approach was not applicable due to poor counting statistics. In this case, the opaque, carbonate enriched siliceous part, laced with transparent veins (see Fig. 3.3), was subjected to track counting and statistical procedures. This should be kept in mind with respect to Table 3.2 and Fig. 3.5 below. The area of the analyzed sample surfaces varied between $\sim 61\,\mathrm{mm}^2$ and $477\,\mathrm{mm}^2$. Despite large apparent differences in internal activity, the exposure time of the detector plates was sufficient to yield track densities that enabled analyses at resolutions of 0.5 mm or lower (> 0.5 mm) for all samples. However, some specimens (e.g. A2R, M17R and O4) would have required prolonged exposure times for statistical analysis at resolutions below 0.5 mm (owing to counting statistics). The mean intensity λ of the point field (the number of points or counted tracks per unit area) of one particular sample was calculated by averaging the intensities of $4\,\mathrm{mm}^2$ squares. Thus, the given uncertainties (standard deviations) reflect the fluctuation of λ on a 2 mm scale. The range of the field intensity values (Table 3.2) covers more than one order of magnitude, with the smallest intensity being 284 ± 127 cm^{-2} (M9RII) and the highest intensity being $13\,306 \pm 2\,962$ cm^{-2} (N1). The CR-39 detector not covered by a sample for recording of the ^{222}Rn-induced background in the shielding box yields a mean intensity of 495 ± 147 cm^{-2}. This means that the enclosed (or potentially penetrating) amount of ^{222}Rn produces intensities of α-radiation comparable to those of the samples with the lowest internal α-activity. However, the background level relevant for the sample-induced track pattern was estimated by determining the track density in detector areas that were in contact to the glue rim during exposure (Fig. 3.1). As mentioned above, this measure is seen as representing most closely the background due to the thin layer of remaining air (and hence ^{222}Rn) between sample and detector. Table 3.2 shows that the estimated field intensity of the background varies from sample to sample, obviously because of mutable distances between glue and detector. Sample O7 yields the highest background value (124 ± 11 cm^{-2}), whereas the lowest value (24 ± 5 cm^{-2}) results for sample N1. Usually, a signal is called significant when its mean minus $2\,\sigma$ (where σ is the standard deviation) is larger than the mean background estimate. Following this condition, all of the samples yield significant signals, except for M5R, O7 and O8 (due to huge spatial variations in track density and hence large standard deviation), and M9RII (owing to low track density in general). The values of λ and the background estimate of all of the samples are presented in Table 3.2.

General patterns of blackening of the IP by β-radiation could be identified as corresponding density patterns of tracks on the microscope images of the track detectors, while the track pattern additionally reveals fine imbalances of α-radiation distribution. Whereas the samples' bulk materials show random distributions of tracks at first sight (without

Table 3.2: The calculated statistical parameters (mean field intensity λ; background estimate, I and n) for the silex samples. The mean field intensity was calculated for a spatial resolution of 2 mm (not background subtracted) and the given uncertainties of λ include the standard deviations only. The extended indices of dispersion, I, are shown for different spatial resolutions (square lengths); n is the number of analyzed squares. The uncertainty of the background estimate is given by the counting error (square root of the counts). For further details, see the text.

Internal code	λ [cm^{-2}]	Background estimate [cm^{-2}]	I (2 mm)	n (2 mm)	I (1 mm)	n (1 mm)	I (0.5 mm)	n (0.5 mm)
A1R	1947 ± 317	76 ± 9	102.7	49	549.6	271	1920.8	1141
A2R[a]	2490 ± 501	80 ± 9	105.1	27	258.2	105	934.6	462
M1R	312 ± 107	60 ± 8	112.7	57	595.0	281	2100.4	1121
M4R	1690 ± 271	52 ± 7	20.2	13	113.7	71	531.7	309
M5R	419 ± 225	28 ± 5	246.5	49	899.6	217	2912.0	865
M9RII	284 ± 217	68 ± 8	62.9	21	315.2	133	1444.1	645
M11R	421 ± 163	72 ± 8	180.0	57	656.2	281	2670.8	1161
M12R	400 ± 120	100 ± 10	214.8	97	1016.8	433	3849.3	1871
M13R	893 ± 248	34 ± 6	83.9	31	371.3	121	1635.9	568
M15R	1300 ± 556	66 ± 8	70.6	9	147.0	37	448.5	167
M16R	2719 ± 598	44 ± 7	144.8	29	415.7	129	1120.4	575
M17R	463 ± 96	38 ± 6	10.6	13	111.0	61	513.2	265
M20R	723 ± 143	44 ± 7	44.7	37	302.4	169	1332.4	781
M26R	387 ± 115	72 ± 8	89.5	49	335.4	193	1417.3	769
N1	13306 ± 2962	24 ± 5	211.4	10	573.8	49	943.4	197
O2R	2791 ± 439	74 ± 9	151.8	55	612.1	259	2079.7	1141
O4	403 ± 149	26 ± 5	85.5	37	355.7	197	1414.3	785
O5	1565 ± 299	38 ± 6	40.2	19	357.5	109	1537.7	547
O6	1657 ± 532	88 ± 9	341.2	49	1593.4	241	4780.4	1057
O7	4315 ± 4032	124 ± 11	1707.5	13	3113.3	73	4950.4	313
O8	710 ± 382	56 ± 7	530.8	61	1841.3	295	4834.6	1177
Empty detector	495 ± 147	-	138.9	82	631.2	442	2223.1	1891
Poisson low	1023 ± 202	-	36.7	25	98.7	81	393.2	337
Poisson high	2084 ± 222	-	21.7	25	114.7	97	367.7	353

[a] The carbonate-rich part was included in the analysis.

statistics), many spotty inclusions and all dark-colored veins coincide with higher track densities. Instances are punctual clusters of tracks in samples M11, M13R, A1R, O2R, O5, O6, O8 and N1 or the detailed mapping of the dark veins of O6, O7 and O8. Examples of developed CR-39 plates for three samples at two different magnifications are shown in Fig. 3.4. Similar to the results of β-autoradiography, the bulk material of all samples (except N1) contains generally low and qualitatively uniformly distributed amounts of α-emitting radionuclides. Dark-colored inclusions and veins, however, yield strongly elevated radiation.

Due to file size considerations, just 50 × magnification images were used for statistical processing with MATLAB. We set the lowest square length to 108 pixels, which corresponds to 0.2 mm at a 50 × magnification and equals the upper limit of the common coarse grain size used in luminescence dating (in the case of silex, fragments are used rather than grains in the narrow sense). Depending on the size of the investigated sample surfaces, the number of squares varied between 1536 and 11 928 for this resolution. The distribution of α-tracks was investigated using a total of four different grid sizes, 108 pixels (0.2 mm), 271 pixels (0.5 mm), 542 pixels (1 mm) and 1084 pixels (2 mm).

In the event that the expected track number per square (deduced from the determined λ values) drops below 1, the assumptions for correct application of the χ^2 distribution test are no longer valid (STOYAN & STOYAN 1994). This is, however, the case for most of the samples when the grid size is reduced to 0.2 mm. Therefore, the 0.2 mm resolution was not included in the analyses. Furthermore, background subtraction was performed assuming that the background estimate follows a Poisson distribution. This means that the average background contribution was calculated for each sample and grid size and subtracted from μ for the calculation of I. For the resolutions 0.5 mm, 1 mm and 2 mm, we calculated the extended index of dispersion I for each sample and compared it to the tabulated χ^2 values at levels of significance of $\alpha = 0.05$. The classification of all of the samples at three different scales is plotted in Fig. 3.5a. All values of I are also shown in Table 3.2.

The classification indicates that there is a general trend of increased clustering when the scale is refined. This can be explained by averaging effects, as the square sizes are enlarged. The point distributions of only two samples (M17R and M20R) follow a Poisson distribution at the coarsest resolution (2 mm). Five of the specimens (M1R, M9RII, M26R, M4R and O5) are located close to the classification boundary as shown in Fig. 3.5a; that is, they show only slight statistical signs of clustering. The point patterns of the remaining samples exhibit more or less heavy clustering, depending on the calculated value of I (Table 3.2). The distribution of counted tracks of silex surface O7 is by far the most clustered one, exceeding the others with I values that are approximately one order of magnitude higher at a 2 mm resolution.

For purposes of verifying and testing the applied categorization procedure, we simulated Poisson fields of different intensities ($\lambda \approx 1000\,\mathrm{cm}^{-2}$ and $\lambda \approx 2000\,\mathrm{cm}^{-2}$) and ran them through the above described operational sequence (details of the stimulation are provided in Section A.2). Whilst the denser field was classified correctly at all resolutions (0.5 mm,

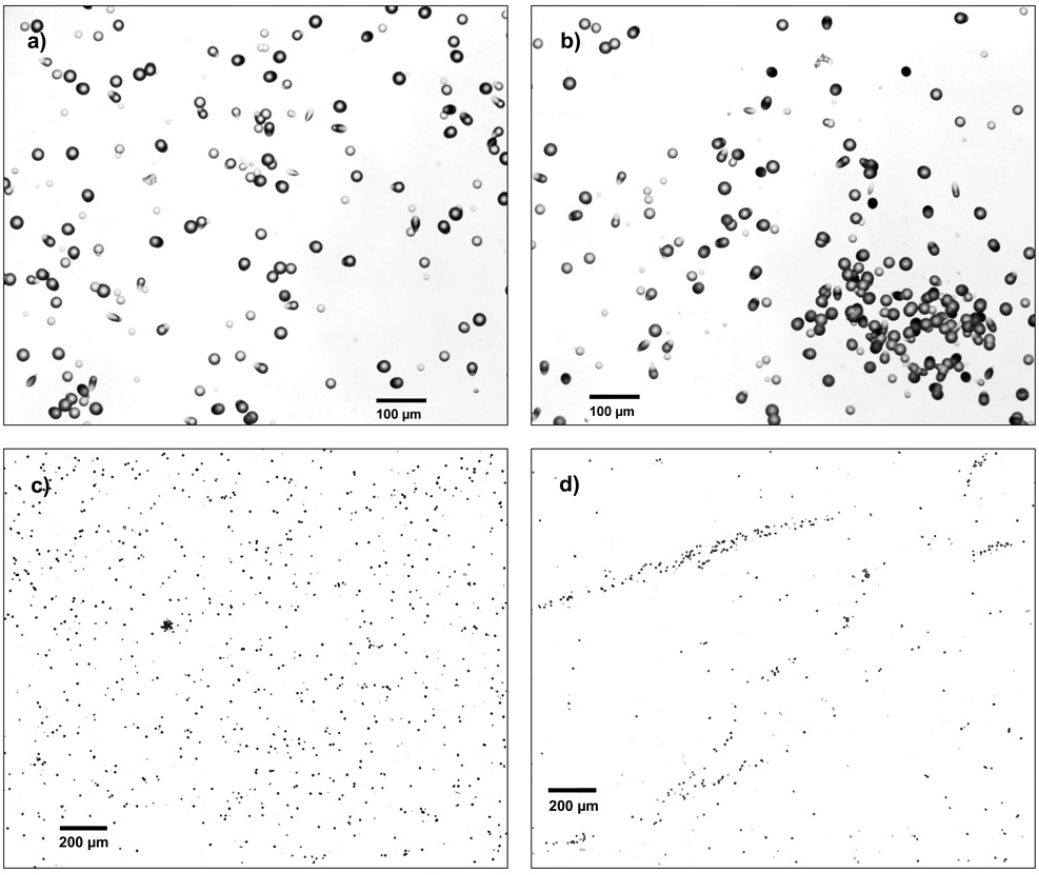

Figure 3.4: Optical microscope images of etched track detectors. (a, b) Different parts of sample N1 at 100 × magnification. Irregularities such as damage in the detector (e.g. in the central upper part of (b)) or adherent dirt are not registered as tracks by the MATLAB routine. Conical-shaped tracks result from oblique incidence of α-particles on the detector. Small and barely visible tracks originate from deeper inside the sample (within the α-range of about 20 mm) and have just reached the detector. (c, d) Track patterns of samples A2R and O8, respectively, photographed at 50 × magnification.

1 mm and 2 mm), the correct result was obtained only for 1 mm resolution at low intensity. However, the deviations of the calculated I value from the corresponding χ^2 value to be classified as a random field are less than 1 % (2 mm resolution) and less than 10 % (0.5 mm resolution). The wrong classification might be the result of statistical fluctuation, as we are dealing with a random process, and there is still a finite probability for a simulated Poisson field to show slight clustering and a probability of erroneous classification (level of significance) of 5 %. Accordingly, the same applies to the track patterns of the silex samples; in other words, there remains a small but certain probability of incorrect allocation. The categorization of the simulated Poisson fields is added in Fig. 3.5a (red diamonds).

Fig. 3.5b reveals that there is no significant statistical correlation between D and λ for a given resolution; that is, between the degree of homogeneous point distribution and the field intensity ($R^2 < 0.01$). The quantity D is used in this context as it is normalized to the number of squares n, so that comparison between samples is valid.

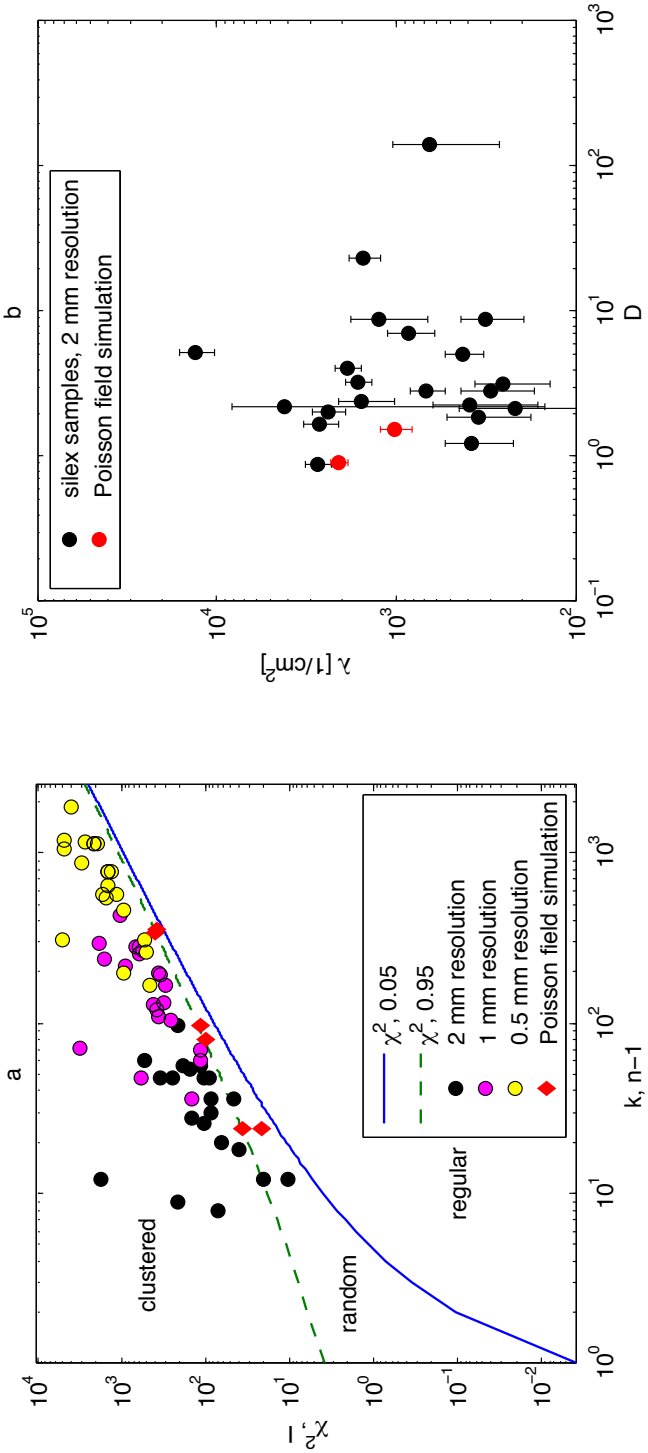

Figure 3.5: Classification of the α-track patterns and the relationship between track distribution and measured field. (a) The computed inverse of the χ^2 cumulative distribution function, plotted against the degrees of freedom k as solid and dashed lines (two-sided, with levels of significance of 0.05). In respect to distribution types, the plot area is thus divided into three parts, as labeled on the figure. The calculated values of the extended index of dispersion I are added for all samples for three different spatial resolutions (see the text for further details). The quantity n denotes the number of analyzed squares for each sample. In addition, the classification of the simulated Poisson fields (two different field intensities) is shown. As for Poisson fields $\sigma^2 = \mu$, the simulated random fields should lie on the line representing the 1:1 relationship between k and I. (b) The relationship between the index of dispersion D (as defined above) for 2 mm resolution and the field intensity λ for each sample. D can be regarded here as a normalized measure for the uniformity of track distribution of the analyzed squares. The simulated Poisson fields ($\lambda \approx 2000\,\mathrm{cm}^{-2}$ and $\lambda \approx 1000\,\mathrm{cm}^{-2}$) are also shown.

3.4 Discussion

Despite the fact that both α- and β-autoradiography are qualitative methods, it can be deduced from the necessity of long exposure durations of the IP and the track detectors that the general levels of internal radioactivity of most of the investigated samples are low compared to expected values for external radiation in most archeological environments. Since prolonged irradiation times will lead to higher track densities in the case of CR-39 plates, this method is also applicable to weakly radiating samples. Beta-autoradiography, however, has come close to its limits. Even longer exposure times might not be able to enhance the signal-to-noise ratio (SNR) of the PSL signal of the IPs. As we only observed visible gradients in internal β-activity for four out of the 21 specimens, β-autoradiography is thus a method for qualitative assessment of the configuration of β-emitters with a resolution of > 1 mm for samples showing (at least partly) higher internal β-activity than the investigated silices.

Alpha-autoradiography, in contrast, has a resolution limited by the size of the etched tracks in the detector, which have a mean size of about 25 µm when using the above described development technique. Therefore, this method is suitable for detecting small-scale differences in internal α-activity. With regard to cited K, U and Th concentrations found for a range of silices (Mercier et al. 1995; Valladas et al. 1999; Richter et al. 2007), α-radiation often plays a dominant role in contributing to the internal dose rate. Accordingly, α-autoradiography is considered to provide the more relevant results for the aims of this investigation. However, the effective internal dose rate, which is corrected for the lower TL production by α-radiation per Gy of β- and γ-radiation, depends on the α-efficiency of the material (expressed as the a-value, b-value or S_α; cf. Valladas & Valladas (1982) and Aitken (1985)). This measure can vary from sample to sample (Mercier et al. 1995; Valladas et al. 1999; Richter et al. 2007) and presumably within one specimen as well. Further research is needed to investigate the local variation of α-efficiency in silex and its correlation with radionuclide/dose distribution. Previous investigations have revealed that there is little interrelationship between TL-producing and U-rich parts within one silex sample (Malik et al. 1973). However, as the α-efficiency significantly influences the dosimetry for samples with non-uniform internal α-radiation, its impact should be considered in more detail in future studies.

The statistical approach for evaluating the α-track images allows quantitative examination of the degree of uniformity in radionuclide spread. Our method of data processing thus clearly differs from those used in previous semi-quantitative or qualitative investigations on this topic (Malik et al. 1973); see also Walton and Templer, pers. comm., cited in Aitken (1985: 216). Automated track counting reduces the effort of manual counting considerably and allows recording of the coordinates for each detected track. For this investigation, the smallest analyzed grid size (0.5 mm) was in the range of the coarse grain size ($\sim$0.1–0.25 mm) used for TL dating of heated silex artefacts. In this regard, gradients

in radionuclide concentrations on a scale of ≥ 0.1 mm are vital, as they result in grain-to-grain variations of deposited radiation dose. However, categorization by the χ^2 test of goodness of fit was not carried out for the smallest grid size (0.2 mm) due to insufficient counting statistics (i.e., field intensity). On a smaller scale (< 0.1 mm), additional effects such as local trap saturation have to be expected if radionuclides are present in locally high concentrations. According to Selo et al. (2009), it seems that the uranium contributing to the internal dose rate is situated outside the grains or crystallites that form the silex (i.e., in the binding material). Unfortunately, we could not investigate these features here because of restraints in the spatial resolution.

The attribution of the samples' track pattern to regular, random or clustered distributions demonstrates that most of the silices show a tendency to form clusters. If this feature is only weakly pronounced, it cannot be recognized on the track image by eye. Furthermore, Poisson field simulations suggest that the degree of correct classification rises with increasing field intensity λ, owing to effects of counting statistics. Consequences for future track detector studies would thus be longer exposure times to enhance the track density.

With regard to more direct archaeological application, the two autoradiography methods described in this paper may provide valuable assistance in raw material sourcing. As a supplement to trace element analyses and related chemical fingerprint approaches, characteristic α- and/or β-radiation patterns, revealed by autoradiography, could enable a more unambiguous differentiation of silex raw materials.

3.5 Conclusion

This study investigated the spatial distribution of radionuclides in a variety of silex raw materials with archeological relevance. With respect to TL dating of burnt lithics, the internal distribution of α- and β-emitters is one factor limiting the precision of TL ages (Tribolo et al. 2006). We applied two autoradiography methods, based on recording either β- or α-radiation and their respective distribution. These methods provide greyscale and track images for direct comparison with the investigated silex surfaces.

Due to generally low internal radioactivity, β-autoradiography approached its detection limit. Accordingly, it showed spatial gradients of β-emitters only in a few cases. Through the provision of higher sensitivity and spatial resolution, α-autoradiography was able to demonstrate smallscale variations in α-activity. In addition, we quantified the overall homogeneity of track distributions of each sample at different scales by statistical means. The Matlab routine for automatic identification and counting of α-tracks yielded satisfactory results, but there is still potential for further improvements in regard to correct detection of clustered or barely visible tracks. Despite these shortcomings, the findings can be regarded as statistically reliable. We found that about one fourth of all samples showed (almost) statistical uniformity (Poisson distribution) in their track pattern, while the others revealed more or less clear signs of radionuclide clustering. Additionally, microdosimetric

effects are becoming even more complicated, as the local variability of α-efficiency is still a widely unknown factor.

For technical reasons, the scales used for statistical analyses were 0.5, 1.0 and 2.0 mm, thus slightly exceeding the common coarse grain size ($\sim$0.10–0.25 mm) in TL dating. Hence, owing to averaging effects, at least the same degree of heterogeneity/clustering has to be expected for the coarse grain scale. Most probably, the trend to cluster increases with decreasing scale, as can be deduced from statistical analysis at various spatial resolutions.

Clustered concentrations of radionuclides result in spatially non-uniform dose deposition. Grains extracted from the vicinity of radiation hot spots or veins with elevated radioactivity receive higher doses compared to grains located far away from high-radiation zones. Thus, we have to expect enhanced scatter between aliquots using multiple-aliquot protocols. Accordingly, single-aliquot regenerative methods are expected to yield overdispersed equivalent dose distributions. The results shown here indicate that α-emitting radionuclides are spatially clustered in the majority of the investigated samples, potentially leading to the above mentioned effects. However, the external radiation originating from surrounding sediment is likely to exceed the internal one in most cases (sometimes by an order of magnitude), so that the effect will be less pronounced. This might not be true for the samples from the Banat region, which exhibit substantial differences in α- and β-activity between bulk material on the one hand and dark veins and inclusions on the other hand. It should be mentioned, however, that usually the samples that are selected for TL dating are only those that are free of macroscopically visible irregularities (veins and inclusions) and hence free of potential "contamination" by other minerals than SiO_2. The investigated specimens further demonstrate the huge variability in the visual nature and radiation characteristics of silex raw materials.

Possible strategies to avoid problems associated with clustered internal activity consist of discarding potentially problematic parts of the artefact (if large enough and applicable) during sample preparation, or making use of spatially resolved TL measurements in which regions of interest (ROIs) can be selected. Such ROIs should then preferably be free of gradients of internal activity and, consequently, spatially resolved measurements could allow the extraction of reliable age information from problematic samples rather than it being necessary to discard them completely.

Acknowledgments

The authors would like to thank Ingrid Koch M.A. and Dr Birgit Gehlen for raw material supply, Christoph Burow, Bastian Wauschkuhn, Stefan Weiß and Ingrid Stein for technical assistance, and Dr Daniel Richter for helpful comments and suggestions on an earlier version of this manuscript. This work was developed within the framework of the CRC 806 "Our Way to Europe", supported by the Deutsche Forschungsgemeinschaft (DFG).

References

Aitken, M., 1985. Thermoluminescence dating. Academic Press, London.

Aspinall, A., Feather, S. W., 1972. Neutron activation analysis of prehistoric flint mine products. Archaeometry 14, 41–53.

Bowman, S., Sieveking, G., 1983. Thermoluminescence dating of burnt flint from Combe Grenal. PACT 9, 253–268.

Floss, H., 1994. Rohmaterialversorgung im Paläolithikum des Mittelrheingebietes. Habelt, Bonn.

Göksu, H. Y., Fremlin, J. H., 1972. Thermoluminescence from unirradiated flints: regeneration thermoluminescence. Archaeometry 14, 127–132.

Göksu, H. Y., Fremlin, J. H., Irwin, H. T., Fryxell, R., 1974. Age determination of burned flint by a thermoluminescent method. Science 183, 651–654.

Haustein, M., 2002. Thermolumineszenzdatierungen an historischen Metallhüttenschlacken. PhD thesis, TU Bergakademie Freiberg.

King, L., 1969. Statistical analysis in geography. Prentice Hall, Englewood Cliffs, NJ.

Malik, S. R., Durrani, S. A., Fremlin, J. H., 1973. A comparative study of the spatial distribution of uranium and of TL-producing minerals in archaeological materials. Archaeometry 15, 249–253.

Mayya, Y., Morthekai, P., Murari, M. K., Singhvi, A., 2006. Towards quantifying beta microdosimetric effects in single-grain quartz dose distribution. Radiation Measurements 41, 1032–1039.

Mercier, N., 1991. Flint palaeodose determination at the onset of saturation. Nuclear Tracks and Radiation Measurements 18, 77–79.

Mercier, N., Valladas, H., Valladas, G., 1995. Flint thermoluminescence dates from the CFR laboratory at Gif: Contributions to the study of the chronology of the Middle Palaeolithic. Quaternary Science Reviews 14, 351–364.

Mercier, N., Valladas, H., Froget, L., Joron, J.-L., Reyss, J.-L., Balescu, S., Escutenaire, C., Kozlowski, J., Sitlivy, V., Sobczyk, K., Zieba, A., 2003. Luminescence dates for the palaeolithic site of Piekary IIa (Poland): comparison between TL of burnt flints and OSL of a loess-like deposit. Quaternary Science Reviews 22, 1245–1249.

Mercier, N., Valladas, H., Froget, L., Joron, J.-L., Reyss, J.-L., Weiner, S., Goldberg, P., Meignen, L., Bar-Yosef, O., Belfer-Cohen, A., Chech, M., Kuhn, S., Stiner, M., Tillier, A.-M., Arensburg, B., Vandermeersch, B., 2007a. Hayonim Cave: a TL-based chronology for this Levantine Mousterian sequence. Journal of Archaeological Science 34, 1064–1077.

Mercier, N., Wengler, L., Valladas, H., Joron, J.-L., Froget, L., Reyss, J.-L., 2007b. The Rhafas Cave (Morocco): Chronology of the mousterian and aterian archaeological occupations and their implications for Quaternary geochronology based on luminescence (TL/OSL) age determinations. Quaternary Geochronology 2, 309–313.

Miyahara, J., 1989. The imaging plate: A new radiation image sensor. Chemistry Today 223, 29–36.

Orlóci, L., 1978. Multivariate analysis in vegetation research. Junk, The Hague.

Peng, T., 2005. Detect circles with various radii in grayscale image via Hough Transform. MATLAB Central, http://www.mathworks.com (accessed 10/04/2011).

Richter, D., Krbetschek, M., Rieser, U., Trautmann, T., Wagner, G., 1999. Spectral investigation of the thermoluminescence of heated flint (silex). Quaternary Geochronology 18, 279–285.

Richter, D., Mercier, N., Valladas, H., Jaubert, J., Texier, P.-J., Brugal, J.-P., Kervazo, B., Reyss, J.-L., Joron, J.-L., Wagner, G., 2007. Thermoluminescence dating of heated flint from the Mousterian site of Bérigoule, Murs, Vaucluse, France. Journal of Archaeological Science 34, 532–539.

Rowlands, J., 2002. The physics of computed radiography. Physics in Medicine and Biology 47, 123–166.

Rufer, D., Preusser, F., 2009. Potential of autoradiography to detect spatially resolved radiation patterns in the context of trapped charge dating. Geochronometria 34, 1–13.

Schmidt, C., Pettke, T., Preusser, F., Rufer, D., Kasper, H. U., Hilgers, A., 2012. Quantification and spatial distribution of dose rate relevant elements in silex used for luminescence dating. Quaternary Geochronology 12, 65–73.

Schweizer, S., 2001. Physics and current understanding of X-ray storage phosphors. Physica Status Solidi a – Applied Research 187, 335–393.

Selo, M., Valladas, H., Mercier, N., Joron, J., Bassinot, F., Person, A., Nouet, J., 2009. Investigations of uranium distribution in flints. Radiation Measurements 44, 615–619.

Stoyan, D., Stoyan, H., 1994. Fractals, random shapes and point fields: methods of geometrical statistics. Wiley, Chichester.

Tribolo, C., Mercier, N., Selo, M., Valladas, H., Joron, J.-L., Reyss, J.-L., Henshilwood, C., Sealy, J., Yates, R., 2006. TL dating of burnt lithics from Blombos Cave (South Africa): Further evidence for the antiquity of modern human behaviour. Archaeometry 48, 341–357.

Valladas, G., Gillot, P. Y., 1978. Dating of the Olby lava flow using heated quartz pebbles: some problems. PACT 2, 141–150.

Valladas, H., 1978. Thermoluminescence dating of burnt stones from prehistoric site. PACT 2, 180–183.

Valladas, H., Valladas, G., 1982. Effet de l'irradiation alpha sur des grains de quartz. PACT 6, 171–178.

Valladas, H., 1985a. Datation par la thermoluminescence de gisements moustériens du sud de la France. PhD thesis, Université Paris VI.

Valladas, H., 1985b. Some TL properties of burnt prehistoric flints. Nuclear Tracks and Radiation Measurements 10, 785–788.

Valladas, H., Mercier, N., Froget, L., Hovers, E., Joron, J.-L., Kimbel, W. H., Rak, Y., 1999. TL dates for the Neanderthal site of the Amud Cave, Israel. Journal of Archaeological Science 26, 259–268.

Valladas, H., Mercier, N., Froget, L., Joron, J. L., Reyss, J. L., Karkanas, P., Panagopoulou, E., Kyparissi-Apostolika, N., 2007. TL age-estimates for the Middle Palaeolithic layers at Theopetra cave (Greece). Quaternary Geochronology 2, 303–308.

4 Quantification and spatial distribution of dose rate relevant elements in silex used for luminescence dating

Christoph Schmidt[a], Thomas Pettke[b], Frank Preusser[c], Daniel Rufer[b], Haino Uwe Kasper[d], Alexandra Hilgers[a]

[a] Institute for Geography, University of Cologne, Otto-Fischer-Str. 4, 50674 Köln, Germany
[b] Institute of Geological Sciences, University of Bern, Baltzerstr. 1+3, 3012 Bern, Switzerland
[c] Department of Physical Geography and Quaternary Geology, Stockholm University, 10691 Stockholm, Sweden
[d] Institute for Geology and Mineralogy, University of Cologne, Zülpicher Str. 49a, 50674 Köln, Germany

Quaternary Geochronology 12, 65-73 (2012)

Abstract

Thermoluminescence (TL) is routinely used to date heated lithic artefacts which mostly consist of silex (a mixture of amorphous opal and microcrystalline chalcedony). Analytical investigations of bulk samples confirmed that these materials contain considerable concentrations of radioactive elements, generating an internal dose rate contribution. Common dosimetric models assume the latter to be homogeneous throughout the sample. If this assumption would prove invalid, this will result in systematic errors in the calculated age, especially in the course of so called "hot spots" of α-emitters (and associated local changes in α-sensitivity) and the dose response characteristics of α-radiation. Laser ablation inductively coupled plasma mass spectrometry (LA-ICP-MS) analyses of 22 silex samples are presented here, quantifying element concentrations at several tens analytical spots per sample. Along with radioactive elements (K, Rb, U, Th), another 21 major, minor and trace elements were measured in order to allow characterization of the impurities present in most of the samples. The dataset provides a detailed picture of the spatial distribution of radionuclides and hence of the uniformity of the internal α- and β-dose rate. It is shown that the silex itself mostly contains low amounts of K (< 0.1 wt.%), U ($< 1.0\,\mu g\,g^{-1}$) and

Th ($< 0.4\,\mu g\,g^{-1}$), and dosimetrically negligible Rb concentrations. Systematically higher concentrations are obtained by ICP-MS measurements of the bulk samples. This matches with the finding that impurities (veins, inclusions) often yield significantly elevated radionuclide concentrations, up to two orders of magnitude higher than the silex values. These veins and inclusions, for example Ca or Mg carbonates and Fe–Mn–oxy-hydroxides, lead to steep gradients mainly in the internal α-radiation field. Alternative approaches are required to account for the non-uniform internal dose rate and improve the reliability of TL dates of problematic samples.

4.1 Introduction

When exposed to ionizing radiation, certain minerals are capable of storing part of the absorbed energy; they act as radiation dosimeters. Events to be dated are related to the erasure of the accumulated radiation dose (reset of the clock), for example by heat which is accompanied by emission of light (thermoluminescence, TL). Accordingly, the amount of measured luminescence in the laboratory is a measure of the time elapsed since the last resetting event. Ionizing radiation is generated by naturally occurring radionuclides (those of the elements K, U and Th and their decay products and, to a lesser degree, Rb) in the surrounding of the dosimeter and/or within the dosimeter itself. The rate of energy transfer (dose rate) determines the speed of luminescence signal (dose) increase over time. As a consequence, correct dose rate determination is crucial to obtain valid age information, since the age is calculated by dividing dose by dose rate. Especially in the case of self-dosing (internal dose rate) of minerals, the distribution pattern of radionuclides can have considerable impact on the effective dose rate, due to micro-scale interaction effects of ionizing radiation and the mineral.

Analogous to quartz, SiO_2 in amorphous, micro- and cryptocrystalline form can also be used as radiation dosimeter. These materials, generally termed "silex", were used by ancient humans to produce tools, and frequently these tools were heated by fire, either intentional or by accident. In case the heating temperature reached about 400–450 °C, the geological luminescence signal was reset and the newly accumulated signal can be used to estimate the time elapsed since ancient heating.

While there are established methods for dose determination by TL (Valladas & Gillot 1978; Aitken 1985; Mercier 1991; Valladas 1992; Richter & Krbetschek 2006), only simple models are applied for internal dose rate assessment, i.e. uniform distribution of radionuclides is usually assumed in the age calculations (Mercier et al. 2007; Richter et al. 2007). Several studies approached the question whether this assumption is justified or not, but the spatial resolution of the methods so far employed was too limited to allow for conclusive statements or the investigation was based on one element only (Aspinall & Feather 1972; Malik et al. 1973; Selo et al. 2009). However, the presence of non-uniform and/or locally high concentrations of radionuclides ("hot spots") entails microdosimetric effects and consequently systematic errors in the age. Tribolo et al. (2006) studied and calculated such effects in detail for their samples from Blombos Cave (South Africa) and obtained differences in age of up to 25 %, depending on the type of U distribution in the samples (uniform or clustered). Therefore, knowledge about the spatial uniformity in internal radiation is crucial to avoid microdosimetric effects on the resulting age.

In contrast to quartz, silex samples often contain considerable amounts of radionuclides, as shown by bulk measurements using for instance neutron activation analysis (Valladas 1985; Mercier et al. 1995). This difference is reflected by the optical appearance; whereas

quartz is mostly white or transparent, silex appears in a variety of different colors and textural compositions. However, most silex samples contain not just pure silica (SiO_2) but also inclusions trapped during formation and mineral phases which entered later into the considered material.

A previous study investigated the distribution of α- and β-emitters in 21 different silex samples, detected by autoradiography (Schmidt et al. 2013). It is shown that radionuclides are mainly unevenly distributed and occur more or less clustered. Moreover, comparison of the radiation patterns with visual appearance suggests that the presence of radioisotopes is to some extent bound to minerals other than SiO_2.

In this study the qualitative approach of Schmidt et al. (2013) is expanded by laser ablation inductively coupled plasma mass spectrometry (LA-ICP-MS) measurements on the same samples to obtain spatially resolved, quantitative information on the concentration of all relevant radioactive elements, down to ng g^{-1} concentration levels. Spatially resolved radionuclide concentrations are then opposed to ICP-MS measurements of the bulk samples for assessing the dosimetric influence of impurities. Furthermore, along with K, Rb, U and Th 21 major, minor and trace elements were measured by LA-ICP-MS for geochemical characterization of the non-siliceous phases and inclusions in the specimens.

4.2 Materials and methods

The samples investigated in this study are the same as described in Schmidt et al. (2013), except for one additional sample (T1). For covering both a wide range of different materials and provenances 22 samples were chosen from Central and Eastern Europe (Germany, Belgium, Poland, Austria, Italy, Hungary and Romania), Jordan and Morocco (Table 4.1).

With respect to the discussion below it is important to consider the common procedures and protocols applied in silex dating. Sample preparation for TL measurements usually includes crushing of the solid rock into small fragments or powder and the obtained sample material is then treated like a granular sample during the subsequent measurement procedures. Whereas single-aliquot regenerative-dose (SAR) procedures are established in optically stimulated luminescence (OSL) dating of sediments (Murray & Wintle 2000), TL dating of heated material is widely based on multiple-aliquot additive- and/or regenerative-dose techniques (Aitken 1985; Mercier et al. 1995; Valladas et al. 2007). The latter often suffers from non-efficient normalization to account for aliquot-to-aliquot differences in luminescence properties.

LA-ICP-MS allows for sequential analysis of major, minor and trace elements from a given spot in solids with a spatial resolution of a few tens of µm. The system used here comprises a Geolas 193 nm ArF excimer laser system (Lambda Physik) combined with an Elan DRC-e quadrupole ICP-MS (Perkin Elmer). Optimization strategies and operating conditions were similar to those reported in Pettke (2008). Ablation rates were tuned to ca. 0.2 µm per pulse and laser pulse rate was set to 10 Hz. Laser beam sizes were generally

Table 4.1: List of investigated samples. The geological origin of some specimens is still unidentified.

Internal code	Denomination	Provenance	Geological origin
A1R	Chalcedony	Ain Zora, Morocco	Tertiary
A2R	Chalcedony	Ain Zora, Morocco	Tertiary
M1R	Tabular hornstone	Abensberg-Arnhofen, Franconia, Germany	Upper Jurassic
M4R	Flint	Orsbach, North Rhine–Westphalia, Germany	Upper Cretaceous
M5R	Flint	Lousberg, North Rhine–Westphalia, Germany	Upper Cretaceous
M9RII	Flint	Rullen, Belgium	Upper Cretaceous
M11R	Quartzite	Lenderscheid, Hessia, Germany	Tertiary
M12R	Flint	Holy Cross Mountains, Poland	Jurassic
M13R	Chalcedony	Salzkammergut, Austria	Unknown
M15R	Flint	Rijckholt, St Geertruid, Belgium	Upper Cretaceous
M16R	Trigonodus hornstone	Dinkelberg, Baden-Württemberg, Germany	Middle Triassic
M17R	Banded hornstone	Kleinkems, Baden-Württemberg, Germany	Upper Jurassic
M20R	Flint	Caredo, Lessinian Mountains, Italy	Unknown
M26R	Flint	Fehmarn, Baltic Sea, Germany	Cretaceous
N1	Flint	Petra region, southern Jordan	Cretaceous
O2R	Radiolarite	Szentgál, Bakony Mountains, Balaton, Hungary	Middle Jurassic
O4	Jasper or chalcedony	Coşava, Banat, Romania	Unknown
O5	Cornelian	Coşava, Banat, Romania	Unknown
O6	Cornelian	Coşava, Banat, Romania	Unknown
O7	Cornelian	Coşava, Banat, Romania	Unknown
O8	Chalcedony	Românești, Banat, Romania	Unknown
T1	Flint	Baltic Sea	Cretaceous

120 µm, except for better resolution of hot spots or zonations as indicated by autoradiography. Here, beam sizes as small as 44 µm were employed. This translates to 80 µm deep ablation craters for 40 s signal duration. Data reduction was done with the SILLS program (version 1.1.0)(Guillong et al. 2008) by carefully evaluating every transient signal with special attention to the radioactive elements K, Rb, U and Th, including spike filtering. Signal sections of homogeneous element intensities were selected for integration. SRM 610 from NIST was used as an external standard material and element abundances were calculated by summing up major element oxides to 99.5 wt.% (Halter et al. 2002). A total of 24 elements were quantified at typical precisions of ± 2 % (2 RSD external reproducibility). Analytical precisions deteriorate when approaching the limits of detection (LOD), largely due to increased counting statistics uncertainties; hence, element concentrations near the respective LOD have typical analytical uncertainties of ± 30 % (Pettke 2008). In fact, for most samples the concentrations of K, U and Th were more than an order of magnitude above the respective detection limits, resulting in corresponding analytical uncertainties of about ± 2 % (2 RSD). When compared to uncertainties associated with environmental dose rate determination, the errors on the element concentration determinations are negligible and therefore not further considered.

Depending on sample size and visual appearance (e.g. silex homogeneity, inclusions), the number of analytical spots varied from 9 to 33. Locations of analysis were guided largely by gradients in radionuclide contents as expected from prior autoradiography. Consequently, homogeneous domains were less intensely analyzed than inhomogeneous domains. Most of the ablation craters had a diameter of 120 µm and a depth of about 100–120 µm what gives an analyzed sample volume and geometry corresponding approximately to the coarse grain size (ca. 100–200 µm) commonly used for luminescence measurements. The grain-to-grain variations of K, U and Th concentrations can be directly related to other element contents, thus giving a picture of their distribution within silex material investigated as bulk for luminescence.

For digestion and liquid-mode ICP-MS measurements, 100–200 mg of powered sample material was digested by high-PT decomposition (180 °C, max. 5 MPa; Loftfields PDS-6) using in all stages Merck Suprapur® grade reagents (HF, $HClO_4$, HNO_3 and HCl). The following procedures were carried out:

1. Digestion (I): 2.5 ml HF, 2.5 ml $HClO_4$, 180 °C, max. 5 MPa (18 h)
2. Evaporation (I): 160 °C (4 h)
3. Addition of 4.0 ml HCl, Evaporation (II): 160 °C (2 h)
4. Digestion (II): 4.0 ml HCl, 130 °C, max. 5 MPa (12 h)
5. Addition of 4.0 ml HNO_3, Evaporation (III): 160 °C (2 h)
6. Addition of 2.0 ml HNO_3, 5.0 ml H_2O, 120 °C

After all evaporation steps, the residue should be nearly dry to avoid losses by sputtering of dry material. Finally, the perfectly transparent solution was transferred with 2 % HNO_3 to a 50 ml volumetric flask and stored in PP bottles. Measurements were performed with a Perkin Elmer/Sciex ELAN 6000 ICP-MS (inductively coupled plasma quadrupole mass spectrometer) following mainly the technique described by Dulski (2000). From the final digestion solution (50 ml) 1–3 ml were brought to 10 ml, resulting in a dilution of up to 5000. Determinations of element concentrations were performed using Ru–Re as internal standards (each 10 ng ml^{-1}) for drift corrections and a three point external calibration. Samples and procedure blanks were measured in batches of five and were bracketed by a calibration cycle. The precision and accuracy of measurements following the described procedure are better than ± 5 %. The accuracy of all determinations was checked using reference materials in each set of analysis, usually 12 samples. The reference materials (Loess-1 (Nussloch), PRI, GSR-4) were treated the same way as samples.

4.3 Results

4.3.1 Description of the surface texture

General textural features (Fig. 4.1) can be summarized as follows: Area A denotes the bulk material (silex, i.e. a mixture of amorphous opal and micro- or cryptocrystalline chalcedony) the specimens are composed of. The colors of the silex vary from translucent and colorless (A2R, T1) to opaque and strongly colored, encompassing white, gray, yellowish, red and brownish (M13R, N1, O2R). The samples M1R and M12R show layering texture, very much like tree rings. Some of the samples contain abundant fragments of bright or dark mineral phases (feature B) of variable size that are distinct from the silex (e.g. M16R, O5). Category C comprises all textures that are associated with cracks. These crack fillings (veins) appear as lines of variable thickness on the sample surface and can be translucent or opaque and colored (M16R, O6). Isolated inclusions (feature D) occur in almost all samples, but their spatial density and distribution (random or clustered) varies considerably between samples. The sizes of inclusions range from about 300 µm (M9RII) down to less than a few µm (A2R, T1). In some cases crusts or host rock material (feature E) enclosing the silices were also analyzed (e.g. A2R, M16R, T1). This is of dosimetric relevance as in some samples silex-enclosing material seems to invade the silex interior along fissures (feature F). Furthermore, the rim can also contain siliceous material (feature F).

4.3.2 Radionuclide concentrations in silex

Table 4.2 reports mean concentration data for K, Th and U in samples, together with the lowest and highest concentrations measured. The relative standard deviations of the mean values serve as indication for the variation of radionuclide concentrations in silex.

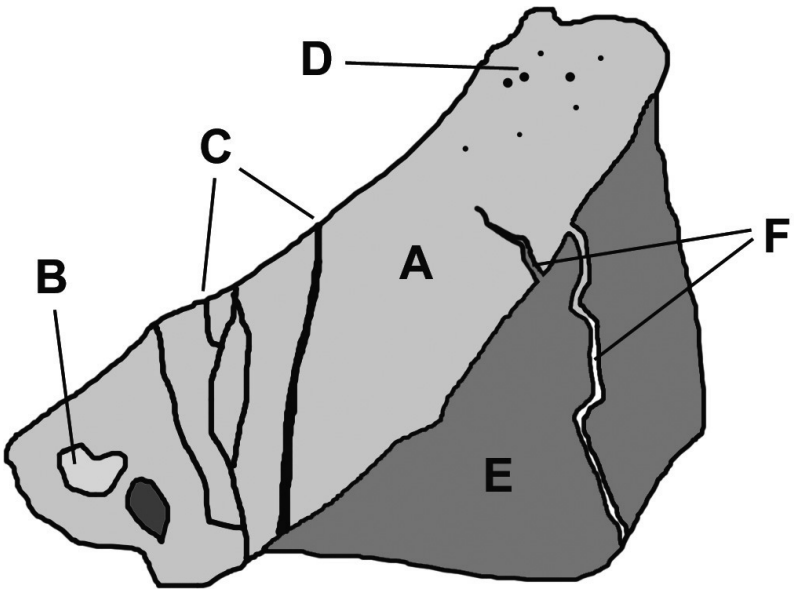

Figure 4.1: Generalized components constituting the samples. A: silex (main component); B: non-silex/foreign phases, included in the silex, but varying in color and/or composition; C: linear crack fillings (veins) with different color as silex; D: small punctual inclusions: E: adherent cortex or host rock material; F: filled fissures and cracks reaching from the cortex or host rock into the silex. It should be noted that not all samples contain all described components.

Additionally, the estimated fractions of the surface assigned as silex (= 100 % – veins and foreign phases) and the number of analytical spots for each specimen are given in Table 4.2. To quantify the total internal dose rate of one particular radioactive element (K, U or Th) on the one hand, and from α-, β- and γ-radiation on the other hand, the respective dose rates (deduced from mean silex values) were calculated using the conversion factors given in Adamiec & Aitken (1998). An a-value of 0.1 had to be assumed as the determination of the α-efficiency for each sample was not possible. Since the α-efficiency may vary significantly for different luminescence emissions (detection wavelengths) and between samples, the computed dose rates represent approximations only (Mercier et al. 1995; Richter & Krbetschek 2006). Rubidium was not included here because of its negligible contribution to the dose rate given the determined concentrations.

Most of the samples yield overall low radionuclide contents in the silex. Potassium concentrations are generally < 0.1 wt.% (except for two samples), U concentrations < 1.0 µg g^{-1} (except for four samples) and Th concentrations < 0.4 µg g^{-1} (except for one sample). In four samples some analytical spots returned Th concentrations below the detection limit of ca. 0.001 µg g^{-1}. In order to determine the influence of slight color differences in layered silex on the internal radiation, we measured element concentrations along a transect of sample M1R. The results are shown in Fig. 4.2a and represent an example of very low radioactivity and nearly homogeneous radionuclide distribution along the analyzed transect. This part of sample M1R is free of veins and inclusions as illustrated in Fig. 4.2, but dark-colored layers within the silex tend to have slightly increased U and Th values

and decreased K values. The rim (left side in Fig. 4.2a) yields elevated K concentrations, whereas U contents faintly decrease.

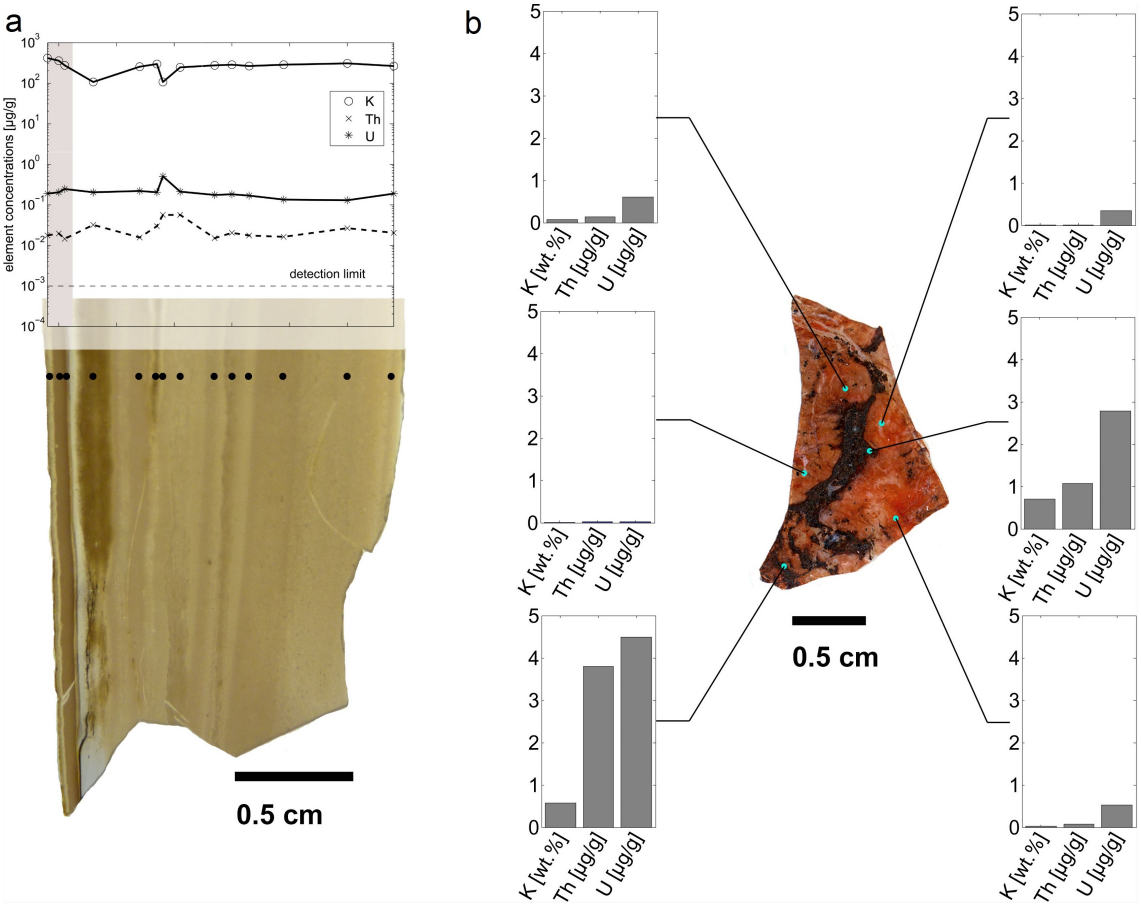

Figure 4.2: Measured concentrations of K, Rb, U and Th in different sample domains. (a) shows element profiles along a transect perpendicular to the layering of sample M1R. (b) presents element contents in six domains of sample O7. For better visualization, the circles indicating the sampling locations are larger than the actual spot sizes of analysis (90–120 µm). Note in (b) that the concentration of K is given in wt.%, whereas Th and U are given in µg g^{-1}.

4.3.3 Radionuclide concentrations in veins and inclusions

Depending on the optical homogeneity and size of veins and inclusions, several analyses were done per sample to measure their element compositions. Table 4.3 summarizes the type of sampled components, the number of pits and the measured concentrations as well as the lowest and highest determined values for K, Th and U. For comparison, the silex mean values from Table 4.2 are also shown.

We observed generally high variability of K, U and Th concentrations in impurities, in some cases covering several orders of magnitude (e.g. M9RII, N1, O6, O7). The highest K concentration is measured in a punctual inclusion in sample M9RII (ca. 3 wt.%), while the veins of sample O4 yield the highest Th value (> 20 µg g^{-1}). Specimen N1 contains by far

Table 4.2: In-situ determined concentrations of K, U and Th in silex. For each element, the calculated arithmetic mean and the relative standard deviation (RSD in %) of the analyzed spots are given. In most cases, the surface fraction of the silex component (i.e. all material minus foreign phases, veins and inclusions) was estimated by use of imaging software and color values of the scanned sample surfaces with an uncertainty of ca. 5 %. Where this was not possible due to inconsistent silex color, the silex surface fraction was estimated by eye. Surface fractions of 100 % can include non-siliceous phases or inclusions too small to assess their areal share. In case analytical spots returned values below the limit of detection (Th minimum values of samples A2R, M11R, M16R, O7), maximum mean and dose rate values were calculated considering the single maximum values. The dose rate calculations are based on the conversion factors given in Adamiec & Aitken (1998) and an a-value of 0.1 is assumed. Since the fraction of the total γ-dose actually deposited within the silex specimen is strongly dependent on its mass and shape, a fixed value of 5 % is considered for calculation of the internal γ-dose rate. All LA-ICP-MS measurements were made using a beam diameter of 120 µm.

	A1R	A2R	M1R	M4R	M5R	M9RII	M11R	M12R	M13R	M15R	M16R	M17R	M20R	M26R	N1	O2R	O4	O5	O6	O7	O8	T1
Surface fraction	100 %	82 %	100 %	100 %	100 %	100 %	100 %	100 %	100 %	95 %	90 %	100 %	100 %	100 %	100 %	95 %	95 %	90 %	80 %	68 %	95 %	100 %
Number of analytical spots	12	9	33	6	13	12	21	18	6	12	7	12	12	12	6	9	9	6	9	9	12	12
Potassium																						
Mean [µg g^{-1}]	900	84	245	540	260	280	60	90	2660	130	320	290	440	144	232	960	610	580	300	370	1660	320
Relative SD [%]	24	18	29	22	16	21	47	14	62	41	48	7	22	3	9	19	20	64	45	126	96	9
Lowest value [µg g^{-1}]	650	68	85	450	210	130	9,6	68	1450	69	75	270	320	136	210	560	442	290	127	6,70	340	280
Highest value [µg g^{-1}]	1160	117	340	770	330	350	105	117	5800	215	520	320	550	152	270	1160	850	1300	570	1470	6000	370
Mean dose rate K [Gy ka^{-1}][a]	0.071	0.0067	0.019	0.043	0.021	0.022	0.0048	0.0071	0.21	0.010	0.025	0.023	0.035	0.011	0.018	0.076	0.048	0.046	0.024	0.029	0.13	0.025
Thorium																						
Mean [µg g^{-1}]	0.36	0.007	0.026	0.165	0.107	0.207	0.074	0.007	1.63	0.039	0.041	0.012	0.142	0.030	0.058	0.31	0.106	0.087	0.058	0.215	0.219	0.082
Relative SD [%]	15	73	52	22	116	39	117	26	55	39	66	21	34	9	13	54	47	51	56	183	95	34
Lowest value [µg g^{-1}]	0.26	<0.001	0.015	0.131	0.022	0.081	<0.002	0.004	0.73	0.020	<0.0004	0.008	0.098	0.026	0.052	0.080	0.060	0.044	0.032	<0.001	0.016	0.071
Highest value [µg g^{-1}]	0.45	0.011	0.074	0.23	0.35	0.40	0.35	0.012	2.73	0.064	0.066	0.017	0.267	0.034	0.071	0.64	0.219	0.139	0.123	1.17	0.67	0.160
Mean dose rate Th [Gy ka^{-1}][a]	0.033	0.00064	0.0024	0.015	0.010	0.019	0.0067	0.00065	0.15	0.0035	0.0038	0.0011	0.013	0.0028	0.0052	0.028	0.010	0.0079	0.0053	0.019	0.020	0.0075
Uranium																						
Mean [µg g^{-1}]	1.45	0.023	0.203	1.13	0.201	0.088	0.176	0.34	0.60	0.56	1.72	0.094	0.40	0.33	11.3	1.90	0.124	0.91	0.68	0.58	0.52	0.26
Relative SD [%]	26	122	36	11	32	37	64	60	51	58	46	17	12	6	49	29	17	49	24	22	88	32
Lowest value [µg g^{-1}]	0.80	0.0009	0.117	0.99	0.146	0.059	0.024	0.192	0.32	0.32	0.44	0.073	0.32	0.30	2.56	1.50	0.097	0.47	0.50	0.34	0.142	0.152
Highest value [µg g^{-1}]	2.41	0.084	0.49	1.35	0.36	0.183	0.48	0.81	1.02	1.44	2.59	0.124	0.49	0.35	18.6	3.07	0.151	1.62	0.96	0.74	1.51	0.44
Mean dose rate U [Gy ka^{-1}][a]	0.54	0.0084	0.075	0.42	0.074	0.033	0.065	0.13	0.22	0.21	0.64	0.035	0.15	0.12	4.2	0.70	0.046	0.34	0.25	0.22	0.19	0.10
Total dose rate, α [Gy ka^{-1}][a]	0.34	0.0054	0.046	0.26	0.050	0.032	0.043	0.075	0.23	0.12	0.38	0.021	0.10	0.073	2.5	0.43	0.034	0.20	0.15	0.14	0.13	0.062
Total dose rate, β [Gy ka^{-1}][a]	0.29	0.010	0.050	0.21	0.053	0.040	0.032	0.057	0.34	0.093	0.28	0.037	0.10	0.060	1.68	0.36	0.069	0.18	0.12	0.12	0.21	0.065
Total dose rate, γ [Gy ka^{-1}][a]	0.0102	0.0002	0.0015	0.0075	0.0017	0.0013	0.0012	0.0020	0.0105	0.0034	0.0102	0.0009	0.0031	0.0021	0.0645	0.0126	0.0017	0.0061	0.0043	0.0043	0.0054	0.0021
Total dose rate [Gy ka^{-1}][a]	0.64	0.016	0.10	0.48	0.10	0.074	0.08	0.13	0.58	0.22	0.67	0.059	0.20	0.14	4.2	0.81	0.104	0.39	0.28	0.26	0.34	0.13

[a] Calculation based on conversion factors of Adamiec & Aitken (1998), assuming an a-value of 0.1 and uniform distribution of K, Th and U in the silex.

Table 4.3: Impurity concentrations of K, U and Th determined in crack fillings (veins) and inclusions of selected samples. Owing to the low number of measurements, the mean was not calculated. For reference, the silex mean concentrations of the respective sample are shown as well (see also Table 4.2). The laser beam diameter varied from 44 µm to 120 µm, according to the size of the analyzed component.

	A1R	A2R	M1R	M4R	M5R	M9RII	M13R	M15R	M16R		M17R	M20R
Sampled component	Vein	Punctual inclusion	Veins	Punctual inclusion	Punctual inclusion	Punctual inclusion	Punctual inclusion	Spacious dark phase	Secondary phases	Punctual inclusion	Vein Vein	Punctual inclusion
Number of analytical spots	7	12	6	3	3	4	6	3	8	3	3	3
K lowest value [µg g^{-1}]	840	113	250	500	370	230	650	290	82	165	250	490
K highest value [µg g^{-1}]	1760	800	370	1310	740	31400	7300	330	362	195	390	4340
K silex mean [µg g^{-1}]	900	84	250	540	260	276	2660	129	320	1320	290	440
Th lowest value [µg g^{-1}]	0.360	0.006	0.014	0.300	0.124	0.450	0.370	0.067	0.006	0.018	0.310	0.190
Th highest value [µg g^{-1}]	2.09	0.360	0.028	0.51	0.57	11.7	4.27	0.089	0.109	0.045	0.87	2.70
Th silex mean [µg g^{-1}]	0.360	0.006	0.026	0.165	0.107	0.207	1.63	0.039	0.041	0.041	0.012	0.142
U lowest value [µg g^{-1}]	1.27	0.280	0.158	2.53	0.210	0.102	0.170	1.04	0.93	0.84	0.077	2.41
U highest value [µg g^{-1}]	17.8	0.70	0.230	7.8	0.340	4.59	1.96	1.19	27.4	3.72	0.132	53.4
U silex mean [µg g^{-1}]	1.45	0.023	0.200	1.13	0.200	0.088	0.60	0.56	1.72	1.72	0.094	0.400

	M26R	N1	O2R	O4	O5		O6	O7		O8		T1
Sampled component	Punctual inclusion	Punctual inclusion	Cloudy inclusion	Dark veins	Dark vein	Punctual inclusion	Dark vein	Dark vein	Light vein	Dark vein	Punctual inclusion	Punctual inclusion
Number of analytical spots	1	6	4	6	3	3	11	12	6	3	3	3
K lowest value [µg g^{-1}]	2960	78	380	270	440	196	103	820	<0.97	580	890	280
K highest value [µg g^{-1}]	2960	250	840	5300	990	390	1960	8280	107	1130	3460	300
K silex mean [µg g^{-1}]	144	230	960	610	580	580	300	370	370	1660	1660	320
Th lowest value [µg g^{-1}]	0.380	0.074	0.011	0.93	0.260	0.065	0.027	0.021	<0.001	10.2	3.63	0.060
Th highest value [µg g^{-1}]	0.380	3.46	0.260	21.2	1.35	6.35	2.42	3.80	0.025	17.4	17.2	0.072
Th silex mean [µg g^{-1}]	0.030	0.058	0.311	0.106	0.087	0.087	0.058	0.220	0.220	0.220	0.220	0.082
U lowest value [µg g^{-1}]	0.330	11.4	2.67	0.250	0.430	0.57	0.51	0.340	0.029	14.0	1.39	0.192
U highest value [µg g^{-1}]	0.330	243	6.08	1.33	1.64	2.15	16.4	10.0	0.69	23.9	3.15	0.400
U silex mean [µg g^{-1}]	0.330	11.3	1.90	0.124	0.91	0.91	0.68	0.58	0.58	0.52	0.52	0.260

the highest concentration of U, in the silex (ca. 11 µg g^{-1}) as well as in spotty inclusions (max. 240 µg g^{-1}). Light or transparent veins are generally very low in radioactive elements. We observed the lowest contents for the colorless veins of sample O7, with K and Th being below the LOD and U below 0.03 µg g^{-1}. In contrast, dark and non-transparent foreign components of the same specimen mostly exhibited elevated values of radionuclides. The concentrations of radioactive elements of six different textural positions of sample O7 are shown in Fig. 4.2b, illustrating exemplarily the pronounced internal heterogeneity of K, U and Th distribution observed for some of the investigated samples.

4.3.4 Comparison of LA-ICP-MS with bulk ICP-MS data

In previous studies ground and mixed sample powders were used for internal dose rate determination. Due to contributions from strong-radiating veins or inclusions (hot spots) it is expected that mixed samples yield higher radionuclide contents than the silex values determined by LA-ICP-MS. To test this hypothesis, additional bulk ICP-MS measurements were carried out on finely ground sample material. We investigated seven specimens and determined their "mixed" concentrations of radioactive elements. Fig. 4.3 shows the plotted ratios (bulk ICP-MS/LA-ICP-MS); the measured concentrations are listed in Table A.1 (Section A.3).

The significant differences in K, U and Th concentrations between single specimens are confirmed by the ICP-MS results. Mean element contents vary by an order of magnitude among the seven samples studied. Comparison of LA-ICP-MS and bulk ICP-MS data reveals that the bulk mean element concentrations exceed the silex mean values in many samples. This coincides with the observation of relatively high radionuclide concentrations measured notably in inclusions but also in some of the veins. Enhanced scatter of K and Th concentrations in silex – and thus large uncertainties of the LA-ICP-MS mean – suggests comparability of the results of both methods for about half of the samples (Table A.1). Moreover, U values overlap within 1 σ uncertainty in all cases. This implies that U, which is mostly the dominant contributor to the internal dose rate, seems to be largely located in the silex itself and not in mineral impurities. In other words, the bulk concentrations are increased more effectively by the amounts of K and Th in crack fillings and inclusions than is the case for U.

The difference of concentrations determined by the two methods is most striking for sample M26R which contains a few strong-radiating hot spots not considered for the silex LA-ICP-MS element concentration data. These hot spots clearly account for the significantly elevated bulk ICP-MS results. Similar influence of high-emitting zones (veins, enclosures) can be inferred for the other samples. However, O6 and O8 yield partly contrasting results, i.e. element concentrations in the silex are higher than the bulk concentrations. These samples contain significant fractions of veins very poor in trace elements; consequently, vein material may also dilute the silex element concentrations, thus lowering the bulk concentrations.

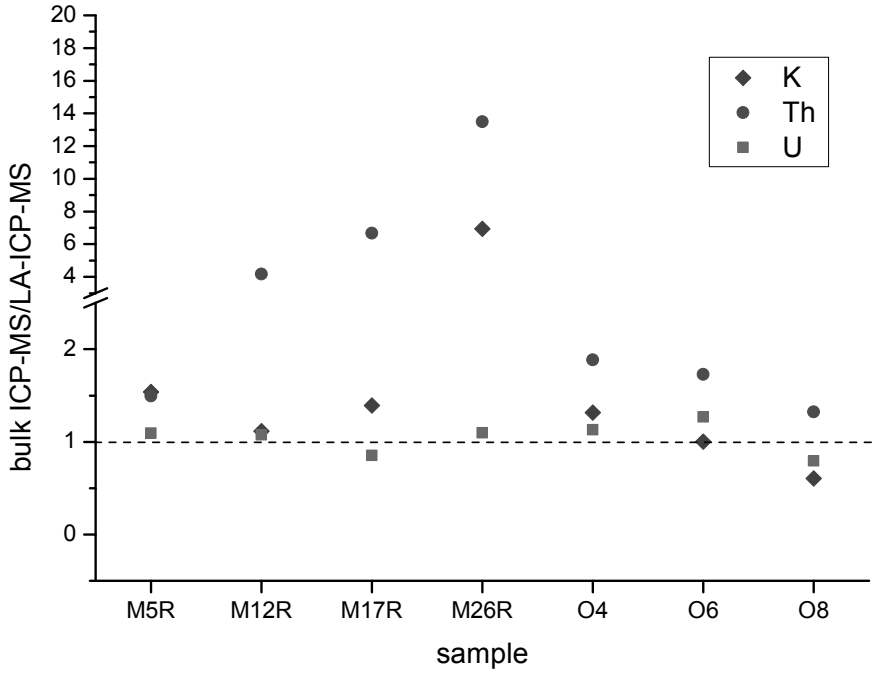

Figure 4.3: Ratio of element concentrations determined by bulk analyses of the specimens normalized to LA-ICP-MS measurements of the silex component only. The uncertainties of each data point (ratio) are not shown for clarity but are given in Section A.3 (Table A.1), together with all measured values.

4.3.5 Geochemical characterization of veins and inclusions

Quartz is able to incorporate many trace elements in several ways. Si^{4+} can be substituted by Ti^{4+}, Ge^{4+}, or by (Al^{3+}, Fe^{3+}, Ga^{3+}) in combination with (Li^{+}, P^{5+}, H^{+}). Incorporation of trace elements in quartz with radii significantly different from that of Si^{4+} is related to extrinsic defects. For instance, small amounts of U and Th (up to ca. 0.2 µg g^{-1}) can be hosted in SiO_2 along structural inhomogeneities (grain boundaries). Higher concentrations of large ions are, however, coupled to non-siliceous phases or mineral inclusions.

In the following, four samples containing typical crack fillings and inclusions are considered exemplarily in more detail to characterize the impurities. By using characteristic ratios of element abundances, we intend to identify the minerals that are associated with increased radiogenic element concentrations revealed by autoradiography and LA-ICP-MS. Tables A.2 and A.3 (Section A.3) present the results of the LA-ICP-MS measurements of selected impurity components ("types") for these samples. In addition to the concentrations of 24 elements in crack fillings and inclusions, the values for the silex of each sample are also shown as reference.

Sample M16R contains almost all types of impurity components as defined in Fig. 4.1. Its crust has a Mg/Ca ratio of ca. 0.5, representative of dolomite ($CaMg(CO_3)_2$). The crack fillings are of the same color as the crust, and all cracks are connected with the

crust. Analysis of the element concentrations in the filled cracks shows that the Mg/Ca ratio is considerably lower than in the crust. Crack fillings are thus probably composed of $CaCO_3$ with trace impurities of Mg, Mn and Fe, mixed with siliceous material. Similar element concentrations were measured in the type B component of M16R, but with less U than in the crack. The inclusion (type D) is rich in Fe, with elevated Cu and Pb (Table A.2), favoring its composition of Fe-oxy-hydroxide weathering products. The contents of radiogenic elements in the inclusion are similar to those of the silex; thus it does not reflect a radiation hot spot. In contrast, the inclusion in sample M20R yields very high concentrations of K, Rb, U and Th along with elevated values of almost all other elements. High contents of P and Y suggest that a rare earth element phosphate phase may be part of the inclusion material. The dark phase in sample O7 (Fig. 4.2b) shows a Fe/Mn ratio characteristic for Fe–Mn-oxy-hydroxides. Similar to the inclusion in sample M20R, this dark phase also yields metal and transition metal concentrations (Cu, Y, Zr, La; Table A.2) far above those of the silex. The dark impurities in sample O7 amount to some 10 % only which is demonstrated by the high proportion of Si. Furthermore, the intensity of red color of this sample correlates well with Fe content; hence, it is identified as hematite. Type C crack fillings in sample O8 show strongly increased metal and transition metal concentrations and a Fe/Mn ratio of ca. 1, pointing to predominance of Fe–Mn-oxy-hydroxide compounds as well.

4.4 Discussion

Our data demonstrate that pure silex is characterized by very low concentrations of K, U and Th, and that silex samples (the bulk archeological material) contains inclusions and cracks/veins enriched of up to two orders of magnitude in these elements. Often, those impurities are characterized by coloration from pale yellow or orange to brown or black, colors that commonly derive from (Mn–)Fe-oxy-hydroxide infiltration or fillings.

Combined analyses of element abundance patterns also indicate the presence of other minerals in some specimens, namely calcium and magnesium carbonate or rare earth element phosphates (Tables A.2 and A.3). The infiltration pattern and crack filling textures of these materials strongly suggest a secondary origin, for example due to weathering of neighboring material of the silices. Redox processes are a likely mechanism for generating the U enrichments associated with the Oxy-hydroxide precipitations.

Of crucial importance for dosimetric dating is the presence and spatial distribution of hot spots and hot zones since they determine the internal radiation field and thus dose deposition. In the case of negligible concentrations of hot spots/zones, the difference to the otherwise homogeneous radiation field is small. The other extreme would be hot spots/zones which are present at very high density and uniform distribution, so that the radiation fields of the single spots/zones overlap. The result is again a homogeneous but more intense radiation field. The required minimum spatial density of fillings or inclusions

to generate a uniform internal dose rate depends on the emitted radiation type. Due to the larger range of β-radiation, pure β-emitters (i.e. hot spots containing only K) need minimum densities that are much smaller than in the case of the short-range α-radiation. However, the studied silex samples (Table 4.1) are to be found somewhere in between these extreme cases with the consequence of radiation fields characterized by more or less steep gradients and hence unknown impact on the effective internal dose rate.

Only two samples (M1R, M17R) are pure silex, effectively lacking crack fillings and inclusions; the other samples contain considerable amounts of impurities in highly variable quantities and distributions. The inclusions in samples M5R, M12R and M13R are evenly spread among the whole sample volume, so that at least for the β-component homogeneous radiation can be assumed. Conversely, the other specimens contain impurities that occur more or less clustered (Schmidt et al. 2013), leading to spatial differences in intensity of α- and β-radiation within the sample.

Burbidge et al. (2009) found that the volume influenced by impurity-induced α-radiation in Mozambican sedimentary quartz is negligible. In contrast, the investigated silex samples mostly contain substantially higher concentrations of veins and impurities whose spheres of radiative influence are difficult to estimate. This problem is further complicated by the fact that not only pure α-emitting spots/zones have to be considered but also β-hot spots or a mixture of both. Additionally, as demonstrated by our measurements, high radionuclide concentrations in silex samples are not exclusively confined to weaknesses and structural defects, but can also be related to intergrown phases.

The comparison of bulk ICP-MS and LA-ICP-MS values for the concentration of radioactive elements showed that bulk concentrations are slightly but systematically higher than pure silex concentrations, due to non-silex material (impurities) rich in radionuclides. These hot spots/zones, however, are characterized by locally very high concentrations of U and Th with the implication that tracks generated by emitted α-particles overlap to some extent. In general, along the tracks far more free charge carriers are generated by highly ionizing α-radiation than high-energetic states are available. The consequences are local saturation effects and a decrease in luminescence sensitivity because part of the energy expended for ionization cannot be stored and is hence lost for luminescence production. Alpha track overlapping further decreases the fraction of stored charge carriers contributing to the luminescence signal and thus the sensitivity, too, compared to the case of low α-emitter concentrations with no track overlapping (Aitken 1984; Mauz et al. 2006). This means, highly concentrated α-emitting radionuclides (those from U and Th and their decay products) are far less effective in producing luminescence as they would be if uniformly distributed (Aitken 1985). Though, this effect is not considered when measuring the bulk and mixed sample for dose rate determination. Accordingly, an erroneously high dose rate leads to age underestimation. The importance of this issue is highlighted by the fact that α-radiation is the dominant contributor to the internal dose rate for many samples (Table 4.2).

Moreover, the determination of the accumulated dose is usually carried out on crushed sample material and requires measurement of several subsamples (aliquots) of each specimen. The natural luminescence signal is compared to the signals measured after irradiation with known laboratory doses and the equivalent dose is then obtained by curve fitting of the dose response curve (signal intensity vs. dose) and extrapolation or interpolation (Aitken 1985; Richter & Krbetschek 2006). Presence of hot spots/zones results in spatially non-uniform dose deposition within the sample, so that enhanced scatter of luminescence intensity between aliquots is observed, even when measuring big aliquots. This, in turn, gives rise to enlarged uncertainty in the curve fit and finally reduced precision in the determined equivalent dose in case multiple-aliquot protocols are used. Normalization procedures such as weight normalization or second glow normalization are often not fruitful due to heterogeneous U and Th distribution and because the natural and complex radiation field cannot be reproduced during laboratory irradiation. For instance, the occurrence of a grain containing a hot spot and thus yielding a high luminescence signal in a few of the aliquots cannot be corrected for by a normalization dose. For a normalization approach to work, the hot spot grain would have to show a sensitivity to β-radiation that is proportional to the α-induced TL signal, for which no indications are given. However, poor reproducibility may not be traced back solely to non-uniform radiation, but might also possibly originate for example from irregular distribution of electron traps and/or luminescence centers.

Another problem in the context of equivalent dose determination arises from the difference in dose response of α- and β-/γ-radiation. It is widely known that α-radiation induces linear growth up to high doses, whereas saturation begins significantly earlier (i.e. at lower doses) for β- and γ-radiation (Zimmerman 1972; Mercier et al. 1992). Highly-ionizing α-radiation is confined to small cylinders of ca. 0.1 µm in diameter (Aitken 1985) and a few µm long (the α-tracks) and within this cylinder TL is in saturation, with the consequence of low luminescence efficiency. Therefore, α-induced TL is proportional to the number of tracks as far as the tracks are not overlapping which is the case only for relatively high doses (because the sample volume is much bigger than the α-tracks) or for local hot spots, as seen above. In contrast, energy of β- and γ-radiation is comparatively spread uniformly within the sample volume, resulting in higher luminescence efficiency but also in earlier saturation with dose (Aitken 1984). If we consider a silex sample with significant internal α-dose rate, we do not take into account the linear dose response caused by this α-component when constructing a dose response curve using laboratory β-irradiation. In the dose range where β- and γ-induced TL begins to saturate non-allowance for α-radiation contribution will result in age underestimation in case multiple-aliquot additive-dose procedures in combination with quadratic or exponential curve fitting are used. In contrast, regeneration dose protocols (both multiple- and single-aliquot) will lead to age overestimation.

As the outermost 2 mm rim of each artefact is removed during sample preparation, the external dose rate contributes only with its cosmic and γ-component to the total dose

rate. Due to its high penetration range (ca. 30 cm in sediment), the γ-radiation field can be seen as spatially uniform in the interior of the silex, because it is usually not larger than a few cm. As a consequence, the higher the contribution of the external dose rate to the total dose rate is, the relatively less important are the effects associated with a spatially inhomogeneous internal dose rate. Accordingly, the uncertainties introduced by complex internal dose rate configuration are reduced if the external dose rate is dominating (Richter 2007). Since most of the studied silex samples contain on average only low amounts of radioisotopes, the negative effects of hot spots/zones are likely to be attenuated by prevailing external radiation. For example, the external dose rate (cosmic and γ-component) of heated Banat flint artefacts (corresponding to the raw material samples O4–O8 in this study) at their finding spots is estimated to be about 1.1 Gy ka^{-1}. According to Table 4.2, this value accounts for ca. 65–90 % of the total dose rate, depending on the sample, if only the silex-induced fraction is considered. Veins and inclusions, however, contribute to a hardly quantifiable amount to the internal dose rate, thus increasing the effect of internal dose rate. By contrast, this relationship inverts for sample N1. In this case the high internal dose rate of at least 4.2 Gy ka^{-1} (Table 4.2) is estimated to be 5–10 times larger than the expected external dose rate. The drawback is that the external dose rate is prone to fluctuate over archaeological time scales, for example due to changing water content in sediment.

The above explanations point out that the accuracy and precision of TL dates of heated silex artefacts could be enhanced significantly if the problems associated with non-uniform internal dose rate could be solved. One possible strategy in terms of physical sample preparation comprises magnetic separation (Porat 2006) in order to extract Fe–Mn-oxy-hydroxides, for which our measurements showed strongly increased U and Th concentrations (Table A.2) and which are likely to have different luminescence properties than silex. Parts of a rock containing such magnetic phases could then be extracted after crushing. Hence, produced fragments (100–200 µm) that are influenced by the short-range α-radiation (a few µm in SiO_2) generated by oxy-hydroxides are removed as well. Another approach preserves the configuration of emitters and dosimeter material and makes use of spatially resolved luminescence detection, where a slice of the sample is produced and its emitted luminescence is recorded by the use of imaging optics and a camera. After luminescence signal readout the sample could be checked for the presence of high-emitting zones/spots, for example by the use of radiography (Rufer & Preusser 2009; Schmidt et al. 2013) or by LA-ICP-MS. In this way, regions of interest can be selected that are far away from hot zones/spots and therefore presumably free of gradients of internal dose rate.

4.5 Conclusions

Determination of element concentrations in numerous analytical spots in 22 silex samples using LA-ICP-MS has shown that pure silex contains mostly low amounts of ra-

dionuclides, compared to expected environmental concentrations at archaeological sites. Dark-colored materials, crack fillings and inclusions typically show strongly increased concentrations of K, U and/or Th. The spatial distribution of non-silex phases and inclusions varies from sample to sample and their 3-dimensional occurrence is difficult to predict. Compositional analyses can be used to characterize the minerals involved in crack fillings and in inclusions. For instance, Fe–Mn-oxy-hydroxides, Ca–Mg–Fe carbonates, clays and phosphates are constituents of some samples studied here. Zones of strongly increased autoradiography response reveal correspondingly high amounts of radioactive elements, causing a non-uniform internal radiation field. In terms of dosimetric dating, this gives rise to micro-scale effects on the determined dose which are difficult to account for. The potential consequences are enhanced data scatter and reduced accuracy and precision for the obtained ages. To overcome these problems, magnetic separation of crushed samples or spatially resolved dosimetry of solid samples seem to be most promising, as further chemical preparation is hampered by intergrowth of siliceous material with contaminating phases.

Acknowledgments

This work was financed by the Deutsche Forschungsgemeinschaft (DFG) within the framework of the Collaborative Research Center 806 “Our Way to Europe”.

References

Adamiec, G., Aitken, M., 1998. Dose-rate conversion factors: update. Ancient TL 16, 37–50.

Aitken, M., 1984. Non-linear growth: Allowance for alpha particle contribution. Ancient TL 2, 2–5.

Aitken, M., 1985. Thermoluminescence dating. Academic Press, London.

Aspinall, A., Feather, S. W., 1972. Neutron activation analysis of prehistoric flint mine products. Archaeometry 14, 41–53.

Burbidge, C., Dias, M., Prudêncio, M., Rebêlo, L., Cardoso, G., Brito, P., 2009. Internal α activity: localisation, compositional associations and effects on OSL signals in quartz approaching β saturation. Radiation Measurements 44, 494–500.

Dulski, P., 2000. Reference materials for geochemical studies: new analytical data by ICP-MS and critical discussion of reference values. Geostandards Newsletter: The Journal of Geostandards and Geoanalysis 25, 87–125.

Guillong, M., Meier, D. L., Allan, M. M., Heinrich, C. A., Yardley, B. W., 2008. Appendix A6: Sills: A Matlab-based program for the reduction of Laser Ablation ICP-MS data of homogeneous materials and inclusions. Mineralogical Association of Canada Short Course 40, 328–333.

Halter, W., Pettke, T., Heinrich, C., Rothen-Rutishauser, B., 2002. Major to trace element analysis of melt inclusions by laser-ablation ICP-MS: methods of quantification. Chemical Geology 183, 63–86.

Malik, S. R., Durrani, S. A., Fremlin, J. H., 1973. A comparative study of the spatial distribution of uranium and of TL-producing minerals in archaeological materials. Archaeometry 15, 249–253.

Mauz, B., Packman, S., Lang, A., 2006. The alpha effectiveness in silt-sized quartz: new data obtained by single and multiple aliquot protocols. Ancient TL 24, 47–52.

Mercier, N., 1991. Flint palaeodose determination at the onset of saturation. Nuclear Tracks and Radiation Measurements 18, 77–79.

Mercier, N., Valladas, H., Valladas, G., 1992. Observations on palaeodose determination with burnt flints. Ancient TL 10, 28–32.

Mercier, N., Valladas, H., Valladas, G., 1995. Flint thermoluminescence dates from the CFR laboratory at Gif: Contributions to the study of the chronology of the Middle Palaeolithic. Quaternary Science Reviews 14, 351–364.

Mercier, N., Valladas, H., Froget, L., Joron, J.-L., Reyss, J.-L., Weiner, S., Goldberg, P., Meignen, L., Bar-Yosef, O., Belfer-Cohen, A., Chech, M., Kuhn, S., Stiner, M., Tillier, A.-M., Arensburg, B., Vandermeersch, B., 2007. Hayonim Cave: a TL-based chronology for this Levantine Mousterian sequence. Journal of Archaeological Science 34, 1064–1077.

Murray, A. S., Wintle, A. G., 2000. Luminescence dating of quartz using an improved single-aliquot regenerative-dose protocol. Radiation Measurements 32, 57–73.

Pettke, T., 2008. Analytical protocols for element concentration and isotope ratio measurements in fluid inclusions by LA-(MC)-ICP-MS. In: Sylvester, P. (Ed.), Laser Ablation ICP-MS in the Earth Sciences: Current practices and outstanding issues. Mineralogical Association of Canada Short Course Series, vol. 40.

Porat, N., 2006. Use of magnetic separation for purifying quartz for luminescence dating. Ancient TL 24, 33–36.

Richter, D., Krbetschek, M., 2006. A new thermoluminescence dating technique for heated flint. Archaeometry 48, 695–705.

Richter, D., 2007. Advantages and limitations of thermoluminescence dating of heated flint from Paleolithic sites. Geoarchaeology 22, 671–683.

Richter, D., Mercier, N., Valladas, H., Jaubert, J., Texier, P.-J., Brugal, J.-P., Kervazo, B., Reyss, J.-L., Joron, J.-L., Wagner, G., 2007. Thermoluminescence dating of heated flint from the Mousterian site of Bérigoule, Murs, Vaucluse, France. Journal of Archaeological Science 34, 532–539.

Rufer, D., Preusser, F., 2009. Potential of autoradiography to detect spatially resolved radiation patterns in the context of trapped charge dating. Geochronometria 34, 1–13.

Schmidt, C., Rufer, D., Preusser, F., Krbetschek, M., Hilgers, A., 2013. The assessment of radionuclide distribution in silex by autoradiography in the context of dose rate determination for thermoluminescence dating. Archaeometry 55, 407–422.

Selo, M., Valladas, H., Mercier, N., Joron, J., Bassinot, F., Person, A., Nouet, J., 2009. Investigations of uranium distribution in flints. Radiation Measurements 44, 615–619.

Tribolo, C., Mercier, N., Selo, M., Valladas, H., Joron, J.-L., Reyss, J.-L., Henshilwood, C., Sealy, J., Yates, R., 2006. TL dating of burnt lithics from Blombos Cave (South Africa): Further evidence for the antiquity of modern human behaviour. Archaeometry 48, 341–357.

Valladas, G., Gillot, P. Y., 1978. Dating of the Olby lava flow using heated quartz pebbles: some problems. PACT 2, 141–150.

Valladas, H., 1985. Some TL properties of burnt prehistoric flints. Nuclear Tracks and Radiation Measurements 10, 785–788.

Valladas, H., 1992. Thermoluminescence dating of flint. Quaternary Science Reviews 11, 1–5.

Valladas, H., Mercier, N., Froget, L., Joron, J. L., Reyss, J. L., Karkanas, P., Panagopoulou, E., Kyparissi-Apostolika, N., 2007. TL age-estimates for the Middle Palaeolithic layers at Theopetra cave (Greece). Quaternary Geochronology 2, 303–308.

Zimmerman, D., 1972. Relative thermoluminescence effects of alpha and beta radiation. Radiation Effects 14, 81–92.

5 Optically stimulated luminescence of amorphous/microcrystalline SiO_2 (silex): Basic investigations and potential in archeological dosimetry

Christoph Schmidt[a], Sebastian Kreutzer[b,c]

[a] Institute for Geography, University of Cologne, Otto-Fischer-Str. 4, 50674 Köln, Germany
[b] Department of Geography, Justus-Liebig-University Giessen, Senckenbergstr. 1, 35390 Giessen, Germany
[c] Geographical Institute, Geomorphology, University of Bayreuth, 95440 Bayreuth, Germany

Quaternary Geochronology 15, 1-10 (2013)

Abstract

Unlike the well-studied optically stimulated luminescence (OSL) signal of (macrocrystalline) quartz, not much is known about OSL from natural amorphous and microcrystalline silicon dioxide. These materials – generally termed "silex" – were widely used for prehistoric tool production, and thermoluminescence (TL) is routinely applied do date the firing event of heated specimens. This study presents data on basic OSL characteristics of silex such as signal composition and component-resolved thermal stability as well as the applicability of OSL for dating of burnt lithic tools. Fitting of LM-OSL curves yielded similar components (mostly five) as observed for quartz, with the photoionization cross-sections being in the same order of magnitude for both materials. Three different methods (LM-OSL pulse annealing, short-shine pulse annealing as well as the varying heating rate method) were applied to study the thermal stability of components and allowed calculating trap parameters E and s, and hence the electron retention lifetime. Only the most light-sensitive ("fast-like") component proved to be of sufficient thermal stability for dating applications, as evidenced from coherent experimental results. All other components already diminished at preheating temperatures $> 200\,°C$. Pulse annealing measurements

further indicate that electron populations sampled by OSL and those responsible for the $\sim 380\,^{\circ}C$ TL-"dating peak" are not identical. Dose recovery tests applying an OSL-SAR protocol with "hot bleach" in between the regeneration cycles showed good reproducibility of a known dose if only the initial OSL signal ($\sim$ 0–0.5 s at 90 % LED power) is used. Finally, obtained OSL-SAR and TL ages based on the blue TL emission are in agreement within errors for two Middle Paleolithic archeological samples showing a "fast-like" component. These results verify the experimental findings of sufficient long-term stability of the initial OSL signal. Since not all silex specimens deliver a bright and stable OSL signal, optical ages of suitable samples may serve as an additional internal check for the paleodose estimate rather than substituting TL as a standard technique for dating of heated silex.

5.1 Introduction

Optically stimulated luminescence (OSL) is an established method to determine the last daylight exposure of sedimentary quartz (Preusser et al. 2008; Wintle 2008). For dating heated quartz, both OSL and TL (thermoluminescence) have been applied, as done for bricks (Bailiff & Holland 2000; Bailiff 2007), for archeometallurgical slags (Haustein et al. 2003) or volcanic materials (Fattahi & Stokes 2003).

In Paleolithic archeological contexts, the heating of stone tools is often the dated event most closely related to past human activities (see Richter et al. (2009) for discussion). These tools mostly consist of amorphous or microcrystalline silica (henceforth termed "silex") showing advantageous cleavage properties. Numerous studies confirmed the applicability of TL to date the last heating above $\sim 400\,^{\circ}\mathrm{C}$ of Middle and Upper Paleolithic silex artefacts (Valladas 1992; Mercier et al. 1995; Richter 2007). OSL, however, has only sparsely been used for dating heated stones from archeological sites: Mejdahl & Bøtter-Jensen (1994) applied a novel OSL measurement protocol to quartz stones, bricks and ceramics; Tribolo et al. (2003) investigated heated quartzite pebbles from Portuguese Upper Paleolithic sites. These materials (quartz, quartzite) are, however, more crystalline than silex (including the varieties flint, chert, hornstone, radiolarite,...) mostly used for tool production. The lacking long-range order of constitutive SiO_4 tetrahedra of the amorphous phase of silex may entail OSL properties different from those of (macrocrystalline) quartz. This topic, however, has remained poorly studied so far. The work of Poolton et al. (1995) includes spectral investigations and revealed both dose-dependent and dose-independent OSL signal components of flint from sites in France, Israel and USA, ascribed to the (micro)crystalline and the amorphous phase of the material, respectively. By comparing OSL pulse annealing data with TL glow curves, the authors suggest the origin of dose-dependent and time-decaying OSL to be associated with a $180\,^{\circ}\mathrm{C}$ TL peak, and therefore they doubt the long-term stability of this signal. Richter & Temming (2006) conducted dose recovery tests of German flint and hornstone samples using an OSL single-aliquot regenerative-dose (SAR) protocol. Due to high recuperation rates and reduced reproducibility of the measurements, they concluded that "OSL dating of flint is probably not possible" (Richter & Temming 2006: 823).

During the last decade, it has been confirmed that the quartz OSL signal is composed of several distinct components featuring different bleachability (photoionization cross-sections) and dose-response characteristics, but also varying thermal stability (Smith & Rhodes 1994; Bailey et al. 1997; Jain et al. 2003; Singarayer & Bailey 2003). These components are termed *fast*, *medium* and *slow* in order of decreasing optical decay rates. Especially one of the *slow*-components (mostly named *slow3* or *slow4*) of quartz is characterized by high saturation dose levels which are associated with high densities of related charge traps (Bailey et al. 1997; Bailey 2000). The presence of similar signal constituents in silex samples would have the potential to extend the dating limit and circumvent the problem of increased bleaching times (as experienced in sediment dating), provided that

ancient heating completely erases this signal. Furthermore, the application of OSL-SAR procedures on heated silex is expected to yield more precise estimates for the paleodose owing to less severe heat treatment and thermal sensitization during regenerative measurements, compared to TL. In addition, the required amount of sample material could be decreased compared to multiple-aliquot protocols, allowing dating artefacts of smaller size.

This study comprises linearly modulated OSL (LM-OSL) measurements and signal deconvolution to investigate signal components and their characteristics in four different silex samples. Most important for retrospective dosimetry, the thermal stability of signal components was assessed using pulse annealing experiments and two different evaluation techniques: (1) the varying heating rates method (Li et al. 1997) and (2) curve fitting of pulse annealing data (Singarayer 2002). We then tested the performance of the thermally most stable component for dating purposes by applying SAR dose recovery tests. Finally, paleodose estimates of archeological silex samples obtained by TL are compared to those derived from OSL-SAR measurements.

5.2 Materials and methods

5.2.1 Samples and sample preparation

Four silex samples were investigated, including two raw material samples and two heated samples excavated at archeological sites. Geological samples comprised Orsbach flint (sample code M3) of dark grayish-brownish appearance as well as dark-grayish Baltic flint (sample code M27). Annealing at 450 °C prior to OSL measurements simulated ancient firing. As a reference for obtained OSL ages, archeological samples Rom16 from the Aurignacian site Românești-Dumbrăviţa I, Romania, and SodTL2 from Sodmein Cave, Egypt (see also Mercier et al. (1999) for another dating study of this site), have already been dated by TL. The material of all samples is addressed as flint, except for Rom16 which consists of chalcedony and amorphous opal.

After removal of the outer 2 mm rim with a water-cooled diamond saw, samples were gently crushed in a steel mortar and sieved to grain sizes of 100–200 µm. The fine grain fraction (∼4–11 µm) was obtained by acetone settling following mainly Zimmerman (1972). Chemical preparation comprised treatment with diluted HCl (10 %) to destroy carbonates. Prepared coarse grain material was fixed on stainless steel discs with silicone spray (8 mm mask); fine grains were placed as α-thin layers on stainless steel discs.

5.2.2 Instrumentation and measurement conditions

Measurements were carried out on Risø TL/OSL DA-15 and DA-20 luminescence readers fitted with EMI 9235QB photomultiplier tubes. N_2 atmosphere was used for measurements >200 °C. Beta-irradiation was done with $^{90}Sr/^{90}Y$-sources delivering dose rates of 0.11–0.15 Gy s^{-1} to coarse grains; α-irradiation was conducted at ∼10 mbar with an

^{241}Am-source generating 0.813 µm^{-2} min^{-1} of α-tracks. Photo-stimulation was provided by blue LEDs (470 Δ 30 nm) with a maximum power density of ∼40 mW cm^{-2} at the sample position. A Hoya U340 glass filter (7.5 mm) limited the detected luminescence emissions to a transmission window between ∼270 and 370 nm for OSL; TL was recorded using a Semrock BrightLine HC 475/50 interference filter (475 Δ 50 nm). Unless stated otherwise (varying heating rate method), heating rates were set to 5 K s^{-1} and samples were preheated at 240 °C for 10 s prior to continuous-wave (CW) and LM-OSL readout which were performed with sample temperature held constantly at 125 °C. Except for short-shine experiments (Section 5.4.1.2), LED power was ramped from 0–90 % for LM-OSL and fixed at 90 % for CW-OSL measurements. All LM-OSL measurements of silex were carried out on a single reader to guarantee identical stimulation characteristics and thus ensure self-consistency of the obtained dataset for determination of the photoionization cross-section.

5.2.3 Data analysis

In the simplest model, LM-OSL curves can be described as the sum of j first-order components (Bulur 1996; Choi et al. 2006):

$$I_{\mathrm{LM-OSL}} = \sum_{i=1}^{j} n_i \, b_i \, \frac{t}{P} \exp\left(-\frac{b_i \, t^2}{2P}\right) \tag{5.1}$$

Here, n is a dimensionless factor proportional to the initially trapped charge concentration, $b = \sigma \cdot \Phi_{\mathrm{max}}$ in s^{-1} the optical detrapping probability with σ (in cm^2) being the photoionization cross-section and Φ_{max} the maximum stimulating photon flux (in s^{-1} cm^{-2}), t is measurement time in s and P the total measurement time in s. Fitting of LM-OSL curves to first-order components was carried out with the $fit\_LMCurve()$ routine implemented in the R (R Development Core Team 2012) package "Luminescence" (version 0.1.7) (Kreutzer et al. 2012) reverting to starting parameters for b and n deduced from published values of quartz samples (Jain et al. 2003). These values were then transformed into x_i (peak position) and I_i (peak maximum) following the formalism in Kitis & Pagonis (2008) (see manual of the R package for further details). The fit was seen as satisfactory when the residuals did not show any structure. For fitting of pulse annealing data with Eq. 5.2, the Origin software (version 8.5) was used. Dose estimates of CW-OSL-SAR measurements were obtained using the Analyst software (version 3.24) (Duller 2007).

5.3 OSL signal components

LM-OSL measurements were carried out on four silex samples (M3, M27, Rom16, SodTL2) to study their OSL signal composition. While LM-OSL signal levels are rather low, even after regenerative doses of 500 Gy used here, the general shape of LM-OSL curves roughly resembles those also observed for some crystalline quartz samples. Comparison of the

background signal measured on "dead discs" (crushed silex, mounted with silicone spray onto discs, after initial signal readout and subsequent annealing) and the LM-OSL signal of an empty disc covered with silicon spray (Fig. 5.1) confirms the presence of a dose-independent, anti-Stokes shifted OSL signal from the sample (Poolton et al. 1995). Tests of the signal reproducibility exclude variability between silicone-covered discs as origin of the observed rise of the LM-OSL curve towards increased stimulation time. Prompt luminescence emission during optical stimulation can occur either with emission energy < absorption energy (Stokes shift) or emission energy > absorption energy (anti-Stokes shift) and is in flint attributed to the amorphous phase (Poolton et al. 1995). CW-OSL measurements of this signal with increasing readout temperature T revealed an exponential dependence of signal intensity on temperature (for $T > 150\,^{\circ}\mathrm{C}$) for three samples (M3, M27, SodTL2), confirming an Arrhenius relation and thus a phonon-assisted process (Raman scattering) (Demtröder 2005; Huntley 2006). The fact that the sum of several exponential functions is able to describe the measured data for all samples suggests several signal components with different activation energies (see Section A.4.2 and Figs. A.16 and A.17 for further details). To obtain the dose-dependent part of the signal for use in dosimetry, the anti-Stokes signal was subtracted from the LM-OSL sum curve. This net signal was then fitted with the R package "Luminescence".

Samples M3 and SodTL2 were best fitted to five components. Detrapping probabilities b derived from the fit as well as calculated photoionization cross-sections σ are summarized in Table 5.1. Component-specific parameters σ of all investigated silex samples and published quartz values are in the same order of magnitude, but differ within quoted uncertainties. Small discrepancies between silex and quartz cross-sections might result from the fitting process. It is, however, not sure that the same mechanisms or electron trap types are responsible for both materials. Hence, we did not adopt the component terminology of Jain et al. (2003) and Singarayer & Bailey (2003), but numbered them consecutively instead (*component 1*, *2* etc.).

Repeated bleaching and dosing (> 2–3 regenerative cycles) induced the growth of an easily bleachable signal component in sample Rom16, as evident from test dose monitoring of the LM-OSL signal in between regeneration cycles. Possibly, this component is of similar origin as the *ultrafast*-component sporadically detected in quartz samples (Jain et al. 2003; Singarayer & Bailey 2003; Goble & Rittenour 2006). Furthermore, especially *component 0* turned out to be problematic for the fitting routine, likely due to the increased impact of "dead channels" at the start of the LM-OSL record; see Singarayer (2002) for discussion. The best fit could be obtained with six components, while the fit of the first peak (designated *component 0* in Table 5.1) is still unsatisfactory (Fig. A.14).

5.4 Thermal stability of the initial OSL signal

LM-OSL measurements proved the presence of an OSL signal component in most silex samples similar to the *fast*-component of crystalline quartz. The latter has shown to be

Table 5.1: Detrapping probabilities b and photoionization cross-sections σ for OSL components of silex samples in comparison to published values for quartz. Parameters b and associated uncertainties were obtained with the fitting routine implemented in the R package "Luminescence" (Kreutzer et al. 2012). Quoted uncertainties approximately reflect the fluctuation of b between aliquots of one sample. Low signal levels did not allow reliably extracting more than *component 1* for sample M27 (see Fig. A.13).

Sample		M3	M27	Rom16	SodTL2		Quartz[a]
Component 0	b [s^{-1}]	–	–	14 ± 1	–	*Ultrafast*	
	σ [cm^2]	–	–	$1.8 \pm 0.1 \times 10^{-16}$	–		7.0×10^{-16}
	σ_{rel}	–	–	14	–		28
Component 1	b [s^{-1}]	1.1 ± 0.1	1.3 ± 0.1	1.0 ± 0.5	1.4 ± 0.1	*Fast*	
	σ [cm^2]	$1.3 \pm 0.1 \times 10^{-17}$	$1.6 \pm 0.1 \times 10^{-17}$	$1.1 \pm 0.6 \times 10^{-17}$	$1.6 \pm 0.1 \times 10^{-17}$		$2.5 \pm 0.3 \times 10^{-17}$
	σ_{rel}	1	1	1	1		1
Component 2	b [s^{-1}]	0.21 ± 0.03	–	0.11 ± 0.01	0.25 ± 0.01	*Medium*	
	σ [cm^2]	$2.5 \pm 0.4 \times 10^{-18}$	–	$1.4 \pm 0.2 \times 10^{-18}$	$3.0 \pm 0.1 \times 10^{-18}$		$5.9 \pm 2.0 \times 10^{-18}$
	σ_{rel}	0.2	–	0.1	0.2		0.2
Component 3	b [s^{-1}]	0.024 ± 0.020	–	0.034 ± 0.005	0.036 ± 0.063	*Slow 1*	
	σ [cm^2]	$2.8 \pm 2.4 \times 10^{-19}$	–	$4.0 \pm 0.6 \times 10^{-19}$	$4.2 \pm 7.4 \times 10^{-19}$		$2.1 \pm 0.5 \times 10^{-19}$
	σ_{rel}	0.02	–	0.03	0.03		0.01
Component 4	b [s^{-1}]	0.0025 ± 0.0044	–	0.0044 ± 0.0017	0.0038 ± 0.0005	*Slow 2*	
	σ [cm^2]	$3.0 \pm 5.1 \times 10^{-20}$	–	$5.2 \pm 2.0 \times 10^{-20}$	$4.5 \pm 0.6 \times 10^{-20}$		$1.2 \pm 0.2 \times 10^{-20}$
	σ_{rel}	0.002	–	0.004	0.003		0.001
Component 5	b [s^{-1}]	0.00053 ± 0.00053	–	0.00078 ± 0.00017	0.00066 ± 0.00005	*Slow 3*	
	σ [cm^2]	$6.2 \pm 6.2 \times 10^{-21}$	–	$9.2 \pm 2.0 \times 10^{-21}$	$7.8 \pm 0.7 \times 10^{-21}$		$1.9 \pm 2.9 \times 10^{-21}$
	σ_{rel}	0.0005	–	0.0008	0.0005		0.0001

[a] Values according to Singarayer & Bailey (2003).

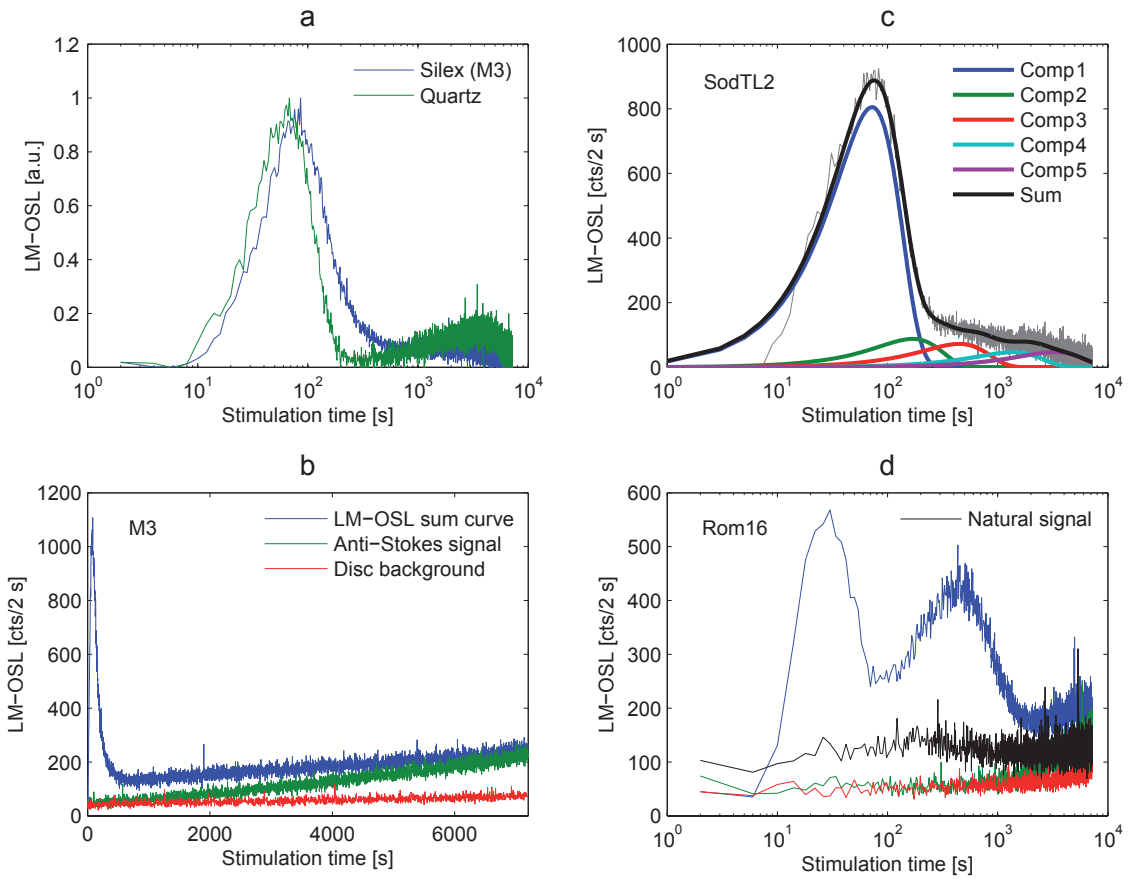

Figure 5.1: LM-OSL curves of silex samples. (a) Comparison of regenerated LM-OSL curves of silex (sample M3) and a Holocene alluvial or colluvial quartz sample from the Trebgasttal near Bayreuth. Both curves are normalized to their peak maximum and shown with the background already subtracted (for the silex sample as described in Section 5.3); measurement parameters were as given in Section 5.2.2 for both samples. The differing positions of the first peak might be explained by the two Risø readers used for data acquisition. (b) Regenerated sum LM-OSL curve of sample M3 after 500 Gy β-irradiation (the same curve as shown in (a)), anti-Stokes shifted signal contributions recorded after initial LM-OSL readout and annealing, and disc background measured on blank discs coated with silicone spray. The net anti-Stokes signal can be obtained by subtraction of the disc background. (c) Deconvolution to five first-order components of sample SodTL2 after the background (including dose-independent anti-Stokes shifted signals) has been subtracted. The residuals are shown in Fig. A.15 (Section A.4.1). (d) Natural (black) and regenerated (blue) LM-OSL curves of sample Rom16. The anti-Stokes shifted signal and disc background are also shown; the color legend is the same as in (b). See main text for further details.

best suited for dating of sediments due to its rapid bleaching characteristics, but also yields sufficient thermal stability for use in dosimetry of the last several Ma (Jain et al. 2003; Singarayer & Bailey 2003). TL dating of heated silex is usually based on the $\sim 380\,^{\circ}C$ TL peak (Mercier et al. 1995) whose bleachability is not well-known (Huxtable 1981; Poolton et al. 1995). Therefore, we studied the relationship between OSL and TL signals using the same emission band (UV). Furthermore, in order to assess the thermal stability of *component 1* of silex samples, its lifetime was determined, derived from the fundamental parameters E (electron trap depth) and s (frequency factor).

5.4.1 Pulse annealing experiments

5.4.1.1 LM-OSL measurements

For samples M3, M27 and SodTL2 regenerative LM-OSL curves were recorded after giving a 500 Gy β-dose, with increasing preheat temperatures in between the cycles (using a heating rate of $5\,\mathrm{K\,s^{-1}}$). Measurement of a test dose of 100 Gy after a fixed preheat of 220 °C for 10 s monitored sensitivity changes. Following LM-OSL measurements, OSL readout at 240 °C was performed for 3600 s to empty all traps prior to the next regeneration cycle. The relatively high regeneration doses were chosen due to the generally low signal levels and to catch also insensitive signal components. All recorded curves were then deconvolved, i.e. fitted to the sum of single components as described in Section 5.2.3. The remnant trapped charge (density of trapped electrons) after increasing preheat temperatures shall be proportional to the quantity n. Assuming first-order kinetics, the obtained pulse annealing curves (remaining signal versus preheat temperature) can then be described by the following equation (Singarayer 2002; Singarayer & Bailey 2003):

$$n = n_0 \exp\left[-\frac{skT^2}{qE}\exp\left(-\frac{E}{kT}\right) + \frac{skT_0^2}{qE}\exp\left(-\frac{E}{kT_0}\right)\right] \tag{5.2}$$

Here, n_0 is proportional to the initial charge concentration, q is the (linear) heating rate, k Boltzmann's constant, T the preheat temperature (in K), T_0 ambient room temperature ($\sim 20\,^\circ\mathrm{C} = 293\,\mathrm{K}$) and E and s as described earlier. This equation was used to fit the pulse annealing data and to determine E and s (as fit parameters) of the respective signal component.

Fig. 5.2 shows the pulse annealing curves for each fitted component of sample M3. If deconvolved to first-order components, the shallow and broad decay of the pulse annealing curves of all components except *component 1* indicates non-first-order kinetics of thermal depletion (Singarayer 2002). Indeed, these curves could not be well fitted to Eq. 5.2 describing first-order pulse annealing processes. The fit was more satisfactory for *component 1* of the samples which allowed extracting the parameters E and s. These values and the corresponding lifetimes are listed in Table 5.2. Due to the onset of thermal depletion at temperatures as low as 200 °C for all slowly bleachable signal components (see Fig. 5.2), it must be inferred that these components are thermally not stable enough for dating applications spanning the Quaternary/Paleolithic (~ 2 Ma). Owing to low count rates and associated severe shifts in values of b of fitting results with increasing annealing temperatures, reliable information on the thermal stability of individual components could not be obtained for sample Rom16. *Component 0* of this sample was observed after preheat temperatures up to 280 °C and appears to be thermally eroded in a similar manner as the other components, although not examined in detail. Moreover, *component 1* was obscured by subsequent components, impeding the approach of short-shines to effectively activate *component 1* only (see next section).

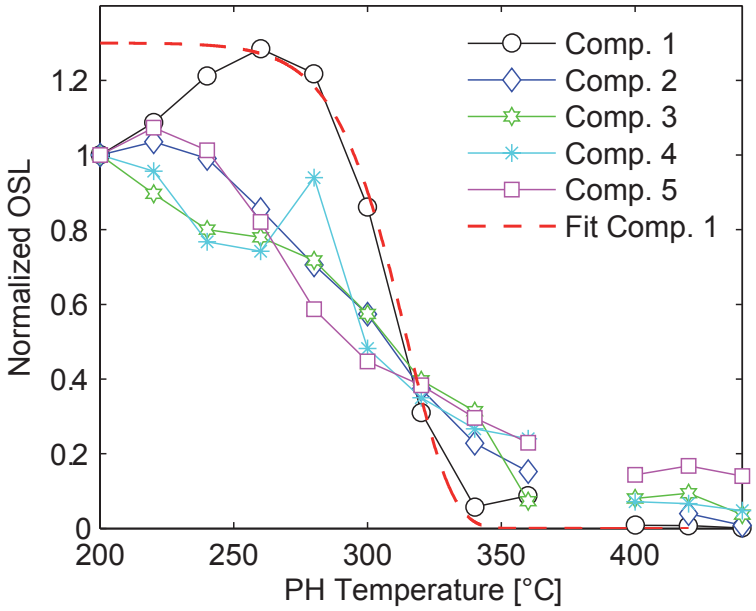

Figure 5.2: LM-OSL pulse annealing data of sample M3. The measurement procedure was as described in Section 5.4.1.1; deconvolution was not possible for the preheat step at 380 °C due to low signal levels. Only the pulse annealing data of *component 1* could be fitted satisfactorily to Eq. 5.2.

5.4.1.2 Short-shine measurements

Thermal depletion of OSL signal *component 1* of samples M3, M27 and SodTL2 was additionally measured by successively increasing preheat temperatures prior to OSL measurement (pulse annealing) after administering a single dose. Short-shine stimulation (0.01 s at 30 % LED power) assured that the contribution of *component 1* to the entire measured signal was maximized, i.e. further components were considered to be negligible. Moreover, sensitivity changes, occurring in the course of repeated irradiation and optical stimulation, are kept to minimum using short-shines. The signal loss due to the short-shine measurements was accounted for by measuring three aliquots of the same samples after a preheat of 160 °C, but without further preheat steps in between the OSL measurements. The average loss, obtained by fitting an exponential function to the average decay curve, was then used to correct the individual short-shines of the pulse annealing experiment. For the following it is thus assumed that the signal loss can be attributed to thermal erosion only (Li & Chen 2001).

Using short-shine measurements, two methods were applied to determine electron trap depth E and frequency factor s of *component 1*. Firstly, pulse annealing curves were fitted to Eq. 5.2 to derive E and s, and thus the lifetime. Here, the data obtained for a heating rate of $0.5\,\mathrm{K\,s^{-1}}$ were used. Secondly, a set of short-shine pulse annealing curves was collected using different heating rates for each curve (varying heating rate method,

VHM). With increasing heating rate, the pulse annealing curve shifts towards higher temperatures, and the reference point to measure this shift is taken to be the temperature of the biggest negative slope. When plotting the OSL reduction rate (i.e. the percentage of signal reduction per °C, or in other words, the first derivative) against temperature, one should obtain a "TL-like" peak whose maximum shifts with heating rate (Duller 1994). According to Li et al. (1997) and Li & Chen (2001), the following equation relates peak maximum T_m and heating rate q for first-order processes:

$$\ln\left(\frac{T_m^2}{q}\right) = \frac{E}{kT_m} + \ln\left(\frac{E}{sk}\right) \tag{5.3}$$

All parameters are as defined for Eq. 5.2. A fit through the data points in a plot of $\ln(T_m^2\, q^{-1})$ versus T_m^{-1} has a slope $E\,k^{-1}$, from which E can be obtained. The frequency factor is then given by $s = E\,k^{-1} \cdot \exp(-c)$, where c is the intercept of the fit with the y-axis.

Fig. 5.3 depicts pulse annealing curves, OSL reduction rates and a plot of $\ln(T_m^2\, q^{-1})$ versus T_m^{-1} from which E and s for sample M3 were obtained. All determined trap parameters of both methods are quoted in Table 5.2. Satisfactory agreement of E and s values using the VHM and fitting of pulse annealing curves is observed. Moreover, applying the latter method to pulse annealing curves recorded with different heating rates, congruent results are obtained within errors, confirming the validity of the approach. However, with respect to the VHM weak OSL signals of most samples introduced a considerable amount of data scatter so that the maximum of the OSL reduction rate (see Fig. 5.3) could not be reliably identified for some curves. Since small variations in T_m have large effects on the determined trap parameters, the VHM is thus considered to yield results of lower confidence. Results of determined electron retention lifetimes of the three methods are shown in Table 5.2.

The rise of the pulse annealing curve in quartz until temperatures of ∼240–270 °C (see Figs. 5.2, 5.3 and 5.4) is attributed to thermally induced migration of holes from reservoir into luminescence centers, explaining the observed sensitivity increase (Bailey 2001). Several components of sensitivity change (types of reservoir centers) have been described for the 110 °C TL peak of quartz, while OSL sensitivity changes in quartz related to the 325 °C TL peak can be accounted for by one type of reservoir center only (Wintle & Murray 1999; Li & Chen 2001). However, due to increased "scatter" in the OSL reduction rate plots, parameters of the reservoir center(s) of silex could not be obtained for the samples studied here (see Fig. 5.3).

5.4.2 Test for anomalous fading

In contrast to the well-defined edges of valence and conduction band in quartz, silex is supposed to yield band-tail states caused by varying bonding angles of SiO_4 tetrahedra of the amorphous phase (Poolton et al. 1995; Demtröder 2005). Due to these expected

Table 5.2: Trap parameters E and s for *component 1* of silex samples, obtained by three different methods. Uncertainties of data derived from fitting of pulse annealing curves are standard errors as returned from the fitting routine in Origin. Retention lifetimes τ of trapped charge are calculated for an ambient temperature of 293 K ($\sim 20\,^{\circ}$C) using the relation $\tau = s^{-1} \exp(E(kT)^{-1})$. Due to difficulties in precise determination of the maximum OSL reduction rate, the VHM yielded no results for sample SodTL2.

	Varying heating rate method			Fitting of LM-OSL pulse annealing curves			Fitting of short-shine pulse annealing curves		
Sample	E [eV]	s [s^{-1}]	τ [Ma]	E [eV]	s [s^{-1}]	τ [Ma]	E [eV]	s [s^{-1}]	τ [Ma]
M3	1.82	1.70×10^{15}	386	1.76 ± 0.26	$3.55 \pm 19.0 \times 10^{14}$	165	1.77 ± 0.17	$2.85 \pm 10.1 \times 10^{14}$	303
M27	1.78	4.82×10^{14}	267	1.87 ± 0.32	$7.00 \pm 46.8 \times 10^{15}$	648	1.78 ± 0.11	$3.05 \pm 6.84 \times 10^{14}$	421
SodTL2	–	–	–	1.78 ± 0.35	$6.72 \pm 48.8 \times 10^{14}$	172	1.71 ± 0.21	$9.44 \pm 41.1 \times 10^{14}$	8.51

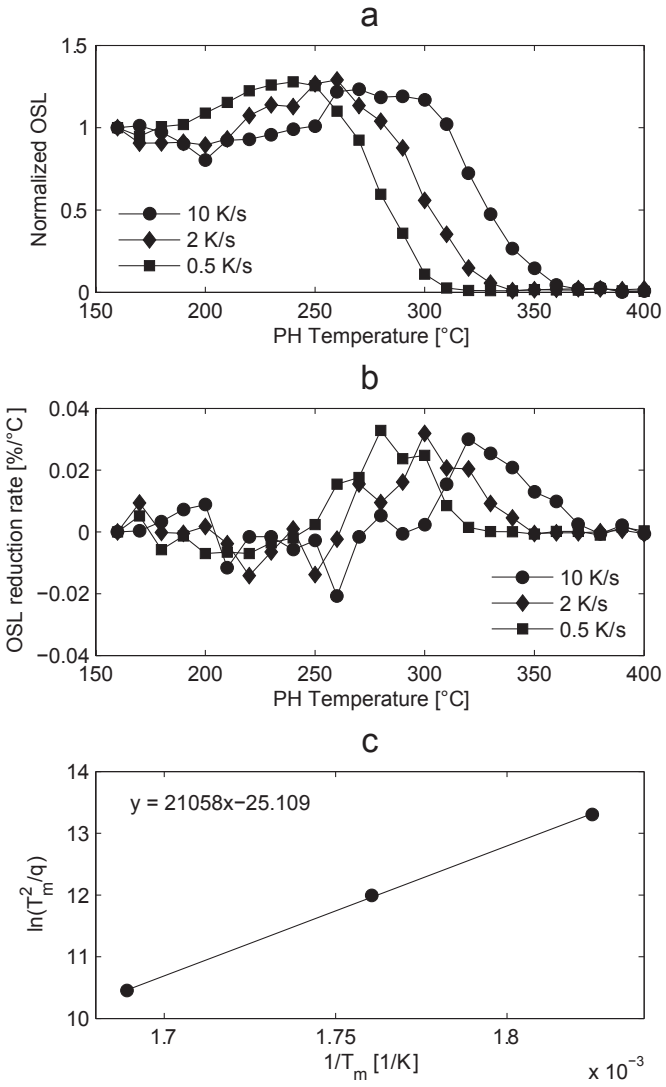

Figure 5.3: Pulse annealing data of the varying heating rate method for sample M3. (a) pulse annealing curves for heating rates as indicated in the legend. (b) OSL reduction rate as a function of preheat temperature. (c) plot of $\ln(T_m^2\, q^{-1})$ versus T_m^{-1}. Trap depth E was obtained from the slope of the linear fit which is $E\, k^{-1}$.

differences in energy band structure between silex and quartz, the OSL emission in the UV of three aliquots of samples M27 and SodTL2 was tested for anomalous fading. The fading test consisted of repeated irradiation of ~ 200 Gy, a 260 °C preheat for 10 s and increasing delay times, respectively, after which the OSL was measured. The measurement of a test dose of ~ 50 Gy after identical preheat conditions in between the regeneration steps recorded sensitivity changes. For data analysis, three signal integrals (0–0.5 s, 0–1.0 s, 3.0–4.0 s) were evaluated to account for signal components of lower bleachability as well. Over the time span suitable for estimating long-term fading rates (in this case > 7000 s after end of irradiation) (Visocekas 1985), no signal fading was observed within uncertainties (Figs. A.18 and A.19).

5.4.3 Relationship between TL and OSL signals in silex samples

TL glow curves and short-shine pulse annealing curves (Section 5.4.1.2) for samples M3 and M27 are shown in Fig. 5.4. UV TL was measured separately on annealed aliquots after receiving a β-dose of 60 Gy. Since sample Rom16 contains an easily bleachable *component 0* and a dominant *component 2*, it was excluded from pulse annealing investigations, as described above.

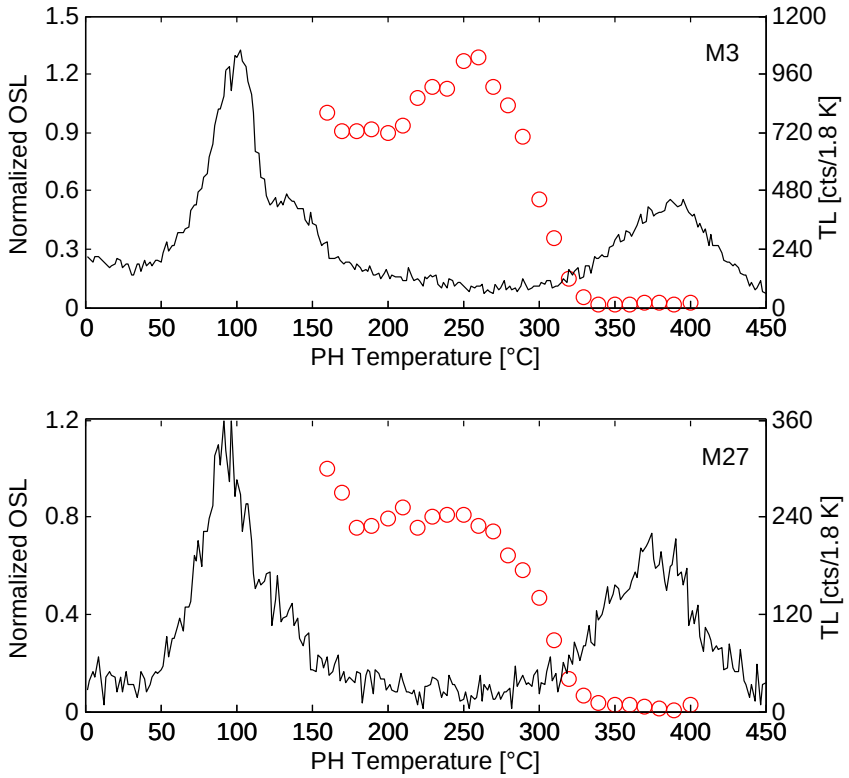

Figure 5.4: Thermal stability of OSL *component 1* of samples M3 (upper plot) and M27 (lower plot) in relation to TL peaks. Both TL and short-shine pulse annealing OSL data (circles, left ordinate) were recorded in the UV band using a rate of $2\,\mathrm{K\,s^{-1}}$ for heating and preheating. OSL counts were normalized to the initial value, measured after a preheat of 160 °C. For further details see main text.

It appears that *component 1* of M3 and M27, as measured by short-shines, is not related to the "dating peak" at 380 °C, because thermal erosion of the OSL signal begins at much lower temperatures and is completed at ∼340 °C. Furthermore, there is no associated TL peak in the temperature range in which the OSL *component 1* is thermally depleted. Glow curves recorded after 50 s CW-OSL bleaching reveal a slight reduction of the 380 °C peak, compared to glow curves recorded without prior bleaching (Fig. A.20), possibly due to sensitivity changes. This observation implies that the high temperature peak is optically insensitive to the blue bleaching spectrum used here and is probably not related to OSL components with lower bleachability (i.e. those which contribute to the OSL signal during

50 s stimulation). However, the ca. 300 °C TL peak of samples Rom16 and SodTL2 is substantially reduced by (blue) optical bleaching, though not fully depleted (Fig. A.20).

5.5 Dose response

As shown above, thermal and optical excitation may stimulate different trap types which may be present in different concentrations, with the implication of varying saturation dose levels. Due to insufficient long-term stability of *components 2–5*, dose response characteristics were investigated for *component 1* only. The measurement sequence included increasing regeneration β-doses up to 1000 Gy whose LM-OSL response was recorded after a 260 °C preheat (10 s), and a 30 Gy test dose correction comprising a cutheat to 240 °C. Dose response curves were constructed using the values of n (being proportional to the trapped charge related to each component) derived from deconvolution (samples M3 and M27) or by CW-OSL measurements while using just the initial signal (sample SodTL2; see also Section 5.6 for measurement conditions). These data could be best fitted to a single-saturating exponential + linear function (Fig. 5.6). Although varying from sample to sample, dose response characteristics of the stable OSL signal are similar to those of UV-blue TL (Mercier 1991), while red TL shows signal growth up to much higher doses (Schmidt, pers. observation). It thus seems unlikely that the use of *component 1* can help to increase the dating range.

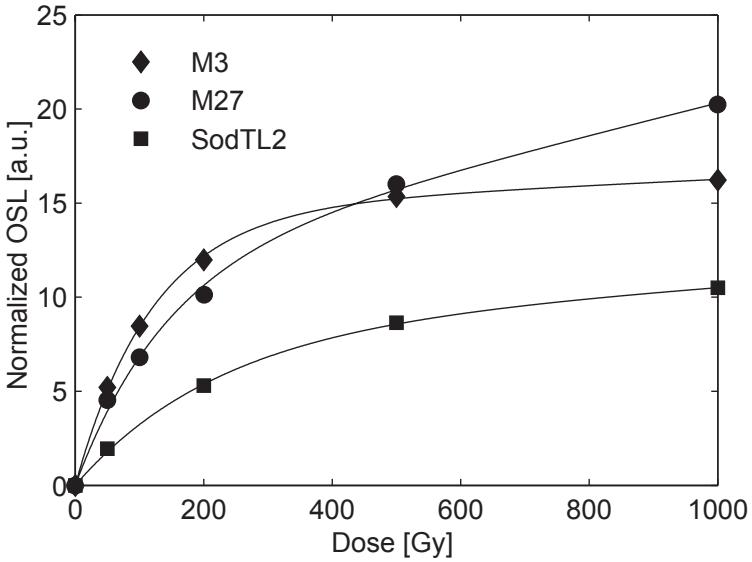

Figure 5.5: OSL dose response curves of silex samples fitted using a saturating exponential + linear function. Test dose corrected regeneration points were obtained by using the parameter n (proportional to the trapped charge concentration) derived from LM-OSL measurements and curve fitting (M3 and M27) and from CW-OSL measurements (SodTL2) whereas in the latter case conditions for readout and data analysis were the same as described in Section 5.6. The preheat temperature for SodTL2 was 260 °C (10 s).

5.6 Dose recovery tests

Previous results suggest sufficient thermal stability of *component 1* of the OSL signal for archeological dating. To test the suitability of this signal in retrospective dosimetry and to find appropriate measurement parameters, dose recovery tests were performed on all silex samples. Archeological luminescence signals were removed by heating to 450 °C before receiving the recovery dose; geological samples were heated twice to assure identical measurement conditions. Measurements followed the SAR protocol given in Murray & Wintle (2003), including a so-called "hot-bleach" (OSL stimulation for 80 s at 280 °C) at the end of each regeneration cycle to reduce recuperation. OSL was measured at 90 % LED power for 80 s and preheat temperatures varied between 220 °C and 280 °C (in 20 °C increments) whereas the cutheat prior to the test dose measurement was set 20 °C lower than the respective preheat temperature. Five aliquots were measured per preheat temperature and the common rejection criteria were applied (recuperation >5 %, recycling ratio outside the range 0.9–1.1) (Murray & Wintle 2000). For archeological samples, the recovery dose approximately met the expected paleodose (Table 5.4). Signal integration limits were set to 0–0.5 s for dose response curve construction and the background was calculated from the integral 60–80 s.

Table 5.3: Results of the preheat DRT for all silex samples. The recovered dose is given as the aliquots' error-weighted mean of the preheat step most closely reproducing the given dose; n denotes the number of accepted aliquots in relation to measured aliquots.

Sample	n	PH [°C]	Given dose [Gy]	Recovered dose [Gy]	Recovered/given dose
M3	5/5	280	60	59.6 ± 2.1	1.00
M27	4/5	240	60	57.7 ± 2.1	0.96
Rom16	5/5	260	60	59.5 ± 3.5	1.00
SodTL2	5/5	260	150	157.3 ± 4.4	1.05

Plots of D_e as a function of preheat temperature are shown in Fig. 5.6 for all samples. Table 5.3 summarizes the results of the DRT while only the best ratios (recovered dose/given dose) and corresponding preheat temperatures are displayed. The given dose could be recovered within ≤ 5 % for samples M3, M27 and SodTL2. As sample Rom16 lacks a prominent OSL *component 1*, the signal used for D_e determination comprises also unstable components (mainly *components 0* and *2*), as deduced from pulse annealing experiments. Hence, although the DRT returns promising results, the suitability of OSL from this sample for dating is highly doubted. For dose evaluation, a preheat temperature was chosen that yielded a measured dose closest to the recovery dose and showed the lowest data scatter. Reference measurements using a SAR protocol without hot bleach demonstrated considerable recuperation (in the order of 50 % of the recovery dose signal), i.e. thermal transfer of charge from optically insensitive traps to OSL traps during

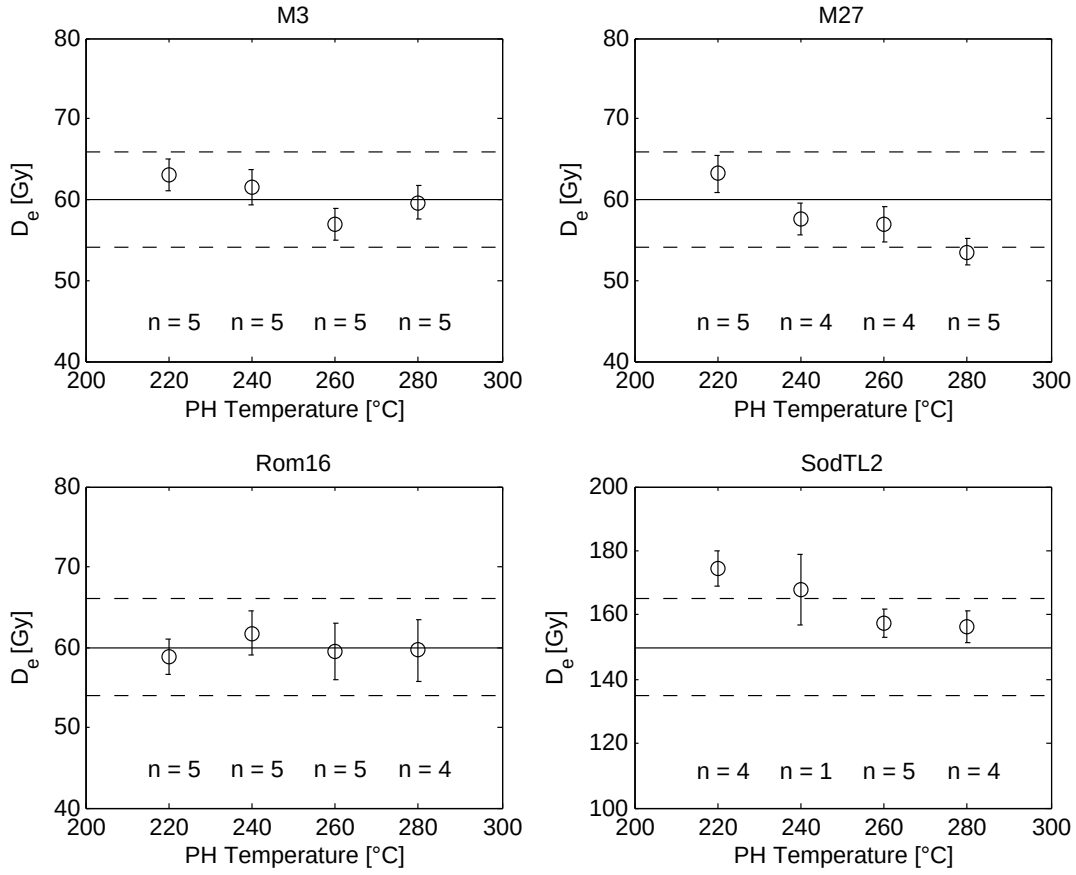

Figure 5.6: Results of the preheat dose recovery test. The recovery dose is indicated in the plots by a solid line, 10 % error bounds by dashed lines. Data points represent the error-weighted means of the recovered dose of individual D_e values. The number of contributing aliquots for each preheat temperature is given in the plots.

preheat. The decay of the signal recorded during hot bleach excluded a time-stable and dose-independent (but temperature-dependent) anti-Stokes signal component as possible origin (Poolton et al. 1995).

5.7 Paleodose estimation of archeological samples

Three archeological silex samples showing utilizable OSL sensitivity were chosen for comparison of paleodose estimates derived by TL and OSL, respectively. In addition to samples Rom16 and SodTL2, the OSL-SAR protocol was applied to a heated flint tool (LP7) from the karstic cave site Las Palomas, Spain; see Medianero et al. (2011) for further details on this site. Dose recovery tests served to adjust the preheat temperature for each sample. The TL equivalent dose (D_e) was measured with a multiple-aliquot additive-dose protocol (Rom16, SodTL2) or a TL-SAR protocol (LP7, due to its small size), using in both cases the blue emission. The accuracy of the TL-SAR protocol was thoroughly tested in the course of dose recovery tests.

While archeological material of Rom16 showed a measurable OSL signal, high scatter of dose points and dose oversaturation of some aliquots impeded determining an equivalent dose for this sample. In contrast, high precision of the D_e of SodTL2 and LP7 resulted from OSL measurements. Since it is known that the α-efficiency is different for TL and OSL (Tribolo et al. 2001; Lai et al. 2008), it was determined separately for both stimulation modes using fine grain separates. Table 5.4 summarizes the results of the TL and OSL measurements; the ratio of TL and OSL ages for samples SodTL2 and LP7 confirms agreement of the ages within $1\,\sigma$ uncertainty.

Table 5.4: Results of equivalent dose determination of archeological silex samples. The multiple-aliquot additive-dose (MAAD) protocol (including supralinearity correction by a multiple-aliquot regenerative-dose curve) and the TL-SAR protocol were used for TL D_e measurements in the blue emission range. The b-value according to Bowman & Huntley (1984) (not to be mixed up with the detrapping probability b) was determined by comparing the luminescence response of fine grain samples to α- and β-irradiation, respectively. n denotes the number of accepted aliquots in relation to measured aliquots.

	OSL				
Sample	PH temperature [°C]	Emission	n	D_e [Gy]	b-value [Gy µm^{-2}]
SodTL2	260	UV (SAR)	9/10	103.9 ± 7.1	0.83 ± 0.13
LP7	260	UV (SAR)	11/11	30.1 ± 1.6	0.33 ± 0.03

	TL				Ratio TL/OSL age
Sample	Emission	n	D_e [Gy]	b-value [Gy µm^{-2}]	
SodTL2	Blue (MAAD)	–	130.3 ± 8.3	1.85 ± 0.25	1.02 ± 0.11
LP7	Blue (SAR)	9/10	35.6 ± 1.7	1.08 ± 0.07	1.08 ± 0.15

5.8 Discussion

The OSL signal of silex samples, measured in the UV, was shown to consist of both dose-dependent and dose-independent parts, as has also been recognized by Poolton et al. (1995). Being of special interest for dosimetry in archeology, the dose-dependent signal was investigated in detail by LM-OSL measurements. Three of the four studied samples showed a prominent peak with high bleachability in the LM-OSL curve. By contrast, sample Rom16 (opal/chalcedony) revealed an even more light-sensitive component induced either by repeated irradiation or bleaching, as this component occurred not until the second or third regeneration cycle and test dose monitoring confirmed its strong sensitization in the course of SAR measurements. Assuming first-order kinetics, five components yielded the best fit for the flint samples (M3, M27 and SodTL2) and six components for Rom16 (due to *component 0*). The calculated photoionization cross-sections σ of the fitted components

differ slightly from that determined for quartz, but both lie in the same order of magnitude. The results of LM-OSL curve fitting are very sensitive to the used model, fitting routine and the choice of start parameters. Beside this, several other factors may influence the determined σ values:

1. In contrast to the majority of quartz samples, silex mostly shows considerable coloration (gray, brown) and thus higher opacity. This might influence absorption characteristics of stimulating and emitted light. However, since there is no systematic shift of cross-section values comprising all components, as would be expected for differing opacities, it is unlikely that this effect plays a major role.

2. Exact linearity of the excitation ramp is required for valid application of LM-OSL formula. This feature was not investigated in this study, but the problem of non-linear ramping has been detected earlier (Singarayer 2002). Depending on the shape of excitation increase, contrasting effects on components of diverging bleachability may result.

3. For calculation of the photo-ionization cross-section, knowledge of the exact power density (respectively the photon flux) at the sample position is required (Choi et al. 2006). This quantity cannot be measured routinely and calculations are usually based on manufacturer's instructions. Deviations from this value thus introduce systematic errors in σ determination. However, since the same reader was used for LM-OSL measurements, the results should be self-consistent.

Of crucial importance for application in dosimetry is the long-term thermal stability of the OSL signal. LM-OSL pulse annealing experiments prove that *component 1* has a lifetime sufficiently long to allow dating back to the beginnings of the Quaternary and the Paleolithic. These results were obtained using three different methods for E and s calculation, namely the curve fitting of LM-OSL and short-shine OSL pulse annealing data as well as the varying heating rate method. The coincidence of obtained parameters for all methods confirms (1) that during short-shine measurements only *component 1* was sampled, providing at the same time the minimum integral for thermally stable OSL signal contributions ($\geq$ 0–0.3 s), and (2) that *component 1* follows first-order kinetics. In contrast, all fitted components of lower bleachability (*components 2–5*) begin to thermally erode at temperatures $> 200\,^{\circ}\mathrm{C}$. Therefore, it is concluded that none of them is stable enough for dating applications. No matter whether or not the fitting to first-order components was justified (excluding *component 1*), the sum curve of *components 2–5* follows the same trend as individual components (approximately linear signal decrease with rising preheat temperatures). Accordingly, fitting the first-order pulse annealing equation failed and two possible reasons for it may be thought (Singarayer 2002). Firstly, thermal eviction of charge from traps might not obey first-order kinetics, although the LM-OSL signal can be fitted to first-order equations at low doses. Secondly, a distribution of trap depths E

with very similar photoionization cross-sections will produce a first-order-like LM-OSL peak, but thermal erosion will lead to a more continuous and less sharp decrease of pulse annealing data, as observed for *components 2–5* of the silex samples studied. The energy band structure of amorphous SiO_2 differs from that of crystalline quartz and features dangling bonds and bandtail-states reaching into the forbidden zone (Poolton et al. 1995; Demtröder 2005). Therefore, it might be suspected that energy levels below the conduction band are less well-defined than is the case for material with long-range order of atoms. This supports the hypothesis of distributions of traps being responsible for the broad and linear decay of pulse annealing curves.

The long-term stability of *component 1* of the OSL signal, as derived from experiments, was confirmed by dating results of archeological silex samples from Middle Paleolithic sites. Both TL and OSL gave identical ages within $1\,\sigma$ uncertainty. When it comes to practical issues of lithic artefact dating, the OSL-SAR protocol has the advantages of shorter measurement times and – as is also the case for TL-SAR procedures (Richter & Krbetschek 2006) – lesser amounts of sample material required for D_e determination. This would allow dating smaller samples than needed for the multiple-aliquot technique. If TL and OSL are applied in combination, coherent ages can serve as an internal check on the accuracy of the results, since different types of traps (TL, OSL) and luminescence centers (e.g. blue or red TL and UV-OSL) are sampled (Westaway & Prescott 2012). However, a drawback of OSL applied to silex is that only part of the investigated samples yield the stable OSL component or OSL at all, and that the OSL sensitivity (at least in the UV) is mostly substantially lower than the blue or red TL sensitivity. This would require a thorough check of every sample for signal composition in advance of D_e measurements. Therefore, OSL may serve as a further validation of TL ages for important samples, but will probably not replace TL as the standard technique for silex dating. Since this paper investigated the blue-stimulated UV-OSL only, future work might address other stimulation energies and detection bands. For instance, the use of green stimulation light is expected to reduce the constant, anti-Stokes shifted signal contribution (Huntley 2006) and thus to enhance the signal-to-noise ratio. Moreover, based on the observation of much brighter blue TL than UV-TL of silex, it might be suspected that green stimulation and blue detection of OSL can increase the number of samples with adequate signal output. Application of the SAR protocol on further archeological samples will help to further assess the potential of OSL for dating silex tools.

5.9 Conclusions

This study investigated OSL signal composition of silex by means of LM-OSL measurements and deconvolution and addressed the thermal stability of individual components using different methods. Our experimental results allow drawing the following conclusions:

1. LM-OSL curves of silex samples were best fitted to five components in most cases, similar to those of quartz, but differing slightly in bleaching characteristics.

2. Only the "*fast*-like" component is thermally stable enough for dating applications. This was deduced from LM-OSL and short-shine pulse annealing measurements as well as the varying heating rate method, which all gave consistent results for trap parameters E and s, and thus the thermal lifetime. All other components show comparatively low thermal stability.

3. The low thermal stability of the poorly bleachable components in silex indicates differing structures of energy bands and trapping states, compared to macrocrystalline quartz.

4. Successful dose recovery tests suggest the general applicability of the OSL-SAR protocol on silex samples showing a "*fast*-like" component.

5. The agreement of TL and OSL ages obtained for two Middle Paleolithic samples confirms our experimental findings on the stability of the "*fast*-like" component.

6. Since UV-OSL and red or blue TL make use of different types of traps and centers, congruent ages may serve as an internal check for the validity of the data.

Acknowledgments

We would like to thank Thomas Kolb (University of Bayreuth) for providing the quartz LM-OSL data as well as Dr. Norbert Mercier and an anonymous reviewer for critical and helpful comments. This work was developed in the framework of the Collaborative Research Center 806 ("Our Way to Europe – Culture-Environment Interaction and Human Mobility in the Late Quaternary") and financed by the Deutsche Forschungsgemeinschaft (DFG).

References

Bailey, R., Smith, B. W., Rhodes, E. J., 1997. Partial bleaching and the decay form characteristics of quartz OSL. Radiation Measurements 27, 123–136.

Bailey, R., 2000. The slow component of quartz optically stimulated luminescence. Radiation Measurements 32, 233–246.

Bailey, R., 2001. Towards a general kinetic model for optically and thermally stimulated luminescence of quartz. Radiation Measurements 33, 17–45.

Bailiff, I., Holland, N., 2000. Dating bricks of the last two millennia from Newcastle upon Tyne: a preliminary study. Radiation Measurements 32, 615–619.

Bailiff, I., 2007. Methodological developments in the luminescence dating of brick from English late-medieval and post-medieval buildings. Archaeometry 49, 827–851.

Bowman, S., Huntley, D., 1984. A new proposal for the expression of alpha efficiency in TL dating. Ancient TL 2, 6–8.

Bulur, E., 1996. An alternative technique for optically stimulated luminescence (OSL) experiment. Radiation Measurements 26, 701–709.

Choi, J. H., Duller, G. A. T., Wintle, A. G., 2006. Analysis of quartz LM-OSL curves. Ancient TL 24, 9–20.

Demtröder, W., 2005. Experimentalphysik 3. Atome, Moleküle und Festkörper. Springer, Berlin and Heidelberg.

Duller, G. A. T., 1994. A new method for the analysis of infrared stimulated luminescence data from potassium feldspars. Radiation Measurements 23, 281–285.

Duller, G. A. T., 2007. *Analyst Version 3.24*. Institute of Geography and Earth Sciences, University of Wales, Aberystwyth. United Kingdom.

Fattahi, M., Stokes, S., 2003. Dating volcanic and related sediments by luminescence methods: a review. Earth-Science Reviews 62, 229–264.

Goble, R., Rittenour, T., 2006. A linear modulation OSL study of the unstable ultrafast component in samples from Glacial Lake Hitchcock, Massachusetts, USA. Ancient TL 24, 37–46.

Haustein, M., Roewer, G., Krbetschek, M., Pernicka, E., 2003. Dating archaeometallurgical slags using thermoluminescence. Archaeometry 45, 519–530.

Huntley, D. J., 2006. Thoughts arising from "Choi, Duller and Wintle: Analysis of quartz LM-OSL curves. Ancient TL 24, 9-20 (2006)". Ancient TL 24, 69–70.

Huxtable, J., 1981. Light bleaching of archaeological flint samples: a warning. Ancient TL 16, 2–4.

Jain, M., Murray, A. S., Bøtter-Jensen, L., 2003. Characterisation of blue-light stimulated luminescence components in different quartz samples: implications for dose measurement. Radiation Measurements 37, 441–449.

Kitis, G., Pagonis, V., 2008. Computerized curve deconvolution analysis for LM-OSL. Radiation Measurements 43, 737–741.

Kreutzer, S., Schmidt, C., Fuchs, M. C., Dietze, M., Fischer, M., Fuchs, M., 2012. Introducing an R package for luminescence dating analysis. Ancient TL 30, 1–8.

Lai, Z. P., Zöller, L., Fuchs, M., Brückner, H., 2008. Alpha efficiency determination for OSL of quartz extracted from Chinese loess. Radiation Measurements 43, 767–770.

Li, S., Chen, G., 2001. Studies of thermal stability of trapped charges associated with OSL from quartz. Journal of Physics D: Applied Physics 34, 493–498.

Li, S.-H., Tso, M.-Y. W., Wong, N., 1997. Parameters of OSL traps determined with various linear heating rates. Radiation Measurements 27, 43–47.

Medianero, F., Ramos, J., Palmqvist, P., Weniger, G., Riquelme, J., Espejo, M., Cantalejo, P., Aranda, A., Pérez-Claros, J., Figueirido, B., Espigares, P., Ros-Montoya, S., Torregrosa, V., Linstädter, J., Cabello, L., Becerra, S., Ledesma, P., Mevdev, I., Castro, A., Romero, M., Martínez-Navarro, B., 2011. The karst site of Las Palomas (Guadalteba County, Málaga, Spain): A preliminary study of its Middle–Late Pleistocene archaeopaleontological record. Quaternary International 243, 127–136.

Mejdahl, V., Bøtter-Jensen, L., 1994. Luminescence dating of archaeological materials using a new technique based on single aliquot measurements. Quaternary Science Reviews 13, 551–554.

Mercier, N., 1991. Flint palaeodose determination at the onset of saturation. Nuclear Tracks and Radiation Measurements 18, 77–79.

Mercier, N., Valladas, H., Valladas, G., 1995. Flint thermoluminescence dates from the CFR laboratory at Gif: Contributions to the study of the chronology of the Middle Palaeolithic. Quaternary Science Reviews 14, 351–364.

Mercier, N., Valladas, H., Froget, L., Joron, J.-L., Vermeersch, P., Van Peer, P., Moeyersons, J., 1999. Thermoluminescence dating of a Middle Palaeolithic occupation at Sodmein Cave, Red Sea Mountains (Egypt). Journal of Archaeological Science 26, 1339–1345.

Murray, A. S., Wintle, A. G., 2000. Luminescence dating of quartz using an improved single-aliquot regenerative-dose protocol. Radiation Measurements 32, 57–73.

Murray, A. S., Wintle, A. G., 2003. The single aliquot regenerative dose protocol: potential for improvements in reliability. Radiation Measurements 37, 377–381.

Poolton, N. R. J., Bøtter-Jensen, L., Rink, W. J., 1995. An optically stimulated luminescence study of flint related to radiation dosimetry. Radiation Measurements 24, 551–555.

Preusser, F., Degering, D., Fuchs, M., Hilgers, A., Kadereit, A., Klasen, N., Krbetschek, M., Richter, D., Spencer, J., 2008. Luminescence dating: basics, methods and applications. Eiszeitalter und Gegenwart 57, 95–149.

R Development Core Team, 2012. R: a language and environment for statistical computing. R Foundation for Statistical Computing, Vienna, Austria, http://www.R-project.org/.

Richter, D., Krbetschek, M., 2006. A new thermoluminescence dating technique for heated flint. Archaeometry 48, 695–705.

Richter, D., Temming, H., 2006. Testing heated flint palaeodose protocols using dose recovery procedures. Radiation Measurements 41, 819–825.

Richter, D., 2007. Advantages and limitations of thermoluminescence dating of heated flint from Paleolithic sites. Geoarchaeology 22, 671–683.

Richter, D., Tostevin, G., Škrdla, P., Davies, W., 2009. New radiometric ages for the Early Upper Palaeolithic type locality of Brno-Bohunice (Czech Republic): comparison of OSL, IRSL, TL and ^{14}C dating results. Journal of Archaeological Science 36, 708–720.

Singarayer, J. S., Bailey, R., 2003. Further investigations of the quartz optically stimulated luminescence components using linear modulation. Radiation Measurements 37, 451–458.

Singarayer, J. S., 2002. Linearly modulated optically stimulated luminescence of sedimentary quartz: physical mechanismsand implications for dating. DPhil thesis, University of Oxford.

Smith, B. W., Rhodes, E. J., 1994. Charge movements in quartz and their relevance to optical dating. Radiation Measurements 23, 329–333.

Tribolo, C., Mercier, N., Valladas, H., 2001. Alpha sensitivity determination in quartzite using an OSL single aliquot procedure. Ancient TL 19, 47–50.

Tribolo, C., Mercier, N., Valladas, H., 2003. Attempt at using the single-aliquot regenerative-dose procedure for the determination of equivalent doses of Upper Palaeolithic burnt stones. Quaternary Science Reviews 22, 1251–1256.

Valladas, H., 1992. Thermoluminescence dating of flint. Quaternary Science Reviews 11, 1–5.

Visocekas, R., 1985. Tunnelling radiative recombination in labradorite: Its association with anomalous fading of thermoluminescence. Nuclear Tracks and Radiation Measurements 10, 521–529.

Westaway, K., Prescott, J., 2012. Investigating signal evolution: A comparison of red and UV/blue TL, and UV OSL emissions from the same quartz sample. Radiation Measurements 47, 909–915.

Wintle, A. G., Murray, A. S., 1999. Luminescence sensitivity changes in quartz. Radiation Measurements 30, 107–118.

Wintle, A. G., 2008. Fifty years of luminescence dating. Archaeometry 50, 276–312.

Zimmerman, D., 1972. Relative thermoluminescence effects of alpha and beta radiation. Radiation Effects 14, 81–92.

6 First chronometric dates (TL and OSL) for the Aurignacian open-air site of Românești-Dumbrăvița I, Romania

Christoph Schmidt[a], Valéry Sitlivy[b], Mircea Anghelinu[c], Victor Chabai[d], Holger Kels[e], Thorsten Uthmeier[f], Thomas Hauck[b], Ion Bălteanu[g], Alexandra Hilgers[a], Jürgen Richter[b], Ulrich Radtke[h]

[a] Institute for Geography, University of Cologne, Otto-Fischer-Str. 4, 50674 Köln, Germany
[b] Institute of Prehistoric Archaeology, University of Cologne, Weyertal 125, 50923 Köln, Germany
[c] Department of History and Letters, Faculty of Humanities, Valahia University of Târgovişte, Str. Lt. Stancu Ion, 34-35, 130115 Târgovişte, Romania
[d] Crimean Branch of the Institute of Archeology, National Ukrainian Academy of Sciences (NUAS) Yaltinskaya street, 2, 95007 Simferopol, Ukraine
[e] Department of Geography, Physical Geography & Geoecology, RWTH Aachen University, Templergraben 55, 52056 Aachen, Germany
[f] Institute of Prehistoric Archaeology, University of Erlangen, Kochstraße 4/18, 91054 Erlangen, Germany
[g] Heritage Advice S.R.L., Str. Nicolae Titulescu, 1, 280/B/63, 510096 Alba Iulia, Romania
[h] University of Duisburg-Essen, Rectorate, Universitätsstr. 1, 45117 Essen, Germany

Journal of Archaeological Science, accepted for publication

Abstract

Currently, absolute dates for the emergence of the Early Upper Palaeolithic and the timing of the earliest dispersal of anatomically modern humans (AMH) into Europe are sparse. This is especially true for regions adjoining the Eastern Mediterranean and Central Europe with its dense clusters of sites along the Austrian and German Danube Valley. This article makes a first step towards filling this gap and, for the first time, presents absolute ages for the open-air site of Românești-Dumbrăvița I (Banat, SW Romania) located close to the Oase Cave where some of the oldest AMH fossils were found. A set of heated artefacts

recently excavated from the Aurignacian layer GH3 was dated by thermoluminescence (TL) and gives early chronometric dates for this technocomplex in Romania.

The luminescence behavior of artefact samples required the use of different multiple- and single-aliquot measurement protocols to obtain reliable age information. In addition, analyses of glow curves and the performance during regenerative-dose measurements allowed us to distinguish two types of samples. Since one group is characterized by poor dose reproducibility, only samples showing reliable luminescence behavior were considered for final age interpretations. As a result, we could determine that the last heating of artefacts from GH3 happened most likely between ~ 39 (single-aliquot age estimate) and ~ 45 ka ago (multiple-aliquot age estimate), with a weighted average age of the GH3 finds of 40.6 ± 1.5 ka (including all data). These dates were confirmed by OSL dating of sediments of the find layer. Such an early age fits well to technological and typological features, which place the dated lithic assemblage at the very beginning of the development of the Aurignacian technocomplex usually seen as a proxy for the earliest wide spread presence of AMH in Europe.

6.1 Introduction

The origin of anatomically modern humans (AMH) in Africa and their dispersal to Eurasia is one of the key topics in prehistoric archeology. The human fossil record now permits the reconstruction of a dispersal of this species from the region of origin in Northeast Africa, where AMH is recorded as early as 200 ka (see McBrearty & Brooks (2000) for an overview), via the Near East into Eurasia. In this scenario, Europe was peopled considerably late, but – according to latest investigations into paleoanthropology and the radiocarbon chronology at Grotta di Cavallo (Benazzi et al. 2011) and Kent's Cavern (Higham et al. 2011) – at a fast pace, but see Banks et al. (2013) and White & Pettitt (2012) for different views on the matter. It is still an open question whether the speed of the earliest peopling of Europe by modern humans, as it is indicated by the fossil record, is best explained by preferred corridors of dispersal (like the Danube Valley: Conard (2002); Conard & Bolus (2003)), or a spatially wide frontier within a "wave of advance"-model (Eswaran 2002). In both models, the Balkans play a crucial role both in the exact dating of the first dispersal of AMH out of Africa into Europe and in the elucidation of possible migratory routes.

It is widely agreed that the Aurignacian and its temporal-spatial variant, the Proto-aurignacian (Bon 2006; Teyssandier 2007), are among the earliest industries securely produced by AMH, see Bailey et al. (2009), or for the case of the Ulluzian Benazzi et al. (2011). These industries are dominated by the full range of Upper Paleolithic features such as standardized microlithic implements, personal ornament and parietal art, as well as large scale land use patterns and social networks. As the earliest chronometric dates for the European Aurignacian (of 36.5 ka uncalBP: Zilhão (2011); or even slightly earlier: Conard (2002); Conard & Bolus (2003); Higham et al. (2012)) are contemporaneous to the oldest AMH fossils in Europe, it is this industry that enables the investigation of the earliest resilient settlement of Northwestern latitudes by members of this species.

Due to its geographical position between the Balkans and Central Europe, Romania holds a strategic position for understanding the early dispersal of AMH and for tracking the emergence of the Aurignacian phenomenon sensu lato. This potential has already been directly proved by the discovery of the oldest anatomically modern Human fossil remains in Europe at Oase Cave (Peştera cu Oase, Southern Banat) in 2002, followed by direct ^{14}C dating to $\sim$35 ka uncalBP (40.7 ka calBP) (Trinkaus et al. 2003). Proper chronological control plays a central role in linking the fossil finds of Oase Cave to the lithic industry produced by the first European AMH. However, the lack of an associated archeological context for the Oase finds, coupled with the traditional view of a long persistence of the Middle Paleolithic and the very late Upper Paleolithic chronology documented across Romania (Cârciumaru 1999; Păunescu 2000; Păunescu 2001), make the story exciting, but less clear. It has remained incomplete as a narrative since no archeological context in the area has documented, at the very least, a comparable chronology (Anghelinu et

al. 2012). Moreover, it is precisely the chronology of the Aurignacian technocomplex in Romania that appears as particularly deficient today.

According to the current state of knowledge (Anghelinu & Niţă in press), the Aurignacian in Romania is, with different degrees of certitude, to be found in several, quite distant regions: The northeastern area, particularly along the Prut river (e.g. Mitoc-Malul Galben: Otte et al. (2007)); along the Danube valley to the south (e.g. Ciuperceni, Vădastra: Păunescu (2000)); Southern Transylvania, with the open air settlements at Poieniţă and Malul Dinu Buzea and several unclear occurrences in cave contexts (Păunescu 2001; Horvath 2009); the North-Western area (Oaş and Maramureş lowlands) with the sites of Călineşti I, Călineşti II, Remetea Şomoş and Boineşti (Dobrescu 2008); and in the South-Western part of Romania (Mogoşanu 1978), with several settlements to be discussed in further details below. All other occurrences remained undated, with the exception of Mitoc-Malul Galben Aurignacian, which provided a rather late chronology (31–29 ka uncalBP).

Of all mentioned areas, the Banat Aurignacian stands apart for several reasons. Apart from their relative proximity to the Oase Cave (Fig. 6.1), the three identified settlements here – Tincova, Coşava and Românești-Dumbrăviţa (Mogoşanu 1978) – provided medium to large collections with undisputable Aurignacian features. In addition, the original excavator promptly compared the Banat occurrences with Krems-Hundssteig in Austria, a settlement itself thought to represent an early phase of the Aurignacian technocomplex, currently acknowledged as the Krems-Dufour type of Aurignacian (Kozlowski 1965; Demidenko 2000-2001; Demidenko & Otte 2007; Demidenko & Noiret 2012).

However, despite the clear similarities documented between the Banat lithic collections and the Krems-Dufour Aurignacian, the initial estimations, based on pollen diagrams and straight geochronological readings of the sedimentary archives (Mogoşanu 1978; Cârciumaru 1989; Cârciumaru 1999), pointed to a time span considerably younger than any known Eurasian Aurignacian occurrence: Herculane I/Tursac for the single layer at Tincova, and Herculane II/Laugerie for the main concentration (level III) at Românești-Dumbrăviţa. According to the Western-based geochronological framework used by Romanian archaeologists those days, slightly changed meanwhile (Bosselin & Djindjian 2002), the Herculane I/ Tursac positive oscillation was taking place around 24.5 and 26.5 ka uncalBP, while the Herculane II/ Laugerie episode was displaying a chronology between 18.5 ka and 19.7 ka uncalBP. Perhaps not surprising, based on the content of the lithic collections, several authors questioned these initial assessments in favor of older geochronological estimations, e.g. Arcy (Chirica et al. 1996) or Hengelo Interstadials (Bălţean 2011), or ignored them altogether (Teyssandier 2003; Teyssandier 2007; Teyssandier 2008; Zilhão 2006). Unfortunately, the Banat Aurignacian sites, altogether lacking organic material, have remained undated so far. It is evident that archeological and palynological arguments are insufficient for establishing a comprehensive regional chronology as the age of the same assemblages fluctuated from $\sim$37 ka uncalBP to $\sim$18 ka uncalBP.

The contradiction between the information provided by the lithic collections and the geochronological estimations based on palynology resulted in new small scale excavations at the site Româneşti-Dumbrăviţa I in 2009 and 2010, coupled with comprehensive sedimentological and tephra analyses, sampling for optically stimulated luminescence (OSL), thermoluminescence (TL) dating, and a full reassessment of the existing lithic collection. Several attempts were made to clarify both the relative and the absolute chronology of the Aurignacian find layers at this settlement. A tephra layer was identified above the main Aurignacian find layer (GH3), but a clear assignment to a known-age eruption has so far failed (D. White, pers. comm. to M. A. 2011). While clearly converging towards a chronology older than previously estimated, today both the archeological and sedimentological methods used have proved to be not sufficient enough for determining more accurately the temporal status of this industry. Fortunately, recent excavations here bore a set of heated artefacts of sufficient size for TL dating, which is capable of providing age estimates of the last – intentional or accidental – exposure to fire and thus most likely directly dates human presence. We therefore present for the first time chronometric data for the Aurignacian industry found at Româneşti-Dumbrăviţa I, obtained using multiple- as well as single-aliquot dating protocols. The implications of an early presence of this technocomplex in South-Western Romania are also briefly discussed.

6.2 The Aurignacian in Banat: reassessing the open-air site at Românești-Dumbrăvița I

6.2.1 Geographical and archeological setting

The Paleolithic open-air site of Româneşti-Dumbrăviţa I (Timiş district) is located at the confluence of the rivers Bega Mare and Bega Mica, occupying about 4 hectares (Fig. 6.1). Situated on a flat, just slightly inclined top of a local river terrace (45°49'02.41" N, 22°19'15.12" E; elevation ∼ 212 m a.s.l.), the huge settlement was established at the periphery of the Poiana Ruscă Mountains. These foothills of the Banat Mountains are situated in the Eastern part of the historical region Banat, close to the edge of the Carpathian Mountains (Kels et al. subm.). Here, a thin cover of silty and loess-like sediments was accumulated during the last glacial period, which has been only poorly studied up to now. The thickness of the loess cover continues to increase towards the Banat Lowland (Conea 1969; Conea et al. 1972).

At Româneşti-Dumbrăviţa I, our test drillings yielded the uppermost gravels of the terrace in a depth of about 2.80 m below surface, followed by 30 cm of bluish-gray, clayish and sandy sediments. Above that, the silt content rises towards the top. Grain size measurements confirm the loessic character of the covering sediments. From a first profile (Fig. 6.2) which was opened in the East of the re-excavated area (position see Fig. 6.3), the uppermost 1.25 m were documented and described (for further details see Kels et al.

(subm.)). For a general allocation and for the needs of archeological documentation during the excavation, the main obvious horizons were labeled as "geological horizons" (GH) according to field observations. All in all, four GHs were identified at Românești-Dumbrăviţa I. The geology and soil development is much more complex as detailed studies in the field and the results from the laboratory have shown. Sedimentary samples were used for different kind of analyses (e.g. grain sizes using a Laser Diffraction Particle Size Analyzer and geochemical measurements like CNS-analysis, pH-value, organic carbon, $CaCO_3$ and multi-elemental analysis using X-Ray Fluorescence (XRF)).

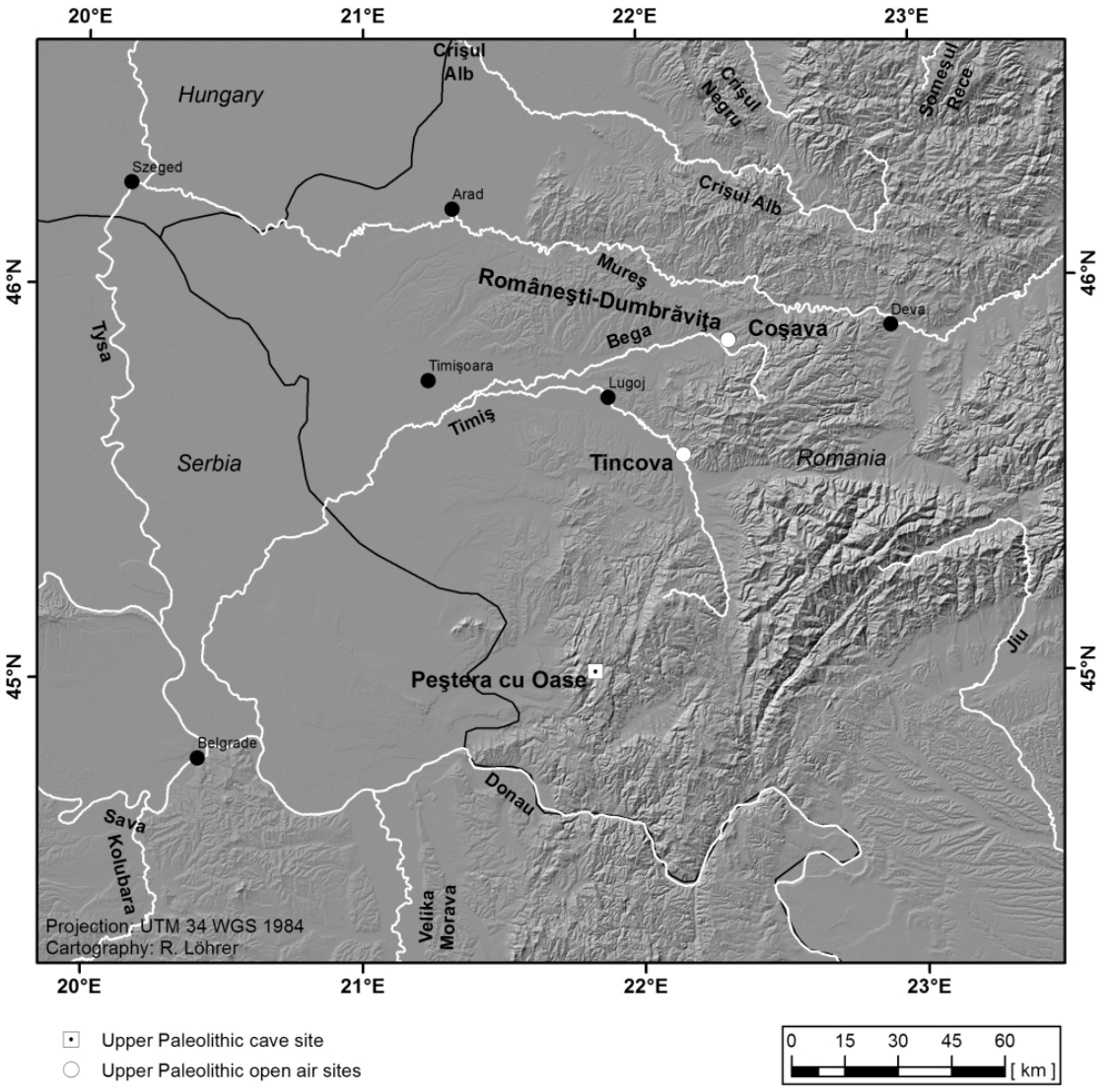

Figure 6.1: Map of SW Romania, showing the Banat region and adjacent countries. The Aurignacian sites of Românești-Dumbrăviţa and Coşava are plotted using the same symbol since they are only 5 km from each other.

Main results show that, although the surface soil is a type of Stagnic Albeluvisol as it is mapped as a typical soil on flat relief positions like at the Românești-Dumbrăviţa I site or

depressions (Ianoş 2002; Liteanu & Ghenea 1966; Mavrocordat 1971), the surface soil depicts a polygenetic development. Element measurements constrained a weathering zone and a leached horizon connected to the highest artefact density of GH3. Former weak fossil soil horizons which are not obvious in the field have been overprinted by the weathering zone and the intense development of the surface soil. The successive building up of the sediment cover, burying the archeological levels, reflects cyclic history: Grain size distribution showed several sedimentary units; the presence of several fossil root channels in different levels is connected to former paleosurfaces which seem to be eroded by fine discordances. The changes in sedimentation are seen as a result of thin aeolian delivery of loess, partially reworked by changes in precipitation and former events of surface run-off.

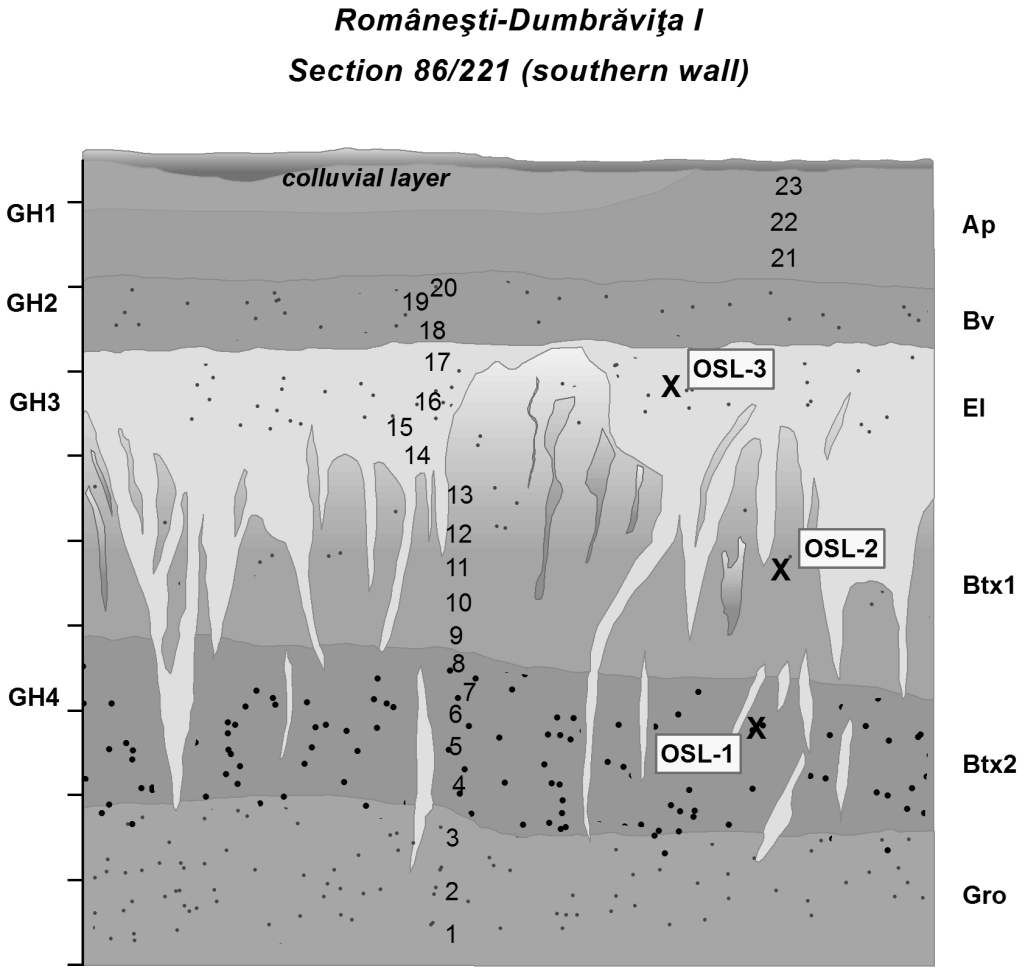

Figure 6.2: Main section 86/221S (positioning in the archeological trench is marked in Fig. 6.3) with numbers of samples for sedimentology and geochemistry (numbers 1-23, see Kels et al. (subm.)), including soil horizons according to FAO. Fine dots = iron patches and concretions, bigger dots = iron-manganese patches and concretions. GH1-4 = "geological horizons" (cmp. levels of artefacts, 10 cm spacing of y-axis ticks), luminescence samples: OSL-1 = Rom-86-222-1 (54.6 ± 6.4 ka), OSL-2 = Rom-86-221-2 (39.3 ± 4.6 ka), OSL-3 = Rom-86-221-3 (26.4 ± 3.0 ka).

F. Mogoşanu excavated the Româneşti-Dumbrăviţa I settlement in two stages (1960–1964 and 1967–1972), opening a large area of about 450 m^2 and identifying 6 archeological

levels in a strict vertical subdivision (Mogoşanu 1972; Mogoşanu 1978; Mogoşanu 1983); see also Chirica et al. (1996), Păunescu (2001), Bălțean (2011). According to him, the Aurignacian (levels II, III, IV and V) was sandwiched between "Quartzitic Mousterian" and Gravettian levels. Level III provided a rich Aurignacian industry of more than 5000 artefacts, including 114 tools (end-scrapers, including carinated ones, predominate over burins, associated with eight Dufour bladelets and some retouched blades, comprising some typical Aurignacian forms). Level IV was documented on an excavated area of $20\,m^2$ and differed from the previous one by the presence of truncated blades/flakes and a decrease in the frequency of end-scrapers, with a corresponding increase in burins. Level V consisted of extended but clustered work-shops with an industry rich in knapping waste and only 38 tools, dominated by burins and with less common Aurignacian pieces.

The new excavations (Sitlivy et al. 2012; Sitlivy et al. in press), while small-scaled ($7\,m^2$), partially changed the original picture of the settlement. They provided 7505 artefacts, including 19 cores and 169 tools, originating from different altitudes of GH3 (Fig. 6.3). The high crop of finds is attributed to wet sieving of the digging, which was not applied by Mogoşanu. Horizontally, the lithic material was dispersed equally across the entire excavated area. The Aurignacian assemblage appears indeed sandwiched between isolated uncharacteristic quartz artefacts (Middle/Early Upper Paleolithic?), namely with lowermost level I at the bottom (GH 4) and the Gravettian level VI at the top (GH 1 and 2). The Aurignacian-looking inventory occurs rarely in the upper part of GH4 and continuously throughout whole GH3, without sterile but with variable vertical artefact density, suggesting repeated occupations and/or palimpsest. Lithic attributes do not show any significant technological changes across the excavated succession. In addition, the presence of many chips along with large items, as well as the vertical and horizontal distribution of finds, and the technological refitting and conjoining of broken artefacts confirm that there was little geological or hydrological sorting of the material. Burnt artefacts are common, forming several clusters, one of which delivered 38 burnt lithics, including 8 samples for TL dating. The assemblage from GH3 differs dramatically from Mogoşanu's record due to the dominance of bladelets/microblades (with often straight lateral profile obtained from prismatic, narrow-faced and few carinated cores) and tools produced on these small blanks ($\sim 50\,\%$ of the tool-kit), especially alternatively retouched Dufours (Fig. 6.4). Detailed information on the lithic assemblage and its features is given in Sitlivy et al. (2012).

The technological data gathered from both old and new assemblages (for details, see Sitlivy et al. (2012)) reflect a common trend, i.e. prevalent laminar/lamellar and occasional flake production. Blade, bladelet and micro-blade production exhibits three dissociated systems based on reduction of (a) prismatic, (b) narrow-faced cores (including burin-like) and (c) carinated pieces (cores and tools). The continuity displayed by all these reduction systems is confirmed by the blade/let scars on the working surfaces of prismatic, narrow-faced and carinated cores (i.e., mixed blade/bladelet, bladelet/micro-blade). The desired laminar blanks include mid-sized blades, quite long and narrow bladelets and tiny

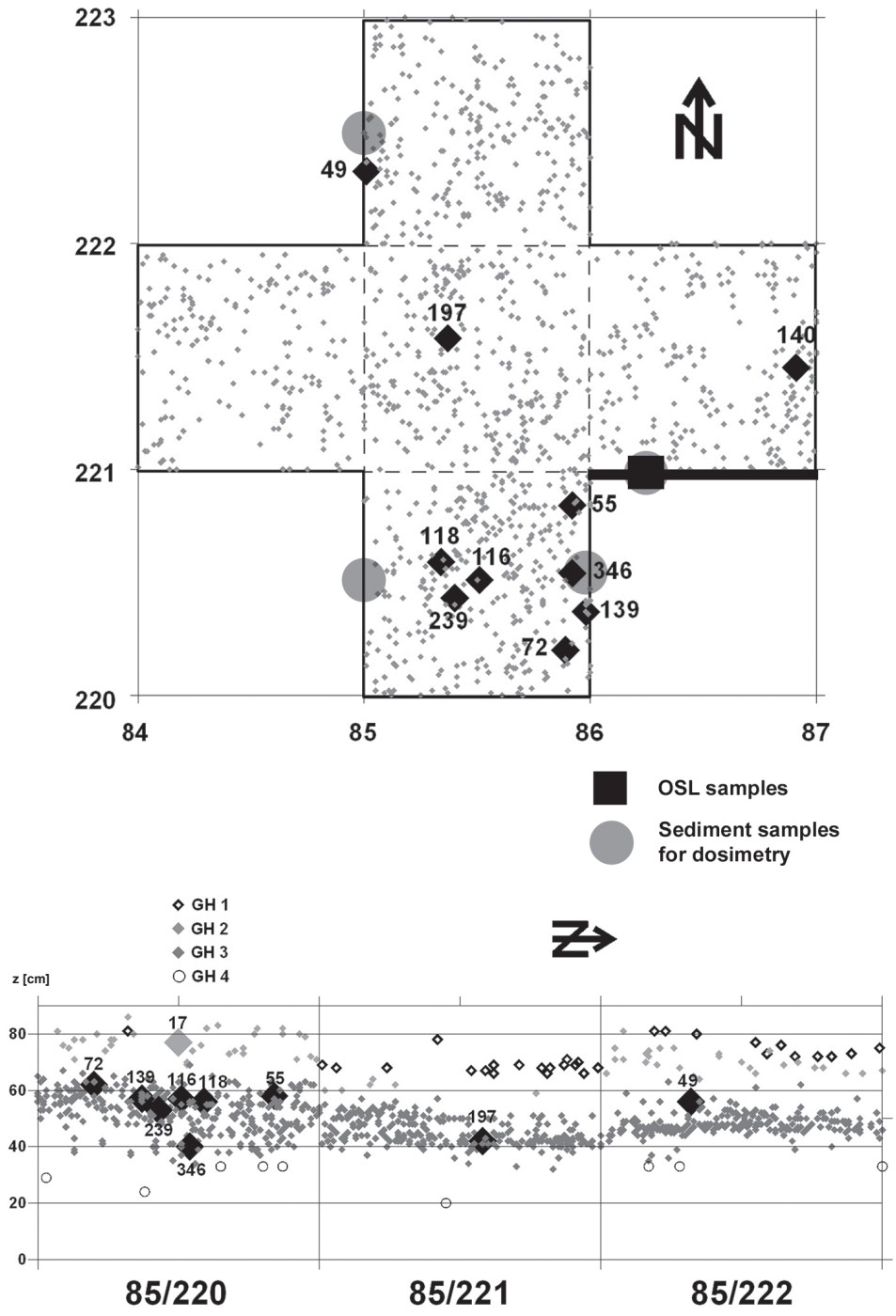

Figure 6.3: Horizontal (upper chart) and vertical (lower chart) view of the excavated square meters in Româneşti-Dumbrăviţa I, showing the location of all lithic finds (grey dots), the dated artefacts (black diamonds) and the sampling position of material for γ-spectrometry of GH3 (upper plot, big grey circles). The thick black line marks the location of the stratigraphic profile shown in Fig. 6.2. The placing of OSL samples is indicated by the black square (for detailed position of OSL samples, see Fig. 6.2). Sample Rom140 (not plotted in the lower figure) is located at a depth of $z = 46$; sample Rom35 originates from a test pit around 15 m from the excavation, but can doubtlessly be attributed to GH3.

micro-blades with straight/curved/twisted profiles. Debitage symmetry (on-axis) of laminar blanks is a dominant feature. As indicated by lipping, bulb patterns and the invisibility of impact points mostly direct percussion using soft stone and organic tools was applied to the laminar production.

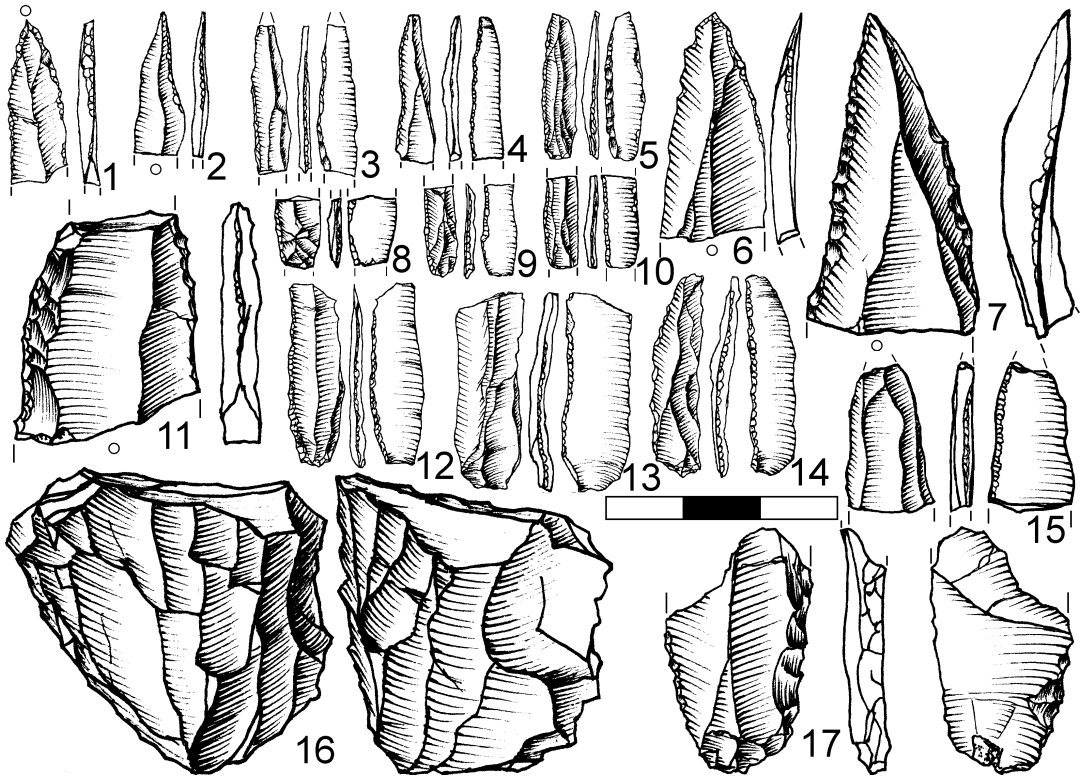

Figure 6.4: Selection of lithic finds at Românești-Dumbrăviţa I, GH3: 1 – Font-Yves point, on bilaterally retouched bladelet; 2 – Font-Yves point, on laterally retouched micro-blade; 3 – Krems point, on alternatively retouched micro-blade; 4, 5, 8–10, 14 – Dufour, on alternatively retouched micro-blades; 6, 7 – pointed blades, obversely retouched; 11, 17 – Aurignacian blades; 12 – Dufour, on alternatively retouched bladelet; 13, 15 – Dufour, on inversely retouched bladelet; 16 – carinated core, unidirectional, sub-pyramidal. Scale: 1 bar equals 1 cm.

The general observations are in line with a rather "archaic/early" Aurignacian character of the corresponding archeological layers. Nevertheless, compared to the old assemblages, the assemblage composition of "micro/macro" artefacts/tools varies considerably for various reasons (e.g. different excavated surfaces and recovering methods, diverse artefact clustering). Based on the commonly adopted approaches for the definition of Aurignacian variability (Zilhão 2006; Teyssandier 2008; Teyssandier et al. 2010; Banks et al. 2013) Românești-Dumbrăviţa I, GH 3 might be evaluated as a Protoaurignacian industry, although several features argue for an Early Aurignacian as well (see discussion below). Moreover, bearing in mind that the "archaic" features alone cannot support a precise chronological scenario, the "early" technological and typological characteristics should be supported by a dating record and multidisciplinary studies.

6.2.2 The lithic material

The majority (∼85–95 %) of the artefacts excavated at Românești-Dumbrăviţa I and all dated samples in this study consist of so-called "Banat flint", the source of which is not yet identified but which may be considered to be of local or meso-local origin (Sitlivy et al. 2012). Raw material is mostly waxy, ochre-colored or brownish and slightly translucent. While no detailed petrographic study was undertaken, microscope analyses indicate that this type of rock is a mixture of chalcedony and amorphous opal. The density of Banat flint is $2.5 \pm 0.1\,\mathrm{g\,cm^{-3}}$ with slight variations between single samples, owing possibly to the different proportions of opal and chalcedony. Heating experiments showed a change in color from ochre or brown to dark red and opaque at temperatures of about 400–450 °C. This color alteration is most probably related to the oxidation of Fe(II) to Fe(III), although the temperatures required for oxidation are higher than those reported by Purdy & Brooks (1971) and Richter (1995). In combination with other signs of heat alteration (e.g. potlids, craquelation), the color can thus serve as a straight indicator of past heat exposure sufficient for TL dating.

6.3 Thermoluminescence dating of heated artefacts

Thermoluminescence is an important means of dating heated lithics of archeological sequences. Here, the event to be dated is the last exposure to fire, and this event is closely connected to the actual occupation of the site by prehistoric humans. The heating of artefacts is usually related to its discard, and spatial constraint of fire impact favors the presence of human fire places, in contrast to the vast nature of wood or grassland fire (Richter et al. 2009). The basic principle of TL dating is time-dependent storage of energy within the molecular structure of siliceous samples. Radioactive elements, mainly U, Th and K, in embedding sediments and within the sample itself deliver this energy via ionizing radiation, due to their radioactive decay. With ongoing irradiation, the stored energy (or dose when normalized to unit mass) increases with time, and is a measure of the time elapsed since the last resetting event, provided that the delivered energy per unit time (the dose rate $\dot{D}$) is known. Times of zero stored energy may be the formation of the mineral or events that reset all previously accumulated energy such as heating above ∼400 °C (Richter et al. 2007). Part of the released energy is emitted as light that can be measured in the laboratory while the sample is heated, giving the thermoluminescence. For each sample, the recorded amount of light is then compared to the light emitted after administering known doses of ionizing radiation and this then permits the determination of an equivalent dose (D_e), i.e. a laboratory dose that produces the same light output as the archeological dose. The age is then obtained by dividing D_e by $\dot{D}$. More information about TL dating in general and the measurement protocols used to determine D_e is given elsewhere (Aitken 1985b; Valladas 1992; Mercier et al. 1995; Richter et al. 2007).

From the excavations in 2009 and 2010, two artefacts from layer GH2 and eleven artefacts from layer GH3 were chosen showing macroscopic signs of heat alteration such as potlids or dark red color (see Section 6.2.2). One sample from GH2 could not be dated due to poor luminescence characteristics (high data scatter, no reproducibility), and one sample from GH3 was obviously not sufficiently heated. Owing to the small size of some artefacts and hence scarcity of sample material, application of the conventionally used multiple-aliquot additive-dose (MAAD) technique was not possible in all cases. Therefore, additional measurement protocols, such as the single-aliquot regenerative-dose (SAR) and the single-aliquot regeneration and added dose (SARA) procedure, were tested for their reliability and applied to the samples.

6.3.1 Preparation and measurement parameters of TL samples

From all samples, the outer rim of at least 2 mm was cut away with a water-cooled diamond saw in dimmed redlight conditions, in order to remove material that was influenced by β- and γ-radiation from surrounding sediment and that was subjected to optical bleaching and potential geochemical alteration (Mercier et al. 1995). The inner cores were then gently crushed in a steel mortar with frequent sieving in between to obtain grain sizes of 100–200 µm. For determination of α-efficiency, finely ground material of $\sim$4–11 µm was extracted by settling in acetone, following mainly Zimmerman (1972). Chemical sample preparation consisted of treatment with 10 % HCl for carbonate destruction. For TL measurements, coarse grains were deposited onto stainless steel discs (9.8 mm in diameter) using silicone oil spray. In case of large aliquots, a monolayer of grains covered the central 8 mm (diameter) of the disc, for small aliquots the central 2 mm. Fine grains were placed as an α-thin layer onto aluminum discs.

All TL measurements were performed on Risø TL/OSL DA-15 and TL/OSL DA-20 readers, equipped with EMI 9235QB photomultiplier tubes, in N_2 atmosphere and using either a UV-blue filter package (BG-39 + GG-400 + Corning 7-59 + Chance Pilkington HA-3), a blue-transmitting Semrock BrightLine HC 475/50 interference filter (FWHM of 50 nm), or a Chroma D630-60 for test of red TL emissions (FWHM of 60 nm). The transmission maximum is around 410 nm for the UV-blue combination with a FWHM of $\sim$60 nm, but asymmetrically shaped towards higher wavelengths. Samples were β-irradiated in the Risø readers with ^{90}Sr/^{90}Y-sources delivering dose rates between 0.10 and 0.11 Gy s^{-1}. Alpha-irradiation was performed in vacuum (10^{-2} mbar) in a Littlemore irradiation facility equipped with ^{241}Am foils (5.32 mCi). During TL measurement, the samples were heated to 450 °C with 2 °C s^{-1}; the background was recorded afterwards and subtracted for each measurement. Equal pre-dose second glow measurements of a fixed test dose (to ensure identical dose history of all aliquots) served for normalization of individual aliquots for multiple aliquot procedures (Galloway & Hong 1996).

6.3.2 Measurement protocols used for TL dating

6.3.2.1 Multiple-aliquot additive-dose technique (MAAD)

The "standard" protocol for heated silex is the MAAD procedure (Aitken 1985b; Mercier et al. 1995) in which initially an additive growth curve is constructed with 4–5 dose points (first growth curve). Depending on the amount of available sample material, 3–5 aliquots contributed to each dose point in this study. A second, regenerative growth curve, created after annealing part of the sample material at 350 °C for 90 minutes (Mercier et al. 1995), allows the determination of the growth curve shape for small doses, which is not displayed by the first growth curve (correction for supralinearity). Extrapolation of the first growth curve to the dose axis and addition of the supralinearity correction give the equivalent dose (D_e). Examples of D_e determination using the MAAD protocol for two TL samples are shown in Fig. A.21 and A.22.

6.3.2.2 Single-aliquot regenerative-dose technique (SAR)

For the first time, Richter & Krbetschek (2006) applied the SAR protocol successfully to heated silex using the red TL emission. Tests with the D630-60 filter revealed for all samples a complete absence of red TL in this transmission window. However, TL signals in the range 450–475 nm were detected, which in quartz probably arise from $[AlO_4]^0$ hole centers (McKeever 1991; Rink et al. 1993). This emission was tested for its suitability for producing reliable age estimates using a SAR protocol. To this end, dose recovery tests were performed on a series of samples that were previously annealed to check if a given laboratory dose in the range of the expected D_e can be correctly reproduced. Additionally, a fading test served to make sure that athermal signal loss is not a problem for this emission. The final measurement procedure included five regenerative dose steps (L_x) enclosing the natural dose point (L_n), a recycling and a zero dose point, according to the general structure given in Murray & Wintle (2000) for OSL measurements. Corrections for sensitivity changes were made by interrupting the regeneration dose steps by measurement of a fixed test dose (T_x). Determination of D_e was then based on the normalized growth curve (L_x/T_x). Especially for dim samples, relatively high test doses (in the range of the lowest regeneration dose or higher) were necessary to avoid increased data scatter due to counting statistics. Preheating to 220 °C for 60 s emptied shallow traps prior to measurement of the thermally stable signal and yielded regenerated glow curve shapes most similar to natural glow curves. The sample was not allowed to cool down after preheating ("stage and continue") (Zöller & Blanchard 2009). Rejection criteria were identical to those usually applied in OSL dating of sediments, i.e. all aliquots showing a recycling ratio between 0.9 and 1.1 passed. Recuperation is not expected to occur in TL dating, as is proved by growth curves typically passing through the origin. With exception of sample Rom17, at least ten aliquots per sample, and in cases of bright samples, two different aliquot sizes (8 and 2 mm) were measured.

6.3.2.3 Single-aliquot regeneration and added dose technique (SARA)

As a backup and to be sure of adequate allowance of potential sensitivity changes occurring during natural and regenerative TL readout, the SARA protocol according to Mejdahl & Bøtter-Jensen (1994) was additionally applied to two samples. Here, equivalent doses of natural aliquots (N) and of aliquots that received different additive laboratory β-doses ($N + \beta$) are determined by a SAR protocol, but without test dose monitoring. These apparent doses are then plotted against the known added doses and extrapolation of the fit to the dose axis gives the "true" D_e at the intercept. Application of this routine provides that the $N + \beta$ signals are not beyond the saturation dose level and that sensitivity changes are dose-independent and equal for all measured aliquots (Mejdahl & Bøtter-Jensen 1994; Lai et al. 2006).

6.3.2.4 Alpha-efficiency determination using the SAR protocol

Silex often contains non-negligible amounts of Th and U and therefore α-radiation contributes to the total dose rate. The reduced efficiency in luminescence production of α-radiation compared to β- or γ-radiation thus necessitates the determination of the a-value (Aitken 1985a). Furthermore, it is known that the α-efficiency can vary from sample to sample, between different temperature regions of the TL glow curve, and also between various TL emissions (Zimmerman 1972; Mercier et al. 1995; Richter & Krbetschek 2006; Polymeris et al. 2011). For these reasons, the a-value was determined for each sample and recorded emission (UV-blue and blue) separately and, where two peaks were analyzed, individually for these two plateau regions as well. In practice, annealed fine grain material (450 °C for 60 minutes) was given a laboratory α-dose which was treated as unknown and recovered using a SAR protocol with β-regeneration doses (as outlined above), the ratio of recovered β-dose to known α-dose being the a-value (Tribolo et al. 2001; Mauz et al. 2006; Polymeris et al. 2011). The stopping power of the dated material was assumed to be identical to that of quartz for the ~ 3.7 MeV α-particles used for irradiation so that the a-value was set equal to the k-value in this study (Aitken 1985a; Lai et al. 2008). For valid application of the described procedure, two further requirements must be met: Both α- and β-dose response are in the linear range, and the sensitivity changes associated with the readout of the α-induced signal can be adequately corrected by a β-test dose.

6.4 Optically stimulated luminescence dating of sediments

In addition to direct dating of the use of artefacts by TL, sediment samples for OSL dating were taken from the find layer itself ($z \sim 45$–50) and from layers below ($z \sim 25$–30) and above ($z \sim 65$–70). The location of the sampled profile within the excavated area is shown in Fig. 6.3. OSL ages represent the time when sampled grains were covered and shaded

by overlaying grains, i.e. the time of sedimentation. Hence, while not as directly related to the site's occupation as TL dates, this method provides the depositional age of the find layer with a resolution of a few centimeters. From the loessic sediments, only the quartz fine grain fraction (4–11 µm) was prepared and used for measurements.

6.4.1 Preparation and measurement parameters

Samples for OSL dating were extracted from sediment blocks taken from the profiles. In dimmed red light conditions in the laboratory the outer surface was carefully removed to discard any material exposed to daylight after sample collection. After sieving ($< 40\,\mu m$), sample material was treated with HCl (10 %) and H_2O_2 (10 %) to destroy carbonates and organic material. Etching in H_2SiF_6 (34 %) for 7 days, followed by washing in HCl (10 %), served to eliminate any feldspar components in the sample. Fine grains were obtained after settling in acetone to isolate grains in the range 4–11 µm (Zimmerman 1972) which were deposited onto aluminum discs. For age evaluation, attenuation factors of radiation within grains according to Mejdahl (1979) and Bell (1980) were used.

6.4.2 Measurement protocol used for OSL dating

For OSL measurements, the standard SAR protocol after Murray & Wintle (2000) was used, including the common rejection criteria (recuperation $> 5\,\%$, recycling ratio outside 0.9–1.1). Preheat plateau tests yielded a temperature region of 220–260 °C with identical dose estimates (see Fig. A.28for a representative example). For the SAR sequence, a preheat of 240 °C for 10 s was thus chosen. Measurement equipment was identical to that described in Section 6.3.1, except for a 7.5 mm Hoya U340 glass filter used for OSL detection. Optical stimulation was carried out by blue LEDs ($470\,\Delta\,30\,nm$), delivering $\sim 36\,mW\,cm^{-2}$ at sample position. For final age calculation, an a-value of 0.035 ± 0.020 was used, implying a comparatively large error margin to account for dose dependencies of α-efficiency in case of β-saturation (Mauz et al. 2006).

6.5 Dose rate determination

For external dose rate determination of TL and OSL samples, low level γ-spectrometry was applied to finely ground sediment samples taken from three to four different depths (z-values of 40, 55, 70 and 77 at the center of the sampled volume) and four different positions (exposed walls) within the excavation (Fig. 6.3) and a nearby geo-profile to assess the variability of U, Th and K concentrations with depth and lateral extension. Taking into account the ~ 30 cm sphere of influence of γ-radiation and the homogeneity of the deposits, sediment samples comprised at least 1400 g and were collected from various positions within this sphere. These samples are considered as being representative for the entirety of material contributing to the artefacts' environmental dose rate. For each dated

artefact, the sediment sample taken most closely to the find spot was used for external dose rate calculation, resulting in a maximum distance between both of ∼90 cm, except for sample Rom35. This artefact originates from a test pit (also GH3) and the closest sediment sample available was ∼2.5 m away. Therefore, dose rate assessment for this sample is potentially less accurate than for other samples; however, we found no indication in field records and laboratory data pointing to this sample having received a significantly different environmental dose rate (see also analytical results, Section 6.6.1). Attenuation of external γ-radiation within the samples was considered according to Valladas (1985). For every OSL sample, surrounding material was collected individually and from the direct vicinity within the γ-range. Gamma-spectrometry allowed measuring K, U and Th concentrations and provides a check for present radioactive disequilibria via calculated parent and daughter activities of decay chains. The cosmic dose rate was evaluated according to Prescott & Hutton (1988). Owing to limited accessibility of the excavation, it was not possible to carry out *in-situ* measurements of environmental dose rate. ICP-MS analyses of material from the inner core of the artefacts (∼0.5 g) were carried out to calculate the internal dose rate from determined K, U and Th concentrations using the conversion factors given in Adamiec & Aitken (1998).

6.6 Dating results

6.6.1 Dosimetry results

The loess-like deposits of the Româneşti-Dumbrăviţa site are free from coarse components such as gravels or blocks and organic material. Results of γ-spectrometry prove that there is no variability (within $1\,\sigma$ measurement uncertainty) in radionuclide concentrations between the five analyzed sediment samples relevant for GH3 (Fig. 6.3 and Table 6.2). Separate analyses of three fractions (∼350 g) of the same sediment samples yielded indistinguishable radioelement concentrations and thus further confirm the radiometric homogeneity of the deposits. We can hence rule out substantial heterogeneities of the external radiation field applicable for the TL samples. Equal activities of the members of the U series, as measured by γ-spectrometry, indicate the absence of recent radioactive disequilibrium. The time-averaged moisture content of the period being dated was estimated to 20 ± 5 %, based on soil genesis of the site (see Section 6.2.1) and the range of determined moisture contents of collected sediment samples, plus an increased uncertainty level to account for past moisture fluctuations. Since the majority of the total dose rate for the TL samples originates from the surrounding soil, its water content has significant influence on TL ages because water absorbs part of the environmental radiation that would otherwise has reached the sample. The same applies to OSL samples. A precise reconstruction of the past (mean) moisture content is impossible, but absolute maximum and minimum age estimates can be obtained by considering the saturation water content and 0 % water content in the calculations. Accordingly, the ages are enhanced by ∼10 %

and reduced by ∼15 %, respectively, depending slightly on individual sample properties. However, both scenarios are unlikely. Employment of more likely water contents of 15 % and 25 % as lower and upper limits results in statistically indistinguishable age estimates. Hence, the uncertainty of ±5 % in the assumed water content of 20 % is taken to be the best approach to account for this unknown quantity (see also the discussion in Richter et al. (2008)).

Concentrations of internal K, U and Th of the artefacts fluctuate by a factor of 3–4 between samples, but account for overall low internal dose rates compared to external dose rates (12–23 % internal/total dose rate, see Table 6.3). Due to the small size of most artefacts and the minor contribution of internal γ-radiation, its attenuation within the sample was seen as negligible (assumption of infinite matrix dose rate). Detailed information on determined external and internal concentrations of radioactive elements as well as the deduced dose rates is given in Table 6.2.

6.6.2 Thermoluminescence behavior of samples

The luminescence signal of Banat flint samples is generally characterized by rather low count rates, although varying between samples. According to the glow curve shape and the number of peaks (recorded in the blue transmission window), we could assign every sample to one of two sample types. Specimens of type 1 yield 3–4 observable, quite narrow peaks, but probably contain additional peaks that would only be separable by glow curve deconvolution. Visible peaks are centered at ∼90–110 °C, ∼150–180 °C, ∼270–300 °C and ∼370–390 °C, using a heating rate of 2 °C s^{-1}, whereas the peak at 150–180 °C sometimes appears as a declining shoulder towards higher temperatures. In contrast, type 2 samples show considerably weaker light output and up to 3 visually distinguishable peaks. They occur at ∼90–110 °C, ∼130 °C and ∼300–320 °C. The shift of the maximum of the 300–320 °C peak towards lower temperatures with increasing dose and its general width indicates either non-first order kinetics or the presence of a composite peak containing components with different dose response. Examples of both sample types are shown in Fig. 6.5. The fact that the glow curve pattern varies significantly between type 1 and type 2 suggests different mineralogical composition, possibly also reflecting different raw material sources. Indeed, there appears to be a correlation between the glow curve shape and the visual nature of the samples, namely the presence or absence of dark-colored veins and inclusions and/or pale mineral inclusions. Accordingly, type 1 samples seem to be of purer composition than type 2 samples, although this is not evident in all cases (see also Fig. A.24).

The difference in glow curves of the two sample types is in line with characteristic dose response behavior, indicated by the saturation dose D_0 in case the dose response follows a single saturating exponential (Aitken 1998; Bøtter-Jensen et al. 2003). For type 1 samples, we determined D_0 values of $>$150–200 Gy and about 30–100 Gy for the 270–

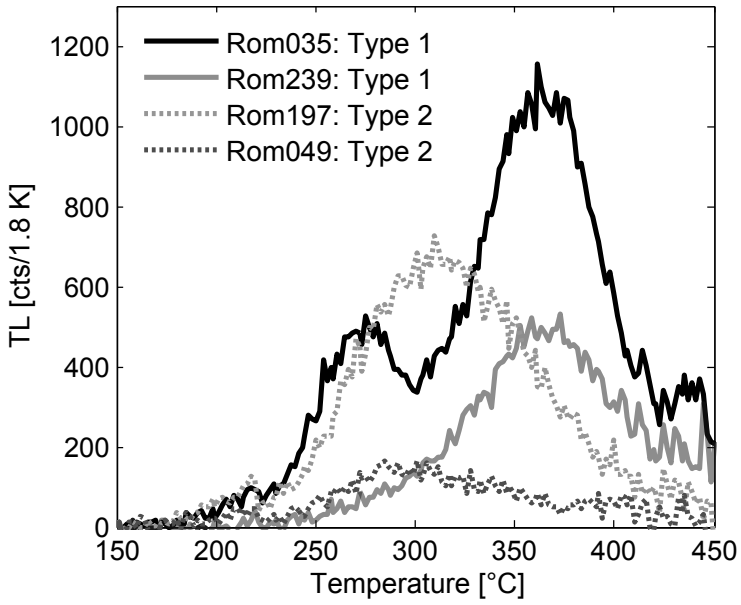

Figure 6.5: Characteristic TL glow curves of sample types 1 and 2, recorded in the blue transmission window.

300 °C and the 370–390 °C peak, respectively. Considerably higher saturation doses were observed for the broad 300–320 °C peak of type 2, lying always above 200–300 Gy and leading to approximately linear dose response in the range covered by additive and regenerative measurements. The condition of D_e being $< 2D_0$ for reliable dose estimation using the SAR sequence was fulfilled for all samples (Wintle & Murray 2006). Moreover, changes in luminescence sensitivity during repeated cycles of irradiation and TL measurements (monitored by a test dose) remained generally < 20 % after 9 successions for sample type 1, while it amounted to up to 350 % for sample type 2 (see also Figs. A.25, A.26 and A.27). Especially for the latter samples severe sensitivity changes were recorded in the first one or two cycles.

6.6.3 TL dose recovery tests

Table 6.1 shows the results of the SAR dose recovery tests of six silex samples. Two peaks in the thermally stable range of sample Rom35 were investigated separately. Except for sample Rom197 (type 2, ~ 20 % underestimation) and the high temperature peak of Rom35 (type 1, ~ 17 % underestimation), the given dose was recovered within an acceptable limit of 8 %, though there appears to be a general and slight tendency for dose underestimation. Given the restricted number of samples subjected to the dose recovery test (due to sample scarcity), at this stage no clear trend emerged whether type 1 or type 2 samples yield more reliable dose estimates. However, it seems plausible to base the assessment of the validity of obtained dates on the dose recovery results of the respective samples.

Table 6.1: Results of the dose recovery test (DRT) of TL samples. Measurement details are given in Sections 6.3.1 and 6.3.2.

Sample	Type	n(accepted)/ n(total)	Temperature region [°C]	Given dose [Gy]	Recovered dose[a] [Gy]	Ratio given/ recovered dose
Rom35	1	4/5	270–310	70	71.8 ± 2.8	0.97
Rom35	1	5/5	340–400	70	59.7 ± 1.9	1.17
Rom55a	2	6/7	320–380	70	65.4 ± 1.9	1.07
Rom72	1	9/10	350–400	60	59.5 ± 1.1	1.01
Rom140	2	10/10	230–280	60	58.2 ± 1.1	1.03
Rom197	2	5/5	230–280	70	57.8 ± 1.3	1.21
Rom239	1	10/10	340–400	60	55.8 ± 1.0	1.08

[a] error-weighted average

6.6.4 TL ages

All relevant data for age calculation are summarized in Tables 6.2 and 6.3. While Table 6.2 contains β- and γ-radiation-related information, Table 6.3 splits the obtained ages into applied measurement protocols and TL emissions entailing a detailed report on the respective a-values and α-dose rates.

Low saturation doses (Rom239) and sparse sample material (Rom116, Rom346) prohibited the use of the MAAD protocol for every sample. One sample (Rom55) was big enough for two parts to be analyzed independently to check the reliability of the measurement procedures and to test for internal inhomogeneities. The temperature region used for signal integration was selected based on heating plateau tests and $D_e(T)$-plateaux, for which examples are given in the Supplement.

The resulting ages for the only sample from GH2 agree well for MAAD and SAR protocols (16.1 ± 1.5 and 15.2 ± 1.3 ka), thus proving an Epi-Gravettian age to the corresponding lithic industry, initially attributed to the Gravettian technocomplex on typological grounds. Artefacts from GH3 give MAAD ages ranging from ∼42 to 48 ka (type 1), with overlapping $1\,\sigma$ uncertainties, while SAR type 1 dates (8 mm) encompass ages between ∼38 and 53 ka. By contrast, MAAD and SAR type 2 ages are substantially higher, covering the range ∼53–116 ka and 54–63 ka, respectively (detailed information on type 2 samples and their ages is given in the Supplement). The validity of this dataset and its reduction towards reliable age estimates is discussed in detail in Section 6.7.1.

6.6.5 OSL ages

Preheat plateau tests for the three quartz fine grain samples gave identical results for preheats in the range 220–260 °C (see Supplement). The homogeneity of the data set allowed us to use the Common Age Model (Galbraith et al. 1999), resulting in ages of 54.6 ± 6.4 ka for the lowermost sample, 39.3 ± 4.6 ka for the find layer and 26.4 ± 3.0 ka for the uppermost sample. Detailed dose and dose rate data are given in Table 6.4.

Table 6.2: Element concentrations of artefact samples and surrounding sediment samples as well as calculated dose rates. All values are given with their $1\,\sigma$ uncertainty.

		Depth	Internal element concentration (artefacts)			Sediment element concentration			Internal dose rate [Gy ka^{-1}]	External dose rate [Gy ka^{-1}][a]
Sample	Level	(z-value)	U [µg g^{-1}]	Th [µg g^{-1}]	K [wt.%]	U [µg g^{-1}]	Th [µg g^{-1}]	K [wt.%]	$\beta + \gamma$	γ + cosmic
Rom17	GH2	77	0.31 ± 0.01	0.31 ± 0.02	0.07 ± 0.01	3.28 ± 0.17	11.89 ± 0.68	1.15 ± 0.05	0.112 ± 0.004	1.171 ± 0.056
Rom35	GH3	–	1.14 ± 0.04	0.39 ± 0.02	0.12 ± 0.01	3.50 ± 0.15	14.39 ± 0.75	1.28 ± 0.04	0.277 ± 0.010	1.276 ± 0.061
Rom49	GH3	56	0.49 ± 0.02	0.22 ± 0.01	0.05 ± 0.01	3.29 ± 0.21	14.00 ± 0.90	1.28 ± 0.07	0.119 ± 0.008	1.263 ± 0.065
Rom55a	GH3	58	0.44 ± 0.01	0.28 ± 0.01	0.05 ± 0.01	3.79 ± 0.25	14.19 ± 0.90	1.27 ± 0.07	0.113 ± 0.003	1.224 ± 0.067
Rom55b	GH3	58	0.46 ± 0.01	0.59 ± 0.03	0.08 ± 0.01	3.79 ± 0.25	14.19 ± 0.90	1.27 ± 0.07	0.153 ± 0.004	1.224 ± 0.067
Rom72	GH3	62	0.72 ± 0.02	0.25 ± 0.01	0.05 ± 0.01	3.57 ± 0.23	13.08 ± 0.91	1.26 ± 0.07	0.159 ± 0.004	1.242 ± 0.065
Rom116	GH3	57	0.32 ± 0.01	0.25 ± 0.01	0.10 ± 0.01	3.57 ± 0.23	13.08 ± 0.91	1.26 ± 0.07	0.133 ± 0.004	1.255 ± 0.065
Rom118	GH3	56	0.55 ± 0.02	0.54 ± 0.03	0.17 ± 0.01	3.57 ± 0.23	13.08 ± 0.91	1.26 ± 0.07	0.235 ± 0.008	1.242 ± 0.065
Rom140	GH3	46	0.88 ± 0.03	0.13 ± 0.01	0.01 ± 0.01	3.79 ± 0.25	14.19 ± 0.90	1.27 ± 0.07	0.145 ± 0.004	1.319 ± 0.068
Rom197	GH3	42	0.97 ± 0.03	0.28 ± 0.02	0.09 ± 0.01	3.29 ± 0.21	14.00 ± 0.90	1.28 ± 0.07	0.224 ± 0.006	1.237 ± 0.065
Rom239	GH3	53	0.46 ± 0.01	0.14 ± 0.01	0.04 ± 0.01	3.57 ± 0.23	13.08 ± 0.91	1.26 ± 0.07	0.102 ± 0.008	1.203 ± 0.065
Rom346	GH3	40	0.57 ± 0.02	0.29 ± 0.01	0.08 ± 0.01	3.79 ± 0.25	14.19 ± 0.90	1.27 ± 0.07	0.157 ± 0.008	1.319 ± 0.068

[a] A water content of $20 \pm 5\,\%$ (water weight over dry soil) was assumed for all samples and a cosmic dose rate of 0.213 ± 0.021 Gy ka^{-1} for GH2 and 0.207 ± 0.021 Gy ka^{-1} for GH3.
External dose rates were additionally corrected for γ-attenuation as a function of sample mass and shape according to Valladas (1985).

6.7 Discussion

6.7.1 TL ages

Although Banat flint is no "common" flint in the narrow sense (as e.g. Baltic flint), rigorous tests of investigated type 1 samples showed their satisfactory behavior as dosimeters. Glow curve shapes of type 1 samples largely equal those from flint samples, a fading test as well as heating- and $D_e(T)$-plateau tests proved the absence of anomalous or thermal erosion over time of the signal used for dating, and dose recovery tests confirmed the reproducibility of a given dose for most samples.

Since the SARA protocol monitors sensitivity changes using a different approach than the SAR protocol, the good agreement between both ages for type 1 samples (Rom35 low temperature peak and Rom72) confirms accurate correction of sensitivity changes. The fact that the SARA age of the high temperature signal of sample Rom35 exceeds the SAR age cannot be explained at present time. In general, type 2 SAR ages are systematically higher than those of sample type 1; the probable reasons are severe and partly unsystematic sensitivity changes observed for type 2, notably during the first TL measurements (i.e. in the course of the measurement of the natural signal) which are obviously not correctable by test dose monitoring. Finally, early onset of dose saturation and thus the need for non-linear extrapolation to obtain MAAD D_e's may have contributed to a reduced level of accuracy of multiple-aliquot dates.

For the TL samples investigated in this study, the influence of systematic errors on age related to internal dose rate characteristics is attenuated by the dominance of the external dose rate (77–88 % of total dose rate). Notwithstanding, potential effects of significant α-radiation contribution as well as of non-uniform internal dose rate have to be considered when estimating the validity of the obtained ages of each sample.

Alpha contribution to the total dose rate leads to a more linear dose response because of the high ionization density of α-radiation (Aitken 1984; Aitken 1985b; Mauz et al. 2006). Reproduction of exact natural irradiation conditions (a mixture of α-, β- and γ-radiation) is impossible in the laboratory. Therefore, if a significant α-dose rate contributes to the total dose rate, the β-induced laboratory growth curve will saturate at much lower doses than does the natural, with the final consequence of age overestimation (Aitken 1984). The effective α-contribution to the total dose rate varies between 3 and 10 % for the samples dated in this study (data not shown). We could detect neither a relationship between linear or exponentially saturating dose response (both for MAAD and SAR protocols) and D_e nor a general connection between α-dose rate and D_e, or it is masked by overall D_e scatter. Consequently, this factor is unlikely to have any significant influence on the obtained ages.

To further investigate the dose distribution within the samples and the performance of regenerative measurements, determined D_e's for each aliquot were plotted against sensitivity corrected natural signals L_n/T_n of the SAR measurements (Fig. 6.6; see Li (2001)

Table 6.3: Detailed age results of type 1 TL samples. Multiple ages of each sample are split into different measurement protocols and aliquot sizes. No D_e could be obtained for Rom 239 (early onset of saturation).

Sample	Level	Protocol[a]	Emission[b]	Temperature interval [°C]	a-value[c]	$\dot{D}_{\alpha,\mathrm{eff}}$ [Gy ka^{-1}]	$\dot{D}_{\mathrm{total}}$ [Gy ka^{-1}]	$\dot{D}_{\mathrm{int}}/\dot{D}_{\mathrm{total}}$ [%]	n[d]	D_e [Gy]	Age [ka]	Average age [ka]
Rom17	GH2	MAAD	UV-blue	270–380	0.078 ± 0.020	0.085 ± 0.022	1.368 ± 0.061	15	–	22.0 ± 2.0	16.1 ± 1.5	15.6 ± 1.4
		SAR	blue	300–350	0.078 ± 0.020[e]	0.085 ± 0.022	1.368 ± 0.061	15	2	20.8 ± 1.6	15.2 ± 1.3	
Rom35	GH3	MAAD	UV-blue	230–250	0.029 ± 0.003	0.100 ± 0.011	1.653 ± 0.061	23	–	78.8 ± 5.5	47.7 ± 3.6	44.1 ± 3.3
		MAAD	UV-blue	300–375	0.029 ± 0.003	0.100 ± 0.011	1.653 ± 0.061	23	–	75.4 ± 1.8	45.6 ± 1.9	
		SAR	blue	270–310	0.022 ± 0.007	0.076 ± 0.024	1.629 ± 0.066	22	9	68.9 ± 4.7	42.3 ± 3.2	
		SAR	blue	340–400	0.022 ± 0.007	0.076 ± 0.024	1.629 ± 0.066	22	7	61.7 ± 5.7	37.9 ± 3.7	
		SAR 2mm	blue	340–400	0.022 ± 0.007	0.076 ± 0.024	1.629 ± 0.066	22	13	58.7 ± 7.3	36.0 ± 4.5	
		SARA	blue	270–310	0.022 ± 0.007	0.076 ± 0.024	1.629 ± 0.066	22	10	72.2 ± 3.7	44.3 ± 2.8	
		SARA	blue	340–400	0.022 ± 0.007	0.076 ± 0.024	1.629 ± 0.066	22	10	80.6 ± 2.5	49.5 ± 2.4	
Rom72	GH3	MAAD	UV-blue	325–410	0.057 ± 0.008	0.117 ± 0.018	1.518 ± 0.068	19	–	63.3 ± 3.8	41.7 ± 3.0	39.7 ± 3.3
		SAR	blue	350–400	0.066 ± 0.022	0.144 ± 0.048	1.545 ± 0.082	20	8	63.4 ± 4.7	41.0 ± 3.6	
		SAR 2mm	blue	350–400	0.066 ± 0.022	0.144 ± 0.048	1.545 ± 0.082	20	8	55.3 ± 4.4	35.8 ± 3.3	
		SARA	blue	350–400	0.066 ± 0.022	0.144 ± 0.048	1.545 ± 0.082	20	10	62.2 ± 4.0	40.3 ± 3.2	
Rom116	GH3	SAR	blue	350–410	0.037 ± 0.005	0.040 ± 0.005	1.428 ± 0.066	12	8	53.7 ± 4.0	37.6 ± 3.2	37.6 ± 3.6
		SAR 2mm	blue	350–410	0.037 ± 0.005	0.040 ± 0.005	1.428 ± 0.066	12	7	53.9 ± 5.3	37.7 ± 4.0	
Rom239	GH3	MAAD	UV-blue	350–400	0.052 ± 0.023	0.072 ± 0.032	1.377 ± 0.073	13	–	–	–	39.2 ± 3.2
		SAR	blue	340–400	0.092 ± 0.033	0.127 ± 0.046	1.432 ± 0.080	16	7	56.2 ± 3.9	39.2 ± 3.2	
Rom346	GH3	SAR	blue	250–300	0.044 ± 0.004	0.079 ± 0.008	1.555 ± 0.069	15	9	83.2 ± 4.6	53.5 ± 3.7[f]	42.3 ± 3.5
		SAR	blue	340–390	0.068 ± 0.028	0.122 ± 0.050	1.598 ± 0.085	18	9	66.8 ± 4.6	41.8 ± 3.5	
		SAR 2mm	blue	250–300	0.044 ± 0.004	0.079 ± 0.008	1.555 ± 0.069	15	7	66.4 ± 4.5	42.7 ± 3.4	
											Weighted average (GH3)	**40.6 ± 1.5**

[a] Unless indicated otherwise, all measurements refer to 8 mm aliquots.
[b] Emission windows correspond to the filter combinations described Section 6.3.1.
[c] The given uncertainty is the standard deviation of single measurements.
[d] Number of accepted aliquots for SAR and SARA procedures, according to the rejection criteria defined in Section 6.3.2.2.
[e] The a-value could be determined for the 410 nm emission only and is therefore used also for the SAR measurements.
[f] Age excluded according to Dixon's outlier test (Rorabacher 1991).

Table 6.4: Analytical data and ages of fine grain OSL samples. n denotes the number of accepted aliquots per sample. The moisture content was estimated to be $20 \pm 5\,\%$ over burial period, ages were calculated using the Common Age model (Galbraith et al. 1999), and an a-value of 0.035 ± 0.020 was applied for age calculation (see main text for further details).

Sample	n	K [%]	Th [µg g^{-1}]	U [µg g^{-1}]	D_e [Gy]
Rom-86-221-1	9	1.20 ± 0.07	14.20 ± 0.91	3.60 ± 0.23	179.1 ± 9.5
Rom-86-221-2	6	1.27 ± 0.07	14.19 ± 0.90	3.79 ± 0.25	133.4 ± 7.2
Rom-86-221-3	9	1.36 ± 0.08	13.96 ± 0.88	3.85 ± 0.25	92.0 ± 4.8

Sample	$\dot{D}_{\alpha,\mathrm{eff}}$ [Gy ka^{-1}]	$\dot{D}_{\beta}$ [Gy ka^{-1}]	$\dot{D}_{\mathrm{total}}$ [Gy ka^{-1}]	Age [ka]
Rom-86-221-1	0.506 ± 0.292	1.460 ± 0.089	3.281 ± 0.344	54.6 ± 6.4
Rom-86-221-2	0.519 ± 0.300	1.525 ± 0.092	3.398 ± 0.354	39.3 ± 4.6
Rom-86-221-3	0.519 ± 0.300	1.583 ± 0.097	3.485 ± 0.356	26.4 ± 3.0

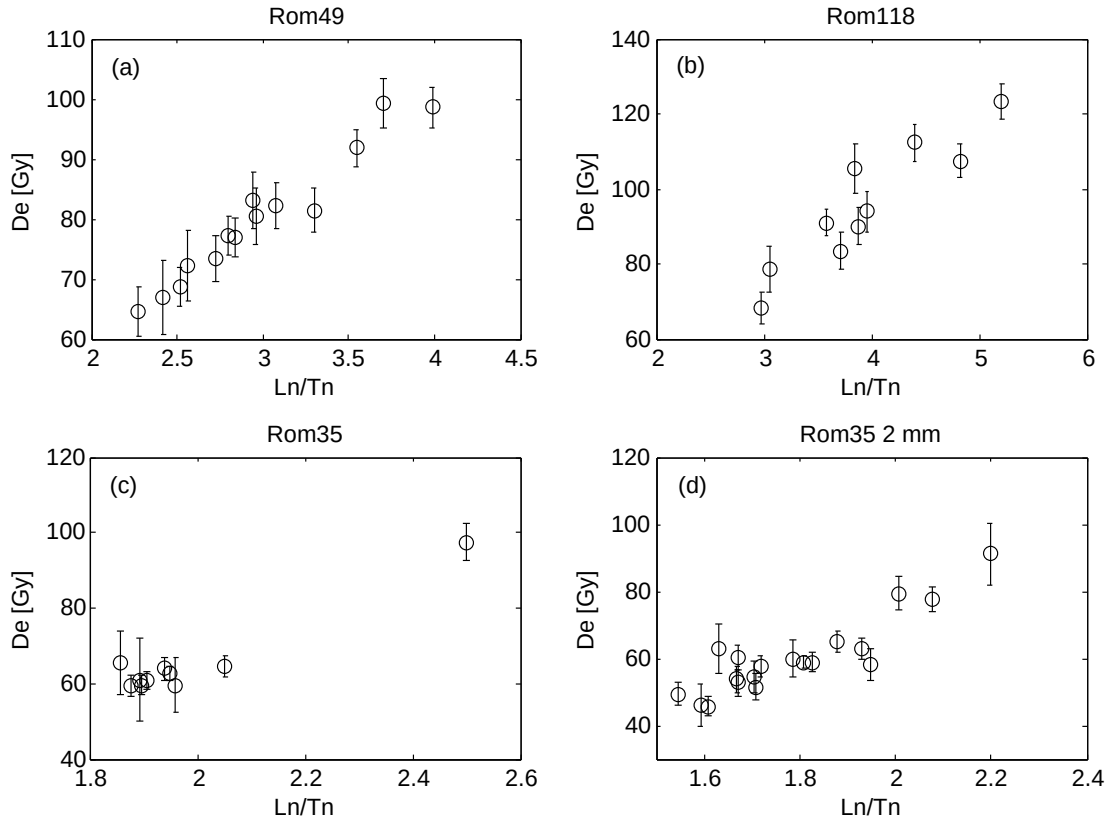

Figure 6.6: Plots of D_e versus L_n/T_n for three samples. The graphs show the obtained SAR D_e's of each aliquot against the sensitivity corrected natural TL signals (L_n/T_n). Samples of type 2 (Rom49, Rom118) yield large spreads of D_e's and L_n/T_n's (a, b), whereas a more narrow D_e distribution and L_n/T_n range is characteristic for sample type 1 (here Rom35; c, d). For further information, see main text.

for an example of application to OSL data). Here, low scatter of L_n/T_n's in line with a narrow D_e distribution stands for sample homogeneity and accurate SAR performance. In contrast, both large dispersion of D_e's and L_n/T_n's indicate either non-uniform dose distribution within the sample, poor sensitivity correction in the course of the SAR sequence or a combination of these factors (while a spread of L_n/T_n is reflected in a corresponding spread of D_e's, i.e. a certain relation between both is expected).

Fig. 6.5 shows the respective plots for three samples, including 8 mm and 2 mm data for Rom35. The D_e spread and interrelation of the depicted quantities correlate with the categorization of the samples in types 1 and 2. Type 1 samples (two distinct TL peaks in the high temperature region) show a significantly more clustered D_e distribution with one or two outliers at maximum, whereas for type 2 samples the D_e values are spread more continuously and the range of L_n/T_n is about three times larger than for type 1. Previous investigations suggest that samples from Românești-Dumbrăviţa I may be affected by zones with elevated radioelement content (hot spots/zones) (Schmidt et al. 2012; Schmidt et al. 2013). Working with both bulk dose and bulk dose rate values would thus introduce systematic errors in age determination which are hardly to quantify, as discussed in detail in the cited papers. In particular, the direct proportionality of dose and dose rate cannot be maintained, as, for instance, the α-efficiency in hot spots may vary with increasing dose so that the here determined a-value must not be applied. For final D_e calculation, outliers according to Dixon's outlier test (Rorabacher 1991), such as the highest D_e of Rom35 in Fig.6.6 (lower left), were hence discarded because they are most likely influenced by dose rate peaks. Since the measured bulk dose rate is, however, influenced by spatially constrained zones with high radioelement content (to a hardly quantifiable degree), the actual dose rate experienced by grains far away from hot spots/zones (i.e., those thought to contribute to the remaining D_e distribution) is certainly lower than the measured one. Therefore, SAR ages presented here should be regarded as minimum ages. This was seen as the best way to handle the specificities of the TL samples.

For final age calculation and archeological interpretation, we selected only dates of samples that exhibit proper luminescence behavior and thus proved to act as reliable dosimeter. Therefore, samples of type 2 were rejected. The remaining data set (MAAD and SAR ages of type 1 samples) showed one outlier (low temperature age of Rom346) according to Dixon's outlier test (Rorabacher 1991). Application of the Shapiro-Wilkins-test ($\alpha = 0.05$) confirmed the origin of individual dates from normally distributed data and thus allowed calculating the weighted average of MAAD and SAR ages.

The reduced data set including only type 1 samples gives weighted average ages of 45.0 ± 1.5 ka ($n = 3$) for MAAD measurements, 40.0 ± 1.4 ka (8 mm, $n = 6$) for SAR measurements and 45.1 ± 1.6 ka for the SARA protocol ($n = 3$). These dates partly contain ages from two peaks of the same glow curves in case a $D_e(T)$-plateau was observed for both peak ranges. Except for sample Rom72, SAR ages obtained for small aliquots (2 mm) agree within uncertainty with those of large aliquots, although the average age based on

2 mm data only is slightly younger (38.2 ± 1.9 ka, $n = 4$). Considering both large and small aliquots gives a SAR weighted average age of type 1 samples of 39.3 ± 1.1 ka, which is statistically not discriminable from the date of large aliquots only. Furthermore, as indicated above, SAR ages must be considered as minimum ages, because the bulk dose rate might be overestimated due to the likely presence of radiation hot spots rich in radioelements. This implies that the true age of the last heating of the artefacts most probably lies in between the SAR and MAAD dates. Taking all type 1 dates together results in a weighted average age of GH3 of 40.6 ± 1.5 ka.

The vertical spread from which artefacts from GH3 were excavated covers a range of ~ 25 cm. This would imply either a succession of several find layers representing repeated occupation over thousands of years or reworking and/or dislocation of lithics after the initial abandonment. The latter hypothesis is supported by the fact that artefacts from different finding depths could be refitted and the general typological uniformity of the collection of GH3 which impedes its further division into meaningful archeological layers. In terms of the key question of this paper – the dating of the last fire exposure of heated artefacts and hence the time of occupation – the issue of post-depositional reworking is of secondary importance as far as the external dose rate has not changed significantly through time. Indeed, the measurements of the environmental radionuclide concentrations at different burial depths (Section 6.6.1) indicate that this was not the case.

6.7.2 OSL ages

Obtained OSL ages are stratigraphically consistent. While D_e's could be determined with comparatively high precision – what is typical for fine grain samples –, the major sources of uncertainty lie in the moisture content that cannot be estimated more precisely than 20 ± 5 % (Balescu et al. 2003; Timar-Gabor et al. 2011) and the error range used for α-efficiency.

The fine grain OSL age below the find layer of 54.6 ± 6.4 ka fits well to obtained TL ages and provides an upper age limit for them. This gives further confidence for excluding type 2 TL samples from which many yield dates older than the OSL age from below GH3. The OSL age determined for the find layer (39.3 ± 4.6 ka, Rom-86-221-2) is in good agreement with the TL SAR ages obtained for heated lithics of type 1, coincides with MAAD TL ages (within $1\,\sigma$ uncertainty) and thus with the average age of GH3 of 40.6 ± 1.5 ka. Given the well-founded assumption that optical dates represent the last daylight exposure, the OSL age determined for the find layer provides a lower age limit for the heating event of the artefacts. Furthermore, this date proves that conditions of environmental irradiation did not change significantly through time, e.g. by surface re-exposure of artefacts. In this respect, perfect coincidence is achieved between the strict TL minimum age (39 ka, SAR protocol, including 2 mm aliquots) and the OSL age for GH3. Furthermore, agreement in OSL ages and TL SAR ages in particular places confidence in the reliable performance of the TL SAR measurement protocol which is not yet routinely applied in silex dating.

Thus, both TL of heated lithics and OSL of sediments supply a coherent chronometric placement for the Aurignacian assemblage at Româneşti-Dumbrăviţa I. For further OSL ages of this site and their sedimentological interpretation, see Kels et al. (subm.).

6.7.3 Archeological and paleoanthropological implications

As mentioned above, the Banat Aurignacian from Tincova, Coşava and Româneşti-Dumbrăviţa has constantly been a subject of typological comparisons, evoking a number of similarities on a European scale (Mogoşanu 1972; Mogoşanu 1983; Kozlowski & Kozlowski 1975; Hahn 1977; Chirica et al. 1996; Bălţean 2011; Demidenko & Noiret 2012). The general typological structure of these inventories suggested a direct connection to the Central and Eastern European Krems type Aurignacian (with a single conventional date of the eponymous site of ~ 35 ka uncalBP or 40.7 ka calBP), including Siuren I, Units H and G (Demidenko et al. 1998; Demidenko & Otte 2007; Demidenko et al. 2012) and Beregovo I (Usik 2008).

In the last decade, the single layered settlement at Tincova was seen as particularly expressive for joining the Protoaurignacian phenomenon, on the basis of the dominance of continuous blade core reduction sequences, which resulted in blades and then elongated bladelets with a straight profile, modified into Krems points and Dufour sub-type bladelets. The Protoaurignacian assignation of Tincova was reinforced by the alleged rarity of carinated scrapers and typical Aurignacian retouch (Teyssandier 2003; Zilhão 2006; Teyssandier et al. 2010; Tsanova et al. 2012). Partially due to the selective publishing and illustration in previous works, the Româneşti-Dumbrăviţa and Coşava collections were generally ignored. However, if one holds on strictly to the same techno-typological perspective, the newly excavated cluster in GH3 at Româneşti-Dumbrăviţa I represents a better candidature for an association with this technocomplex.

In fact, the newly recovered industry from GH3 at Româneşti-Dumbrăviţa I displays more "archaic" features than Tincova or other Banat assemblages, quite visible, for instance, in the core structure (only two carinated nuclei), the higher frequency of bladelet rectilinear profiles and especially in the abundance of Dufour sub-type bladelets with alternate retouch placement. Aurignacian blades and retouch are also rare. Thus, Româneşti-Dumbrăviţa I GH3 clearly documents a bladelet/micro-blade (rather than blade) production that matches Protoaurignacian better. The new TL data (average age of GH3 of $45.6 \sim 1.6$ ka) presented here strengthen this attribution, fitting in the acknowledged chronological range of the Protoaurignacian/Early Aurignacian across Europe in calibrated radiocarbon terms (Zilhão 2006; Higham et al. 2011; Higham et al. 2012).

Notwithstanding, as noticed throughout our studies, the Banat assemblages, especially Româneşti-Dumbrăviţa I, also feature a combination of Proto- and Early Aurignacian traits (Sitlivy et al. in press; Sitlivy et al. 2012). This trend was recently observed in different regions of Europe, e.g. in perspective of the "mixed" look of the lithic assemblage C 4c4 at Isturitz, sandwiched between Proto- and Early Aurignacian industries

and dated to 37,180 ± 420 a uncalBP (Normand & Turq 2005; Szmidt et al. 2010), or dissociated bladelet production system in Fumane, layers A2, A3 (Broglio et al. 2005) with new radiocarbon ages of ∼ 35.5 ka unclBP or 41.8 and 40.8 ka calBP (Higham et al. 2009; Higham et al. 2011). Further uncommon associations, such as split-base points and Protoaurignacian lithics, were also reported (Szmidt et al. 2010). In addition, new radiocarbon ages of some key sites in South-eastern and Central Europe evidence not only a greater antiquity than previously thought, but also show that quasi-contemporaneous industries may be quite different. For example, at Franchthi Cave, the lithic assemblages with the CI tephra (corroborated by new ages of 35 ka uncalBP or 39–40 ka calBP) appear totally "non-Protoaurignacian" and fully Early Aurignacian/Aurignacian 1 (Douka et al. 2011). Recent researches at Willendorf II/layer 3 evidence the early Aurignacian and dated to around 38–39 ka uncalBP, evoking the early Aurignacian technology of Southern Germany (e.g. Geissenklösterle, AH III) and Aurignacian I in France, (Nigst 2006; Nigst & Haesaerts 2012). These finds, much like the newly obtained chronology of the Early Aurignacian at Geissenklösterle (Higham et al. 2012), seriously threaten the clear cut techno-typological and chronological distinction between the Proto- and the Early Aurignacian (Mellars 2006).

Inner functional variability and/or a currently underreported Aurignacian stylistic manifestation might be equally responsible for the mixed technological features we also noticed in Banat. To current knowledge, it is premature to postulate an intermediary unit, whatever the label used. It is worth noticing, however, that this phenomenon currently displays a comparably vast and early dispersal across Europe, partially matching both the Protoaurignacian and the Early Aurignacian. Moreover, its chronological range appears statistically indistinguishable from them as well.

6.8 Conclusions

Although the dated lithics provided some methodical challenges, we could show that a multiprotocol approach allowed the determination of the firing time of some of the burnt artefacts from GH3 at Româneşti-Dumbrăviţa I. Owing to early onset of dose saturation and scarce sample material of some specimens, multiple-aliquot protocols failed in numerous cases, and single-aliquot procedures were tested for their accuracy. Adequate sensitivity correction throughout the measurement sequence is crucial here and, according to the degree of successful correction, we could divide the samples into two groups. Using further dosimetric considerations and analysis of D_e-L_n/T_n-plots, we were able to distinguish valid TL ages from those ages likely influenced by systematic errors. The dated samples were most likely heated between 39.3 ± 1.1 ka (weighted average of SAR type 1 ages which represents the minimum age) and 45.0 ± 1.5 ka ago (weighted average of MAAD type 1 ages, practically identical to SARA type 1 ages). Consideration of all type 1 ages gives an average age of GH3 of 40.6 ± 1.5 ka. This could be confirmed by quartz OSL fine grain ages of the find layer (GH3).

The unexpectedly old individual dates of ∼39–45 ka for the Aurignacian industry at Românești-Dumbrăviţa I GH3 highlight the complexity and industrial variability of this technocomplex in its initial phases. However, the recent comprehensive observations made on the lithic collections show the vulnerability of the narrow archeological definitions of the Proto-/Early Aurignacian, leaving their application open to debate. Although still based on work in progress, the large series of common features linking Românești-Dumbrăviţa I, Coşava and Tincova strongly suggest that the latter observation holds for the entire Banat record. Further refining the chronological and taxonomic status of these industries would prove crucial for the key scenarios related to the Aurignacian penetration towards Western Europe. To current knowledge, however, on both geographical and chronological grounds, the Banat settlements seem to occupy an intermediate position between the Balkans – e.g. Kozarnika, ∼39 ka uncalBP (Sirakov et al. 2007; Tsanova et al. 2012) – and some Central/Eastern European (e.g. Willendorf II, layer 3, Krems-Hundssteig, Beregovo I) comparable occurrences (Protoaurignacian/Early Aurignacian).

At the same time, the recently documented chronology fits well to the wide-scaled Eurasian scenario of AMH dispersal. More or less explicitly, given their geographical proximity, the Protoaurignacian at Tincova was seen as the likely cultural proxy for the Oase AMH finds (Zilhão 2006; Bălțean 2011). It is now obvious that Românești-Dumbrăviţa I, statistically overlapping the chronology of the Oase fossils (∼35 ka uncalBP and 40.7 ka calBP) may claim a similar status. At minimum, the early timing for this fully Upper Paleolithic industry, lacking any connection to the local Middle Paleolithic, reinforces the impression of allogeny for the Aurignacian technological package in this European area.

Acknowledgments

We thank Dr. Sebastian Kreutzer and Manfred Fischer at the University of Bayreuth for kindly performing α-irradiation. This work was financed by the Deutsche Forschungsgemeinschaft (DFG) within the framework of the CRC 806 “Our Way To Europe. Culture-Environment Interaction and Human Mobility in the Late Quaternary”. Dating of artefacts was conducted by the Institute of Geography at the University of Cologne in frames of project F2 “Application of Luminescence and Electron-Spin-Resonance-Dating in Geoarcheological Studies”. Fieldwork at Românești-Dumbrăviţa and subsequent analysis of lithic materials was carried out by the Department of History and Letters at “Valahia” University of Târgoviște, the Institute of Prehistoric Archeology of the University of Cologne and the Chair of Physical Geography and Geoecology at RWTH Aachen in the context of project B1 “The Eastern Trajectory: Last Glacial Paleogeography and Archeology of the Eastern Mediterranean and of the Balkan Peninsula”.

References

Adamiec, G., Aitken, M., 1998. Dose-rate conversion factors: update. Ancient TL 16, 37–50.

Aitken, M., 1984. Non-linear growth: Allowance for alpha particle contribution. Ancient TL 2, 2–5.

Aitken, M., 1985a. Alpha particle effectiveness: numerical relationship between systems. Ancient TL 3, 22–25.

Aitken, M., 1985b. Thermoluminescence dating. Academic Press, London.

Aitken, M., 1998. An introduction to optical dating. The dating of Quaternary sediments by the use of photon-stimulated luminescence. Oxford University Press, Oxford.

Anghelinu, M., Niţă, L., in press. What's in a name: The Aurignacian in Romania. Quaternary International.

Anghelinu, M., Niţă, L., Sitlivy, V., Uthmeier, T., Băltean, I., 2012. Looking around Peştera cu Oase: The beginnings of Upper Paleolithic in Romania. Quaternary International 274, 136–157.

Bailey, S. E., Weaver, T. D., Hublin, J.-J., 2009. Who made the Aurignacian and other early Upper Paleolithic industries? Journal of Human Evolution 57, 11–26.

Balescu, S., Lamothe, M., Mercier, N., Huot, S., Balteanu, D., Billard, A., Hus, J., 2003. Luminescence chronology of Pleistocene loess deposits from Romania: testing methods of age correction for anomalous fading in alkali feldspars. Quaternary Science Reviews 22, 967–973.

Băltean, I., 2011. The Palaeolithic in Banat. In: Tasic, N., Drasovean, F. (Eds.), The Prehistory of Banat I. The Palaeolithic and Mesolithic. Academiei, Bucharest.

Banks, W. E., d'Errico, F., Zilhão, J., 2013. Human-climate interaction during the Early Upper Paleolithic: testing the hypothesis of an adaptive shift between the Proto-Aurignacian and the Early Aurignacian. Journal of Human Evolution 64, 39–55.

Bell, W., 1980. Alpha dose attenuation in quartz grains for thermoluminescence dating. Ancient TL 12, 4–8.

Benazzi, S., Douka, K., Fornai, C., Bauer, C. C., Kullmer, O., Svoboda, J., Pap, I., Mallegni, F., Bayle, P., Coquerelle, M., Condemi, S., Ronchitelli, A., Harvati, K., Weber, G., 2011. Early dispersal of modern humans in Europe and implications for Neanderthal behaviour. Nature 479, 525–529.

Bon, F., 2006. A brief overview of Aurignacian cultures in the context of the industries of the transition from the Middle to the Upper Paleolithic. In: Bar-Yosef, O., Zilhão, J. (Eds.), Towards a definition of the Aurignacian. Proceedings of the Symposium held in Lisbon, Portugal, 2002, Trabalhos de Arqueologia 45. Instituto Português de Arqueologia, Artes Graficas, Lisbon, 133–144.

Bosselin, B., Djindjian, F., 2002. Un essai de reconstitution du climat entre 40.000 bp et 10.000 bp à partir de séquences polliniques de tourbières et de carottes océaniques et glaciaires à haute resolution. Archeologia e Calcolatori 13, 275–300.

Bøtter-Jensen, L., McKeever, S. W. S., Wintle, A. G., 2003. Optically stimulated luminescence dosimetry. Elsevier, Amsterdam.

Broglio, A., Bertola, S., Stefani, M. D., Marini, D., Lemorini, C., Rossetti, P., 2005. La production lamellaire et les armatures lamellaires de l'Aurignacien ancient de la grotte de Fumane (Monts Lessini, Venetie). In: Brun-Ricalens, F. L. (Ed.), Productions lamellaires attribueés a l'Aurignacien: Chaînes opératoires et perspectives technoculturelles. ArcheoLogiques, T. 1. Musée national d'histoire et d'art, Luxembourg, 415–436.

Cârciumaru, M., 1989. Contexte stratigraphique, paléoclimatique et chronologique des civilisations du Paléolithique moyen et supérieur en Roumanie. L'Anthropologie 93, 99–122.

Cârciumaru, M., 1999. Le Paléolithique en Roumanie. Préhistoire d'Europe 7. J. Millon, Grenoble.

Chirica, V., Borziac, I., Chetraru, N., 1996. Gisements du Paléolithique supérieur ancien entre le Dniestr et la Tissa. Helios, Iaşi.

Conard, N. J., Bolus, M., 2003. Radiocarbon dating the appearance of modern humans and timing of cultural innovations in Europe: new results and new challenges. Journal of Human Evolution 44, 331–371.

Conard, N., 2002. The timing of cultural innovations and the dispersal of modern humans in Europe. Terra Nostra 6, 82–94.

Conea, A., 1969. Profils de loess en Roumanie. In: Fink, J. (Ed.), La stratigraphie des loess d'Europe. Bulletin de l'Association française pour l'étude du Quaternaire. Suppl. INQUA, 127–134.

Conea, A., Bally, R., Canarache, A., 1972. Guidebook to excursion of the INQUA Loess Symposium in Romania. In: Guidebooks to excursions. Geological Institute, Bucharest, 10–54.

Demidenko, Y. E., 2000-2001. The European Early Aurignacian of Krems-Dufour type industries: a view from Eastern Europe. European Prehistory 16-17, 147–162.

Demidenko, Y. E., Chabai, V. P., Otte, M., Yevtushenko, A. I., Tatartsev, S. V., 1998. Siuren-I, an Aurignacian site in the Crimea (the investigations of the 1994–1996 field season). In: Otte, M. (Ed.), Anatolian prehistory. At the crossroads of two worlds, Vol. 1, ERAUL 85. Liège, 367–413.

Demidenko, Y. E., Noiret, P., 2012. The Siuren-I Aurignacian of Krems-Dufour type industries in the context of the European Aurignacian. In: Demidenko, Y. E., Otte, M., Noiret, P. (Eds.), Siuren I rock-shelter. From late Middle and Early Upper Paleolithic to Epi-Paleolithic in Crimea. The Paleolithic of Crimea, IV. ERAUL 129, Liège, 343–357.

Demidenko, Y. E., Otte, M., 2007. Siuren I (Crimea) as a key site for Aurignacian industries of Krems-Dufour type in Eastern Europe. In: Bicho, N. F. (Ed.), From the Mediterranean

basin to the Portuguese Atlantic shore: papers in honor of Anthony Marks. Promontoria Monografica 07, Universidade do Algarve, 101–107.

Demidenko, Y. E., Otte, M., Noiret, P., 2012. Siuren I rockshelter. From late Middle and Early Upper Palaeolithic to Epi-Paleolithic in Crimea. The Palaeolithic of Crimea, IV. ERAUL 129, Liège.

Dobrescu, R., 2008. Aurignacianul din Transilvania. Renaissance, Bucharest.

Douka, K., Perles, C., Valladas, H., Vanhaeren, M., Hedges, R. E. M., 2011. Franchthi Cave revisited: the age of the Aurignacian in south-eastern Europe. Antiquity 85, 1131–1150.

Eswaran, V., 2002. A diffusion wave out of Africa. Current Antropology 43, 749–774.

Galbraith, R., Roberts, R., Laslett, G., Yoshida, H., Olley, J., 1999. Optical dating of single and multiple grains of quartz from Jinmium rock shelter, nothern Australia: Part I, experimental design and statistical models. Archaeometry 42, 339–364.

Galloway, R., Hong, D., 1996. Concerning the normalization of additive dose optically stimulated luminescence data from quartz. Ancient TL 14, 1–5.

Hahn, J., 1977. Aurignacien. Das ältere Jungpaläolithikum in Mittel-und Osteuropa. Fundamenta A/9, Böhlau, Köln, Wien.

Higham, T., Bassel, L., Jacobi, R., Wood, R., Bronk Ramsey, C., Conard, N. J., 2012. Testing models for the beginnings of the Aurignacian and the advent of figurative, art and music: The radiocarbon chronology of Geißenklösterle. Journal of Human Evolution 62, 664–676.

Higham, T., Brock, F., Peresani, M., Broglio, A., Wood, R., Douka, K., 2009. Problems with radiocarbon dating the Middle to Upper Palaeolithic transition in Italy. Quaternary Science Reviews 28, 1257–1267.

Higham, T., Compton, T., Stringer, C., Jacobi, R., Shapiro, B., Trinkaus, E., Chandler, B., Gröning, F., Collins, C., Hillson, S., O'Higgins, P., FitzGerald, C., Fagan, M., 2011. The earliest evidence for anatomically modern humans in northwestern Europe. Nature 479, 521–524.

Horvath, I., 2009. The Early Upper Palaeolithic in Romania: past and current research. In: Camps, M., Szmidt, C. (Eds.), The Mediterranean from 50 000 to 25 000 BP: Turning points and new directions. Oxbow Books, Oxford, 137–162.

Ianoş, G., 2002. General considerations on the soil cover of Banat (Romania). Geographica Pannonica 6, 13–16.

Kels, H., Protze, J., Sitlivy, V., Hilgers, A., Zander, A., Anghelinu, M., Lehmkuhl, F., subm. Genesis of loess-like sediments and soils at the foothills of the Banat Mountains, Romania – Examples from the Paleolithic sites Romanesti and Cosava. Quaternary International.

Kozlowski, J. K., Kozlowski, S. K., 1975. Pradzieje Europy od XL do IV tysiaclecia p. n. e. Panstwowe Wydawnictwo Naukowe, Warsaw.

Kozlowski, J., 1965. Studia nad zróznicowaniem kulturowym w Paleolicie górnym Europy Srodkowej. Prace Archeologiczne 7, Krakow.

Lai, Z. P., Zöller, L., Fuchs, M., Brückner, H., 2008. Alpha efficiency determination for OSL of quartz extracted from Chinese loess. Radiation Measurements 43, 767–770.

Lai, Z., Murray, A. S., Bailey, R. M., Huot, S., Bøtter-Jensen, L., 2006. Quartz red TL SAR equivalent dose overestimation for Chinese loess. Radiation Measurements 41, 114–119.

Li, S.-H., 2001. Identification of well-bleached grains in the optical dating of quartz. Quaternary Science Reviews 20, 1365–1370.

Liteanu, E., Ghenea, C., 1966. Cuaternarul din România. Studii tehnice şi Economice Seria H, 1, Bucharest.

Mauz, B., Packman, S., Lang, A., 2006. The alpha effectiveness in silt-sized quartz: new data obtained by single and multiple aliquot protocols. Ancient TL 24, 47–52.

Mavrocordat, G., 1971. Die Böden Rumäniens. Giessener Abhandlungen zur Agrar- und Wirtschaftsforschung des Europäischen Ostens 58, Duncker & Humblot, Berlin.

McBrearty, S., Brooks, A. S., 2000. The revolution that wasn't: a new interpretation of the origin of modern human behavior. Journal of Human Evolution 39, 453–563.

McKeever, S. W. S., 1991. Mechanisms of thermoluminescence production: Some problems and a few answers? Nuclear Tracks and Radiation Measurements 18, 5–12.

Mejdahl, V., 1979. Thermoluminescence dating: beta-dose attenuation in quartz grains. Archaeometry 21(1), 61–72.

Mejdahl, V., Bøtter-Jensen, L., 1994. Luminescence dating of archaeological materials using a new technique based on single aliquot measurements. Quaternary Science Reviews 13, 551–554.

Mellars, P., 2006. Archaeology and the dispersal of modern humans in Europe: Deconstructing the "Aurignacian". Evolutionary Anthropology 15, 167–182.

Mercier, N., Valladas, H., Valladas, G., 1995. Flint thermoluminescence dates from the CFR laboratory at Gif: Contributions to the study of the chronology of the Middle Palaeolithic. Quaternary Science Reviews 14, 351–364.

Mogoşanu, F., 1972. Information générale sur le Paléolithique du Banat (Sud-Ouest de la Romanie). Dacia N.S. 16, 5–27.

Mogoşanu, F., 1978. Paleoliticul din Banat. Biblioteca de Arheologie 32.

Mogoşanu, F., 1983. L'Aurignacien du Banat. In: Otte, M. (Ed.), Aurignacien et Gravettien en Europe I. ERAUL 13, Liège, 223–237.

Murray, A. S., Wintle, A. G., 2000. Luminescence dating of quartz using an improved single-aliquot regenerative-dose protocol. Radiation Measurements 32, 57–73.

Nigst, P., 2006. The first modern humans in the Middle Danube Area? New evidence from Willendorf II (Eastern Austria). In: Conard, N. J. (Ed.), When Neanderthals and modern humans met. Kerns, Tübingen, 269–304.

Nigst, P., Haesaerts, P., 2012. L'Aurignacien en Basse Autriche : résultats préliminaires de l'analyse technologique de la couche culturelle 3 de Willendorf II et ses implications pour la chronologie du Paléolithique supérieur ancien en Europe centrale. L'Anthropologie 116, 575–608.

Normand, C., Turq, A., 2005. L'Aurignacien de la grotte d'Isturitz (France): la production lamellaire dans la séquence de la salle de Saint-Martin. In: Ricalens, F. L., Bordes, J., Bon, F. (Eds.), Productions lamellaires attribuées à l'Aurignacien: Chaînes opératoires et perspectives technoculturelles. XIV congrès de l'UISPP, Liège, 2001. Imprimerie Fr. Faber, Mersch. Grand-Duché de Luxembourg, Luxembourg, 375–392.

Otte, M., Chirica, V., Haesaerts, P., 2007. L'Aurignacien et le Gravettien de Mitoc-Malu Galben (Moldavie Roumaine). ERAUL 72, Liège.

Păunescu, A., 2000. Paleoliticul şi mezoliticul din spaţiul cuprins între Carpaţi şi Dunăre. Agir, Bucharest.

Păunescu, A., 2001. Paleoliticul si epipaleoliticul din spaţiul transilvan. Agir, Bucharest.

Polymeris, G. S., Afouxenidis, D., Raptis, S., Liritzis, I., Tsirliganis, N. C., Kitis, G., 2011. Relative response of TL and component-resolved OSL to alpha and beta radiations in annealed sedimentary quartz. Radiation Measurements 46, 1055–1064.

Prescott, J. R., Hutton, J. T., 1988. Cosmic ray and gamma ray dosimetry for TL and ESR. Nuclear Tracks and Radiation Measurements 14, 223–227.

Purdy, B., Brooks, H., 1971. Thermal alteration of silica minerals: an archaeological approach. Science 173, 322–325.

Richter, D., 1995. Brennversuche zur Überprüfung der makroskopischen Bestimmung von Hitzeeinwirkung auf Gerölle. In: Scheer, A. (Ed.), Eiszeitwerkstatt, Experimentelle Archäologie. Museumsheft 2 des Urgeschichtlichen Museums Blaubeuren, 85–99.

Richter, D., Krbetschek, M., 2006. A new thermoluminescence dating technique for heated flint. Archaeometry 48, 695–705.

Richter, D., Mercier, N., Valladas, H., Jaubert, J., Texier, P.-J., Brugal, J.-P., Kervazo, B., Reyss, J.-L., Joron, J.-L., Wagner, G., 2007. Thermoluminescence dating of heated flint from the Mousterian site of Bérigoule, Murs, Vaucluse, France. Journal of Archaeological Science 34, 532–539.

Richter, D., Tostevin, G., Škrdla, P., 2008. Bohunician technology and thermoluminescence dating of the type locality of Brno-Bohunice (Czech Republic). Journal of Human Evolution 55, 871–885.

Richter, D., Tostevin, G., Škrdla, P., Davies, W., 2009. New radiometric ages for the Early Upper Palaeolithic type locality of Brno-Bohunice (Czech Republic): comparison of OSL, IRSL, TL and ^{14}C dating results. Journal of Archaeological Science 36, 708–720.

Rink, W. J., Rendell, H., Marseglia, E. A., Luff, B. J., Townsend, P. D., 1993. Thermoluminescence spectra of igneous quartz and hydrothermal vein quartz. Physics and Chemistry of Minerals 20, 353–361.

Rorabacher, D. B., 1991. Statistical treatment for rejection of deviant values: critical values of Dixon's "Q" parameter and related subrange ratios at the 95 % confidence level. Analytical Chemistry 63, 139–146.

Schmidt, C., Pettke, T., Preusser, F., Rufer, D., Kasper, H. U., Hilgers, A., 2012. Quantification and spatial distribution of dose rate relevant elements in silex used for luminescence dating. Quaternary Geochronology 12, 65–73.

Schmidt, C., Rufer, D., Preusser, F., Krbetschek, M., Hilgers, A., 2013. The assessment of radionuclide distribution in silex by autoradiography in the context of dose rate determination for thermoluminescence dating. Archaeometry 55, 407–422.

Sirakov, N., Tsanova, T., Sirakova, S., Taneva, D., Krumov, I., Dimitrova, I., Kovacheva, N., 2007. Un nouveaufaciès lamellaire dudébut de Paléolithique supérieur dans les Balkans. Paléo19 (Le Gravettien: entités régionales d'une paléoculture européenne), Les Eyzies.

Sitlivy, V., Chabai, V., Anghelinu, M., Uthmeier, T., Kels, H., Niţă, L., Băltean, I., Vesselsky, A., C. Ţuţu, C., in press. Preliminary reassessment of the Aurignacian in Banat (Southwestern Romania). Quaternary International.

Sitlivy, V., Chabai, V., Anghelinu, M., Uthmeier, T., Kels, H., Hilgers, A., Schmidt, C., Niţă, L., Băltean, I., Veselsky, A., Hauck, T., 2012. The earliest Aurignacian in Romania: New investigations at the open air site of Româneşti-Dumbrăviţa I (Banat). Quartär 59, 85–130.

Szmidt, C. C., Brou, L., Jaccottey, L., 2010. Direct radiocarbon (AMS) dating of split-based points from the (Proto)Aurignacian of Trou de la Mère Clochette, Northeastern France. Implications for the characterization of the Aurignacian and the timing of technical innovations in Europe. Journal of Archaeological Science 37, 3320–3337.

Teyssandier, N., 2003. Les débuts de l'Aurignacien en Europe. Discussion à partir des sites de Geissenklösterle, Willendorf II, Krems-Hundssteig et Bacho Kiro. PhD thesis, Université de Paris X - Nanterre.

Teyssandier, N., 2007. En route vers l'Ouest. Les débuts de l´Aurignacien en Europe. BAR International Series 1638, Oxford.

Teyssandier, N., 2008. Revolution or evolution: the emergence of the Upper Paleolithic in Europe. World Archaeology 40, 493–519.

Teyssandier, N., Bon, F., Bordes, J.-G., 2010. Within projectile range. Some thoughts on the appearance of the Aurignacian in Europe. Journal of Anthropological Research 66, 209–229.

Timar-Gabor, A., Vandenberghe, D., Vasiliniuc, S., Panaoitu, C., Panaiotu, C., Dimofte, D., Cosma, C., 2011. Optical dating of Romanian loess: A comparison between silt-sized and sand-sized quartz. Quaternary International 240, 62–70.

Tribolo, C., Mercier, N., Valladas, H., 2001. Alpha sensitivity determination in quartzite using an OSL single aliquot procedure. Ancient TL 19, 47–50.

Trinkaus, E., Rodrigo, M̃. R., Mircea, G., Moldovan, O., 2003. Early modern human cranial remains from the Peştera cu Oase, Romania. Journal of Human Evolution 45, 245–253.

Tsanova, T., Zwyns, N., Eizenberg, L., Teyssandier, N., Le Brun-Ricalens, F., Otte, M., 2012. Le plus petit dénominateur commun: réflexion sur la variabilité des ensembles lamellaires du Paléolithique supérieur ancien d'Eurasie. Un bilan autour des exemples de Kozarnika (Est des Balkans) et Yafteh (Zagros central). L'Anthropologie 169, 469–509.

Usik, V. I., 2008. The Upper Paleolithic of Transcarpathia: chronology and cultural affinity of Beregovo I Aurignacian. In: Materials and investigations of Carpathian and Volyn archeology 12., 49–67.

Valladas, H., 1985. Datation par la thermoluminescence de gisements moustériens du sud de la France. PhD thesis, Université Paris VI.

Valladas, H., 1992. Thermoluminescence dating of flint. Quaternary Science Reviews 11, 1–5.

White, M., Pettitt, P. B., 2012. Ancient digs and modern myths: the age and context of the Kent's Cavern 4 Maxilla and the earliest Homo sapiens specimens in Europe. European Journal of Archaeology 15, 392–420.

Wintle, A. G., Murray, A. S., 2006. A review of quartz optically stimulated luminescence characteristics and their relevance in single-aliquot regeneration dating protocols. Radiation Measurements 41, 369–391.

Zilhão, J., 2006. Neandertals and Moderns mixed, and it matters. Evolutionary Anthropology 15, 183–195.

Zilhão, J., 2011. Aliens from outer time? Why the "Human Revolution" is wrong, and where do we go from here? In: Condemi, S., Weniger, G.-C. (Eds.), Continuity and Discontinuity in the Peopling of Europe: One Hundred Fifty Years of Neanderthal Study. Springer, Heidelberg, 331–366.

Zimmerman, D., 1972. Relative thermoluminescence effects of alpha and beta radiation. Radiation Effects 14, 81–92.

Zöller, L., Blanchard, H., 2009. The partial heat – longest plateau technique: Testing TL dating of Middle and Upper Quaternary volcanic eruptions in the Eifel area, Germany. Eiszeitalter und Gegenwart 58, 86–106.

7 Applied dating: Further case studies from Paleolithic sites

From different study areas of the CRC 806, sets of heated silex artefacts were handed out for TL dating. The time of the last heating was estimated under consideration of the methodological results from previous chapters (especially those dealing with dose rate distribution). Mainly three reasons promoted the use of single-aliquot regenerative-dose (SAR) protocols instead of, or in combination with multiple-aliquot additive-dose (MAAD) procedures. Firstly, more than half of the artefacts were too small or of "disadvantageous" shape to extract enough material for MAAD sequences. Secondly, D_e distributions obtained by SAR measurements helped to assess the degree to which the sample is affected by radiation hot spots. Finally, SAR protocols allow comparing age estimates using different TL emissions (e.g. blue and red emissions) what provides a further check of the validity of the results (if ages agree).

While the red TL (RTL)-SAR protocol has been tested and applied successfully to silex artefacts (Richter & Krbetschek 2006), the method's applicability to other emissions such as the often dominant blue emission has not been investigated so far. To address this topic seems the more important as there are types of siliceous materials completely lacking an orange-red TL emission (see the samples described in Section 6.3.2.2). Since emitted luminescence in the UV range does not show ideal properties for dating and sample preparation (Richter et al. 1999) and is mostly of low intensity, the blue emission centered at ~ 475 nm and its suitability for SAR dating was studied in detail. Dose recovery tests on archeological samples and laboratory-heated raw material served to check the accuracy and precision of the technique. As the only samples, artefacts from the site Vale Boi (Portugal) originate from archeological strata already dated by ^{14}C, thus delivering independent age control.

7.1 General measurement parameters and procedures

All silex samples were mechanically and chemically prepared as described in Section 6.3.1. For large samples that yielded at least ~ 0.6 g prepared material, MAAD protocols were measured using either the UV-blue (centered at ~ 410 nm) or the blue emission (centered at ~ 475 nm); transmission characteristics of the filter combinations are shown in Fig. B.1. Details on the detected wavelengths for individual samples are given in the sections for

Figure 7.1: Study area of the CRC 806 and TL dated sites. The arrows represent the spread of anatomically modern humans from the source region to Central Europe. The dashed arrow indicates that this route is still a matter of debate. Map modified from www.freeworldmaps.net (accessed 22/07/2012).

each site. Smaller artefacts were dated by use of the SAR protocol for which DRT's on laboratory-heated silex raw material as well as on archeological samples confirm at least satisfactory performance using the blue emission ($< 9\,\%$ deviation of recovered and given dose, see Sections B.2.1 and C.1.2). Red TL DRT's yielded similar results, as is described in more detail in Section B.2.2. Since individual samples showed substantially different amounts of sensitivity changes (with implications for the accuracy of the SAR protocol), DRT's were conducted for each specimen whenever enough sample material was available. For all samples, large aliquots (8 mm diameter) were used and the heating rate was set to $5\,\mathrm{K\,s^{-1}}$ for UV-blue and blue TL measurements, and to $2\,\mathrm{K\,s^{-1}}$ for RTL measurements. All multiple-aliquot data were normalized using the equal pre-dose second glow procedure, i.e. all aliquots received the same cumulative β-dose prior to measurement of the normalization dose (see also Section 6.3.2.1). For TL measurements, the OSL unit was removed from the Risø reader to reduce the distance of the sample to the detector and thus to enlarge the amount of collected photons.

Alpha-efficiency was determined by comparing the TL intensity (of the same temperature interval as used for D_e calculation) of annealed fine grain material (4–11 µm) induced by α-radiation delivered by a monoenergetic ^{241}Am-source with the intensity induced by

a known dose from a $^{90}Sr/^{90}Y$ β-source. The used α-source has an activity of ~ 30 MBq and delivers to α-thin layers of fine grains 0.167 ± 0.005 Gy s^{-1}, respectively generates 0.813 ± 0.026 µm^{-2} min^{-1} of α-tracks within the sample. Alpha-irradiation was performed evacuated at ~ 10 mbar in the Lexsyg Research reader of Freiberg Instruments. Beta-sources of the Risø readers delivered dose rates between ~ 0.10 and 0.15 Gy s^{-1} with a calibration error of 5 %.

Finely ground material of the cores of the silex samples served to determine the internal concentration of K, Th and U by ICP-MS, from which the internal dose rate was calculated according to the conversion factors given in Adamiec & Aitken (1998). Sample preparation for ICP-MS analyses and measurement procedures were as described in Section 4.2.

To assess the performance of the SAR protocol and the degree of uniform dose distribution within each sample, obtained single D_e's were plotted against the corrected natural luminescence intensity (L_n/T_n). Even for idealized measurement conditions (e.g. a DRT), a natural variation of L_n/T_n values is expected, which is reflected in a corresponding variation of D_e values. Comparing the spread of D_e's from DRT's on the one hand and from natural dose measurements on the other hand allows appraising if natural D_e results are "overdispersed". In contrast to sediment samples, where overdispersion may be attributed either to microdosimetry, postdepositional mixing, heterogeneous bleaching of grains or a combination of these factors, overdispersion in adequately heated silex samples is expected to arise solely from non-uniform internal dose distribution caused by hot spots or hot zones. A narrow D_e distribution (comparable to the DRT results) hence suggests largely uniform internal dose distribution on the scale of the used aliquot size. It must be noted, however, that due to limited machine capacity and low amounts of sample material at most 10–20 aliqouts per sample could be measured, which is not enough to determine statistical parameters, e.g. the overdispersion parameter (Galbraith & Roberts 2012). A narrow range of observed L_n/T_n values indicates homogeneous luminescence properties between aliquots of one sample and proper correction of sensitivity changes in the course of the SAR sequence. A large spread of L_n/T_n between aliquots, however, denotes that there is no common growth curve and that sensitivity correction by a test dose does not work reliably in these cases. Examples of D_e-L_n/T_n-plots for DRT's and natural dose measurements of the samples from Sodmein cave are shown in Fig C.6. Additional measurement results (heating plateau tests, results of the DRT's and D_e-L_n/T_n-plots) for all samples of the following sections are given in Chapter C.

7.2 Vale Boi (Portugal)

7.2.1 Geographical and archeological setting of the site

About 2 km from the Atlantic coast, the site (and village) Vale Boi is located in a limestone valley in the southwestern part of the Algarve, Portugal (37° 05 '23" N, 8° 48 '34 " W). The site itself ranges from the Terrace, a plateau a few meters above the valley floor, via a

slope to a rockshelter in a limestone outcrop at the top of the ridge (Fig. 7.2) (Bicho et al. 2003; Manne et al. 2012). Especially the Terrace locality yielded comprehensive cultural layers from the Mousterian to the Neolithic, including Gravettian, Solutrean, Magdalenian and Mesolithic strata. Layers 4 and 5 contain Gravettian assemblages, with layer 5 being the earliest dated Gravettian on the Iberian Peninsula (Manne et al. 2012; Marreiros et al. in press). The good preservation of faunal remains at this site allows studying the diet of site occupants and related exploitation of oceanic and terrestric resources over a period of at least 10 ka (Bicho & Haws 2008; Manne et al. 2012; Bicho & Haws 2012).

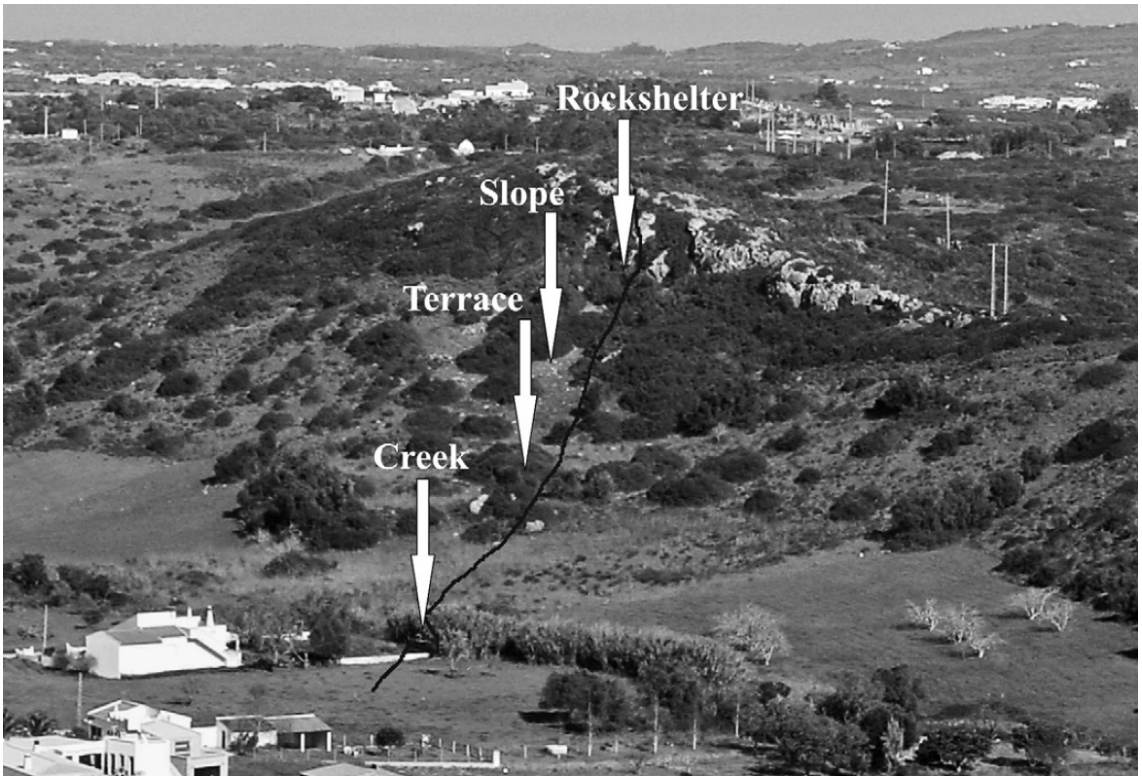

Figure 7.2: Setting and localities of the Vale Boi site. From Manne et al. (2012).

The loamy deposits of Layer 4 bore several heated, gray to dark-gray flint artefacts which were collected for TL dating. In terms of this study, not the novelty of the date itself is of relevance, but the fact that independent age control of the Gravettian layers is available in form of radiocarbon dates. This enables a check of the general accuracy of the method.

7.2.2 Methods for dose and dose rate determination

Fire exposure of the chosen artefacts was obvious from potlids, craquelation and the color alteration towards dark gray. The four pieces having sufficient size for TL dating were prepared according to the procedure given in Section 6.3.1. Scarcity of sample material impeded the use of coarse grain multiple-aliquot techniques for D_e determination, so that

the TL-SAR protocol was applied to the strong emission in the blue band. The MAAD procedure could be conducted on fine grain separates only for the two biggest samples. To ensure the applicability of the SAR protocol to this set of samples, a DRT was carried out as described in Section C.1.2, administering recovery doses in the range of the expected D_e. Furthermore, the influence of annealing temperature and duration prior to artificial irradiation was studied while (1) performing a cutheat to 500 °C or (2) holding at 400 °C for 1 h.

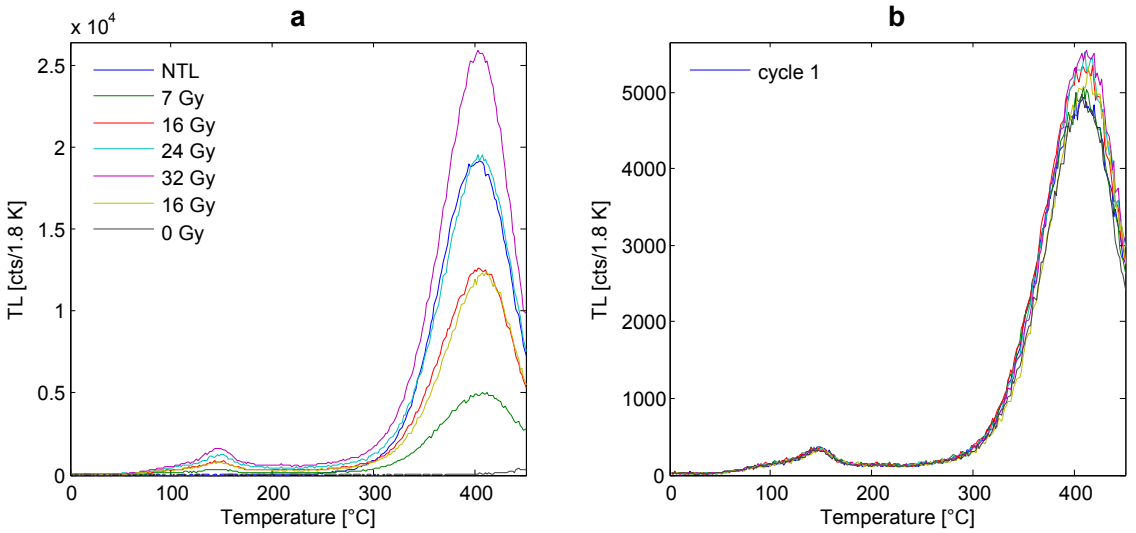

Figure 7.3: TL glow curves of sample VBT2 recorded in the course of the blue TL-SAR protocol. (a) Natural and regenerated glow curves after background subtraction. (b) glow curves of a fixed test dose of 7 Gy, recorded in between the regeneration cycles.

The site of Vale Boi exhibits a mixture of compacted loam and interspersed limestone rocks and boulders of varying size, and thus heterogeneity of the environmental radiation field is expected. Since the original findspots of the artefacts and their underlying deposits have already been destroyed at the time of visit and artefact inspection, no *in-situ* measurements of γ-radiation could be performed. Assessment of the strength of the radiation field by dosimeters buried in exposed walls of the excavation was seen as tainted with considerable uncertainties, due to the random occurrence of limestone rocks being generally poor in radionuclides. The impossibility of reconstructing the exact irradiation geometry of individual artefacts thus introduces a considerable level of uncertainty into the determination of the external dose rate. The best approach was seen in collecting representative sediment samples from corresponding layers in the excavation walls for laboratory analyses. Although this approach suffers the similar shortcomings as the dosimeter method, it additionally enables a check for radioactive disequilibria. For age calculation, the mean of the radioelement concentrations determined for two sediment samples was used, and an additional uncertainty of 20 % (due to their heterogeneity) was added to the standard deviation. Based on measurements of sediment from OSL sampling and the site's topogra-

phy, the moisture content of the sediment (water mass over dry sediment) was assumed to be 10 % over burial time, and an increased uncertainty level of ± 7 % accounted for unknown moisture variations in the past.

7.2.3 Results

The results of the DRT are shown in Table C.1 and Fig. C.3. After sensitivity correction, excellent agreement could be observed between given and recovered dose. Using a cutheat to 500 °C prior to artificial irradiation, the given dose could be reproduced within 1 %, while this value increases to 5 % if prolonged annealing at 400 °C was carried out to erase the natural signal. The results of the heating plateau tests of samples from Vale Boi are shown in Fig. C.2, the D_e as a function of temperature (D_e-plateau test) for sample VBT2 in Fig. 7.4. ICP-MS analyses revealed low concentrations of K (< 0.03 wt.%), Th ($< 0.08\,\mu g\,g^{-1}$) and U ($< 0.16\,\mu g\,g^{-1}$) for the VBT series, except for VBT5 which shows enhanced U content, and VBT3 with radioelement contents $\sim$ 40–200 times larger than for the other samples. Similar radionuclide concentrations were obtained by γ-spectrometry of the two sediment samples from Layer 4. Secular equilibrium of the decay chains indicates constancy of the Th- and U-induced dose rate; however past radioelement mobility cannot be categorically ruled out. All analytical data as well as results of luminescence measurements are summarized in Table 7.1.

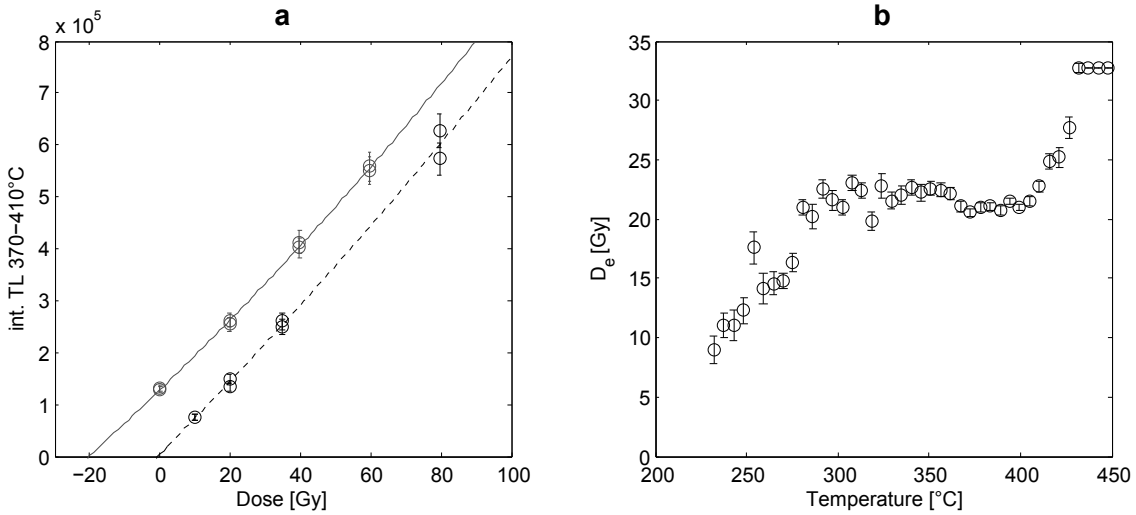

Figure 7.4: MAAD dose response and D_e-plateau of sample VBT2. (a) Additive (solid) and regenerative (dashed) dose response curves after second-glow normalization, fitted with quadratic functions. (b) D_e-plateau of the same sample.

7.2.4 Discussion of the results

When comparing the AMS radiocarbon data of the Gravettian find layer 4 of 29,278–30,209 calBP ($2\,\sigma$) obtained for charcoal (Manne et al. 2012) and considering archeological

Table 7.1: Analytical data, measurement results and calculated ages for silex samples from Vale Boi. The quoted values of K, Th and U concentrations refer to the ICP-MS measurements of interior material of the silex samples. For calculation of the external dose rate, concentrations of 2.37 ± 0.50 wt.% K, $9.90 \pm 2.14\,\mu g\,g^{-1}$ Th and $2.42 \pm 0.52\,\mu g\,g^{-1}$ U were used, based on γ-spectrometry of sediment samples from Layer 4. Dose response curves were fitted with quadratic functions (supralinear growth).

Sample	Protocol	Grain size [µm]	Temp. [°C]	n[a]	D_e [Gy]	b-value [Gy µm^2]	K [wt.%]	Th [µg g^{-1}]	U [µg g^{-1}]
VBT1	MAAD	4–11	370–410	–	20.1 ± 0.7	1.63 ± 0.06	0.030 ± 0.003	0.080 ± 0.008	0.14 ± 0.01
VBT1	SAR	100–200	350–410	9/10	21.6 ± 0.4	1.63 ± 0.06	0.030 ± 0.003	0.080 ± 0.008	0.14 ± 0.01
VBT2	MAAD	4–11	370–410	–	21.5 ± 1.0	1.22 ± 0.04	0.020 ± 0.002	0.030 ± 0.003	0.16 ± 0.02
VBT2	SAR	100–200	350–410	10/10	25.2 ± 0.4	1.22 ± 0.04	0.020 ± 0.002	0.030 ± 0.003	0.16 ± 0.02
VBT3	SAR	100–200	350–410	9/10	29.1 ± 0.5	1.35 ± 0.05	5.32 ± 0.48	5.59 ± 0.56	5.95 ± 0.60
VBT5	SAR	100–200	350–410	10/10	25.8 ± 0.2	1.37 ± 0.11	0.020 ± 0.002	0.020 ± 0.002	1.64 ± 0.16

Sample	Protocol	$\dot{D}_\alpha$ [Gy ka^{-1}]	$\dot{D}_\beta$ [Gy ka^{-1}]	$\dot{D}_{\gamma+\mathrm{cosm.}}$ [Gy ka^{-1}][b]	$\dot{D}_{\mathrm{total}}$ [Gy ka^{-1}]	$\dot{D}_{\mathrm{int.}}$ [% $\dot{D}_{\mathrm{total}}$]	Age [ka]
VBT1	MAAD	0.060 ± 0.004	0.046 ± 0.003	1.292 ± 0.172	1.398 ± 0.172	8	**14.4 ± 1.7**
VBT1	SAR	0.060 ± 0.004	0.046 ± 0.003	1.292 ± 0.172	1.398 ± 0.172	8	**15.5 ± 1.8**
VBT2	MAAD	0.046 ± 0.006	0.040 ± 0.003	1.292 ± 0.172	1.398 ± 0.172	6	**15.4 ± 1.9**
VBT2	SAR	0.046 ± 0.006	0.040 ± 0.003	1.292 ± 0.172	1.398 ± 0.172	6	**18.3 ± 2.3**
VBT3	SAR	2.270 ± 0.206	5.180 ± 0.386	1.319 ± 0.172	–	–	–
VBT5	SAR	0.508 ± 0.064	0.256 ± 0.023	1.306 ± 0.172	2.070 ± 0.191	37	**12.5 ± 1.1**

[a] Number of accepted in relation to measured aliquots.
[b] Corrected for influence of moisture content and for γ-attenuation within the sample.

Figure 7.5: Profile at Vale Boi, showing the location of sample collection (Layer 4) and interspersed limestone fragments. Photo: Dr. Nicole Klasen.

typology of the artefacts, the determined luminescence age must be seen as clearly too young. For sample VBT3, the abnormally high values of internal K, Th and U as well as their relative abundances indicate a systematical error either of sample preparation (accidental inclusion of cortex or rim material, or imperfection of the chemical digestion) or of mass-spectrometric measurements. Therefore, the determined internal dose rate was regarded as not reliable and no age was calculated for this sample.

The fact that MAAD and SAR ages are very similar (although not congruent) indicates that the systematic error leading to age underestimation is likely not related to the procedures used for paleodose estimation. Moreover, alteration of the α-efficiency or the moisture content (within meaningful boundaries) does not allow for substantially older ages. Therefore, the significant age underestimation – taking the radiocarbon data as a reference – might be related to dose rate overestimation or accidental light bleaching of the measured sample material. While the outer rim of each sample of at least 2–3 mm was removed prior to further sample preparation, bleaching and thus reduction of the archeological dose cannot be ruled out certainly. On the other hand, the small size of the Vale Boi artefacts impeded discarding a thicker rim. Concerning the dose rate calculation, it must be mentioned that the deposits at the Terrace are charcterized by randomly distributed limestone blocks and fragments of different size which are poorer in radionuclides than the soil matrix. Guibert et al. (1998) measured radionuclide concentrations of limestone of about one magnitude smaller than in the surrounding soil. This or a similar scenario might

apply here as well, and the γ-dose rate is prone to substantial spatial variations, depending on the configuration of limestone blocks within the ~ 30 cm range of γ-radiation. Although small limestone fragments were part of the analyzed γ-spectrometry samples, the potential influence of massiv blocks in the vicinity of the dated artefact could not be accounted for. Due to the fact that the TL samples were submitted when the excavation was already finished, the exact irradiation geometry (position of limestone fragments and blocks relative to the TL sample) was impossible to reconstruct. To match the radiocarbon data, the total dose rate would have to be reduced by $\sim 50\,\%$. Taking into account the setting of the site with abundant limestone blocks, this scenario is absolutely conceivable. These findings once more point up that careful (non-invasive) radiometric measurements (Guérin & Mercier 2012) by specialists already during excavation or sophisticated dose rate reconstruction (Guibert et al. 1998) are a fundamental prerequisite to obtain accurate age estimates.

7.3 Sodmein Cave (Egypt)

7.3.1 Geographical and archeological setting of the site

Sodmein Cave is situated at the narrowest position along a wadi break-through in a Tertiary limestone massif about 35 km northwest of Qusir (Fig 7.6) (Pricket 1979; Moeyersons et al. 2002). A hogback of the Thebes limestone hosts Sodmein Cave which lies ~ 15–20 m above the present floor of Wadi Sodmein. While seepage tunnels and dripstones indicate that karstic processes have taken action, the evolution of the cave in the present form can be traced back to the collapse of a former cavity. About 4 m of stratified occupational deposits make Sodmein Cave to a unique site in the Eastern desert of Egypt (Moeyersons et al. 2002).

The special relevance of Sodmein Cave becomes evident when considering its location along a possible corridor of dispersal of anatomically modern humans from their eastern or southern African source region northwards to the Levant (pers. comm. O. Bubenzer). Archeological archives preserved at Sodmein Cave may thus provide valuable information about the time of human occupation which can further be linked to climatic proxy-data from marine, lacustrine and terrestrial archives. According to Moeyersons et al. (2002), faunal and floral remains of the Pleistocene record enable identifying several wet periods from which the last interglacial (isotopic stage 5e) was the most humid one. Today's hyperaridity and hostile conditions in the Egyptian Sahara further emphasize the importance of suitable climatic circumstances to promote human mobility along this route. In particular for the objectives of the CRC 806, Sodmein Cave hence represents one of the key sites potentially allowing to increase the rare data records east of the Nile valley.

Although discovered in the 1970's (Pricket 1979), excavations were conducted by the Belgian Middle Egypt Prehistoric Project (BMEPP) of the Leuven University from 1990 onwards (Vermeersch et al. 1994; Moeyersons et al. 2002). At least ten layers could

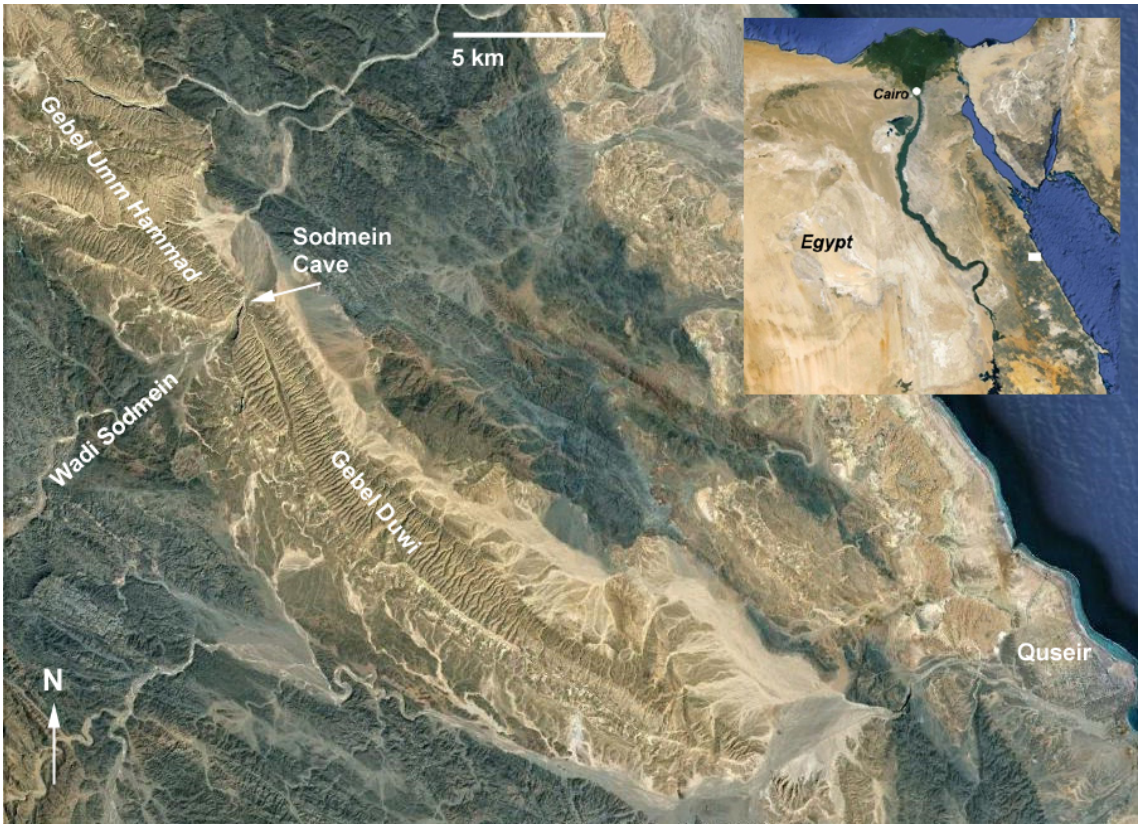

Figure 7.6: Location of Sodmein cave (26° 14' 44" N, 33° 58' 28" W). Satellite image from Google Earth (GeoEye, taken 22/11/2005, accessed 08/07/2012).

be distinguished which generally contain low artefact concentrations. The stratigraphy of a section in sector B is shown in Fig. 7.7; more details on the cave deposits can be found in Moeyersons et al. (1996). Following Neolithic layers B and C, layer D contains Upper Paleolithic artefacts, and charcoal from a hearth was ^{14}C-dated to 25.2 ± 0.5 ka BP. Layers E to J yield Middle Paleolithic inventories. Radiocarbon dating of charcoal from the disconformity of layers F and G and from organic layer G gave minimum ages of ≥ 45 ka BP and $\geq 30/\geq 44.5$ ka BP, respectively (Mercier et al. 1999; Moeyersons et al. 2002). In the lowest layer (J complex or Middle Paleolithic layer 5), near the base of layer I, a large hearth was excavated, composed of three ash layers that merge to one broad band towards the cave entrance. Mercier et al. (1999) dated six heated flint fragments from two large blocks located at the Western and Eastern end of the hearth, see also Fig. 2 in Mercier et al. (1999). All six calculated TL ages are identical within measurement uncertainties, giving a mean of 118 ± 8 ka and placing the occupation of Middle Paleolithic level 5 at the beginning of isotopic stage 5. During recent excavations in the frame of the CRC 806, further heated flint blocks were unearthed from the Middle Paleolithic hearth in complex J and submitted for TL dating. Detailed coordinates and the locations of the five samples are given in Table 7.2 and Fig. 7.8.

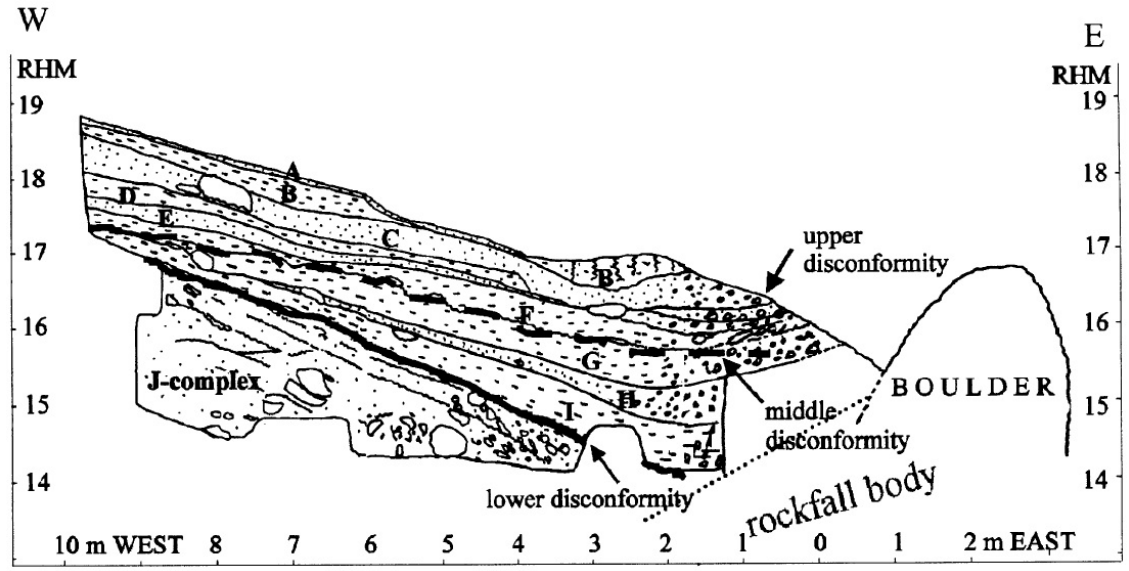

Figure 7.7: Stratigraphy of a section in sector B along 40 m north, Sodmein Cave. The relative height in meters (RHM) refers to the grid of the excavation, the individual layers are labeled with letters A to J. From MOEYERSONS et al. (2002).

7.3.2 Methods for dose and dose rate determination

Since two of the three samples were of sufficient size (> 7 g core material after removal of the 2 mm rim), the results of two TL emissions and two measurement protocols were compared. Both the MAAD protocol and the SAR protocol were used for equivalent dose determination employing the blue TL emission, while the SAR procedure allowed D_e calculation for the blue and the red TL emission. For the latter, DRT's were performed as well.

Environmental dose rates applicable to the samples were estimated by *in-situ* measurements with a γ-probe as well as by laboratory γ-spectrometry of collected surrounding material. The determined moisture content of collected sediment samples from layer J ($\sim 0.5\,\%$) does certainly not represent the mean content over the entire burial time. Firstly, the walls of the excavation have been exposed for sustained periods prior to sample collection and thus have been dried out. Secondly, OSL samples taken from the opposite wall of the trench gave water contents of ~ 3.5–$4.5\,\%$. For this reason, and to take into account past fluctuations in precipitation, ages were calculated assuming a water content of $4 \pm 3\,\%$ (water mass over dry mass of the sediment). Due to the relatively large size of samples SodTL1 and SodTL2, attenuation of external γ-radiation was calculated considering sample shape and mass according to VALLADAS (1985). For the small sample SodTL0, this effect was assumed to be negligible. Rough estimates for SodTL1 – the specimen with the highest internal dose rate – show that the amount of γ self-dosing is less than $\sim 0.03\,\mathrm{Gy\,ka^{-1}}$ and non-consideration would imply an error in age of $< 1.5\,\%$ (AITKEN 1985). It is thus disregarded in the following.

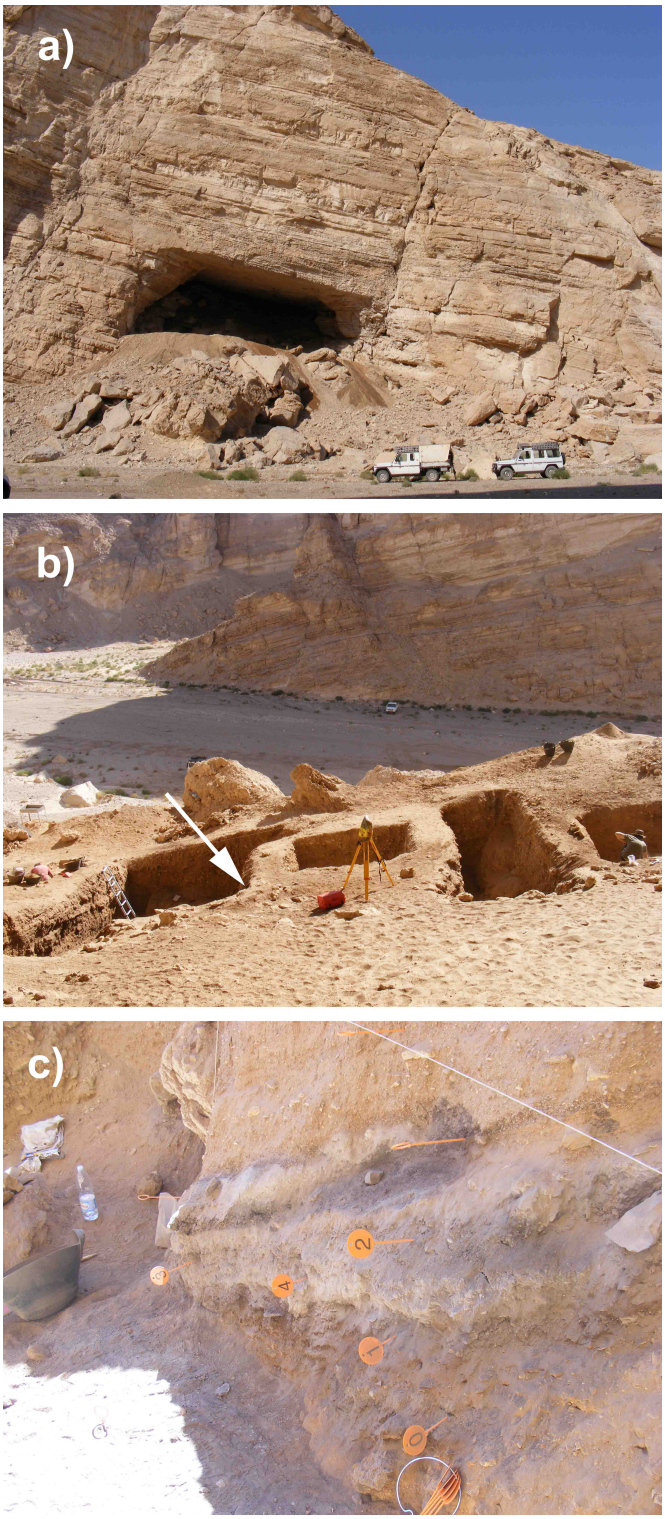

Figure 7.8: Excavations at Sodmein Cave and location of dated flint samples. (a) Photo showing the position of Sodmein cave in the limestone massif and above the present floor of Wadi Sodmein. (b) Excavated square meters in sector B; for details on the excavation see e.g. Mercier et al. (1999) or Moeyersons et al. (2002). The arrow points towards the exposed wall with the hearths from which the samples were taken. (c) Exact locations of the flint samples; the numbers refer to the laboratory code used; the stratigraphy of this section is shown in Fig. 2 in Mercier et al. (1999). All photos: Dr. Alexandra Hilgers.

Table 7.2: Codes and coordinates of SodTL samples. The samples taken in 1993 (ME93/489) and 1995 (ME95/56) are those dated by Mercier et al. (1999). Provided by courtesy of Prof. Dr. Philip Van Peer (Catholic University of Leuven).

Year	Field ID	East	North	Elevation	Ref	Correlation
2010	2040	-5.78	38.16	15.08	SodTL0	Below 1993/1995 samples
2010	2041	-5.51	38.15	15.13	SodTL1	No exact correlation
2010	2042	-5.52	37.97	15.37	SodTL2	Correlates with ME95/56
2010	2043	-4.51	38.02	14.82	SodTL3	No exact correlation
2010	2044	-5.13	37.98	15.06	SodTL4	Correlates with ME95/56
2010	2045	-4.10	39.61	14.74	SodTL5	Correlates with ME93/489
1993	ME93/489	-2.57	38.11	14.38	Upper ash layer	
1995	ME95/56	-5.95	38.40	15.30	Middle ash layer	

7.3.3 Results

From the six samples (SodTL0–SodTL5) selected according to their grayish-pinkish appearance induced by heating, only three proved suitable for TL dating. The others were either no flint or calcined and brittle from heating at temperatures $> 540\,^{\circ}\mathrm{C}$ (Richter & Temming 2006), so that these were excluded. The heating plateau test of the remaining three samples (SodTL0, SodTL1, SodTL2) indicated complete signal resetting during heating (Fig. C.5), what was also confirmed for SodTL1 and SodTL2 by D_e-plateau tests (Fig. 7.9c).

Gamma-spectrometry of surrounding sediment indicated the absence of radioactive disequilibria in the U decay chain between ^{226}Ra and ^{214}Bi. Although the organic-rich sediments at Sodmein Cave are prone to U mobilization in connection with percolating water, arid climatic conditions during most of the burial time as well as the protected position beneath a rock shelter practically preclude severe U enrichment or leaching of the cave deposits. The combined dose rate (γ and cosmic) deduced from γ-spectrometry for the three samples is systematically higher than the *in-situ* measured values by about 30–50 %. The reason for this deviation can be seen in the limestone boulders and rocks (poor in radionuclides) that are present in the profile, but not in the sample material analyzed by γ-spectrometry. Since the measurements conducted directly at the findspots are seen as representing more closely the radiation actually received by the samples and since these values are in agreement with the data collected by Mercier et al. (1999) (*in-situ* with $CaSO_4$:Dy dosimeters), age calculations are based on *in-situ*-measured dose rates.

The SAR DRT's conducted for all three samples showed large differences of recorded sensitivity changes experienced during the sequence. While sensitivity changes remained $< 15\,\%$ after eight cycles for SodTL0 and SodTL1, they reached up to 30 % (red TL) and 45 % (blue TL) for sample SodTL2. The fact that the recycling ratios of the latter sample are always < 1 suggests the presence of sensitivity changes which cannot be corrected for by the test dose. Indeed, the results of the DRT for SodTL2 confirm the problem of adequate sensitivity correction because the given dose is not recovered within measure-

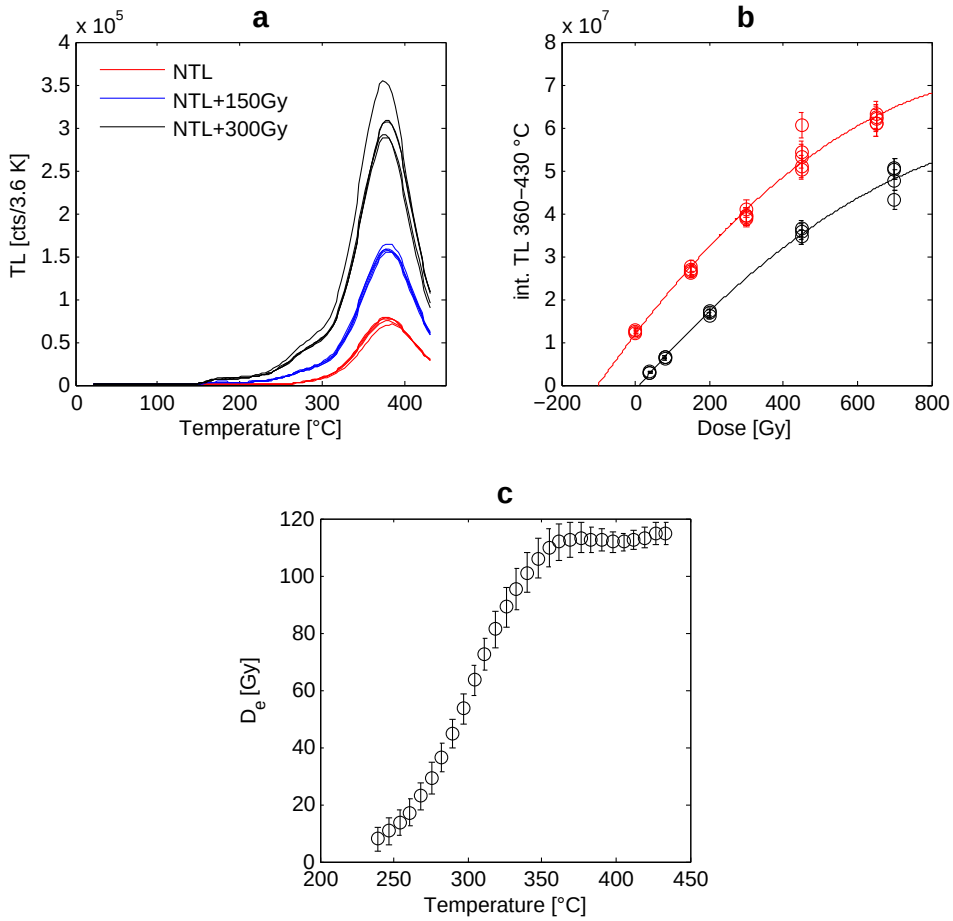

Figure 7.9: MAAD measurement results for sample SodTL2. (a) Glow curves of natural aliquots and those having received an additive dose, after second glow normalization (not all glow curves are shown). The records show the typical TL peak at $\sim 380\,^{\circ}\mathrm{C}$ also observed for samples Sod TL0 and SodTL1. (b) Additive- and regenerative-dose response curves (red and black, respectively), fitted with quadratic functions, using the TL signal of the plateau region. The two lowest dose points of the regenerative curve were not used for determination of the supralinearity correction due to reasons discussed in Section 1.3.4.1. (c) Calculated D_e as a function of temperature (supralinearity correction not yet included).

ment uncertainties, but the calculated D_e is overestimated by $\sim 14\,\%$ for both emissions (Table C.2). Whereas the trend for slight dose overestimation is also observed for SodTL0 and SodTL1, deviations between given and recovered dose are $< 9\,\%$, with the RTL results being slightly more accurate than the BTL results.

Due to small sample size, only SAR ages could be obtained for SodTL0. When assuming similar performance of the SAR protocol during D_e measurement of natural aliquots and during the DRT, a slight dose overestimation must be expected. However, the ages of SodTL0 of $120 \pm 11\,\mathrm{ka}$ and $123 \pm 15\,\mathrm{ka}$ for both the blue and red emission, respectively, are in good agreement with the ages quoted by Mercier et al. (1999) for samples 95/96 from the middle ash layer. However, SodTL0 appears to originate from below the lowest ash layer (Fig. 7.8c). In accordance with stratigraphy, samples SodTL1 and SodTL2 yield

significantly lower ages. Since these samples are larger and DRT's were only moderately successful, age calculations based on MAAD measurements were also performed. Both samples give concordant ages of 86 ± 10 ka (SodTL1) and 87 ± 9 ka (SodTL2). All relevant analytical data, measurement results and calculated ages are summarized in Table 7.3. As the only sample from Sodmein Cave, SodTL2 delivered an OSL signal suitable for optical dating (see Chapter 5 for details). The date of 86 ± 9 ka is coherent with the TL-MAAD age of the same sample.

7.3.4 Discussion of the results

A plot of D_e versus sensitivity corrected natural luminescence signal (L_n/T_n) for each sample is shown in Fig. C.6, together with the results of DRT's. The fact that in these plots all D_e-values form a plateau (within measurement uncertainties) and the effectiveness of the second glow normalization performed in the course of the MAAD measurements suggest a largely uniform distribution of internal radioelements. Hence, no serious errors related to radiation hot spots are expected. However, the spread of values for L_n/T_n, as shown in Fig. C.6, indicates that the SAR protocol works more accurately for SodTL0 than for SodTL1 and SodTL2. For all samples, the internal dose rate makes up at least half of the total dose rate (up to 72 % in case of SodTL2), thus reducing the errors introduced by heterogeneity of the γ-radiation fields and past moisture fluctuations. Although both the blue TL and the red TL-SAR give comparable results (Table 7.3), these ages must be considered as maximum ages, because DRT's of the SodTL samples have proven the tendency of dose overestimation for this protocol (Table C.2). By contrast, the excellent performance of the MAAD measurements leaves no doubt on their accuracy. From the methodological point of view, the MAAD ages of SodTL1 and SodTL2 are thus seen as representing better the date of the samples' last heating than the results obtained by the SAR protocol, which is obviously not the best choice for the studied specimens. The same is valid also for sample SodTL0, but its small size precluded MAAD measurements. However, since it showed less severe sensitivity changes during SAR cycles than SodTL2, the relative amount of age overestimation is probably < 8 %, as deduced from DRT's. The MAAD ages are further supported by the OSL age of 86 ± 9 ka obtained for SodTL2 (see Chapter 5) which is statistically indistinguishable from the TL-MAAD age.

The calculated ages are stratigraphically coherent within uncertainties. SodTL0 comes from below the lowest ash layer and also yields the highest age of 121 ± 9 ka (weighted mean of BTL and RTL SAR results). Samples SodTL1 and SodTL2 from the lower and middle ash layer at the western end of the trench are significantly younger, while both MAAD dates overlap within calculated uncertainty (86 ± 10 ka and 87 ± 9 ka, respectively). When correlating the present MAAD data with the ages obtained by Mercier et al. (1999), significant discrepancies are noticed, while SAR ages are largely in agreement with ages from the 1990's. Sample SodTL0 lies stratigraphically below all samples dated by Mercier et al. (1999), but yields a comparable date with regard to their samples from the middle and

Table 7.3: Analytical data, measurement results and ages of SodTL samples. Only the bold ages are seen as accurate and taken as a basis for discussion of the results, while ages of SodTL0 are clearly maximum ages. For further details on the used protocols and calculated ages, see the main text.

Sample	Protocol	Emission	Temp. [°C]	n[a]	D_e [Gy]	K [wt.%]	Th [µg g^{-1}]	U [µg g^{-1}]	b-value [Gy µm^2]	$\dot{D}_{\text{ext.}}$ [Gy ka^{-1}][b]
SodTL0	SAR	Blue	380–410	5/5	112.8 ± 6.6	0.15 ± 0.005	0.23 ± 0.02	0.54 ± 0.07	1.92 ± 0.14	0.50 ± 0.05
SodTL0	SAR	Red	360–380	11/20	104.7 ± 6.4	0.15 ± 0.005	0.23 ± 0.02	0.54 ± 0.07	1.24 ± 0.48	0.50 ± 0.05
SodTL1	MAAD	Blue	360–420	–	155.6 ± 8.9[c]	0.08 ± 0.002	0.14 ± 0.01	2.33 ± 0.30	1.67 ± 0.17	0.57 ± 0.05[d]
SodTL1	SAR	Blue	380–410	10/10	170.6 ± 9.4	0.08 ± 0.002	0.14 ± 0.01	2.33 ± 0.30	1.67 ± 0.17	0.57 ± 0.05[d]
SodTL1	SAR	Red	350–390	14/15	165.2 ± 9.6	0.08 ± 0.002	0.14 ± 0.01	2.33 ± 0.30	1.48 ± 0.45	0.57 ± 0.05[d]
SodTL2	MAAD	Blue	360–430	–	130.3 ± 8.3[e]	0.14 ± 0.004	0.12 ± 0.01	1.45 ± 0.19	1.85 ± 0.25	0.64 ± 0.05
SodTL2	SAR	Blue	380–410	10/10	167.4 ± 9.2	0.14 ± 0.004	0.12 ± 0.01	1.45 ± 0.19	1.85 ± 0.25	0.64 ± 0.05
SodTL2	SAR	Red	340–380	10/10	151.6 ± 11.6	0.14 ± 0.004	0.12 ± 0.01	1.45 ± 0.19	1.49 ± 0.17	0.64 ± 0.05
SodTL2	SAR (OSL)	UV	–	9/10	103.9 ± 7.1	0.14 ± 0.004	0.12 ± 0.01	1.45 ± 0.19	0.83 ± 0.13	0.64 ± 0.05

Sample	Protocol	Emission	$\dot{D}_\alpha$ [Gy ka^{-1}]	$\dot{D}_\beta$ [Gy ka^{-1}]	$\dot{D}_{\gamma+\text{cosm.}}$ [Gy ka^{-1}][f]	$\dot{D}_{\text{total}}$ [Gy ka^{-1}]	$\dot{D}_{\text{int.}}$ [% $\dot{D}_{\text{total}}$]	Age [ka]
SodTL0	SAR	Blue	0.260 ± 0.036	0.202 ± 0.011	0.478 ± 0.050	0.941 ± 0.067	49	**119.8 ± 11.0**
SodTL0	SAR	Red	0.169 ± 0.068	0.202 ± 0.011	0.478 ± 0.050	0.849 ± 0.088	44	**123.3 ± 14.8**
SodTL1	MAAD	Blue	0.895 ± 0.146	0.407 ± 0.044	0.501 ± 0.051	1.803 ± 0.189	72	**86.3 ± 9.6**
SodTL1	SAR	Blue	0.895 ± 0.146	0.407 ± 0.044	0.501 ± 0.051	1.803 ± 0.189	72	94.6 ± 10.7
SodTL1	SAR	Red	0.796 ± 0.264	0.407 ± 0.044	0.501 ± 0.051	1.704 ± 0.288	71	96.9 ± 16.5
SodTL2	MAAD	Blue	0.605 ± 0.113	0.324 ± 0.028	0.563 ± 0.052	1.493 ± 0.143	62	**87.3 ± 9.4**
SodTL2	SAR	Blue	0.605 ± 0.113	0.324 ± 0.028	0.563 ± 0.052	1.493 ± 0.143	62	112.1 ± 11.7
SodTL2	SAR	Red	0.498 ± 0.086	0.324 ± 0.028	0.563 ± 0.052	1.386 ± 0.120	59	109.4 ± 12.0
SodTL2	SAR (OSL)	UV	0.276 ± 0.057	0.324 ± 0.028	0.563 ± 0.052	1.163 ± 0.093	52	**85.7 ± 8.8**

[a] Number of accepted in relation to measured aliquots.
[b] As measured *in-situ* with the γ-probe.
[c] D_e includes a suprealinearity correction of 20.8 ± 5.2 Gy.
[d] Value based on interpolation and Mercier et al. (1999); see main text for explanations.
[e] D_e includes a suprealinearity correction of 17.4 ± 4.4 Gy.
[f] Corrected for influence of moisture content and for γ-attenuation within the sample.

upper ash layer. While SodTL1 is not correlated to a previously dated specimen, SodTL2 corresponds stratigraphically to sample 95/56 of Mercier et al. (1999). The latter yields ages of ∼ 109–119 ka, which are coherent with the blue and red TL SAR ages of the present study, but are significantly (at $1\,\sigma$ level) older than the MAAD and OSL ages for SodTL2 ($\sim 87 \pm 9$ ka and $\sim 86 \pm 9$ ka). Possible explanations for this mismatch might be (1) the stratigraphic indifference of the large hearth at Sodmein Cave and thus difficulties of unambiguous sample allocation, (2) post-depositional re-location or (3) subsurface refiring of the dated samples.

Granted that MAAD ages are accurate, the results presented here imply several occupational phases over a period of ∼ 35 ka. As noted in Mercier et al. (1999), the TL age associated with the lowest ash band fits to TL and OSL ages of wet periods in the Eastern Sahara (deduced from distinct lake phases). Indeed, the TL dates of SodTL samples correlate well with interglacial periods MIS 5e (SodTL0, below lowest ash layer) and MIS 5a (SodTL1 and SodTL2, lower and middle ash layer) (Martinson et al. 1987). On archeological grounds, the new data might support the theory that the Nubian complex dispersed from the Nile valley into formerly arid regions during wet climatic conditions (Van Peer 1998).

7.4 Las Palomas (Spain)

7.4.1 Geographical and archeological setting of the site

The site of Las Palomas (36° 59' 5" N, 4° 52' 41" W) is located near Teba (Málaga, southern Spain) in a karst complex of the West Peñarrubia Mountains. Karstic dissolution generated a system of caves and morphologic elements, including the main cave, several "galleries", a chasm called "Sima" and a doline. The continuous stratigraphic sequences preserved in Las Palomas as well as lithic and faunal remains and thus evidence of human occupation represent promising features of this site to contribute to the archeological and climatic record of this region. Among the investigated bones are those of rhino, red deer, wild boar, Spanish ibex and lynx; it is, however, still unclear whether these animals were anthropogenic prey or died in the cave for natural reasons. Most of the discovered artefacts have been knapped on grey flint. A preliminary analysis of the lithic tools as well as further information on geological/geographical settings and mammal remains can be found in Medianero et al. (2011) from where also the facts in this section are taken. Investigations of the profile along the Sima yielded several heated flint artefacts which were separated for TL dating. The dates shall allow a first temporal assignment of the lithic finds, as no radiocarbon dates are available up to present. All samples eventually suited for dating originated from layers in the lower section and were sepatared from each other ∼ 2 m horizontally and ∼ 0.4 m vertically (see Fig. 7.10); detailed coordinates are listed in Table 7.4. In addition, seven OSL samples were collected from the middle and lower part of the Sima section which are, however, not part of this work.

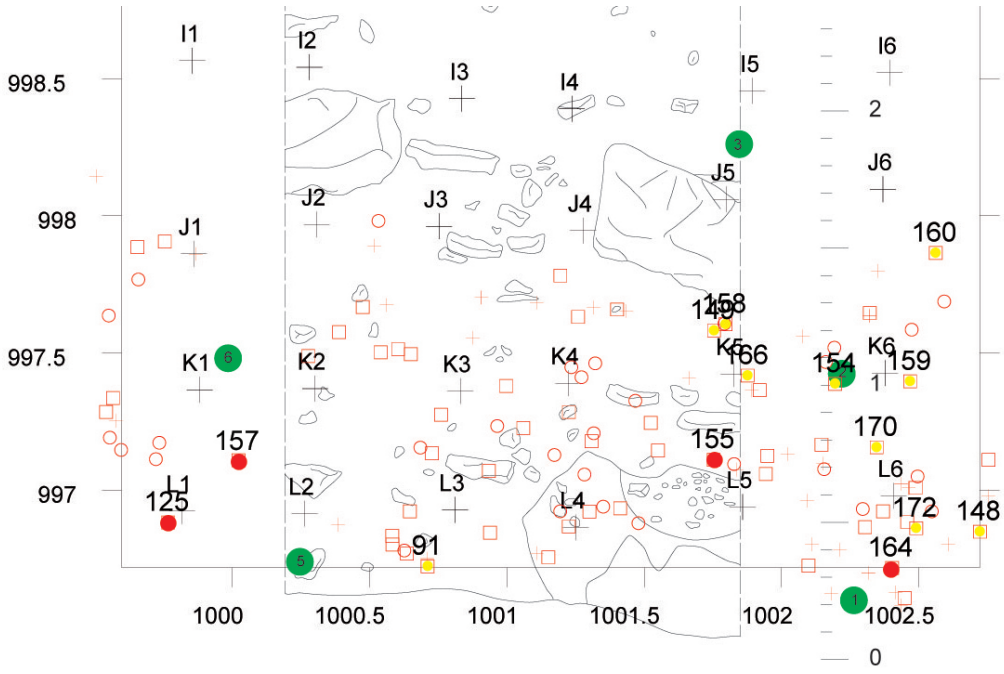

Figure 7.10: Drawn section of the Sima at Las Palomas, showing the lowermost 2 m. The upper part of the 6 m profile is not shown here. Squares = silex, circles = carbon, green dots = OSL samples and positions where *in-situ* γ-measurements were carried out, red dots = dated silex artefacts with numbers according to Table 7.4. Provided by courtesy of PD Dr. Martin Kehl (University of Cologne).

7.4.2 Methods for dose and dose rate determination

All submitted TL samples (lab code LP) were too small to provide enough material for MAAD measurements after preparation. Before application of the blue TL SAR protocol, dose recovery tests were carried out to assess its accuracy for the Las Palomas samples. The recovery dose was set to 40 Gy, which is in the order of the expected D_e, as estimated from initial test measurements. The protocol included four regeneration doses, a zero and a repeat point; the sensitivity-corrected dose response curve was fitted to a single saturating exponential function (however, almost linear dose response was observed). The results are shown in Table 7.5. Due to very low amounts of material of sample LP11, no DRT could be conducted.

The dose rate was assessed by *in-situ* measurements with the γ-probe while the holes from OSL sampling were used (see Fig 7.10). For individual TL samples, the dose rate values determined at the locations closest to their findspots were chosen for age calculations. Since sediments in karst caves are characterized by abundant limestone rocks and blocks of varying size, heterogeneities of the environmental radiation is expected. This was accounted for by increasing the uncertainty of the external dose rate to cover deviations from the measured values which the samples could have experienced in the worst case. An additional amount of uncertainty was added corresponding to a $\pm 10\,\%$ moisture fluctuation over burial time. Due to the small size of all dated artefacts, internal γ-absorption was considered as negligible.

Table 7.4: Codes and coordinates of dated Las Palomas samples. The cited coordinates refer to the new grid of the Sima (see Fig. 7.10).

Lab code	Archeological code (old/new)	x	y	z
LP1	1602/125	998.0650	999.7669	996.8832
LP4	1671/155	998.1182	1001.7521	997.1118
LP5	1671/155	998.1182	1001.7521	997.1118
LP7	1681/(157/167/177)	1001.7770	1000.0453	997.1665
LP11	1711/164	1001.7197	999.7884	996.7173

Table 7.5: DRT results of Las Palomas samples. n denotes the number of measured aliquots (all were accepted).

Sample	n	Given dose [Gy]	Recovered dose [Gy]	Ratio (given/recovered)
LP1	6	40	43.4 ± 1.1	0.92
LP4	6	40	40.7 ± 0.9	0.98
LP5	1	40	42.0 ± 2.6	0.95
LP7	6	40	40.4 ± 0.9	0.99

7.4.3 Results

Heating plateau tests showed that four of the nine submitted samples have not been heated sufficiently in the past to allow TL dating (see Figs. C.7, C.8 and C.9). Dose recovery tests suggest that the blue TL SAR protocol is suitable for paleodose estimation of the sample series. Within quoted uncertainty, the given dose could be recovered for three of the four tested samples, and the deviation is $\sim 8\,\%$ for LP1. Typical glow curves and dose response behavior for Las Palomas samples is shown in Figs. 7.11 and 7.12 for one aliquot of LP5. Gamma-spectrometry of surrounding material of three OSL samples (Fig. 7.10, samples 1, 4 and 7, the latter being not located within the drawn profile) showed the absence of radioactive disequilibria. The calculated ages are cited in Table 7.6 and span the range of 51 ka – 84 ka.

7.4.4 Discussion of the results

While no direct comparison could be drawn between additive-dose and regenerative-dose protocols for the Las Palomas samples, results of the DRT indicate accurate dose estimates of archeological samples. Of course, there could have been undetected sensitivity changes during the first heating in the laboratory, but the trend of observed sensitivity changes during the SAR cycles render this scenario unlikely. Furthermore, the SAR protocol appeared to be the only way to date the small-sized Las Palomas samples. The low scatter of

Table 7.6: Analytical data, measurement results and ages of Las Palomas samples.

Sample	Temp. [°C]	n^{a}	D_e [Gy]	K [wt.%]	Th [µg g^{-1}]	U [µg g^{-1}]	b-value [Gy µm^2]	$\dot{D}_{\text{ext.}}$ [Gy ka^{-1}]^{b}
LP1	350–410	6/6	44.3 ± 0.9	0.060 ± 0.005	0.32 ± 0.03	0.20 ± 0.02	1.28 ± 0.06	0.434 ± 0.062
LP4	370–410	11/11	37.3 ± 0.6	0.110 ± 0.009	0.34 ± 0.03	0.13 ± 0.01	1.74 ± 0.19	0.525 ± 0.122
LP5	370–410	4/4	69.3 ± 1.7	0.080 ± 0.006	0.23 ± 0.02	0.39 ± 0.04	1.72 ± 0.09	0.525 ± 0.122
LP7	380–410	9/10	35.6 ± 1.7	0.070 ± 0.006	0.51 ± 0.05	0.18 ± 0.02	1.08 ± 0.07	0.434 ± 0.062
LP11	370–410	4/4	51.1 ± 1.5	0.130 ± 0.010	0.37 ± 0.04	0.35 ± 0.04	1.64 ± 0.12	0.434 ± 0.045

Sample	$\dot{D}_{\alpha}$ [Gy ka^{-1}]	$\dot{D}_{\beta}$ [Gy ka^{-1}]	$\dot{D}_{\text{total}}$ [Gy ka^{-1}]	$\dot{D}_{\text{int.}}$ [% $\dot{D}_{\text{total}}$]	Age [ka]
LP1	0.082 ± 0.007	0.085 ± 0.005	0.601 ± 0.063	27	**73.7 ± 7.5**
LP4	0.086 ± 0.010	0.114 ± 0.007	0.725 ± 0.126	27	**51.4 ± 8.4**
LP5	0.175 ± 0.018	0.126 ± 0.008	0.826 ± 0.127	36	**83.9 ± 12.3**
LP7	0.077 ± 0.007	0.095 ± 0.006	0.606 ± 0.063	27	**58.8 ± 6.5**
LP11	0.167 ± 0.020	0.163 ± 0.010	0.774 ± 0.049	45	**66.9 ± 4.8**

[a] Number of accepted in relation to measured aliquots.
[b] As measured *in-situ* with the γ-probe. Uncertainties were additionally corrected for assumed moisture fluctuation during burial.

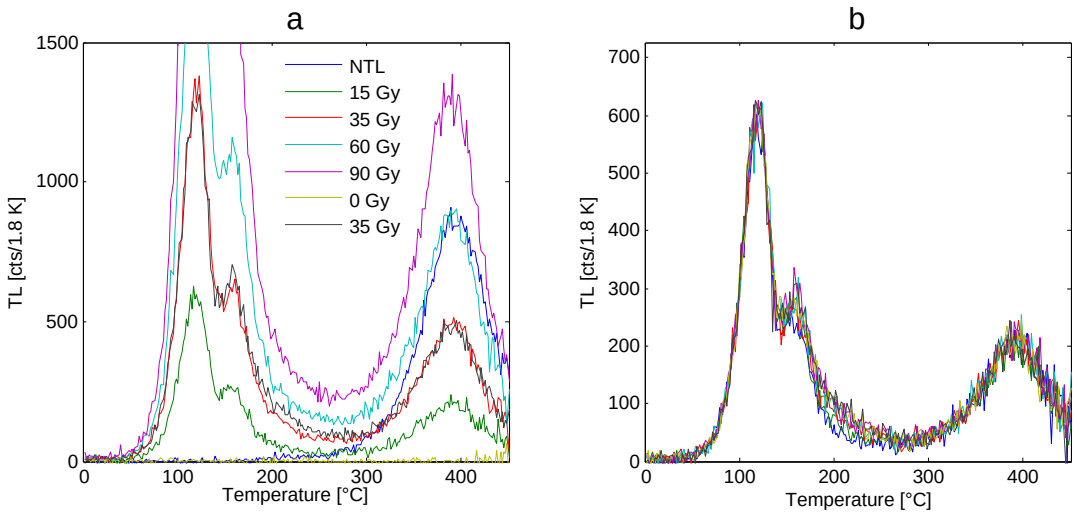

Figure 7.11: TL glow curves of sample LP5. Congruent glow curves of the repeated dose (35 Gy, plot a) and of the test dose (b) confirm little sensitivity changes throughout the measurement sequence.

the samples' individual SAR D_e-values suggests a quite uniform dose distribution within the specimens (Fig. C.10), while low concentrations of K, Th and U reduce the percentage of internal dose rate to total dose rate to 27–43 %. Since the external dose rate plays the dominant role, its imprecise estimation – related to unknown moisture contents in the past and the distances of artefact find spots and *in-situ* measurements – leads to increased 1 σ uncertainties of determined ages.

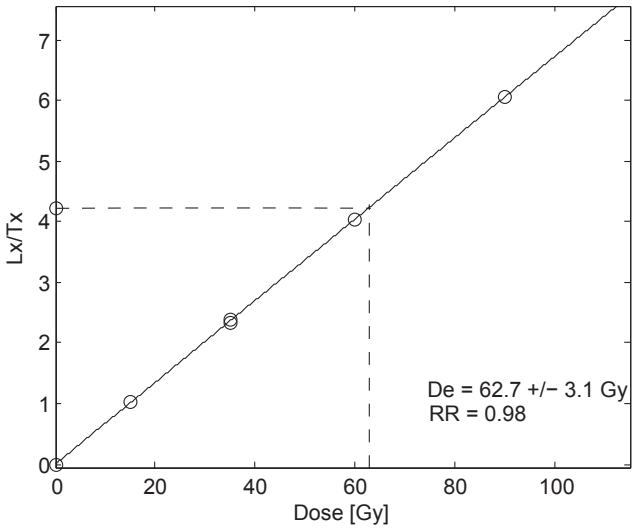

Figure 7.12: Sensitivity-corrected dose response for sample LP5 (RR = recycling ratio).

It is unclear at this time, whether the dated TL samples come from the same cultural layer or not. Therefore, and due to increased scatter of obtained ages, the mean was not

calculated. Ages are not in stratigraphic order, although overlapping within uncertainties, with sample LP5 showing the highest age ($\sim 84 \pm 12$ ka). This is particularly peculiar, since this sample was obviously found at the same spot as LP4 which yields an age ~ 30 ka younger. Conceivable scenarios for this discrepancy may be (1) wrong allocation of one of the finds (LP4, LP5) during excavation or afterwards, (2) relocation of one sample within the profile or (3) incomplete ancient heating of LP5. At present, none of these hypotheses can be ruled out. Although rather imprecise in terms of TL ages, the data obtained for the Middle Paleolithic silex samples from Las Palomas allow a first assessment of the time of Neanderthal occupation of this cave site. For the dated samples, rather poor estimates of the environmental dose rate could be obtained, limiting the overall precision of the TL ages. However, continuing excavations may yield further heated artefacts with the possibility of accompanying *in-situ* radiation measurements and thus more accurate dose rate data.

References

Adamiec, G., Aitken, M., 1998. Dose-rate conversion factors: update. Ancient TL 16, 37–50.

Aitken, M., 1985. Thermoluminescence dating. Academic Press, London.

Bicho, N., Stiner, M., Lindly, J., Ferring, C., Correia, J., 2003. Preliminary results of the Upper Paleolithic site of Vale Boi, southwestern Portugal. Journal of Iberian Archaeology 5, 51–65.

Bicho, N., Haws, J., 2008. At the land's end: Marine resources and the importance of fluctuations in the coastline in the prehistoric hunter–gatherer economy of Portugal. Quaternary Science Reviews 27, 2166–2175.

Bicho, N., Haws, J., 2012. The Magdalenian in central and southern Portugal: Human ecology at the end of the Pleistocene. Quaternary International 272-273, 6–16.

Galbraith, R. F., Roberts, R. G., 2012. Statistical aspects of equivalent dose and error calculation and display in OSL dating: An overview and some recommendations. Quaternary Geochronology 11, 1–27.

Guérin, G., Mercier, N., 2012. Field gamma spectrometry, Monte Carlo simulations and potential of non-invasive measurements. Geochronometria 39, 40–47.

Guibert, P., Bechtel, F., Schvoerer, M., Müller, P., Balescu, S., 1998. A new method for gamma dose-rate estimation of heterogeneous media in TL dating. Radiation Measurements 29, 561–572.

Manne, T., Cascalheira, J., Évora, M., Marreiros, J., Bicho, N., 2012. Intensive subsistence practices at Vale Boi, an Upper Paleolithic site in southwestern Portugal. Quaternary International 264, 83–99.

Marreiros, J., Cascalheira, J., Bicho, N., in press. Flake technology from Early Gravettian of Vale Boi (Portugal). In: Pastoors, A., Peresani, M. (Eds.), Flakes not blades: The role of flake production at the onset of the Upper Paleolithic in Europe. Wissenschaftliche Schriften des Neanderthal Museums 5, Mettmann.

Martinson, D. G., Pisias, N. G., Hays, J. D., Imbrie, J., Moore, T. C., Shackleton, N. J., 1987. Age dating and the orbital theory of the Ice Ages: Development of a high-resolution 0 to 300,000-year chronostratigraphy. Quaternary Research 27, 1–29.

Medianero, F., Ramos, J., Palmqvist, P., Weniger, G., Riquelme, J., Espejo, M., Cantalejo, P., Aranda, A., Pérez-Claros, J., Figueirido, B., Espigares, P., Ros-Montoya, S., Torregrosa, V., Linstädter, J., Cabello, L., Becerra, S., Ledesma, P., Mevdev, I., Castro, A., Romero, M., Martínez-Navarro, B., 2011. The karst site of Las Palomas (Guadalteba County, Málaga, Spain): A preliminary study of its Middle–Late Pleistocene archaeopaleontological record. Quaternary International 243, 127–136.

Mercier, N., Valladas, H., Froget, L., Joron, J.-L., Vermeersch, P., Van Peer, P., Moeyersons, J., 1999. Thermoluminescence dating of a Middle Palaeolithic occupation at Sod-

mein Cave, Red Sea Mountains (Egypt). Journal of Archaeological Science 26, 1339–1345.

Moeyersons, J., Vermeersch, P. M., Van Peer, P., Van Neer, W., Beeckman, H., De Coninck, E., 1996. Sodmein Cave site, Red Sea Mountains, Egypt: Development, stratigraphy and palaeoenvironment. In: Pwiti, G., Soper, R. (Eds.), Aspects of African Archaeology. Papers from the 10th Congress of the Panafrican Association for Prehistory and Related Studies, Harare, 53–62.

Moeyersons, J., Vermeersch, P. M., Van Peer, P., 2002. Dry cave deposits and their palaeoenvironmental significance during the last 115 ka, Sodmein Cave, Red Sea Mountains, Egypt. Quaternary Science Reviews 21, 837–851.

Pricket, M., 1979. Quseir regional survey. In: Whitcomb, D., Johnson, J. (Eds.), Quseir Al-Qadim 1978 Preliminary Report. American Research Centre in Egypt, Cairo, 257–349.

Richter, D., Krbetschek, M., Rieser, U., Trautmann, T., Wagner, G., 1999. Spectral investigation of the thermoluminescence of heated flint (silex). Quaternary Geochronology 18, 279–285.

Richter, D., Krbetschek, M., 2006. A new thermoluminescence dating technique for heated flint. Archaeometry 48, 695–705.

Richter, D., Temming, H., 2006. Testing heated flint palaeodose protocols using dose recovery procedures. Radiation Measurements 41, 819–825.

Valladas, H., 1985. Datation par la thermoluminescence de gisements moustériens du sud de la France. PhD thesis, Université Paris VI.

Van Peer, P., 1998. The Nile corridor and the Out-of-Africa model. An examination of the archaeological record. Current Antropology 39, 115–140.

Vermeersch, P. M., Van Peer, P., Moeyersons, J., Van Neer, W., 1994. Sodmein Cave site, Red Sea Mountains (Egypt). Sahara 6, 31–40.

8 Summary and discussion

This chapter intends to summarize and discuss the main results of the present thesis and to place the findings in a wider context. Therefore, it includes at first a general classification of dated events with focus on archeological contexts to assess the role of thermoluminescence of heated silex in relation to the method of radiocarbon dating. After addressing the core findings of Chapters 2–7, a short outlook is given on possible future directions of silex dating.

8.1 Types of dated events

Any archeological research concerned with the succession and/or contemporaneity of prehistoric inventories is paramountly reliant on chronological information. Stratigraphic evidence and thus relative references alone impede the investigation and understanding of processes of transition, advance or retreat for which the temporal dimension is the crucial factor. Accordingly, achievement of chronometric control for archeological "information carriers" or related environmental archives is compulsory part of analyses of prehistoric sites. The applicability of dating methods, however, is strongly linked to the availability of dateable material which differs among archeological periods on the one hand and between various environmental conditions on the other hand. The validity of temporal constraints and relations (e.g. contemporaneity of technocomplexes) depends on both the accuracy and precision of the dates.

Dating results – i.e. ages – are not pure numbers, but are always quoted with a confidence interval (mostly $1\,\sigma$, referring to a $\sim 68.3\,\%$ probability that the true age lies within the cited uncertainty boundaries, assuming Gaussian distribution of measurement results). Rather than being absolute ages, chronometric dates are thus statements on probabilities. Increasing the confidence interval (e.g. to $2\,\sigma \mathrel{\widehat{=}} 95.5\,\%$) also enlarges the likelihood of the true age to lie within the cited range. While *precision* is defined by the scatter of the data, *accuracy* is a measure of the deviation of determined age (mean value) and the true age (which is of course not known in most circumstances). Poor accuracy relates to systematic (and directed) errors which can be eliminated, in contrast to precision, being associated with undirected errors. This means that precise ages do not necessariliy have to be accurate and, vice versa, accurate ages can be accompanied by considerable imprecision (Geyh 2005).

The most preferred dating method in archeological contexts is the radiocarbon technique, clearly due to the high precision of the results. If the site lacks carbon-bearing

material, alternative approaches are required, such as luminescence dating that is applicable to omnipresent minerals like quartz and feldspar. These two dating methods shall be used in the following to illustrate the key question concerned with the event which is actually being dated and how this date is related to the initial question, i.e. the processes or events we are interested in. For each date, and especially when combining ages derived by different methods, the value of the information with regard to the original problem must be clarified. In this context, the typology of dated events, as introduced by Dean (1978) and discussed by Richter et al. (2009), is particularly helpful to provide a theoretical framework for the issues addressed above. For the sake of simplicity and to point out the main features, this concept is reduced to the three most important terms being of relevance for radiocarbon and luminescence dating, following Richter et al. (2009). The *dated event* is the event for which the date actually applies. On the contrary, the *target event* describes the event or process of archeological relevance, in most cases the occupation of a site. These two types of events do not necessarily coincide on a chronological scale, but can show considerable and sometimes unknown temporal "offsets", as outlined below. The dated and the target event are linked by the *bridging event* whose knowledge is a prerequisite for establishing a causative relation between the obtained age and the initial question.

Starting with *radiocarbon dating*, the dated event is the death of an organism. In case of human fossils, the dated event will mostly be identical to the target event, if systematic errors in age determination are neglected. These errors are, for instance, connected to the contamination of collagen by modern carbon from atmospheric CO_2, leading to age underestimation (Higham 2011). The situation becomes more complex for plant remains, charcoal in most cases. Although implicitly assumed as originating from human fireplaces, this relation can be demonstrated in the least archeological settings. There are mainly two factors hampering the creation of a bridging argument to relate the death of a tree with human agency: (1) the fire could have been a natural one, or (2) the charcoal might have been relocated prior to final deposition (either pre- or post-depositional, e.g. via slope wash processes or bioturbation) with the implication that the ^{14}C age measured is not correlated to human presence at the site. Therefore, evidence for the charcoal to be present *in-situ* as well as cogent indications of a spatially confined hearth are conditions for bringing together dated and target event (Richter et al. 2009).

Apart from the difficulty to establish the bridging event for charcoal and other plant remains, radiocarbon dating faces further methodic challenges and limitations. Thus, a degree of accuracy is partly pretended that is actually not given. Since an all-encompassing illustration of obstacles in radiocarbon dating clearly goes beyond the scope of this thesis, just a few important issues considered as most relevant are listed.

1. Owing to the half life of ^{14}C and technical limits, the dateable range goes back not farther than ~ 50 ka (Geyh 2005; Weninger & Jöris 2008).

2. It is known that the atmospheric ^{14}C concentration was not constant over the last 50 ka, leading to temporal changes in the initial $^{14}C/^{12}C$ ratio. Nonconsideration of this fact entails errors in determined ages; therefore ^{14}C ages have to be calibrated in order convert the radiocarbon scale into the calendar time scale. While the reconstruction of past ^{14}C levels is possible with dendrochronologic datasets back to $\sim$12 ka (Reimer et al. 2009), marine, atmospheric and terrestrial archives (e.g. marine cores, ice cores, corals, U-/Th-dated speleothems) allow calibration for the last 60 ka (Fairbanks et al. 2005; Weninger & Jöris 2008). The calibration curve (radiocarbon ages vs. calendar ages) implies an age difference of up to several thousand years between calibrated and uncalibrated dates. Due to ongoing research, calibration data and thus calibrated ^{14}C ages change with time. Being of major archeological relevance, the time interval spanning the Middle to Upper Paleolithic transition ($>$ 35 ka ^{14}C) is characterized by a plateau in the calibration curve, thus complicating precise calibration in this region and reducing the value of the radiocarbon technique for this question, see Fig. 3 in Weninger & Jöris (2008). Different calibration curves and mathematic algorithms for transformation are combined in several calibration programs (e.g. CalPal: http://www.calpal-online.de/; OxCal: http://c14.arch.ox.ac.uk; Fairbanks: http://radiocarbon.ldeo.columbia.edu/research/radcarbcal.htm; CALIB: http://calib.qub.ac.uk/calib/). A comparison of these programs shows that computed ages differ, depending on the program and the position on the time scale. For Holocene dates, calibration results of programs are indistinguishable, largest deviations (up to $\sim$1000 a) are observed in the region 14–20 ka ^{14}C and 30–32 ka ^{14}C between the Fairbanks program and the others (Weninger et al. 2007).

3. Especially for older samples, contamination of samples with modern carbon becomes an important issue. Post-depositional mixing in case bulk samples are to be dated, or absorption of humic acids by charcoal are examples for which the radiocarbon method gives too young ages for the event of interest (Scharpenseel & Schiffmann 1977; Geyh 2005). While new preparation techniques (ultrafiltration) appear to overcome difficulties associated with degraded collagen of bone samples, considerable parts of archeological work and interpretations are based on dates obtained with older preparation techniques leading to underestimated ages (Weninger & Jöris 2008; Higham 2011). Consequently, all radiocarbon dates $>$ 30 ka should be treated with great care and are to be interpreted as minimum ages (Geyh 2005).

The dated event in case of OSL dating of sediments is the last exposure to sunlight of quartz or feldspar grains. Except for sediment movements directly or indirectly caused by human action (e.g. colluvial processes as a consequence of deforestation), the dated event is not immediately linked to the target event (time of human settlement). Moreover, the assumption of the last light exposure to be the actually dated event might not be fully correct if heterogeneous bleaching or bioturbation play a role. Sampling of the (mostly

heterogeneous) archeological find layer itself is often accompanied by "lumpy" dosimetry and reduced precision of the obtained age which further represents a mean age of the sampled sediment column (as e.g. given by the diameter of OSL tubes used for sample collection). Even if the first layer of sedimentary grains deposited on an abandoned site can be seen as temporally almost identical to the abandoning, the sampling resolution for OSL is too coarse to actually represent this event. Hence, there is no direct connection to establish between the sedimentation (dated event) and human presence (target event). Nonetheless, OSL samples sandwiching the find horizon can provide bracketing ages which may help for temporal allocation of archeological strata.

The most direct connection between the dated event and the event of archeological interest must be attributed to thermoluminescence dating of heated artefacts. Rapid heating of silex usually causes mechanical damages, increased brittleness and thus often a degradation of raw material (see Section 1.2.3), so that the firing of lithics is seen as being related to their discard and hence the actual occupation of the site. Accordingly, this method most directly reflects human presence with dated and target event being almost congruent. Of course, the possibility of natural fires must be taken into consideration, but several reasons point to human campfires in most circumstances, as discussed in Section 1.3 and in Richter et al. (2009). Most importantly, the temperatures of most wood and grassland fires are too low to completely reset the TL signal, and spatially confined signs of heat impact (burnt soil, distribution of heated artefacts) instead of their vast spread, as would be indicative of natural fires, clearly favors an anthropogenic cause of fire (Bellomo 1993; Richter 2007b).

8.2 The role of the internal dose rate for silex dating

In luminescence dating, the preferred condition of constant radiation fields through space and time is given only in the rarest cases. Apart from spatial gradients of environmental radiation, its temporal fluctuation, e.g. due to changes in moisture content or radioactive disequilibria, is among the most crucial imponderabilities limiting both dating accuracy and precision. Unlike the majority of quartz samples, silex often contains significant amounts of radionuclides. The resulting internal dose rate can be boon or bane: if uniform and comparable to or larger than the environmental one, the constancy of self-dosing through time reduces the dependence on the – not exactly known and potentially unsteady – external radiation. In other words, the higher the percentage of internal to total dose rate is, the lesser will be the uncertainties related to lumpy and changing external dosimetry (Richter 2007a). However, if internal K, Th and U are not evenly distributed among the sample's interior, but concentrated in so-called "hot spots" or "hot zones", microdosimetric effects will mask the benefits from high internal dose rates. Using homogenized samples (powder, grains) for measurements, the following effects are expected, while the absolute and relative importance of each depends on the individual configuration of α- and β-emitters within the sample:

1. Enhanced scatter of multiple- and single-aliquot data in case of low density of hot spots, and thus reduced precision of dates. Because the complex natural radiation field cannot be reproduced in the laboratory, normalization procedures are not capable of fully compensating for aliquot-to-aliquot scatter.

2. High K, Th and/or U concentrations in hot spots/zones cause rapid saturation of charge traps in their vicinity (a few tens of µm for α-radiation and $\sim$1–2 mm for β-radiation, see Section 1.3.3). This is not accounted for by application of calculated bulk/mean internal dose rates, leading to age underestimation.

3. Alpha-track overlap in and close around α-hot spots further decreases α-efficiency, which is usually not considered in the course of bulk sample measurements and again causes age underestimation.

Consequently, it becomes evident that any correlation between dose sensitivity of the material and its radioelement distribution accounts for systematic errors of bulk luminescence ages. The present thesis addressed the question whether and to what degree there are heterogeneities of internal radiation fields of silex samples and if their characteristics (uniformity, strength) cause the above listed effects to play a significant role. Some studies already approached this question during the past four decades (see Sections 3.1 and 4.1 for a summary). However, these investigations were either based on one element only or limited in their spatial resolution (e.g. comparing two halfs of one specimen). Furthermore, they covered only a few samples of silex, a material which is known to exhibit great variability (Section 1.2). Therefore, complementary methods and modern techniques were applied here to study both the degree of uniformity of internal radiation fields and absolute concentrations of radioelements present in over 20 different specimens.

The imaging plates used in β-autoradiography allow taking an image of the intensity of β-radiation at the plane surface of a cut silex sample. Resulting digitized images provide a qualitative assessment of strength and spatial variability of β-radiation, according to the gray-values (the α-component is completely shielded and γ-radiation causes uniform blackening). Moreover, regions of high β-activity can be traced back by comparison of autoradiography images and the sample surface itself. The results show that most silex samples contain β-emitters at or below the detection limit of this method since it is difficult to distinguish background noise from sample signals, even after prolonged exposure times. A few samples, however, caused clearly visible black spots or lines on the autoradiographs which can be relocated at the sample surface as dark spots or cracks, obviously filled with foreign material (Fig. 3.3).

The record of β-homogeneity was supplemented by α-autoradiography because the latter often plays an important or even dominant role in self-dosing. Polycarbonate plates (CR-39), attached to the same sample surfaces as used for β-autoradiography, conserve the impact of α-particles which are visible as α-tracks after development (etching) of the

detector. Besides qualitative evaluation of Th and U distribution, a statistical approach was applied to determine the degree of homogeneity. This approach included a *Matlab* routine for automatic track counting and localization for employing a classification method for point fields as used also in other subjects (e.g. animal or vegetation ecology). With certain levels of confidence, the present track field could be assigned as random ($\widehat{=}$ uniform Th and U distribution) or clustered ($\widehat{=}$ α-hot spots or zones) for varying spatial resolutions. While about half of the samples do not show clustered α-tracks, as assessed by visual inspection, statistical assignment proves that the vast majority yields more or less clustered α-activity. As expected, averaging takes effect at coarser scaling what is obvious from comparison of the classification results of 0.5 mm, 1.0 mm and 2.0 mm resolutions (Fig. 3.5).

Finally, absolute concentrations of radioelements in the same set of silex samples were determined by laser ablation inductively coupled plasma mass spectrometry (LA-ICP-MS). This modern technique enables determining the elemental composition down to ng g^{-1} levels of sampled volumes as small as $^{1}/_{1000}$ mm^3, providing a detailed picture of K, Th and U contents in the siliceous matrix, cracks and inclusions. In addition to radioelements, more than 20 other major, minor and trace elements were measured for geochemical characterization of impurities which are present in virtually all silex samples. The finding of autoradiography investigations could be confirmed by LA-ICP-MS measurements: Whereas pure silex contains mostly low amounts of K (< 0.1 wt.%), Th ($< 0.4\,\mu g\,g^{-1}$) and U ($< 1.0\,\mu g\,g^{-1}$), impurities such as filled cracks and mineral or organic inclusions yield radioelement concentrations up to two orders of magnitude higher than those of the matrix. As also evident by autoradiography, the color of impurities roughly corresponds to radionuclide contents, i.e. dark color mostly indicates high radioactivity. To evaluate the consequences when determining the internal dose rate from K, Th and U values of bulk samples, comparative measurements were carried out, opposing matrix concentrations as derived from LA-ICP-MS to bulk values obtained by ICP-MS. Except for one sample, systematically higher bulk values were found, underlining the significance of impurities for internal dosimetry. Among others, Fe–Mn-oxy-hydroxides, Ca or Mg carbonates, clays and phosphates are shown to be part of sampled cracks and inclusions.

The three-dimensional distribution of impurities does not follow any regular pattern, varies from sample to sample and is thus difficult to predict for the specimen as a whole. However, for the majority of samples, only a small fractional volume is occupied by hot spots/zones, implying that sample homogenization at a coarse grain scale ($\sim$ 100–200 µm) might not be sufficient to average out the rare occurrence of regions with highly elevated activity, even when large aliquots (> 1000 grains) are used. In other words, measured aliquots are expected to be influenced by hot spots to different degrees. Accordingly, the problems listed at the beginning of this section will be of relevance, at least for a considerable part of the studied samples.

Revisiting hypotheses/questions 2 and 3 posed in Section 1.1, the results of dosimetric investigations prove that there are substantial gradients of internal dose rate for a notable

part of the investigated samples, with corresponding effects on accuracy and precision of TL ages. Therefore, alternative methods of sample preparation or measurement techniques are required to eliminate or reduce the radiometric impact of impurities.

8.3 New approaches for silex dating: single-aliquot protocols and optically stimulated signals

While the single-aliquot regenerative-dose (SAR) protocol is routinely applied in optical dating of sedimentary quartz, the equivalent dose (D_e) is mostly determined using the multiple-aliquot additive-dose (MAAD) approach for heated silex artefacts (see Section 1.3.4). The latter method yields valid results for homogeneous samples and well below dose saturation. However, if these conditions are not complied, increased uncertainty may result and D_e determination based on extrapolation is error-prone and requires more sophisticated approaches (Valladas & Gillot 1978; Mercier 1991; Mercier et al. 1992). The motivation to study the applicability of the single-aliquot method to silex dating can be seen in the more detailed resolution of obtained dose information. While the MAAD evaluation returns one D_e value, a distribution of D_e values can be gathered by applying the SAR protocol. Especially in terms of non-uniform dose distribution within the silex sample, the more detailed information may provide valuable insights into internal dosimetry. Furthermore, the application of the MAAD measurement routine assumes a minimum size of the artfact to be able to extract at least 0.5–1.0 g of prepared sample material. Indeed, a considerable part of silex artefacts dated in the course of this thesis was too small for multiple-aliquot measurements and could only be dated by the SAR approach (Chapter 7). The SAR protocol principally requires only one aliquot (ca. 10 mg of sample material) for D_e determination. Although in practice far more than only one subsample is measured for statistical reasons, this method allows dating samples of smaller size which would not be dateable using MAAD protocols.

The major problem faced in SAR application is the adequate correction of sensitivity changes occurring during repeated irradiation and heating (TL) or bleaching (OSL). Based on only minor sensitivity changes ($< 10\,\%$ for most of the measured samples) observed for the red TL (RTL) emission of flint, Richter & Krbetschek (2006) proposed and successfully tested a RTL SAR protocol without sensitivity monitoring and two regeneration steps only. The red emission of silex is further known to exhibit high saturation dose levels (see Section 1.3.2.3), making it attractive for dating older samples and to extend the dateable age range. Own measurements, however, revealed problems related to RTL: a few silex specimens showed an increase of test dose response of up to 80 % after 2 cycles (sample SodTL0), confirming substantial sensitivity changes. Therefore, the RTL SAR protocol was extended by test dose measurements in between the regeneration steps to account for sensitivity changes. In addition, the blackbody radiation (thermal background) recorded during RTL measurements exceeds the actual sample signal, so that poor reproducibility

of background signals introduces additional data scatter or even precludes further analysis of some aliquots. Section B.2.2 also adresses this topic. Moreover, samples from the site Românești-Dumbrăviţa I (Romania) yielded no RTL emission at all. These reasons led to the search for other suitable emissions for the SAR protocol. As UV luminescence signals from silex have proven to be not well-suited for dosimetry (Richter et al. 1999; Richter & Krbetschek 2006), the strong blue emission around 470 nm was investigated (see also Section 1.3.2.3). Fig. B.1 shows the transmission window of the used interference filter (HC 475/50).

The general sequence of the blue TL SAR protocol followed mainly the one usually applied in quartz optical dating (Murray & Wintle 2000). Dose recovery tests (DRT's) of various silex samples (archeological as well as geological and annealed ones) served to test the accuracy and precision of the protocol. Details and results are summarized in Section B.2.1 and demonstrate that the given dose can be recovered within $< 9\,\%$ for the two geological and three archeological samples under investigation. Furthermore, comparison with the results from the extended RTL SAR protocol (see above) confirms that the blue emission produces at least equally reliable dose estimates for the studied samples. However, direct comparison of D_e's from archeological samples using blue and red SAR protocols is not valid because α-efficiencies may be different for both emissions. In this thesis, almost all samples were measured using more than just one detection waveband (multi-protocol or multi-emission dating) for cross-checking protocols and obtained ages. Here, the agreement of ages related to different sampled luminescence centers (those responsible for the UV-blue, blue and red emissions) provides a confirmation of their sufficient thermal stability. Consequently, an increased level of confidence and validity of determined ages is achieved.

The TL SAR procedure using the blue and/or red emission was applied to all archeological samples which were dated. Dose recovery tests and comparison with MAAD ages showed that this approach is not equally suitable for all kinds of silex material. For instance, samples from the site Românești-Dumbrăviţa I yielded partly poor dose reproducibility using the blue TL SAR protocol (sample type 2, see Section 6.6.2) while excellent performance of this protocol could be observed for samples from Vale Boi and Las Palomas. The slight discrepancies discovered between the fine grain MAAD ages and the blue TL SAR ages for samples VBT1 and VBT2 of 8 % and 19 %, respectively, cannot be explained at this time. While for these samples, regenerative measurements led to higher ages than additive-dose sequences, the situation is vice versa for artefacts from Românești-Dumbrăviţa I (type 1 samples); here, MAAD ages are higher than SAR ages. Age overestimation for both the blue and red emission of samples from Sodmein Cave led to inaccurate results for this approach, as indicated by DRT's and comparison with MAAD ages. As the latter agree with OSL ages (Section 7.3.3) and no problems related to severe radiation hot spots in the samples could be evidenced to cast doubt on MAAD results, regenerative TL measurements proved to yield ages systematically too old. In general, no trend became apparent

whether the blue or the red TL emission shows more serious sensitivity changes, at least for the samples investigated in this thesis. However, since blue luminescence mostly exceeds the red one (based on the commonly used photomultiplier) and due to the difficulties of reproducible backgrounds for RTL measurements, the blue TL SAR protocol is seen as the preferable procedure. In any event, DRT's are considered as a necessary means to assess the applicability of the TL SAR protocol to the samples under study. Although there might be sensitivity changes during readout of the natural luminescence signal (which are not correctable by the following test dose measurement), the SAR procedure is seen as the best approach to obtain age information, particularly for small artefacts.

Over the past decade, it has been shown that the optically stimulated luminescence (OSL) signal of (macrocrystalline) quartz consists of several components which are related to distinct types of trapped electron populations (Smith & Rhodes 1994; Bailey et al. 1997; Bailey 2000). These types of electron traps occur in different concentrations within the crystal what is the reason for different saturation dose levels of the components. Especially *slow*-components are often characterized by comparatively high saturation doses, as found for UV-OSL of sedimentary quartz (Bailey 2000; Singarayer & Bailey 2003). However, in OSL dating of sediments the use of one of the *slow*-components is mostly impeded by their poor bleachability. But if the luminescence signal is reset by heat instead of light (e.g. in the case of burnt lithics), zeroing of the *slow*-components can be assumed what potentially allows making use of their advantageous dose response behavior. Further advantages of OSL in comparison to TL might lie in the less severe heat treatment in the course of (regenerative) measurements, hence potentially less pronounced sensitivity changes and more accurate results of SAR procedures. Therefore, one part of this thesis addressed the topic of OSL signal composition of silex, the components' basic properties as well as the applicability of OSL for dating heated silex in archeological contexts.

Curve fitting was applied to LM-OSL curves to deconvolve the bulk signal of silex samples into individual first-order components (see Section 1.3.2.4 for theoretical background). Three of the four investigated silex samples were best fitted to five components, one sample showed an additional, heating- or radiation-induced component of very high optical sensitivity. The bleachability of components, indicated by the value of the photoionization cross-section, slightly differs from literature values, but not systematically. As a fundamental requirement for retrospective dosimetry, the thermal stability of individual components was assessed by LM-OSL and short-shine pulse annealing experiments in combination with curve fitting of the pulse annealing data (remaining OSL versus preheat temperature) and the varying heating rate method (Li et al. 1997; Li 2001; Singarayer & Bailey 2003). Indicated by thermal erosion of the OSL signal at temperatures as low as 200 °C, all components except the one with the best bleachability (termed *component 1*) proved to be not stable enough for dating applications spanning the Middle Paleolithic. For *component 1*, however, fundamental trap parameters E and s derived from three different methods are in good accordance, and an electron retention lifetime was calculated

for this component sufficiently long to be suited for dating at least the last 2 Ma. Preheat dose recovery tests were conducted to check the general applicability of the SAR protocol after Murray & Wintle (2000) to silex samples. Using comparatively high preheat temperature (260 or 280 °C), good agreement was achieved between given and recovered dose, even for the sample lacking *component 1*. A survey among archeological, heated silex samples showed that not all specimens yield *component 1* or an OSL signal at all. However, if *component 1* was present, coherent ages were obtained for two Middle Paleolithic samples (SodTL2 and LP7) by OSL (blue stimulated and detected in the UV) on the one hand and by TL (blue detection, MAAD and SAR, respectively) on the other hand. This finding further proves the long-term stability of this distinct OSL component.

Experimental results of the thermal stability indicate that electron populations accounting for the OSL signal are not identical to that contributing to the 380 °C "dating peak". Furthermore, coherent MAAD TL ages and OSL SAR ages as well as the dose overestimation observed for the TL SAR protocol (both blue and red emission) of sample SodTL2 suggest that sensitivity changes are less problematic for optical than for thermal stimulation. The fact that different electron and center populations can be sampled using different stimulation modes and detection filters opens up the possibility for an internal check of the obtained age, as also discussed in Westaway & Prescott (2012). Since the saturation dose of the UV OSL signal of the four investigated samples is in the same order of magnitude as the blue TL signal, the dating limit can probably not be enhanced using OSL. It must be noted that the α-efficiency for UV OSL, as determined for the two archeological samples, is significantly lower than that for blue and red TL, as also found by Tribolo et al. (2001) for quartzite. For important samples, additional determination of the OSL age can thus be seen as a reassuring procedure and an internal backup for the accuracy of the TL age.

By using a photomultiplier with higher quantum efficiency and by selection of more appropriate stimulation and detection conditions, the signal-to-noise ratio of OSL from silex might be considerably increased. For instance, green laser stimulation in combination with interference detection filters which are more accurately centered on the emission peaks (e.g. 380 nm or 470 nm) would reduce Raman scattering of excitation photons (at least for UV detection) and thus lead to higher net signal levels. In this respect, it also remains to be tested whether comparative single grain measurements of natural dose and administered laboratory dose (DRT) along with D_e-L_n/T_n-plots can provide more detailed information about internal dose distribution within silex samples.

8.4 Applied TL dating of heated lithics: achievements and problems

Due to less required sample material, the SAR protocol enabled dating of about 40 % more samples in this study than would have been possible just with multiple-aliquot tech-

niques. The TL SAR protocol has shown to work reliably for most samples, indicated by sucessful DRT's. In case SAR ages turned out to be not accurate, they were rejected in the interpretation in favor of MAAD ages or, accordingly, SAR ages taken as maximum ages (e.g. samples from Sodmein Cave). Many artefacts were at the lower size limit so that not enough material for DRT's was available. If, in such circumstances, only five to seven aliquots contributed to the final D_e, this result is certainly less reliable than ages of samples for which a DRT could be performed or for which additional MAAD ages could be gathered. Nevertheless, the SAR protocol proved to be of great value to increase the number of heated artefacts suitable for luminescence dating.

As outlined in detail in Chapters 3 and 4, non-uniformity of the internal dose rate may result in inaccruate and imprecise age estimates. In the course of SAR TL dating of the sample series from Românești-Dumbrăviţa I, it was suggested to use a plot of D_e versus L_n/T_n (sensitivity corrected natural TL) as a proxy for the presence of zones within the sample characterized by abnormally high dose rate. Accordingly, a D_e-plateau or a spread of D_e values comparable to DRT results indicate largely uniform distribution of radioelements. This approach, however, is valid only under the assumption that either the hot spot concentration is comparatively low or individual aliquots carry fewer grains as to average out differences in dose accumulated on a single grain level. Reduction of aliquot size was mostly impeded by dim TL signals, so that it is supposed that fine imbalances of dose distribution could not be identified. Nevertheless, substantial and spatially constraint non-uniformities ought to be detectable by this approach. In addition, the dispersion of values of L_n/T_n allows assessing the performance of the SAR sequence with regard to sensitivity correction.

The problem of non-uniform internal radiation was most apparent for the samples from Românești-Dumbrăviţa I. While those classified as type 2 samples (Section 6.6.2) showed substantial dispersion of equivalent doses (compared to DRT's), most samples of type 1 satisfied the criterion of a narrow D_e distribution (D_e-plateau within errors) to be considered for age determination of the find layer. However, selection of D_e values from this plateau only (within $1\,\sigma$, and discarding higher D_e values) in combination with a dose rate determined on bulk sample material results in minimum ages. Thus, heterogeneous character of the silex samples from Românești-Dumbrăviţa I hampered precise age determination of the time of occupation, but the true age most probably lies between the average SAR minimum age (~ 40 ka) and the average MAAD age (~ 45 ka). Largely uniform internal dose rate could be attributed to all other samples dated in this study, based on their D_e-L_n/T_n-plots (Figs. C.4, C.6 and C.10). It was thus not considered necessary to exclude any data.

The common problem faced when the external dose rate is to be assessed in excavations is that the original irradiation geometry is already destroyed when the heated silex sample for TL/OSL dating is discovered. In general, *in-situ* measurements of environmental radiation by use of highly-sensitive artificial dosimeters (e.g. α-Al_2O_3:C or BeO) is

preferred (Kalchgruber 2002; Tribolo et al. 2006; Sommer et al. 2007; Sommer et al. 2008; Schwenke 2008; Richter et al. 2010). For the samples dated in the present study, this was not possible in all cases due to temporally limited access to the excavated sites (Românești-Dumbrăviţa I) or the destruction of any sediment layers comparable to the find layers (Vale Boi). In the event of big rocks or blocks present in archeological layers (e.g. in caves or limestone regions), lateral gradients in γ-radiation may reach substantial extents so that dose rates determined by buried *in-situ* dosimeters might not represent the "true" values at the finding spot. For such circumstances, tedious and rather complex simulation and reconstruction methods have been developed (Brennan et al. 1997; Guibert et al. 1998). Such simulations, however, require detailed recording of shape, size, position and orientation of each inhomogeneity (e.g. limestone block) while excavating, being laborious and time consuming. Guérin & Mercier (2012) propose a non-invasive/non-destructive and successive *in-situ* measurement during excavation which allows reconstruction also of heterogeneous γ-radiation fields. For archeological excavations this might be the best approach to assess the actual environmental dose rate received by the artefact. The estimation of the moisture content of artefact-bearing sediments represents a basic limitation for increasing the accuracy and precision of a luminescence age. While the present water content can be measured in the laboratory, this value most likely was subject to substantial fluctuations during burial time, e.g. due to climatic changes. Upper and lower boundaries of water content are given by dry and saturated states, but the representative mean moisture content must be estimated from climatic records (if available) and/or the specific history of the site.

The sites from which artefacts were dated in this study, entailed various and partly challenging settings with respect to environmental dose rate determination. Homogeneous loessic sediments generated a uniform γ-radiation field for the dated artefacts from Românești-Dumbrăviţa I, but the water content could not be contained more precisely than $20 \pm 5\,\%$ (Section 6.6.1). By contrast, changing moisture content over time is expected to be less severe in cave sites, such as Las Palomas. Here, *in-situ* γ-probe measurements were carried out at several positions in the excavated chute to best capture the radiation levels relevant for the dated samples. However, to take into account potential temporal and local fluctuations, an additional moisture uncertainty of $10\,\%$ was added for age calculation. Similar conditions apply to the rock shelter Sodmein Cave with its heterogeneous deposits. However, the moisture content could be limited more precisely to $4 \pm 3\,\%$, due to the fact that the site is located in a region which has been (hyper-)arid for most of the burial time. Limestone fragments within the occupational layers at the site Vale Boi probably introduced severe gradients of γ-radiation which, however, could not be reconstructed because heated artefacts were handed out after excavation. The best approach possible was to collect samples for laboratory γ-spectrometry with varying "concentrations" of lithic fragments to assess the range of possible dose rates applicable to the artefact samples (see Section 7.2.2). Results and comparison with radiocarbon dates obtained for charcoal

of the Gravettian find layer show that the dose rate could obviously not be determined correctly because TL ages are significantly younger (by $\sim 50\,\%$) than radiocarbon data. Other causes for this disagreement can be practically rouled out, because MAAD and SAR protocols gave approximately identical D_e's, and other influencing variables such as the α-efficiency or the moisture content have too little impact on the calculated age as to explain the observed discrepancies.

To conclude, the huge compositional variability of silex used for lithic tool production requires individual assessment of dosimetry characteristics of each sample. This can be achieved by single-aliquot measurements and inspection of the resulting D_e distribution and the sensitivity-corrected natural TL of the aliquot (L_n/T_n). Of equal importance as D_e determination is the careful record of environmental radiation already during excavation of the site. The examples given in Chapter 7 illustrate that submission of heated silex artefacts for TL dating after completion of the pit is never recommendable and leads to valid results only in the least cases.

8.5 Outlook: spatially resolved dating of silex

The investigations in Chapters 3 and 4 have shown that radiation fields in lots of silex samples are not homogeneous. "Conventional" sample preparation comprises the crushing and homogenization of the sample's interior, in combination with HCl etching to destroy carbonates. This technique may be advantageous for homogeneous samples. It leads, however, to reduced accuracy and precision in case inclusions or foreign phases in the sample induce sharp peaks of dose rate. Furthermore, it cannot be ruled out that minerals other than SiO_2 are part of the measured sample material. These may show differing luminescence behavior and distort the determined radiation dose.

These difficulties related to the general impurity of silex ask for alternative approaches, especially for samples with severe influence of hot spots/zones which would have to be discarded otherwise. One possible procedure makes use of single-aliquot measurements to obtain more detailed insights into dose distribution within the sample, as shown in Chapter 6 and Section 8.3. Discrimination between suitable parts of a sample and regions with radioactivity peaks can be achieved by preservation of the original configuration of radiative elements. Instead of crushing, the specimen is cut in slices which serve both for dose and dose rate measurements. Generally, there are two approaches for spatially resolved luminescence measurements (Greilich 2004):

1. Spatially resolved stimulation (e.g. by a focused laser beam in case of OSL) and detection by an integrating device (e.g. photomultiplier)

2. "Bulk" stimulation and spatially resolved detection (e.g. by a CCD-camera)

For obvious difficulties of spatially resolved heating of a slice (with sufficient resolution), option 1 is excluded for TL measurements. With regard to the second option, early

investigations on photographing luminescence emitted by quartz date back to the 1980s (Huntley & Kirkey 1985; Hashimoto et al. 1986). Technical and methodological developments (Duller et al. 1997; Habermann et al. 2000; Spooner 2000) paved the way for more recent and applied studies on high resolution (HR-)OSL mainly focussing on OSL-dating the construction of monuments and buildings via the light shielding of rock or brick surfaces (Bailiff & Holland 2000; Greilich et al. 2005). TL was recorded using imaging systems by Spooner (2000) and Olko et al. (2008); Clark-Balzan & Schwenninger (2012) give a more detailed review of previous research in HR-luminescence detection.

Making use of spatially resolved detection, the recorded image of the emitted TL or OSL from a sample slice can be processed and the D_e of each pixel (i.e. corresponding quadrant on the slice) evaluated individually after a SAR procedure has been carried out. At this point, hot spots should appear as abnormally high D_e values, and only those pixels are combined to a representative matrix-D_e that lie within a D_e-plateau region. Contaminating phases (veins, inclusions) in a silex sample will thus not further contribute to the D_e distribution. Spatially resolved luminescence detection (HR-TL/-OSL) goes along with spatially resolved dose rate determination, to be carried out after dose measurements. Autoradiography can be used to qualitatively and – if calibrated – quantitatively check the investigated slice for radiation heterogeneities (see Chapter 3). However, other methods are also applicable such as neutron-induced fission track analysis, as done by Wagner et al. (2005), or the use of LA-ICP-MS measurements to determine radioelement concentrations at multiple spots at the measured surface. It remains to be tested whether highly sensitive artificial dosimeters such as Al_2O_3:C or BeO allow assessment of the dose rate experienced by certain regions of interest (ROIs with D_e-plateau). These dosimeters would have to be placed in direct contact to the sample surface and the evaluation afterwards be made spatially resolved, e.g. by a CCD-camera.

However, HR-luminescence dating of rock surfaces (slices) also yields challenges. Usually, half of the entire irradiation geometry (one hemisphere, $2\,\pi$) is not accessible to dose rate measurements, so that the missing part is assumed as being symmetrical to the investigated slice. For the two halfs of a cut silex artefact, at least the cutting width of the sawing blade ($\sim 1\,\mathrm{mm}$) is lost for further investigations. Additionally, problems related to regions with varying opacity arise what appears relevant especially for OSL (different light absorption properties for excitation and emitted light) and for silex samples which may show regions with varying opacity at a small scale (see Section 1.2). Another difficulty might be the spatially resolved determination of α-efficiency (Aitken & Wintle 1977; Greilich 2004).

References

Aitken, M., Wintle, A. G., 1977. Thermoluminescence dating of calcite and burnt flint: The age relation for slices. Archaeometry 19, 100–105.

Bailey, R., Smith, B. W., Rhodes, E. J., 1997. Partial bleaching and the decay form characteristics of quartz OSL. Radiation Measurements 27, 123–136.

Bailey, R., 2000. The slow component of quartz optically stimulated luminescence. Radiation Measurements 32, 233–246.

Bailiff, I., Holland, N., 2000. Dating bricks of the last two millennia from Newcastle upon Tyne: a preliminary study. Radiation Measurements 32, 615–619.

Bellomo, R., 1993. A methodological approach for identifying archaeological evidence of fire resulting from human activities. Journal of Archaeological Science 20, 525–553.

Brennan, B., Schwarcz, H., Rink, W., 1997. Simulation of the gamma radiation field in lumpy environments. Radiation Measurements 27, 299–305.

Clark-Balzan, L., Schwenninger, J.-L., 2012. First steps toward spatially resolved OSL dating with electron multiplying charge-coupled devices (EMCCDs): System design and image analysis. Radiation Measurements 47, 797–802.

Dean, J., 1978. Independent dating in archaeological analysis. Advances in Archaeological Method and Theory 1, 223–255.

Duller, G. A. T., Bøtter-Jensen, L., Markey, B. G., 1997. A luminescence imaging system based on a CCD camera. Radiation Measurements 27, 91–99.

Fairbanks, R. G., Mortlock, R. A., Chiu, T.-C., Cao, L., Kaplan, A., Guilderson, T. P., Fairbanks, T. W., Bloom, A. L., Grootes, P. M., Nadeau, M.-J., 2005. Radiocarbon calibration curve spanning 0 to 50,000 years BP based on paired ^{230}Th/^{234}U/^{238}U and ^{14}C dates on pristine corals. Quaternary Science Reviews 24, 1781–1796.

Geyh, M., 2005. Handbuch der physikalischen und chemischen Altersbestimmung. Wissenschaftliche Buchgesellschaft, Darmstadt.

Greilich, S., 2004. Über die Datierung von Gesteinsoberflächen mittels optisch stimulierter Lumineszenz. PhD thesis, Universität Heidelberg.

Greilich, S., Glasmacher, U., Wagner, G., 2005. Optical dating of granitic stone surfaces. Archaeometry 47, 645–665.

Guérin, G., Mercier, N., 2012. Field gamma spectrometry, Monte Carlo simulations and potential of non-invasive measurements. Geochronometria 39, 40–47.

Guibert, P., Bechtel, F., Schvoerer, M., Müller, P., Balescu, S., 1998. A new method for gamma dose-rate estimation of heterogeneous media in TL dating. Radiation Measurements 29, 561–572.

Habermann, J., Schilles, T., Kalchgruber, R., Wagner, G. A., 2000. Steps towards surface dating using luminescence. Radiation Measurements 32, 847–851.

Hashimoto, T., Hayashi, Y., Koyanagi, A., Yokosaka, K., Kimura, K., 1986. Red and blue colouration of thermoluminescence from natural quartz sands. Nuclear Tracks and Radiation Measurements 11, 229–235.

Higham, T., 2011. European Middle and Upper Palaeolithic radiocarbon dates are often older than they look: problems with previous dates and some remedies. Antiquity 85, 235–249.

Huntley, D. J., Kirkey, J. J., 1985. The use of an image intensifier to study the TL intensity variability of individual grains. Ancient TL 3, 1–4.

Kalchgruber, R., 2002. α-Al_2O_3:C als Dosimeter zur Bestimmung der Dosisleistung bei der Lumineszenzdatierung. PhD thesis, Universität Heidelberg.

Li, S.-H., Tso, M.-Y. W., Wong, N., 1997. Parameters of OSL traps determined with various linear heating rates. Radiation Measurements 27, 43–47.

Li, S.-H., 2001. Identification of well-bleached grains in the optical dating of quartz. Quaternary Science Reviews 20, 1365–1370.

Mercier, N., 1991. Flint palaeodose determination at the onset of saturation. Nuclear Tracks and Radiation Measurements 18, 77–79.

Mercier, N., Valladas, H., Valladas, G., 1992. Observations on palaeodose determination with burnt flints. Ancient TL 10, 28–32.

Murray, A. S., Wintle, A. G., 2000. Luminescence dating of quartz using an improved single-aliquot regenerative-dose protocol. Radiation Measurements 32, 57–73.

Olko, P., Czopyk, L., Klosowski, M., Waligórski, M. P., 2008. Thermoluminescence dosimetry using TL-readers equipped with CCD cameras. Radiation Measurements 43, 864–869.

Reimer, P., Baillie, M., Bard, E., Bayliss, A., Beck, J., Blackwell5, P., Ramsey, C. B., Buck, C., Burr, G., Edwards, R., Friedrich, M., Grootes, P., Guilderson, T., Hajdas, I., Heaton, T., Hogg, A., Hughen, K., Kaiser, K., Kromer, B., McCormac, F., Manning, S., Reimer, R., Richards, D., Southon, J., Talamo, S., Turney, C., van der Plicht, J., Weyhenmeyer, C., 2009. Intcal09 and Marine09 radiocarbon age calibration curves, 0–50,000 years cal BP. Radiocarbon 51, 1111–1150.

Richter, D., Krbetschek, M., Rieser, U., Trautmann, T., Wagner, G., 1999. Spectral investigation of the thermoluminescence of heated flint (silex). Quaternary Geochronology 18, 279–285.

Richter, D., Krbetschek, M., 2006. A new thermoluminescence dating technique for heated flint. Archaeometry 48, 695–705.

Richter, D., 2007a. Advantages and limitations of thermoluminescence dating of heated flint from Paleolithic sites. Geoarchaeology 22, 671–683.

Richter, D., 2007b. Feuer und Stein – Altersbestimmung von steinzeitlichem Feuerstein mit Thermolumineszenz. In: Wagner, G. (Ed.), Einführung in die Archäometrie. Springer, Berlin and Heidelberg. 33–49.

Richter, D., Tostevin, G., Škrdla, P., Davies, W., 2009. New radiometric ages for the Early Upper Palaeolithic type locality of Brno-Bohunice (Czech Republic): comparison of OSL, IRSL, TL and ^{14}C dating results. Journal of Archaeological Science 36, 708–720.

Richter, D., Dombrowski, H., Neumaier, S., Guibert, P., Zink, A. C., 2010. Environmental gamma dosimetry with OSL of α-Al_2O_3:C for in-situ measurements. Radiation Protection Dosimetry 141, 27–35.

Scharpenseel, H. W., Schiffmann, H., 1977. Radiocarbon dating of soils, a review. Zeitschrift Pflanzenernährung und Bodenkunde 140, 159–174.

Schwenke, M., 2008. Optimierung eines Auswerteverfahrens für Optisch Stimulierte Lumineszenz (OSL) mit Berylliumoxid. MA thesis, TU Dresden.

Singarayer, J. S., Bailey, R., 2003. Further investigations of the quartz optically stimulated luminescence components using linear modulation. Radiation Measurements 37, 451–458.

Smith, B. W., Rhodes, E. J., 1994. Charge movements in quartz and their relevance to optical dating. Radiation Measurements 23, 329–333.

Sommer, M., Freudenberg, R., Henniger, J., 2007. New aspects of a BeO-based optically stimulated luminescence dosimeter. Radiation Measurements 42, 617–620.

Sommer, M., Jahn, A., Henniger, J., 2008. Beryllium oxide as optically stimulated luminescence dosimeter. Radiation Measurements 43, 353–356.

Spooner, N. A., 2000. A photon-counting imaging system (PCIS) for luminescence applications. Radiation Measurements 32, 513–521.

Tribolo, C., Mercier, N., Valladas, H., 2001. Alpha sensitivity determination in quartzite using an OSL single aliquot procedure. Ancient TL 19, 47–50.

Tribolo, C., Mercier, N., Selo, M., Valladas, H., Joron, J.-L., Reyss, J.-L., Henshilwood, C., Sealy, J., Yates, R., 2006. TL dating of burnt lithics from Blombos Cave (South Africa): Further evidence for the antiquity of modern human behaviour. Archaeometry 48, 341–357.

Valladas, G., Gillot, P. Y., 1978. Dating of the Olby lava flow using heated quartz pebbles: some problems. PACT 2, 141–150.

Wagner, G. A., Glasmacher, U. A., Greilich, S., 2005. Spatially resolved dose-rate determination in rocks and ceramics by neutron-induced fission tracks: fundamentals. Radiation Measurements 40, 26–31.

Weninger, B., Danzeglocke, U., Jöris, O., 2007. Comparison of dating results achieved using different radiocarbon-age calibration curves and data. http://www.calpal.de/calpal/files/CalCurveComparisons.pdf (accessed 22/06/2012).

Weninger, B., Jöris, O., 2008. A ^{14}C age calibration curve for the last 60 ka: the Greenland-Hulu U/Th timescale and its impact on understanding the Middle to Upper Paleolithic transition in Western Eurasia. Journal of Human Evolution 55, 772–781.

Westaway, K., Prescott, J., 2012. Investigating signal evolution: A comparison of red and UV/blue TL, and UV OSL emissions from the same quartz sample. Radiation Measurements 47, 909–915.

9 Abstract

Thermoluminescence (TL) dating of heated silex artefacts represents an important chronometric tool for Middle to Upper Paleolithic archeological contexts. Since the firing of these lithics can legitimately be attributed to human agency, this method provides direct age estimates of the occupation of a site. However, in relation to other dating methods, the precision of TL dates is comparatively low, and the often observed "overdispersion" in ages of obviously syndepositional finds indicates additional sources of scatter mainly disregarded so far. This thesis examines potential sources of both imprecision and inaccuracy of age estimates as well as the capability of alternative approaches to overcome or reduce these shortcomings of the TL method applied to heated silex.

Besides assessing the influence of spurious luminescence signal contributions from sample carriers on determined dose, focus is set on investigating strength and uniformity of the internal dose rate of silex samples and resulting effects on the age. Being constant over burial time, self-dosing may either decrease the influence of elusive and variable external radiation – in case of homogeneous radioelement distribution within the sample – or introduce systematic errors and enhanced data scatter, if radiation is concentrated in "hot spots". With α- and β-autoradiography and laser ablation inductively coupled plasma mass spectrometry (LA-ICP-MS), both qualitative and quantitative approaches served to draw a detailed picture on presence and spatial distribution of hot spots and associated impurities in thick sections of over 20 silex specimens. While the low β-activity of most samples is rarely visible on respective autoradiographs, recorded α-tracks revealed zones and spots with strongly increased Th and U concentrations. Comparison of autoradiographs with sample surfaces shows a clear relationship between track density and impurities or filled cracks. These findings are confirmed by LA-ICP-MS: In contrast to the low radioactivity of pure silex, most kinds of impurities are related to strongly increased radiation. If this is not accounted for, micro-dosimetric effects may lead to random and systematic errors in age determination.

Additionally, the performance of TL single-aliquot regenerative-dose (SAR) protocols for dating small-sized samples and as a diagnostic tool for non-uniform dose distribution in the samples was tested. For both the blue ($\sim 475\,\mathrm{nm}$) and red ($\sim 630\,\mathrm{nm}$) TL emission it was found that the degree of adequate sensitivity-correction by test dose monitoring strongly depends on the properties of individual samples. However, laboratory doses could be well reproduced for most specimens. By comparing D_e distributions from natural dose measurements and dose recovery tests and regarding the value range of sensitivity cor-

rected natural signals (L_n/T_n), assessment of sample homogeneity and SAR dose response behavior is enabled, respectively.

Unlike for commonly used TL, few is known about optically stimulated luminescence (OSL) of silex. However, access to specific, optically sensitive trap populations (e.g. *slow*-components) and more gentle heat treatment in the course of SAR sequences may yield the benefits of increased saturation dose levels (and hence upper dating limits) and reduced systematic errors, respectively. Therefore, fundamental properties such as signal composition and thermal long-term stability of silex OSL were studied and its applicability to heated samples evaluated. First-order fitting of linearly modulated (LM-) OSL curves showed best results for five components in most cases. Pulse annealing experiments and the varying heating rate method, however, attested only the best bleachable component sufficient thermal stability. Successful dose recovery tests and OSL ages in agreement to TL ages of the same samples validate the general applicability of this OSL component for dating. However, since not all silex varieties show an optical signal at all, this approach may be regarded as complementary to TL and reassuring for important samples.

In the applied part of this thesis, several sets of heated artefacts from Middle and Upper Paleolithic sites in Portugal, Spain, Romania and Egypt were TL and OSL dated. Gravettian samples from Vale Boi (Portugal) were submitted for dating after termination of the excavation, so that environmental radiation could not be determined accurately. This is very likely the reason for the significant deviation between radiocarbon dates of the same layer and TL ages, because SAR and multiple-aliquot additive-dose (MAAD) ages of the same sample agree and other influencing variables such as the α-effciency or the moisture content have too little impact on the calculated age as to explain the observed discrepancies. The SAR approach allowed dating the relatively small silex samples from the cave site Las Palomas (Spain). Here, successful dose recovery tests indicated the suitability of the measurement procedure, and *in-situ* measurements of γ-radiation provided more accurate dose rate information. As a result, TL ages between ~ 51 and ~ 84 ka allow a first chronometric assessment of the formerly undated archeological remains. Artefacts from the Aurignacian site Românești-Dumbrăviţa I (Romania) proved to be more problematic, as part of them had to be discarded due to poor dose reproducibility. SAR measurements, dose recovery tests and their detailed analyses suggested internal non-uniformities of most samples, so that only rigorous data filtering allowed extraction of reliable age estimates. Due to the luminescence behavior of dated samples, the occupation of the site could, however, not be narrowed down to a range smaller than ~ 39–45 ka, giving a weighted average age of 40.6 ± 1.5 ka for the Aurignacian find layer. Furthermore, two TL emissions (blue and red) and two protocols (SAR and MAAD) were applied to heated silex from Sodmein Cave (Egypt). Dose recovery tests showed uncorrectable sensitivity changes of the TL signal, rendering the TL SAR sequence inaccurate for these samples. Consequently, age estimates are based on TL MAAD and OSL SAR data; for the smallest sample only a TL SAR maximum age can be given. Coming from different depths of a huge hearth,

TL ages of dated samples indicate a large time span to be condensed in the archeological deposits, probably reaching from MIS 5e to MIS 5a.

10 Kurzzusammenfassung

Thermolumineszenz (TL) erhitzter Silex-Artefakte stellt eine bedeutende Datierungsmethode für Mittel- und Jungpaläolithische Fundsituationen dar. Da die Erhitzung der Werkzeuge mit großer Sicherheit menschlichem Handeln zuzuschreiben ist, liefert diese Methode direkte Alter für die prähistorische Besiedlung. In Relation zu anderen Datierungsmethoden weisen TL-Alter jedoch eine vergleichsweise geringe Präzision auf, und die vielfach beobachtete Altersdivergenz von Funden aus der gleichen Schicht deutet auf zusätzliche, bisher wenig beachtete Fehlerquellen hin.

Die vorliegende Arbeit untersucht mögliche Ursachen verringerter Genauigkeit und Präzision von TL-Altern an erhitztem Silex sowie das Potential alternativer Ansätze zur methodischen Weiterentwicklung. Neben dem Einfluss von Lumineszenz-Störsignalen von Probenträgern auf die bestimmte Dosis einer Probe stehen vor allem die Untersuchung der Stärke und Homogenität der internen Dosisleistung von Silex sowie entsprechende Auswirkungen auf das berechnete Alter im Mittelpunkt. Als zeitlich konstante Größe kann die "Selbstbestrahlung" einer Probe entweder den Einfluss der oft schwer fassbaren und veränderlichen externen Dosisleistung verringern (im Falle von homogener Radionuklidverteilung in der Probe) oder aber zu systematischen Fehlern und verringerter Präzision führen, falls die Strahlung in "Hot Spots" konzentriert ist. Mit α- und β-Autoradiographie und laser ablation inductively coupled plasma mass spectrometry (LA-ICP-MS) dienten sowohl quantitative als auch qualitative Methoden dazu, detaillierten Einblick in Anzahl und Verteilung von Hot Spots sowie assoziierten mineralogischen Unreinheiten in über 20 Silex-Proben zu gewinnen. Während die geringe β-Aktivität der meisten Proben auf den Autoradiographien kaum sichtbar war, zeigte die Verteilung der α-Spuren Zonen von deutlich erhöhtem Th- und U-Gehalt. Der Vergleich von Autoradiographien und den Probenoberflächen weist einen klaren Zusammenhang zwischen Spurdichte und mineralogischen Unreinheiten nach. Bestätigt werden diese Befunde durch LA-ICP-MS, wonach reiner Silex sehr geringe Radioaktivität aufweist, die meisten Unreinheiten aber mit erhöhter Strahlung einhergehen. Berücksichtigt man dies nicht im Datierungsprozess, können mikrodosimetrische Effekte zu systematischen und zufälligen Fehlern bei der Altersberechnung führen.

Weiterhin wurde das Potential von TL single-aliquot regenerative-dose (SAR) Messprotokollen zur Datierung kleiner Silex-Proben und zum Nachweis ungleichmäßiger Dosisverteilung im Inneren einer Probe getestet. Sowohl für die blaue ($\sim 475\,\mathrm{nm}$) als auch für die rote ($\sim 630\,\mathrm{nm}$) TL-Emission hängt der Grad erfolgreicher Sensitivitätskorrektur mittels

Testdosismessungen sehr stark von individuellen Probeneigenschaften ab. Für die meisten Proben jedoch konnten applizierte Labordosen innerhalb der Messunsicherheit reproduziert werden. Der Vergleich von D_e-Verteilungen natürlicher Dosismessungen und von "dose recovery tests" sowie der Wertebereich der sensitivitätskorrigierten Lumineszenzsignale (L_n/T_n) erlauben eine Einschätzung der Probenhomogenität bzw. der Änderung der Dosissensitivität zu Beginn des SAR-Zyklus.

Im Gegensatz zur TL ist nur wenig bekannt über optisch stimulierte Lumineszenz (OSL) von Silex. Die Beprobung spezieller, optisch sensitiver Elektronenfallenpopulationen (z.B. *slow*-Komponenten) und geringere thermische Einwirkungen während regenerativer Messungen könnten zum einen den Vorteil höherer Sättigungsdosen bringen (und damit den datierbaren Zeitraum verlängern), zum anderen systematische Fehler im Zuge der Sensitivitätskorrektur verringern. Deshalb wurden grundlegende Eigenschaften der OSL von Silex, wie etwa die Zusammensetzung des Signals und dessen thermische Langzeitstabilität, untersucht und die Anwendbarkeit von OSL zur Silex-Datierung getestet. Kurvenanpassung (Kinetik erster Ordnung) von "linearly modulated" (LM-) OSL-Daten zeigte für fünf Signalkomponenten die besten Ergebnisse. "Pulse annealing"-Experimente und die Methode variabler Heizraten attestierten jedoch nur der optisch sensitivsten Komponente ausreichende thermische Stabilität. Erfolgreiche "dose recovery tests" und übereinstimmende OSL- und TL-Alter der gleichen Probe bestätigen die generelle Anwendbarkeit dieser Signalkomponente für die Datierung. Da jedoch nicht alle Silex-Varietäten ein OSL-Signal zeigen, muss diese Methode als komplementär zur TL und als Rückversicherung für wichtige Proben angesehen werden.

Als anwendungsbezogener Teil dieser Arbeit wurden mehrere Proben-Serien erhitzter Artefakte aus Mittel- und Jungpaläolithischen Fundplätzen in Portugal, Spanien, Rumänien und Ägypten mittels TL und OSL datiert. Für Gravettian-zeitliche Proben aus Vale Boi (Portugal) konnte wegen der erfolgten Abtragung des originären Fundkontextes die externe Dosisleistung nur unzureichend bestimmt werden. Dies ist sehr wahrscheinlich der Grund für die signifikante Abweichung zwischen ^{14}C-Altern der Fundschicht und den TL-Altern, da SAR-Alter und multiple-aliquot additive-dose (MAAD)-Alter der selben Probe übereinstimmen und andere Einflussgrößen wie der Feuchtigkeitsgehalt oder die α-Sensitivität zu geringen Einfluss auf das Alter haben, um die Unterschiede erklären zu können. Die SAR-Methode erlaubte weiterhin die Datierung kleiner Artefakte aus der Höhlenfundstelle Las Palomas (Spanien). Gute Dosisreproduzierbarkeit bestätigte die Eignung des Protokolls für die Proben; vor-Ort Messungen ermöglichten zudem eine genauere Quantifizierung der γ-Dosisleistung. Resultierende TL-Alter zwischen $\sim$51 und $\sim$84 ka geben eine erste chronometrische Einschätzung der vormals undatierten archäologischen Ablagerungen. Artefakte der Aurignacian-Fundstelle Românești-Dumbrăviţa I (Rumänien) stellten sich als problematischer heraus, da ein erheblicher Teil der Stücke wegen schlechter Dosisreproduzierbarkeit verworfen werden musste. SAR-Messungen, "dose recovery tests" sowie deren detaillierte Analysen deuteten auf heterogene Dosisleistungs-

verteilung hin, so dass nur striktes Filtern der Daten zu zuverlässigen Altern führte. Aufgrund der Lumineszenzeigenschaften der Proben konnte die Zeit der Besiedlung nicht näher als ~ 39–45 ka eingegrenzt werden, wobei sich rechnerisch ein gewichtetes Mittel von $40{,}6 \pm 1{,}5$ ka für die Aurignacian-Fundschicht ergibt. Weiterhin wurden Silex-Fundstücke aus der Sodmein-Höhle (Ägypten) mit zwei Messprotokollen (SAR und MAAD) und zwei verschiedenen TL-Emissionen (blau und rot) datiert. Dose recovery tests zeigten unkorrigierbare Sensitivitätsänderungen, so dass die SAR-Daten als ungenau zu betrachten sind. Deshalb basieren die berechneten Alter auf TL-MAAD- und OSL-SAR-Daten; für die kleinste Probe konnte jedoch nur ein SAR-Maximalalter angegeben werden. Die Alter der Proben, die aus unterschiedlichen Schichten einer großen Feuerstelle stammen, weisen auf eine chronologische Tiefe der archäologischen Ablagerungen hin, die wahrscheinlich vom MIS 5e zum MIS 5a reicht.

Appendices

A Supplementary material of publications

A.1 Supplementary material for Chapter 2

During the investigation of empty sample carries, several figures and plots were produced, for which it was not possible to show them in the article. This document contains additional fgures. It may help the interested reader to further assess the outcome of our experiments. All experiments are described in detail in the article or in the caption of the figures. The figures are ordered in terms of the sample carrier materials.

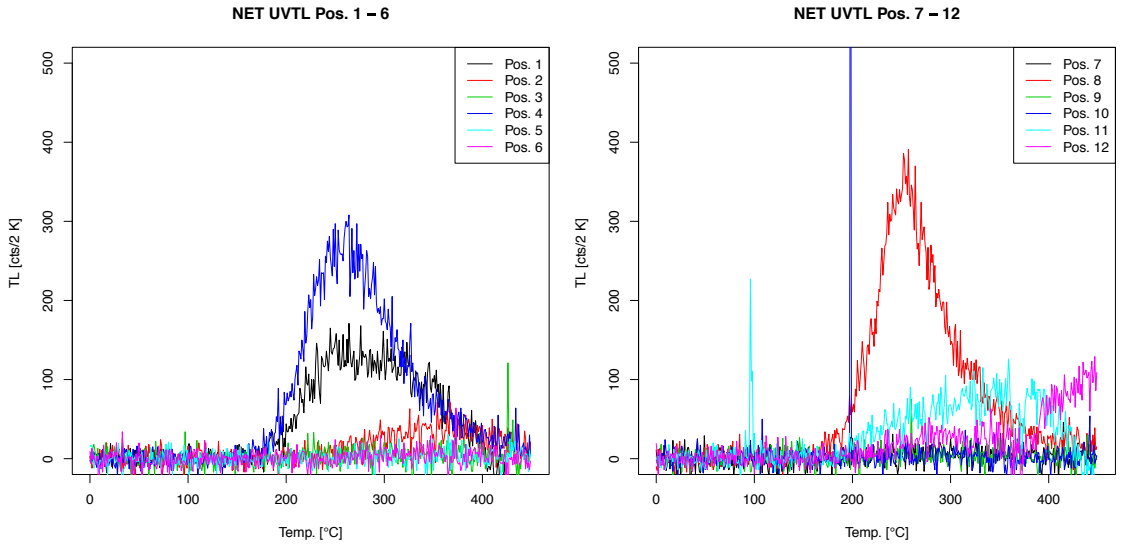

Figure A.1: UVTL signal of 12 empty, used and cleaned Al discs, measured using N_2 without irradiation and background subtraction. The discs were heated up to 430 °C with a heating rate of $2\,\mathrm{K\,s^{-1}}$. Three out of 12 discs show a remarkable peak between 200 and 300 °C. For one sample a small peak at ca. 350 °C was recorded. The TL signal originating from the black body radiation is negligible.

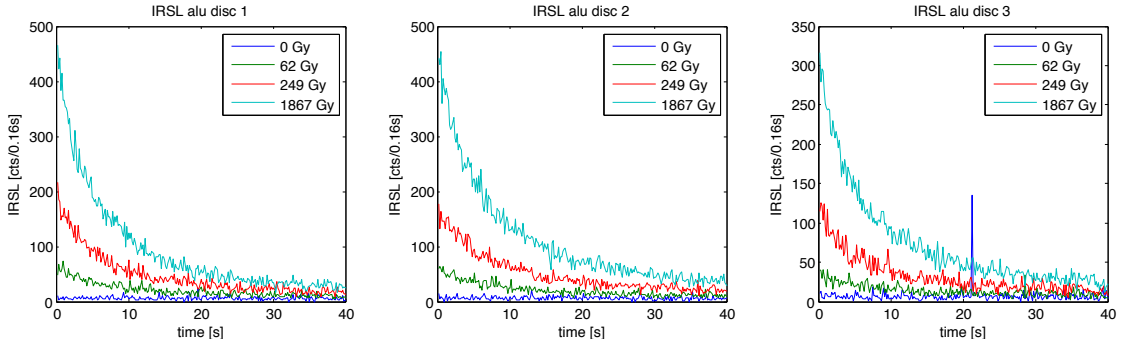

Figure A.2: IRSL signal of three clean, empty Al discs after preheating. After measuring the natural signal, the discs received β-doses of ca. 62, 249 and 1867 Gy.

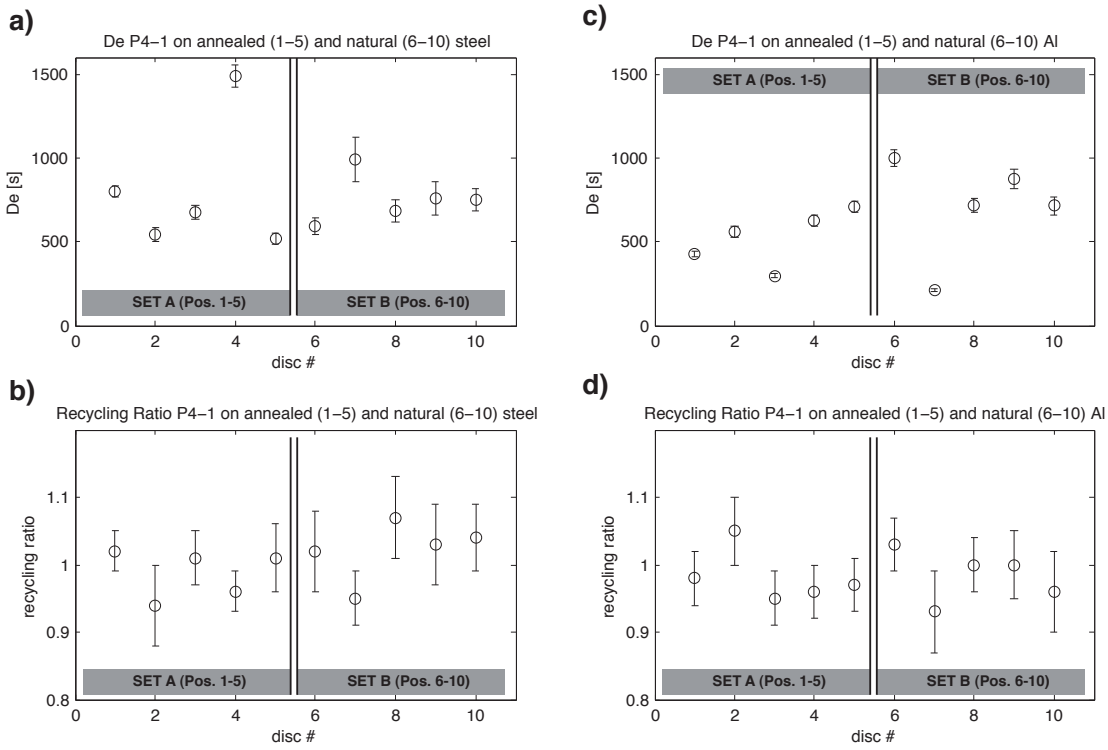

Figure A.3: Results of D_e estimation with BOSL of a loess coarse grain (100–200 µm) quartz sample from Nussloch/Germany (sample code: BT781, compare P4-1 unit in Tissoux et al. (2010) and Zöller et al. (1988)) for Al and steel discs. Ten discs were measured for every disc type and divided in two subsets of five discs each. The first subset (set A) contains discs which were annealed at 500 °C for 30 s previous to the D_e determination. For the second subset (set B) no annealing was carried out. The figure shows the measured D_e (a) for steel and (c) for Al discs and the corresponding recycling ratios (b) for steel and (d) for Al discs. The annealing procedure slightly reduces the error of each individual D_e. This effect is more pronounced for steel discs than for Al discs.

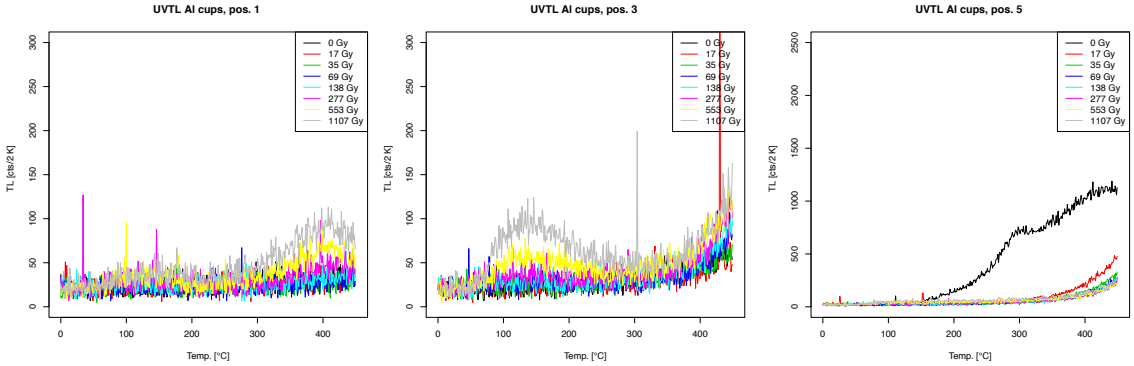

Figure A.4: UVTL measurements without background subtraction on new, empty Al cups with increasing β-doses up to ca. 1 kGy. The cups show a negligible 110 °C peak for high β-doses. The high natural peak on the third plot results from an accidental loss of N_2 during the measurement.

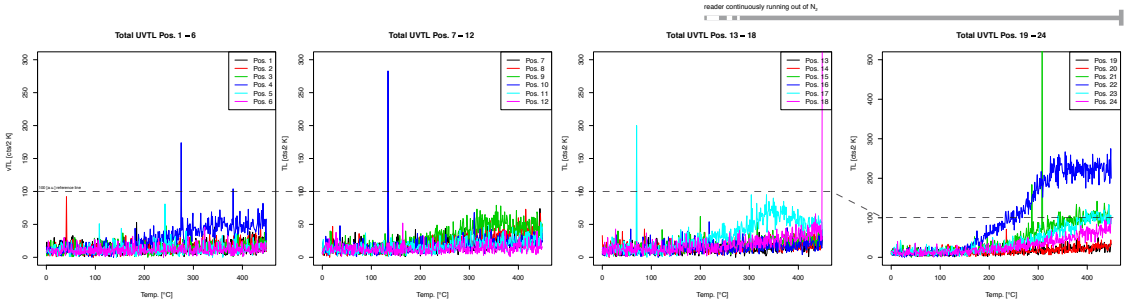

Figure A.5: Measurement of the natural UVTL signal of 24 new Al cups without background subtraction in a N_2 atmosphere. To reproduce the effect of N_2 loss during the measurement (Fig. A.4) the N_2 concentration was continuously lowered during the measurement. The Al cups are free from spurious signals if N_2 is used.

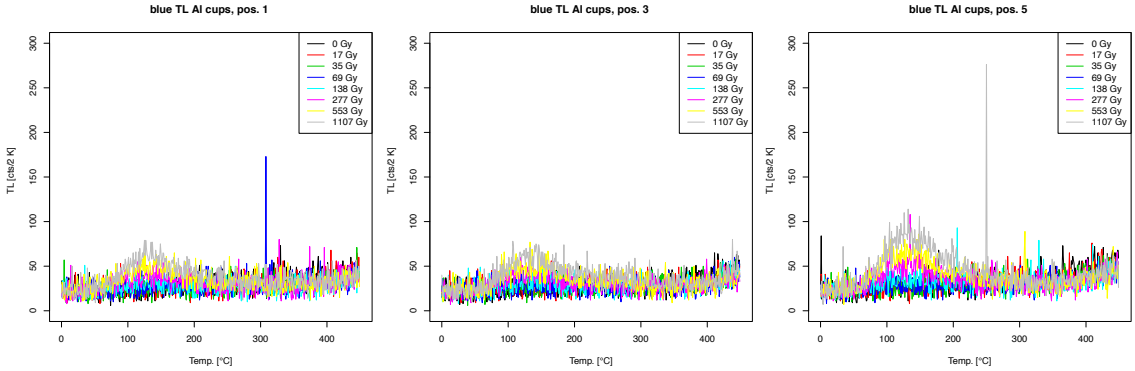

Figure A.6: Natural and regenerated TL signals without background subtraction, measured in the blue detection window using N_2. The samples were β-dosed up to ca. 1 kGy. The investigated Al cups show no markedly natural or regenerated BTL signal.

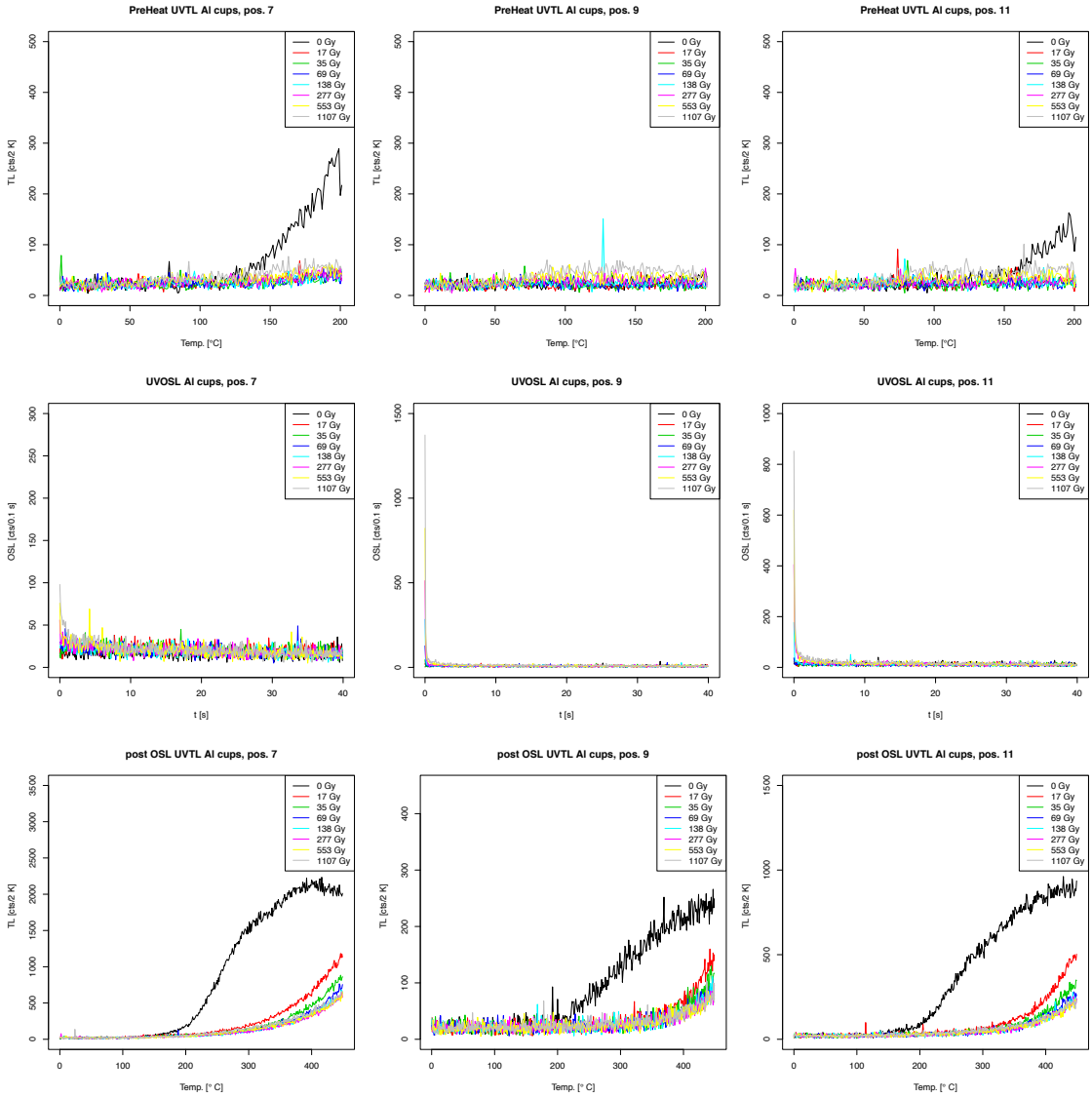

Figure A.7: The natural and regenerated **BOSL** signals, detected in the UV window, were recorded for three Al cups at 125 °C for 40 s (middle row). The measurements included a preheat step (200 °C for 10 s, upper row) before and a final TL measurement up to 430 °C after OSL readout to detect photo-transferred and optically unbleachable signal contributions (lower row). The cups were β-dosed up to ca. 1 kGy. No N_2 was used. For β-doses < 500 Gy the Al cups are free from substantial BOSL signals. For higher doses, a peak in the foremost signal channels was detected.

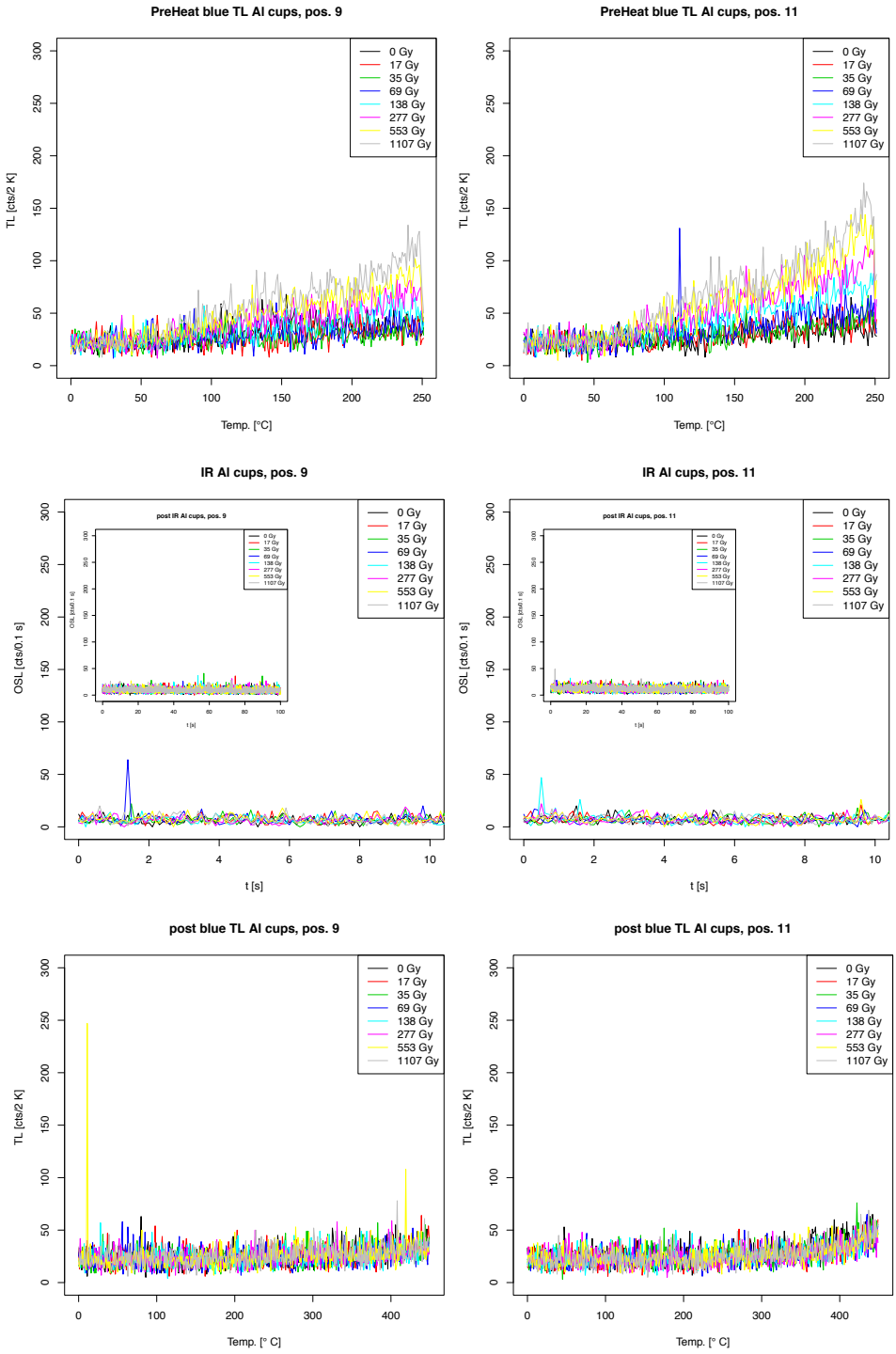

Figure A.8: The natural and regenerated **IRSL** signals in the blue detection range were recorded for three Al cups in a N_2 atmosphere. The measurements included a preheat step (250 °C for 60 s), IRSL stimulation at 50 °C for 100 s and subsequent IRSL stimulation (post-IR IRSL) at 225 °C for 100 s (only the first 10 s of each shine down curve are shown). A TL measurement up to 430 °C finished the measurement cycle. The cups were β-dosed up to ca. 1 kGy. Over the investigated dose range the Al cups are free from IRSL signals.

A.2 Supplementary material for Chapter 3

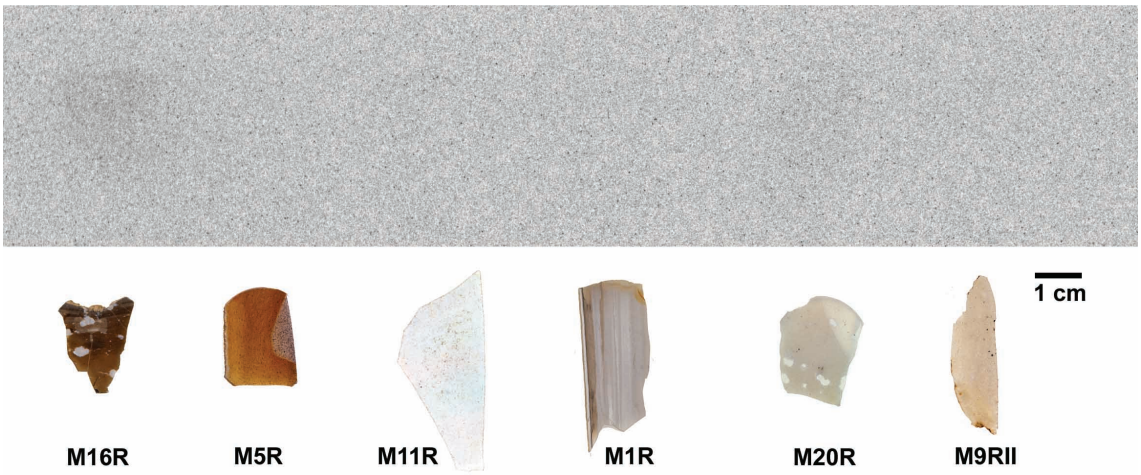

Figure A.9: Beta-autoradiographs and color scans of sample batch 2.

Figure A.10: Beta-autoradiographs and color scans of sample batch 3.

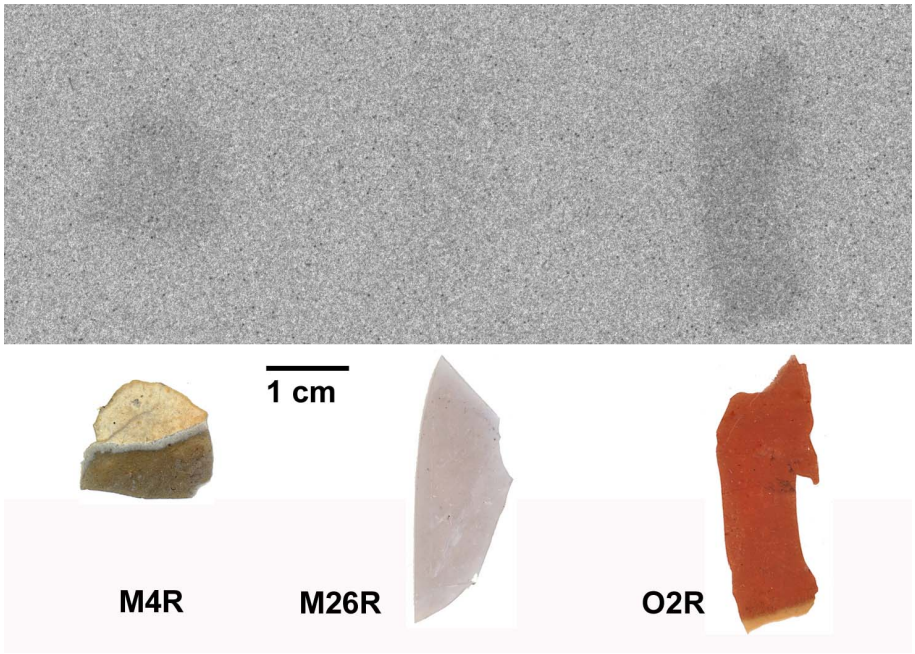

Figure A.11: Beta-autoradiographs and color scans of sample batch 4.

MATLAB code used for simulation of Poisson fields, slightly modified from http://www-math.bgsu.edu/z/rfim/ (last access 15/03/2011):

```
m = 500; % avg number of points
s = 0;
N = -1;
while (s<m)
s = s - log(rand);
N = N + 1; % N ∼ Poisson(m)
end
a = rand(N,1); % Poisson process points in R^2
b = rand(N,1);
```

MATLAB code for identification and localization of α-tracks in scans of CR-39 detectors:

Load image and convert into gray scale

```
M=imread('09_50x_aufstitch_cut2.jpg');
R=M(:,:,1);G=M(:,:,2);B=M(:,:,3);
Y=uint8(0.299*double(R)+0.587*double(G)+0.114*double(B));
Y = 255-Y;
image(Y);colormap gray;
```

```
fig1 = figure(1);
pos1 = get(fig1,'Position');
imshow(Y);
axis image
```

Find circles

```
[accum, circen, cirrad] = CircularHough_Grd(Y, [0.5, 20],45,8);
```

Sort circle matrix (N,2) and delete identical entries (concentric circles)

```
crc = sortrows(circen,1);
% Sort rows of circle matrix in ascending order
crc = unique(crc,'rows');
% delete redundant entries
Diff = length(circen)-length(crc);
% number of double counted tracks
```

Plot circles in the image with tracks

```
fig2 = figure(1);
pos2 = get(fig2,'Position');
image(Y);colormap gray;
hold on;
plot(crc(:,1),crc(:,2),'r+');
axis image
```

2D binning of the image (ROIs) of variable size

```
pix = 100;
% number of pixels per side of square
nx = floor(length(Y)/pix);
% number of columns that fit in image
ny = floor(length(Y(:,2))/pix);
% number of rows that fit in image
xval = crc(:,1);
yval = crc(:,2);
M = [];   % Create matrix to store the xval's
for q = 1:nx;
M = [M xval-q*pix];   % subtract pix
```

```
if q < nx+1;   % reduced xval's now stored in M
q+1;
end;
end;
N = [];
for r = 1:ny;
N = [N yval-r*pix];
if r < ny+1;
r+1;
end;
end;
[x col] = min(abs(M));
[y row] = min(abs(N));

% find minimum of absolute values, i.e. x = pix, 2*pix etc.
% x and y should be zero or at least less than ~ 3
% col is the cumulative number of tracks in the columns and
% the boarder marks for the ROIs
% row is not useful since the y values in the pk matrix are not
% ordered (finding the absolute minimum gives arbitrary values!)

D = [col(1,1)];
for h = 1:nx-1;
D = [D;col(:,h+1)-col(:,h)];
if h < nx-1;
h+1;
end
end

% D is vector that contains the differences between the x boarder
% marks, e.g. x2-x1, x3-x2 etc.

maxD = max(D);
```

Store x and y coordinates of the columns in a cell array

```
pkcol1 = [crc(1:col(1),1) crc(1:col(1),2)];
clear L
L(1,:) = crc(1:col(1),1),crc(1:col(1),2);
for i = 1:(length(col)-1);
```

```
L(i+1,:) = crc(col(i):col(i+1),1),crc(col(i):col(i+1),2);
if i < length(col);
i+1;
end;
end;
% L is a cell array (dimension: length(col),2) that contains
% the x and corresponding y coordinates of the tracks
% in the first, second, third, ... column of the image
```

Find number of tracks in separate rows for each column

```
clear counts
for j = 1:nx;
for i = 1:ny;
number = find((i-1)*pix <= Lj,2(:,1) & Lj,2(:,1) <= i*pix);
counts(i,j) = length(number);
end;
end;
% counts is a matrix containing the numbers of tracks in each
% square (nx,ny)
clear err
err = round(sqrt(counts));
% poisson error, also given as matrix of the squares
```

Save the count matrix and the poisson error in txt-file

```
dlmwrite('N1_100pix.txt',counts,'delimiter','\t','precision',3,...
'newline', 'pc');
dlmwrite('N1_100pix.txt', err, '-append','roffset', 1, 'delimiter',
'\t',...
'newline', 'pc');
```

A.3 Supplementary material for Chapter 4

Table A.1: Numerical results of comparative LA- and bulk ICP-MS measurements of selected silex samples.

	K [wt.%]					
	LA	1 σ uncertainty	Bulk	1 σ uncertainty	Bulk/LA	1 σ uncertainty
M5R	0.026	0.004	0.040	0.003	1.5	0.3
M12R	0.009	0.001	0.010	0.001	1.1	0.2
M17R	0.029	0.002	0.040	0.003	1.4	0.1
M26R	0.0144	0.0004	0.100	0.007	6.9	0.5
O4	0.061	0.012	0.080	0.006	1.3	0.3
O6	0.030	0.013	0.030	0.002	1.0	0.5
O8	0.17	0.16	0.100	0.007	0.6	0.6

	Th [µg g^{-1}]					
	LA	1 σ uncertainty	Bulk	1 σ uncertainty	Bulk/LA	1 σ uncertainty
M5R	0.11	0.13	0.16	0.02	1.5	1.8
M12R	0.007	0.002	0.030	0.003	4.2	1.2
M17R	0.012	0.003	0.08	0.01	6.7	1.6
M26R	0.030	0.003	0.41	0.04	13.5	1.8
O4	0.11	0.05	0.20	0.02	1.9	0.9
O6	0.06	0.03	0.10	0.01	1.7	1.0
O8	0.22	0.39	0.29	0.03	1.3	2.4

	U [µg g^{-1}]					
	LA	1 σ uncertainty	Bulk	1 σ uncertainty	Bulk/LA	1 σ uncertainty
M5R	0.20	0.06	0.22	0.03	1.1	0.4
M12R	0.34	0.20	0.36	0.04	1.1	0.7
M17R	0.09	0.02	0.08	0.01	0.9	0.2
M26R	0.33	0.02	0.36	0.04	1.1	0.1
O4	0.12	0.02	0.14	0.02	1.1	0.2
O6	0.68	0.16	0.86	0.10	1.3	0.3
O8	0.52	0.45	0.41	0.05	0.8	0.7

	Rb [µg g^{-1}]					
	LA	1 σ uncertainty	Bulk	1 σ uncertainty	Bulk/LA	1 σ uncertainty
M5R	0.59	0.31	0.73	0.04	1.2	0.7
M12R	0.08	0.02	0.11	0.01	1.4	0.3
M17R	4.11	0.24	4.93	0.25	1.2	0.1
M26R	0.18	0.02	3.00	0.15	16.9	1.7
O4	1.77	0.35	1.89	0.09	1.1	0.2
O6	1.39	0.45	1.22	0.06	0.9	0.3
O8	5.32	4.85	3.34	0.17	0.6	0.6

Table A.2: LA-ICP-MS results for major, minor and trace elements, as measured in various types of impurities of selected silex samples. All concentrations are given in µg g^{-1}.

Sample	Type	Li	B	Na	Mg	Al	Si	P	K	Ca	Ti	Mn	Fe
M16R	E	22	10.9	500	212000	4010	37200	280	3460	385000	191	500	8000
M16R	A	5.7	55	185	300	1200	463000	3.40	520	1020	24	0.78	138
M16R	B	5.6	3	30	860	1030	97100	15.9	340	557000	70	620	2440
M16R	F	8.8	5	18	2060	230	91600	16.3	82	565000	2.18	540	2670
M16R	D	1.56	58	24	2090	270	30500	50.3	165	3820	47	93	715000
M20R	A	7.3	61	370	50	1310	463000	12.3	540	470	79	0.70	300
M20R	D	163	30	530	580	15300	426000	14000	4340	4610	2200	12.0	3920
O7	B	17.7	42	270	1760	13600	435000	104	7090	680	380	5500	14600
O7	A	0.75	3.3	40	62	530	464000	9.8	220	450	11.1	9.6	1070
O8	A	1.70	3.3	84	177	1440	463000	4.7	690	480	25	4.7	430
O8	C	1.05	12.4	150	720	2990	364000	1780	1130	1320	88	80800	75800

Sample	Type	Cu	Ga	Ge	Rb	Sr	Y	Zr	La	Ce	Pb	Th	U
M16R	E	9.9	1.35	0.302	11.9	250	2.2	3.9	2.9	4.4	10.0	0.55	1.59
M16R	A	1.73	0.34	0.81	2.48	11.8	0.034	0.71	0.022	0.045	0.37	0.056	2.6
M16R	B	4.0	0.26	0.23	2.18	139	2.61	1.25	0.22	0.43	1.84	0.109	3.2
M16R	F	0.22	0.048	0.54	0.26	56	2.68	0.100	0.23	0.52	0.46	0.006	27
M16R	D	77.3	0.170	2.24	0.87	106	0.29	0.50	0.075	0.104	380	0.045	3.7
M20R	A	2.19	0.32	0.81	1.47	3.0	0.94	1.64	1.36	0.83	0.46	0.169	0.46
M20R	D	36	16.2	28	36	1280	10000	39	690	420	179	2.70	53
O7	B	5.6	4.3	1.26	22	18.4	14.1	32.9	1.42	6.7	66	1.07	2.8
O7	A	0.50	0.40	0.81	0.66	0.78	0.066	1.91	0.038	0.083	0.146	0.065	0.53
O8	A	0.39	0.38	0.64	2.18	0.90	0.55	0.98	0.0157	0.066	0.51	0.028	0.190
O8	C	647	5.1	5.1	4.39	225	40	12.7	52	220	10500	10.2	16.1

Table A.3: Element ratios and mineralogical interpretation of various types of impurities of selected silex samples.

	Type	Mg/Ca	Fe/Mn	Interpretation
M16R	E	0.55	16	Impure calcium or magnesium carbonate
M16R	A	0.30	176	Silex
M16R	B	0.0015	3.9	Impure calcium carbonate
M16R	F	0.0036	5.0	Impure calcium carbonate
M16R	D	0.55	7680	Fe-oxy-hydroxide weathering products
M20R	A	0.11	435	Silex
M20R	D	0.13	327	Mixture of various minerals, rare earth elements-phosphate phase
O7	B	2.6	2.7	Impure Fe–Mn-oxy-hydroxide (hematite) within siliceous material
O7	A	0.14	112	Silex, colored by microcrystalline hematite
O8	A	0.37	92	Silex
O8	C	0.54	0.94	Impure Fe–Mn-oxy-hydroxide within siliceous material, Pb oxide

A.4 Supplementary material for Chapter 5

A.4.1 LM-OSL signal deconvolution of silex samples

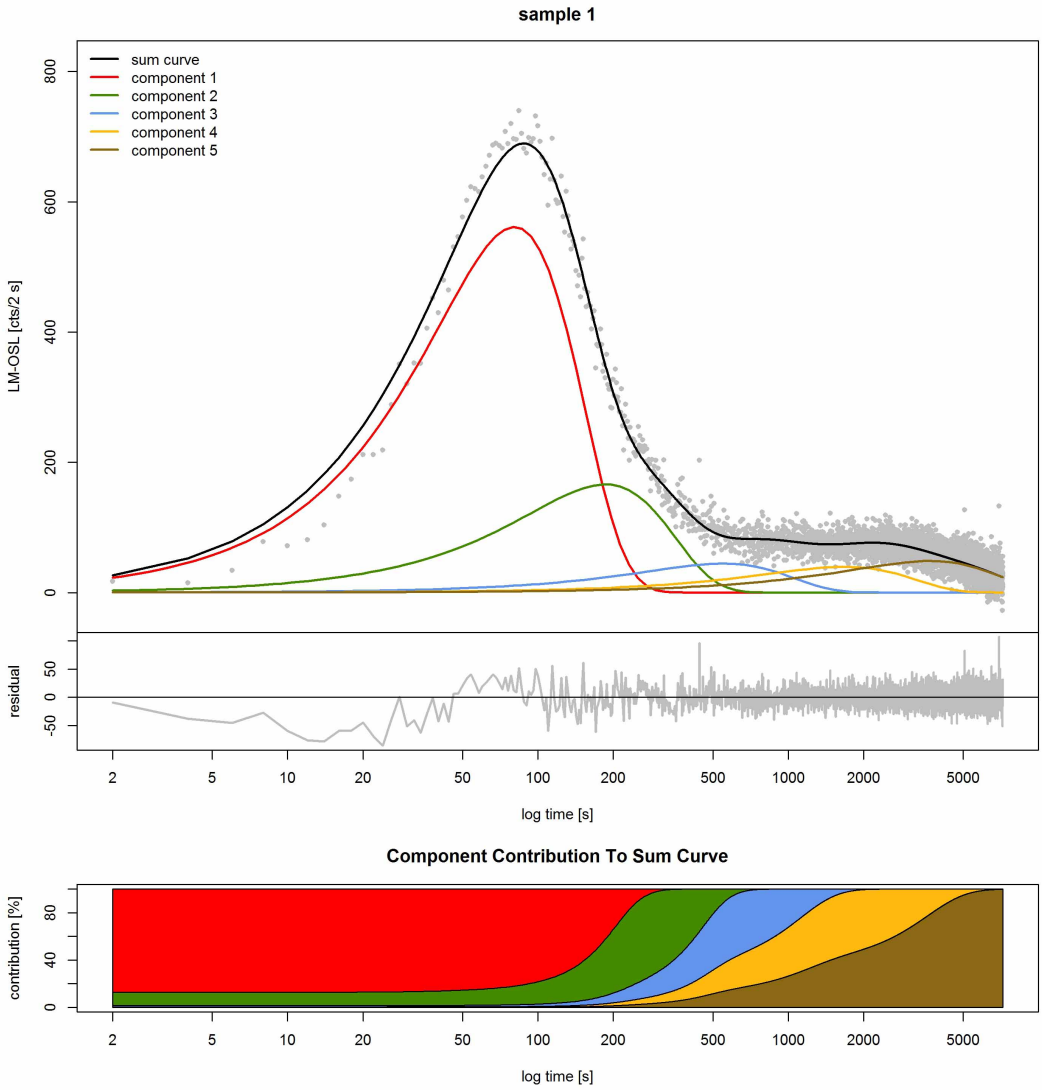

Figure A.12: LM-OSL sum curve and fitting results of silex sample M3. Measurement parameters and fitting procedure as described in Sections 5.2.2 and 5.2.3.

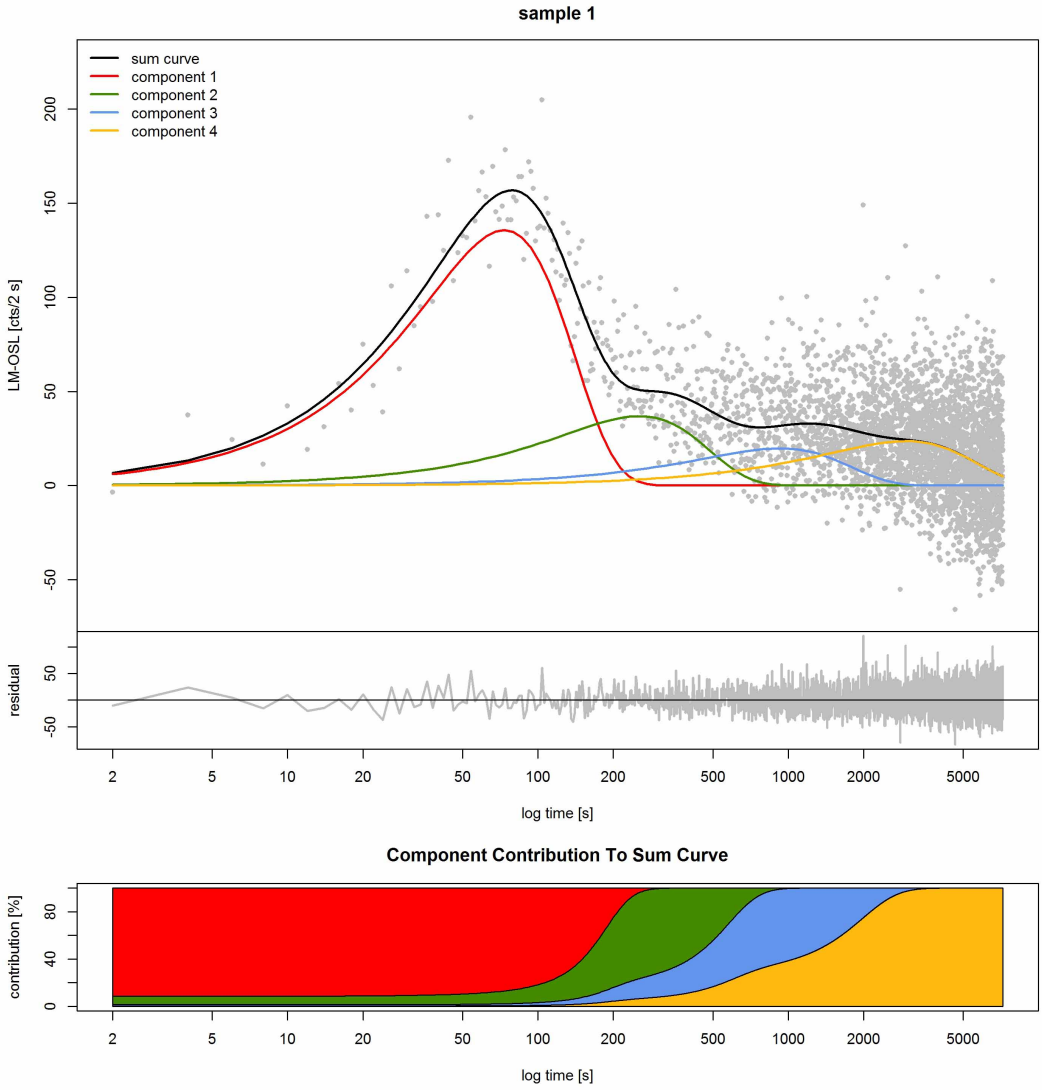

Figure A.13: LM-OSL sum curve and fitting results of silex sample M27. Measurement parameters and fitting procedure as described in Sections 5.2.2 and 5.2.3.

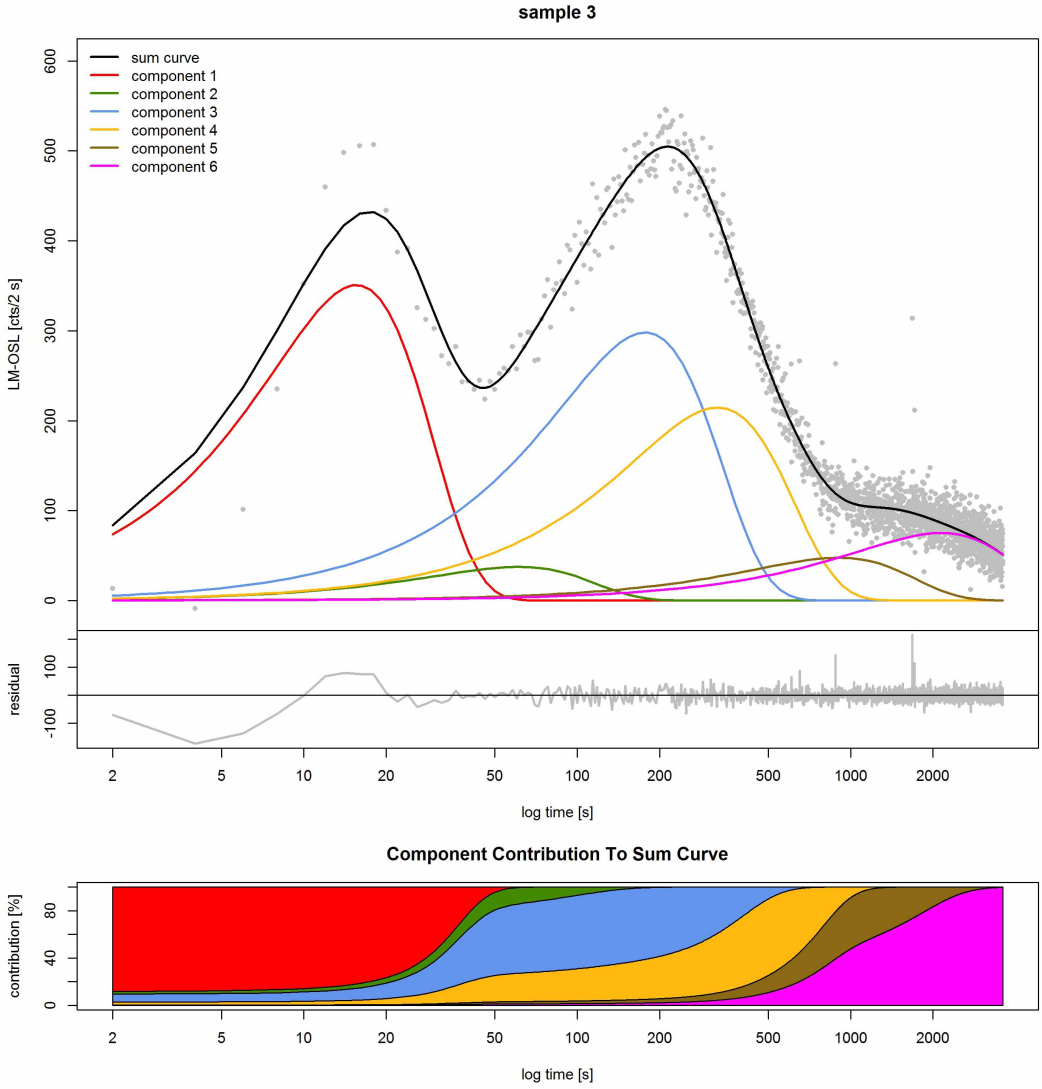

Figure A.14: LM-OSL sum curve and fitting results of silex sample Rom16. Measurement parameters and fitting procedure as described in Sections 5.2.2 and 5.2.3. Designation of individual components differs from that of the main text (due to automatic naming of components by the fitting routine): *component 1* in the plot corresponds to *component 0*, and so forth.

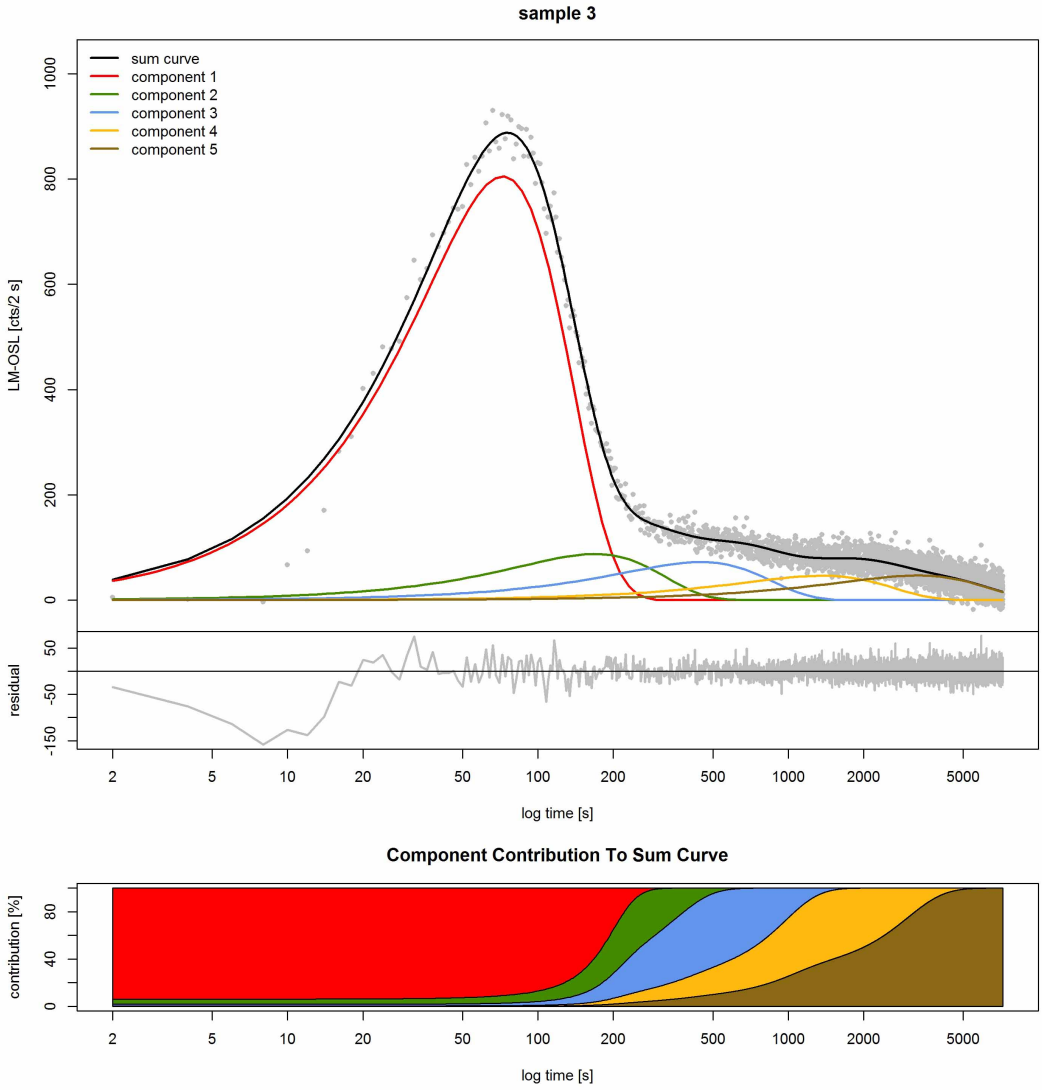

Figure A.15: LM-OSL sum curve and fitting results of silex sample SodTL2. Measurement parameters and fitting procedure as described in Sections 5.2.2 and 5.2.3.

A.4.2 Anti-Stokes shifted luminescence

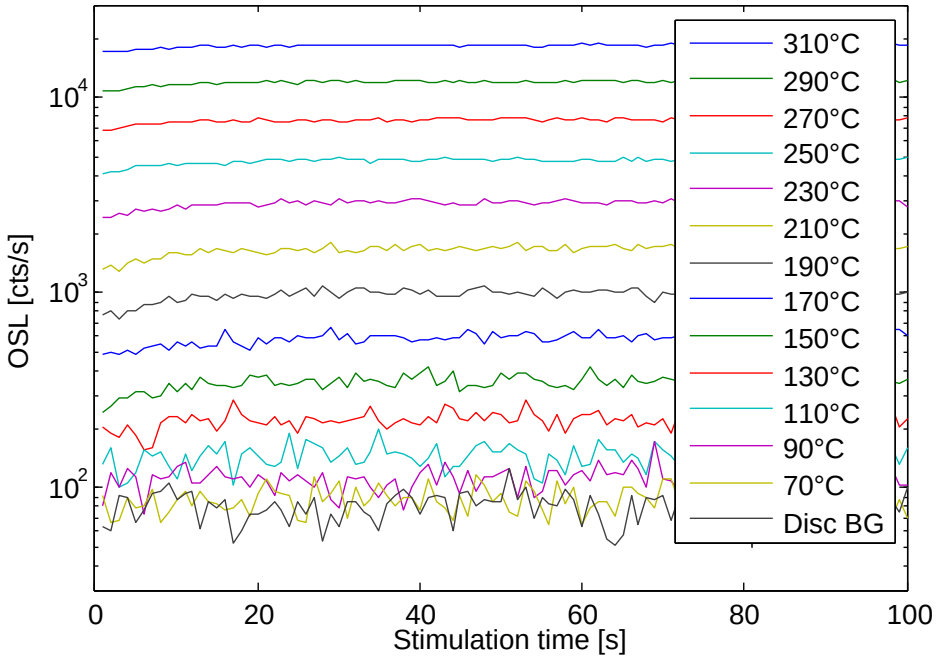

Figure A.16: Dose-independent OSL signal of silex sample M27 with measurement temperature. OSL of "hot-bleached" (500 s at 280 °C) sample material was measured for 100 s (90 % LED power, blue stimulation at 470 Δ 30 nm) at increasing measurement temperatures (70–310 °C at 20 °C increments) without any irradiation and using a 7.5 mm Hoya U340 glass filter for signal detection. The OSL background of an empty disc is also shown. Within the shown variance, this signal did not change up to measurement temperatures of 310 °C. Though not monitored, sensitivity changes are not considered to contribute significantly to the signal increase of more than two orders of magnitude in the course of the measurement sequence.

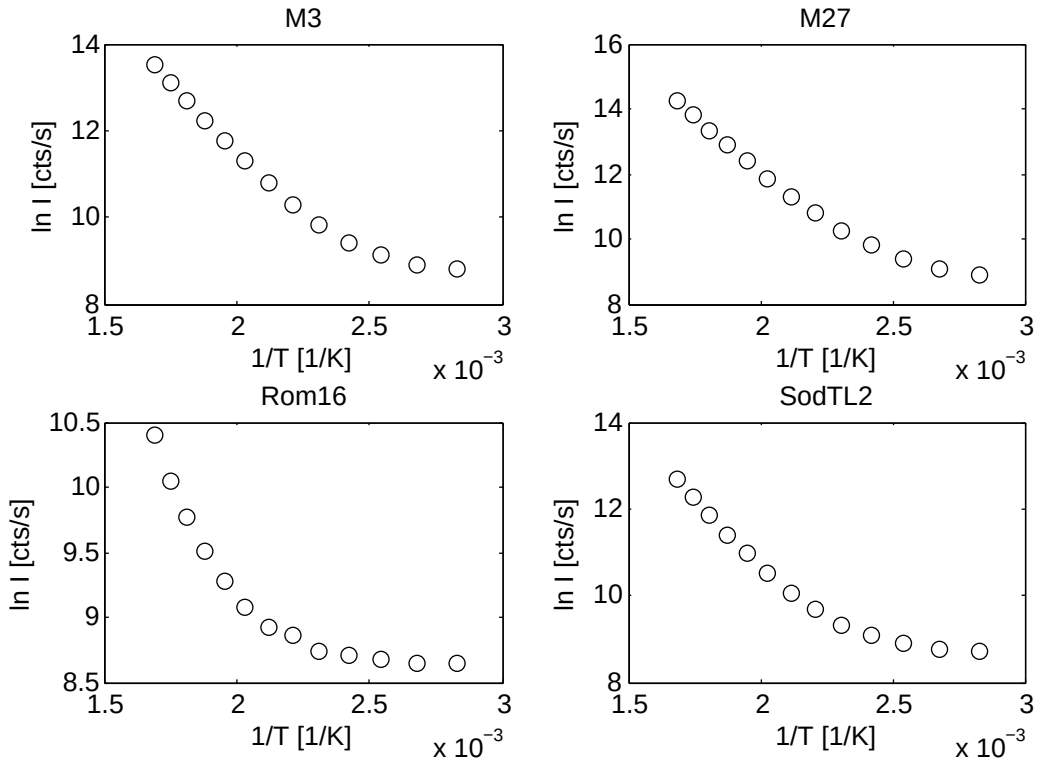

Figure A.17: Arrhenius plots showing the logarithmized intensity of anti-Stokes shifted luminescence (ln I) against the inverse of measurement temperature (T^{-1}). Measurement temperature was increased from 70 °C to 310 °C in 20 °C increments and OSL was measured for 100 s (90 % LED power, blue stimulation at 470 Δ 30 nm, detection with 7.5 mm Hoya U340 filter). Silex samples were "hot-bleached" (500 s at 280 °C) prior to measurement of the anti-Stokes shifted signal. The thermal background in this detection window is (within variance) constant up to the highest measurement temperature. The exponential dependence of anti-Stokes signal on temperature (e.g. M3, M27) for $T > 130$ °C is in accordance with the model of thermally induced population of excited states from which charge carriers relax to the ground state, causing thus the anti-Stokes shift (absorption energy < emission energy) (Demtröder 2005). The fact that the sum of several exponential functions is suitable for fitting the data for all samples suggests several signal components with different activation energies.

A.4.3 Fading tests

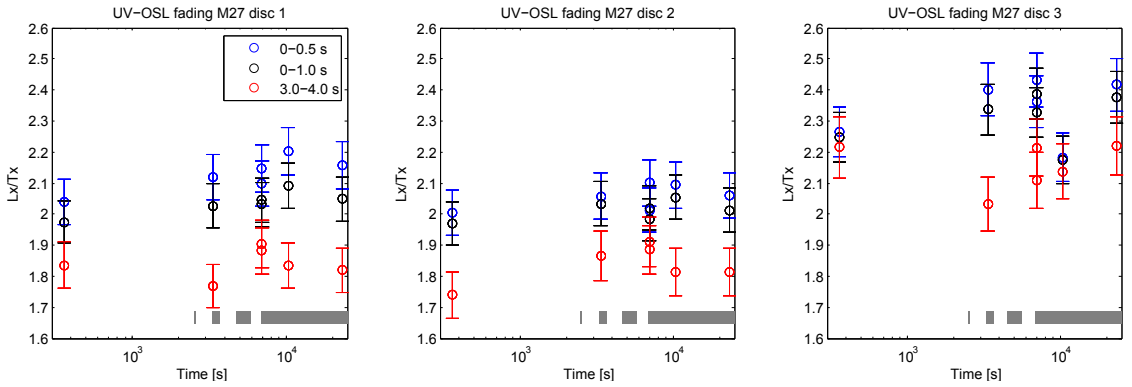

Figure A.18: Results of the fading test for sample M27. Sensitivity-corrected luminescence signal intensities for three aliquots are plotted against time since laboratory irradiation. Different signal integration intervals (0–0.5 s, 0–1.0 s, 3.0–4.0 s) were evaluated to investigate the stability of components with lower bleachability. It should be emphasized here that the data points acquired earlier than ∼7000 s after end of the irradiation cannot be used to estimate potential fading (Visocekas 1985; Aitken 1985). The region suitable for estimating fading rates is indicated in the figure by the continuous gray bar.

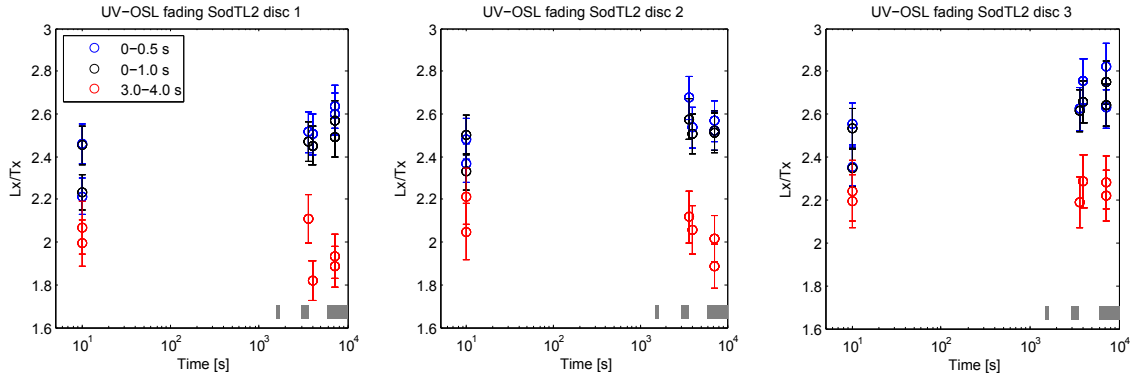

Figure A.19: Results of the fading test for sample SodTL2. Sensitivity-corrected luminescence signal intensities for three aliquots are plotted against time since laboratory irradiation. Different signal integration intervals (0–0.5 s, 0–1.0 s, 3.0–4.0 s) were evaluated to investigate the stability of components with lower bleachability. It should be emphasized here that the data points acquired earlier than ∼7000 s after end of the irradiation cannot be used to estimate potential fading (Visocekas 1985; Aitken 1985). The region suitable for estimating fading rates is indicated in the figure by the continuous gray bar. Unfortunately, it was not possible to extend storage times. Although fading rates cannot be determined from this plot, it demonstrates the overall reproducibility (within errors) of the OSL signal of silex. Nevertheless, measurements for both M27 and SodTL2 give no indication for fading.

A.4.4 Residual TL after OSL readout

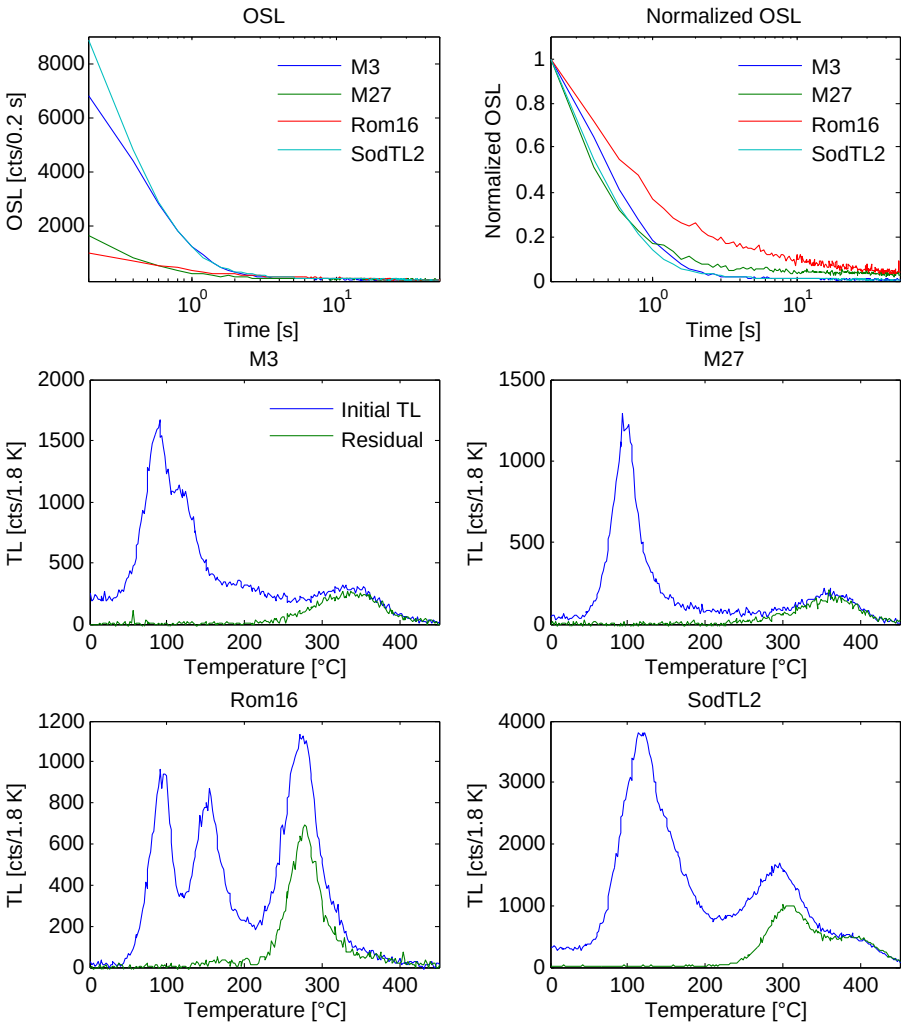

Figure A.20: OSL decay curves and TL residuals of silex samples. Decay curves (upper left) were recorded after 200 Gy regenerative β-doses and a 220 °C preheat for 60 s. Subsequent to OSL readout, residual TL curves (green) were measured using the same emission (UV) as for OSL. Afterwards, TL curves (200 Gy β-irradiation) were measured again without prior bleaching, termed here as "initial TL" (blue). The curves were not corrected for sensitivity changes. The OSL decay rate of sample Rom16 is smaller than for the other samples since *component 0* is not sensitized yet, and *component 2* dominates the emission (see Section 5.3 for further information).

A.5 Supplementary material for Chapter 6

A.5.1 Glow curves and dose response curves of multiple-aliquot additive-dose protocol

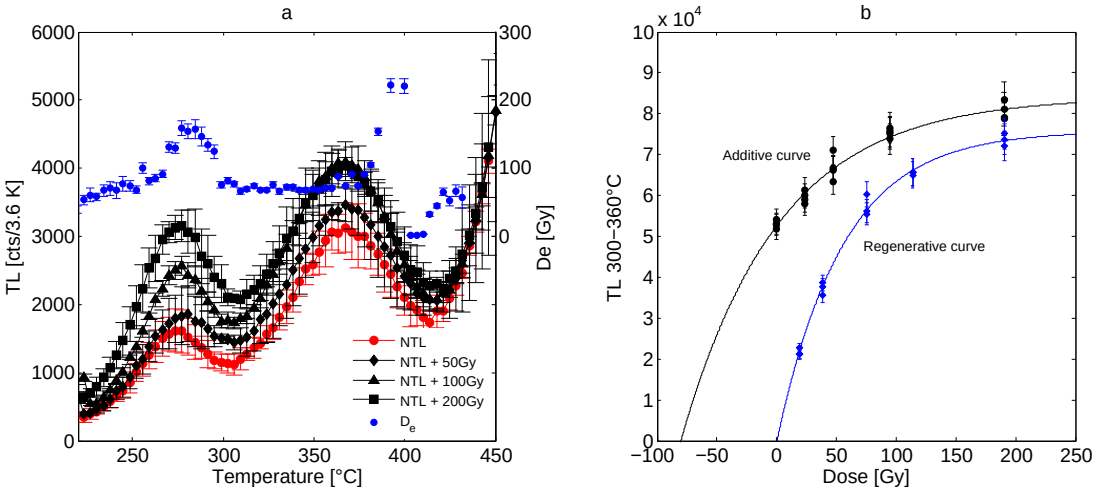

Figure A.21: (a) Additive-dose glow curves (shown as average of all curves per dose step with $1\,\sigma$ uncertainty) and $D_e(T)$-plot and (b) dose-response curves for the additive and regenerative irradiation for sample Rom35. The large extrapolation needed to obtain an additive D_e introduces additional uncertainty and renders MAAD ages less reliable than SAR ages.

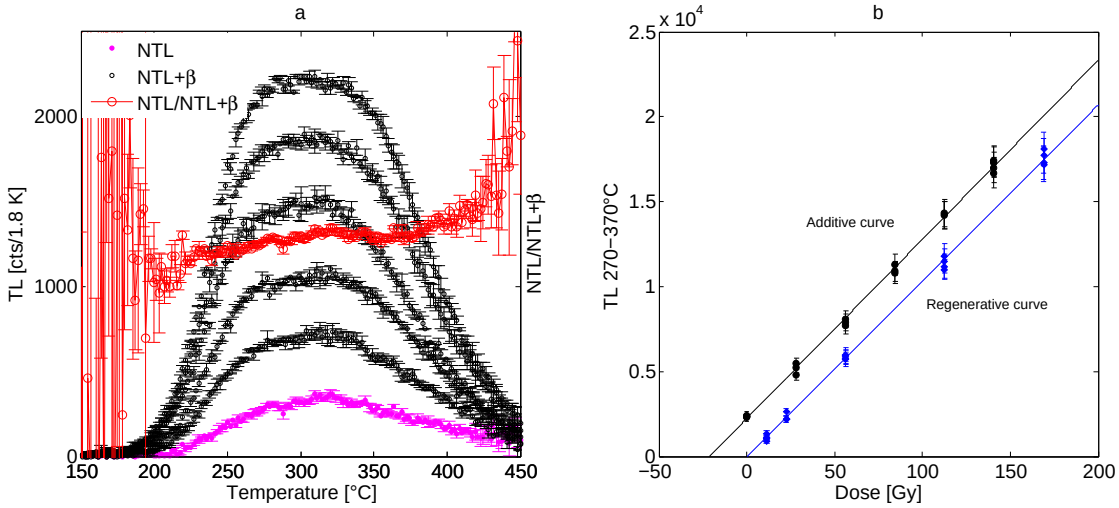

Figure A.22: (a) TL glow curves (natural and additively dosed), heating plateau and (b) dose-response of sample Rom17. Multiple-aliquot glow curves of this sample are shown as average per dose step with $1\,\sigma$ uncertainty. The temperature region 270–370 °C (as evident from the heating plateau) was used to construct the dose response curves.

A.5.2 Apparent equivalent dose plotted against added dose (SARA protocol)

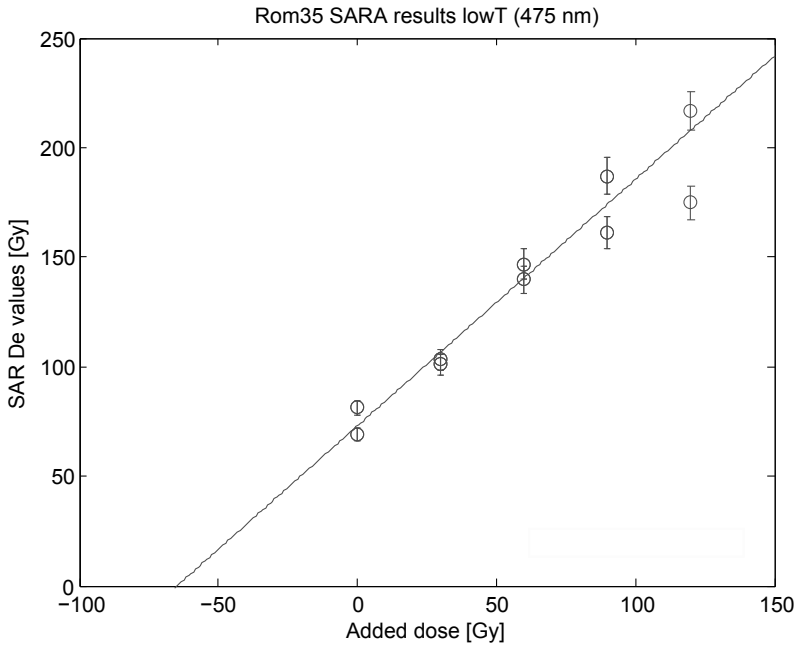

Figure A.23: Example of SARA performance of the low-temperature peak of sample Rom35.

A.5.3 Photographs of examples of sample type 1 and sample type 2

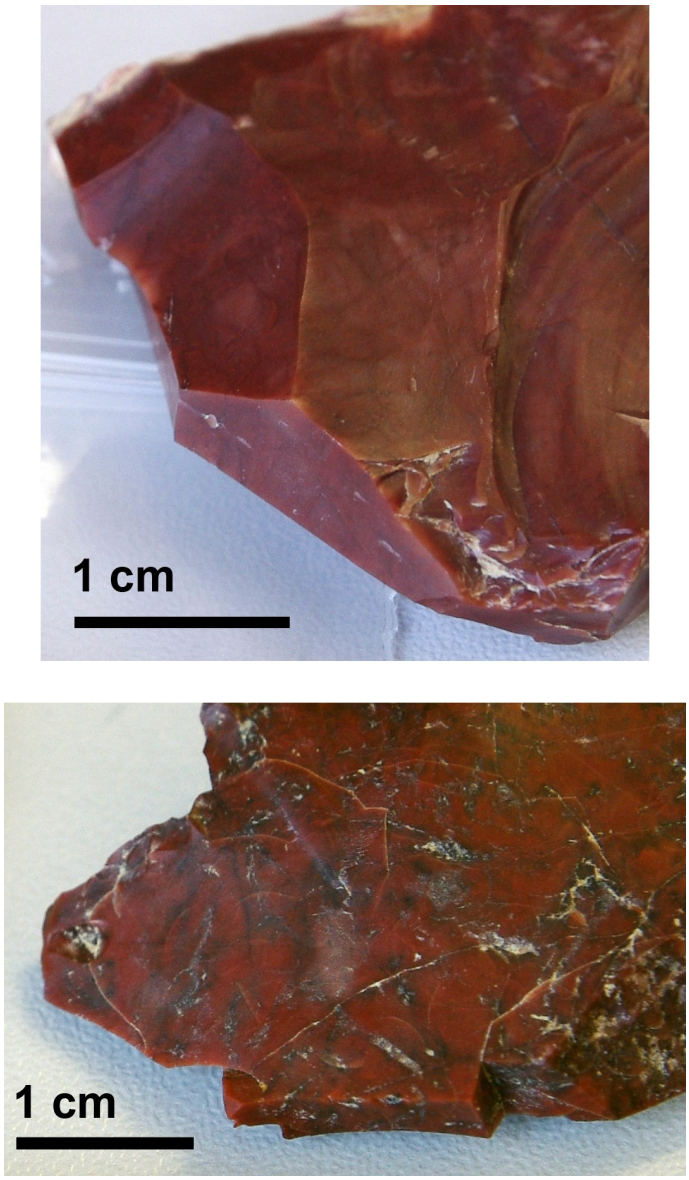

Figure A.24: Comparison of optical appearance of sample type 1 and sample type 2. Shown is sample Rom72 (type 1, above) and Rom118 (type 2, below).

A.5.4 Rejection of type 2 samples

The following figures demonstrate the contrasting performance of type 1 and type 2 samples when conducting TL SAR measurements. Note that in the left graph the dose response is not corrected for sensitivity changes.

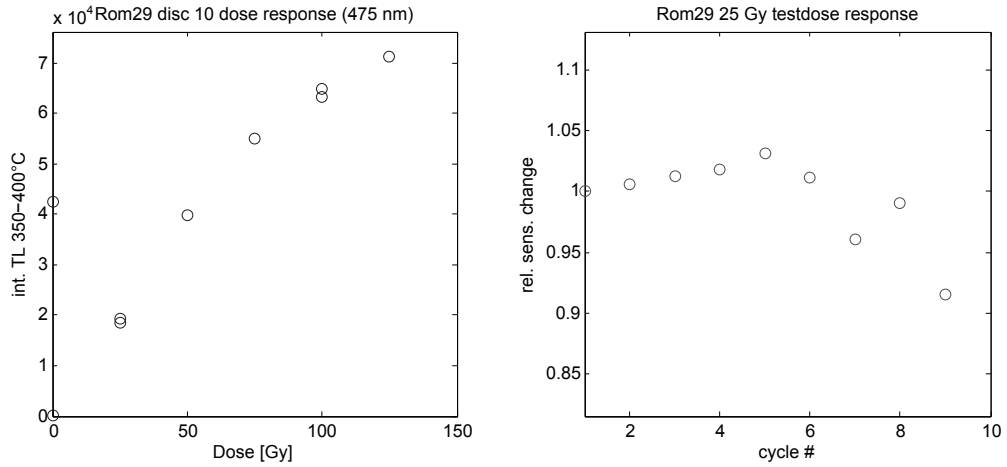

Figure A.25: SAR performance of sample Rom72, representative for sample type 1.

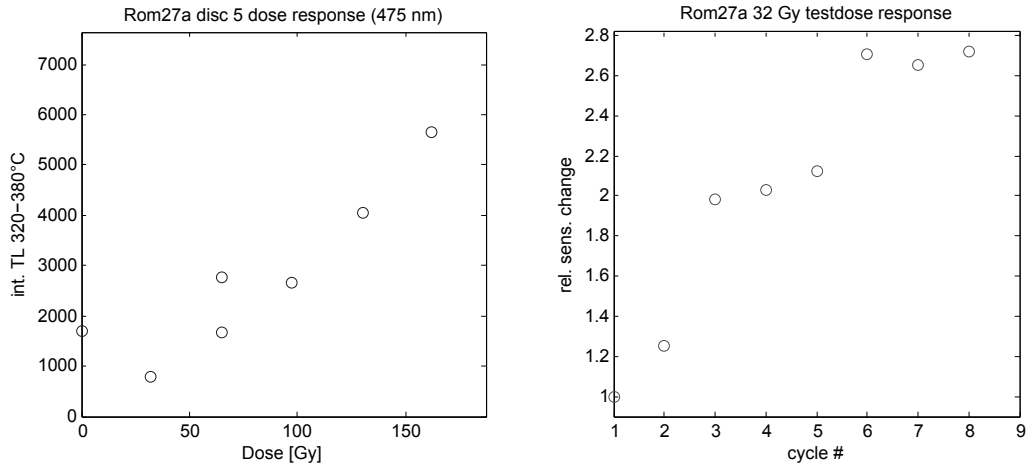

Figure A.26: SAR performance of sample Rom55a (disc 5), representative for sample type 2.

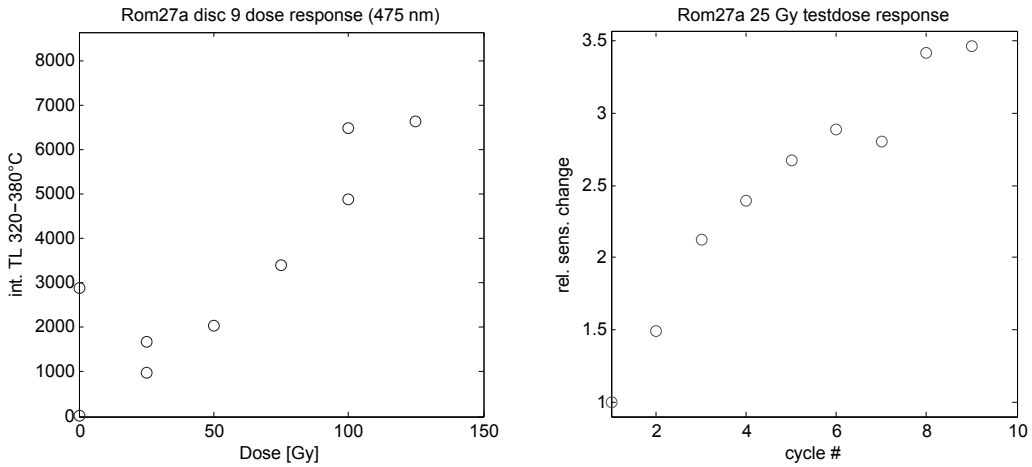

Figure A.27: SAR performance of sample Rom55a (disc 9), showing the most severe case of sensitivity changes observed during SAR measurements.

A.5.5 Preheat plateau test for OSL fine grain samples

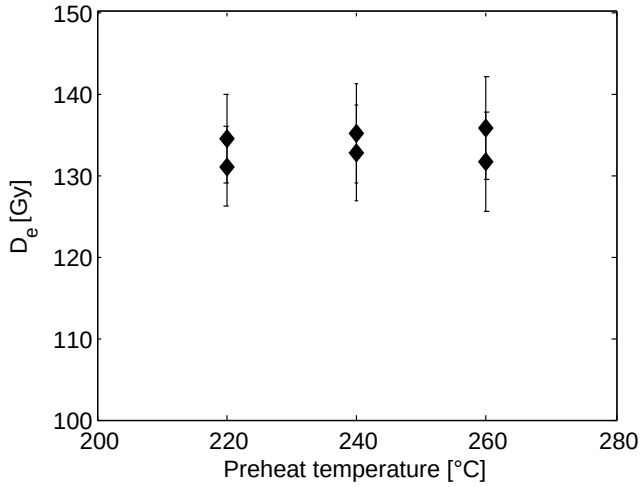

Figure A.28: Preheat plateau of fine grain OSL sample Rom86-221-2 (sample within find layer).

A.5.6 TL dating results of type 2 TL samples

Table A.4: TL dating results of type 2 samples.

Sample	Sample type	Protocol[a]	Emission[b]	Temperature interval [°C]	a-value[c]	$\dot{D}_{\alpha,\mathrm{eff}}$ [Gy ka^{-1}]	$\dot{D}_{\mathrm{total}}$ [Gy ka^{-1}]	$\dot{D}_{\mathrm{int}}/\dot{D}_{\mathrm{total}}$ [%]	n[d]	D_e [Gy]	Age [ka]
Rom49	2	MAAD	UV-blue	270–320	0.077 ± 0.030	0.117 ± 0.046	1.499 ± 0.080	16	–	122.3 ± 34.8	81.6 ± 23.0
		SAR	blue	270–320	0.074 ± 0.016	0.113 ± 0.025	1.495 ± 0.094	16	–	–	–
Rom55a	2	MAAD	UV-blue	320–380	0.080 ± 0.033	0.114 ± 0.047	1.451 ± 0.080	16	3	77.7 ± 13.8	53.5 ± 9.0
		SAR	blue	320–380	0.113 ± 0.023	0.162 ± 0.033	1.499 ± 0.075	18	–	–	–
Rom55b	2	SAR	blue	320–380	0.041 ± 0.016	0.070 ± 0.027	1.447 ± 0.073	15	8	–	–
Rom118	2	MAAD	UV-blue	270–315	0.037 ± 0.005	0.077 ± 0.019	1.548 ± 0.067	20	–	61.9 ± 8.9	40.0 ± 5.8
		SAR	blue	270–315	0.066 ± 0.011	0.127 ± 0.022	1.600 ± 0.094	23	4	–	–
Rom140	2	MAAD	UV-blue	300–400	0.023 ± 0.002	0.059 ± 0.005	1.523 ± 0.069	13	–	90.4 ± 15.9	59.3 ± 10.5
		SAR	blue	350–400	0.026 ± 0.002	0.066 ± 0.006	1.530 ± 0.069	14	8	96.9 ± 7.4	63.3 ± 5.5
		SAR 2mm	blue	350–400	0.026 ± 0.002	0.066 ± 0.006	1.530 ± 0.069	14	8	72.0 ± 5.8	47.1 ± 4.2
Rom197	2	MAAD	UV-blue	230–280	0.018 ± 0.008	0.052 ± 0.023	1.513 ± 0.070	18	–	175.2 ± 7.8	115.8 ± 7.0
		SAR	blue	230–280	0.031 ± 0.004	0.090 ± 0.012	1.551 ± 0.067	20	9	84.1 ± 4.8	54.2 ± 3.7

[a] Unless indicated otherwise, all measurements refer to 8 mm aliquots.
[b] Emission windows correspond to the filter combinations described Section 6.3.1.
[c] The given uncertainty is the standard deviation of single measurements.
[d] Number of accepted aliquots for SAR and SARA procedures, according to the rejection criteria defined in Section 6.3.2.2.

References

Aitken, M., 1985. Thermoluminescence dating. Academic Press, London.

Demtröder, W., 2005. Experimentalphysik 3. Atome, Moleküle und Festkörper. Springer, Berlin and Heidelberg.

Tissoux, H., Valladas, H., Voinchet, P., Reyss, J., Mercier, N., Falguères, C., Bahain, J.-J., Zöller, L., Antoine, P., 2010. OSL and ESR studies of aeolian quartz from the Upper Pleistocene loess sequence of Nussloch (Germany). Quaternary Geochronology 5, 131–136.

Visocekas, R., 1985. Tunnelling radiative recombination in labradorite: Its association with anomalous fading of thermoluminescence. Nuclear Tracks and Radiation Measurements 10, 521–529.

Zöller, L., Stremme, H., Wagner, G. A., 1988. Thermolumineszenz-Datierung an Löss-Paläoboden-Sequenzen von Nieder-, Mittel- und Oberrhein/Bundesrepublik Deutschland. Chemical Geology (Isotope Geoscience Section) 73, 39–62.

B Dose recovery tests

To test the reliability and robustness of measurement protocols, dose recovery tests (DRT's) are commonly carried out. A known dose from a calibrated source (mostly a β- or γ-source) is given to a zeroed aliquot and the protocol under consideration is applied in order to determine the equivalent dose. The closer this dose is to the given dose, the better is the protocol expected to work. There are further indicators for the appropriateness of regenerative-dose procedures, namely the *recycling ratio* and – in case of optical stimulation – the *recuperation*. The first quantity is the ratio of a dose point and a repeat point of the same dose later in the measurement sequence and intends to check proper correction for sensitivity changes. This value should lie between 0.9 and 1.1 for the protocol to give accurate results. Recuperation describes the presence of a luminescence signal after a 0 Gy regeneration dose has been administered. Since thermal stimulation to temperatures of $\sim 450\,^{\circ}\mathrm{C}$ is assumed to erase the signal completely, recuperation is not expected to occur during TL regeneration.

Table B.1: Geological samples used for dose recovery tests.

Internal code	Denomination	Provenance	Geological origin
M3	Flint	Orsbach, Germany	Upper Cretaceous
M7	Flint	Rullen, Belgium	Upper Cretaceous
M20	Flint	Caredo, Lessinian Mountains, Italy	Unknown
M27	Flint	Fehmarn, Baltic, Sea, Germany	Cretaceous
O8	Chalcedony	Banat region, Romania	Unknown

In the course of the present thesis, DRT's were carried out to evaluate the sample preparation and measurement protocols subsequently used for the dating of archeological samples. Geological samples were subjected to DRT's after having been heated and receiving a β- or γ-dose. Several TL emissions were tested; the used filters and their transmission spectra are depicted in Fig. B.1. All measurements were conducted using a Risø TL-DA 20 reader, equipped with an EMI 9235QB photomultiplier and a $^{90}\mathrm{Sr}/^{90}\mathrm{Y}$ β-source delivering $\sim 0.11\,\mathrm{Gy\,s^{-1}}$.

It must be noted that the data quoted here serve the purpose of checking the reliability of measurement protocols applied to artificially heated raw material as well as the appropriateness of sample preparation. All other DRT results are placed in the respective section of Chapter 7 concerned with the dated site.

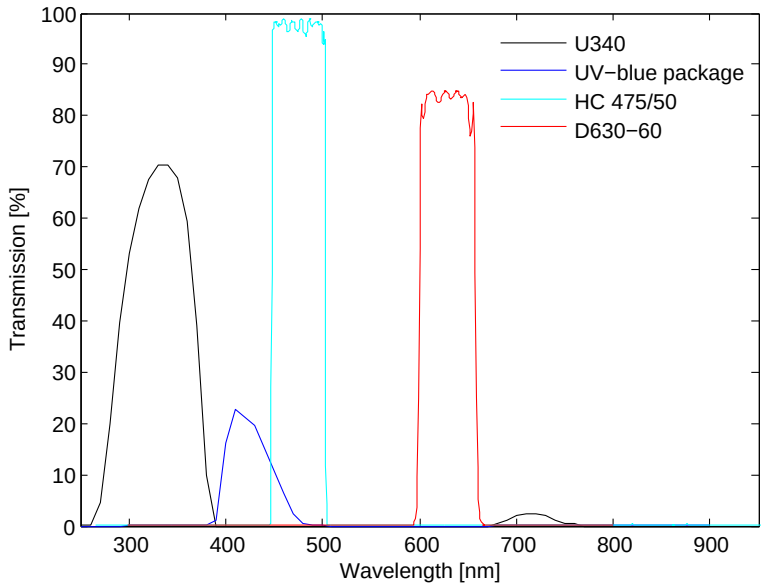

Figure B.1: Transmission spectra of the filters used for the dose recovery tests. The magnitude of transmission depends on the thickness of the filters and are here shown for the values given in the text, except for U340 whose spectrum is shown for 4.3 mm thickness.

B.1 Dose recovery tests using multiple-aliquot additive-dose (MAAD) protocols

The general lack of material impeded the performance of MAAD DRT's for archeological samples. Some samples from the site Româneşti-Dumbrăviţa I (Romania, Chapter 6) yielded sufficient material, but their poor measurement reproducibility excluded them from being used for testing the reliability of a protocol (as is demonstrated for raw material sample O8 from Romania and its large uncertainty level). For DRT's, samples were mechanically and chemically prepared for measurements according to the procedure given in Section 6.3.1. Since the MAAD protocol is a well-established method (Mercier et al. 1995; Richter 2007), DRT's were less extensive as in the case of SAR protocols. Two different luminescence emissions were investigated.

B.1.1 Ultraviolet emission ($\sim 340 \pm 40$ nm)

Three samples (M3, M27, O8) were first heated on the whole in the muffle oven at 500 °C for 30 Min. to simuate ancient firing, received then a γ-dose of 71.2 or 142.4 Gy and were measured with a MAAD protocol after usual sample preparation. The delay between irradiation and measurement was approximately three months. One portion of the sample material was used to construct the additive-dose response curve, i.e. the five sets of four aliquots each were irradiated with increasing β-doses. The other portion of the sample

material was annealed in the muffle oven (350 °C for 90 Min.) and the six sets of four aliquots were given β-regeneration doses. To reduce the scatter between single aliquots, discs were fully covered with sample material (8 mm mask). All measurements were carried out in a N_2 atmosphere with a heating rate of $5\,K\,s^{-1}$ and a maximum heating temperature of 450 °C, unless stated otherwise. Background measurement followed immediately the measurement of the sample signal. For equivalent dose determination, the temperature region yielding a D_e-plateau was chosen; Section 1.3.4.1 provides further details on the MAAD routine; Table B.2 summarizes the results of the DRT's.

Table B.2: Results of the MAAD DRT of geological samples. All measurements were performed with a heating rate of $5\,K\,s^{-1}$ and a 7.5 mm thick Hoya U340 filter between sample and photomultiplier. A linear fit was used for calculating the D_e.

Sample	Given dose [Gy]	Plateau [°C]	Recovered dose [Gy]	Supralinearity correction [Gy]	Total dose recovered [Gy]
M27	71.2	300–380	42.6 ± 6.7	5.9 ± 1.0	48.7 ± 7.7
M3	142.2	280–365	134.8 ± 8.3	–	134.8 ± 8.3
O8	142.2	305–390	138.3 ± 30.8	–	138.3 ± 30.8

Within measurement uncertainties, the given dose can be reproduced for samples M3 and O8, whereas the large error of the D_e of sample O8 can be attributed to poor reproducibility and overall low signal intensities. The exact reasons why the recovered dose of sample M27 significantly underestimates the given dose remain unclear at the moment. Richter et al. (1999) report slight fading and sensitivity to red laboratory light for the UV emission of silex what is a possible explanation for the general tendency of dose underestimation of this emission.

B.1.2 Ultraviolet-blue emission ($\sim 410 \pm 30$ nm)

Having received the same pre-treatment as described in the last section, a MAAD DRT was performed for sample M27 using the UV-blue emission around 410 nm. Measurement parameters equal that of the UV measurements, the filter package, however, comprised a 4 mm Corning 7-59, a 1 mm BG-39, a 3 mm GG-400 and a 4 mm HA-3 filter. Fig. B.2 shows the D_e-plateau, and evaluation of the temperature region 300–360 °C gives a D_e of 62.2 ± 2.0 Gy including a supralinearity correction of 8.1 ± 1.3 Gy. While this value is closer to the given dose (71.2 Gy), the problem of dose underestimation persists. At the moment, no final explanation can be given as sample preparation and measurement techniques do obviously not differ significantly from those published in literature (Valladas 1992; Mercier et al. 1995; Richter et al. 2008).

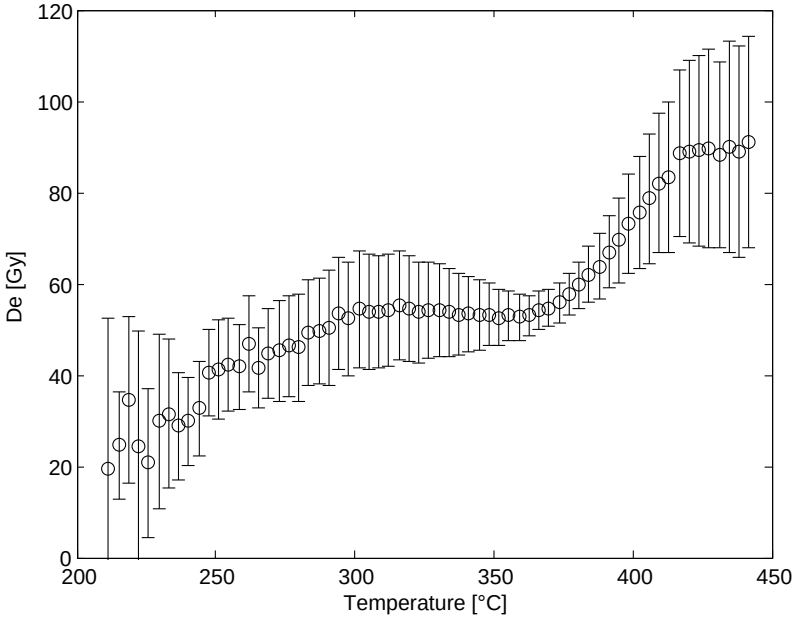

Figure B.2: UV-blue MAAD D_e-plateau of sample M27 (DRT). For equivalent dose evaluation the temperature region 300–360 °C was used.

B.2 Dose recovery tests using single-aliquot regenerative-dose (SAR) protocols

B.2.1 Blue emission (475 ± 25 nm)

Geological samples M3 and M7 were treated as described in Section B.1.1. The given doses were recovered using a TL SAR protocol and an interference filter transmitting wavelengths of 475 ± 25 nm (HC 475/50). Table 1.2 contains the generalized measurement procedure also used for DRT's. Further measurement parameters are given in the captions of Tables B.3 and B.4.

The results show that a given dose can be reproduced within 10 % for all measured aliquots, but mostly with lesser deviations. A slight trend for dose underestimate is highly visible, the reasons for which are unclear at the moment. The two samples under study show severe sensitivity changes in the course of the SAR protocol (up to factors of 2 or more at the end of all cycles). Although the recycling ratio indicates an appropriate correction of sensitivity changes, it might be a shift in dose response in the course of the first TL measurement that causes the observed underestimation. Most of the archeological samples for which the D_e was measured using this emission yielded lower sensitivity changes, so that the discrepancy between "true" and determined dose is expected to be smaller than here.

Table B.3: Results of the DRT of geological sample M3. The regeneration steps were 10, 18, 25, 32, 40, 0 and 25 Gy in case of a given laboratory dose of 25 Gy and 20, 35, 50, 65, 80, 0 and 50 Gy for a laboratory dose of 50 Gy. Testdoses were 10 and 20 Gy, respectively. The integrated counts from the temperature interval 370–420 °C were used to construct the dose response curves which were fitted with a single saturating exponential function. Recuperation was below 1 % for all measured aliquots and is not quoted here.

Aliquot	Given dose [Gy]	Recovered dose [Gy]	Recycling ratio
1	25.0	27.8 ± 1.5	0.94
2	25.0	22.3 ± 1.3	0.98
3	25.0	22.5 ± 1.2	1.01
4	25.0	24.0 ± 1.3	1.00
5	25.0	23.8 ± 1.3	0.97
6	25.0	23.5 ± 1.3	1.00
7	50.0	45.9 ± 2.4	1.03
8	50.0	48.0 ± 2.6	1.05
9	50.0	51.0 ± 2.9	1.05
10	50.0	47.7 ± 2.5	1.04

Table B.4: Results of the DRT of geological sample M7. Measurement conditions were the same as for sample M3, except for the signal integration limits which were set to 350–400 °C here.

Aliquot	Given dose [Gy]	Recovered dose [Gy]	Recycling ratio
1	25.0	24.1 ± 1.4	1.01
2	25.0	24.8 ± 1.4	1.02
3	25.0	25.2 ± 1.5	1.02
4	25.0	22.9 ± 1.2	1.03
5	25.0	24.6 ± 1.3	1.00
6	25.0	24.1 ± 1.4	1.07
7	50.0	45.8 ± 2.5	1.04
8	50.0	47.4 ± 2.5	1.04
9	50.0	46.8 ± 2.5	1.03
10	50.0	48.4 ± 2.6	1.02

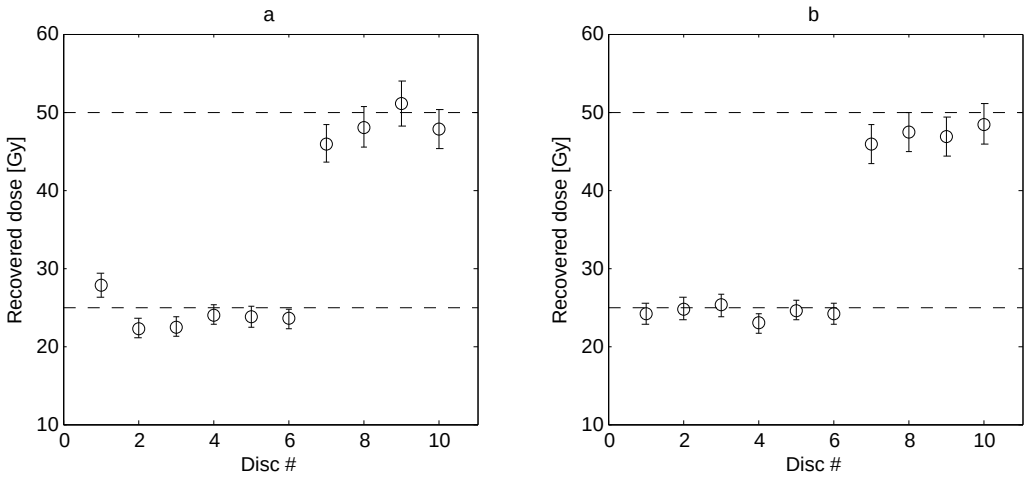

Figure B.3: Results of the DRT of samples M3 (a) and M7 (b). The first six aliquots received initial doses of 25 Gy, the last four aliquots doses of 50 Gy. The recovered doses are shown with their $1\,\sigma$ uncertainties; the dashed lines represent the given doses.

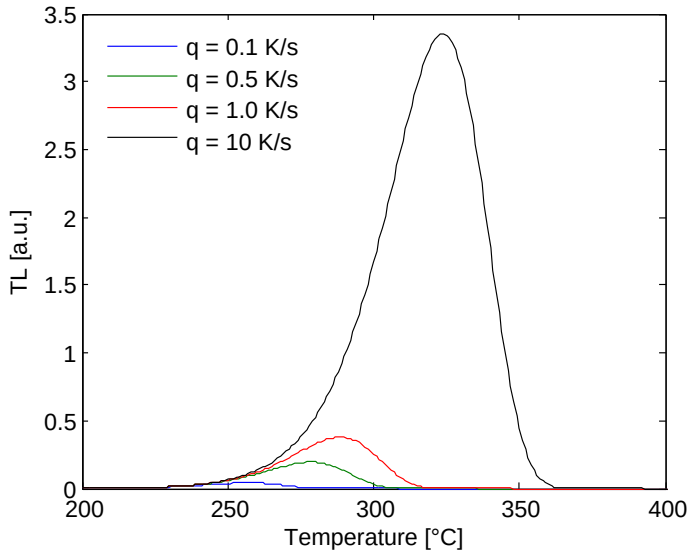

Figure B.4: Variation of peak temperature and glow curve area with heating rate. The parameters used for the simulated curves of first-order kinetics are the same as in the caption of Fig. 1.16, with q being the heating rate.

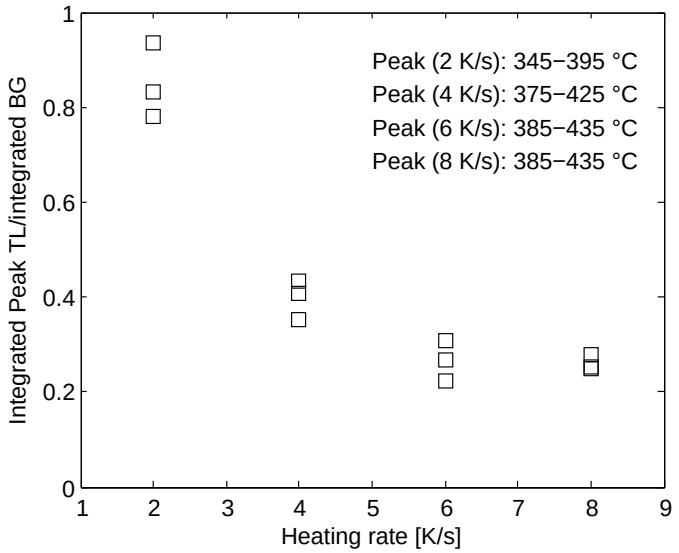

Figure B.5: Variation of signal-to-noise ratio (SNR) with heating rate. Three aliquots of sample M27 were measured for each heating rate. Their individual SNR's are shown as black squares. As a results of peak shift along the temperature axis with increasing heating rate, the integration limits were adjusted to the peak maximum and encompass a temperature region of 50 °C for all aliquots.

B.2.2 Red emission (630 ± 30 nm)

A technical difficulty of measuring the red TL (RTL) emission of luminescent samples is its strong interference with blackbody radiation at high temperatures (above $\sim 300\,^{\circ}\mathrm{C}$). Especially for dim samples, the luminescence signals are not visible in the glow curve until the thermally induced background is subtracted. The choice of sample holders (discs) with reproducible background is thus crucial to avoid problems of fluctuating background levels and to obtain reliable RTL signals. Extensive experiments (see also Chapter 2) proved stainless steel discs (not polished) to yield the most reproducible background measurements. Therefore, this kind of discs was used for all RTL measurements.

It is well-known that the position of a TL peak on the temperature axis depends on the heating rate: the smaller the heating rate, the lower will the peak temperature be (Fig. B.4). Thermal lag between the disc and the sample grains may, however, counteract and shift the peak towards higher temperatures. Moreover, background subtraction problems become increasingly noticeable at higher peak temperatures and thus higher heating rates. On the other hand, the area under a glow curve (cts versus T) increases with heating rate (Fig. B.4). While the absolute number of released photons remains the same for all heating rates, the peaks measured with a low heating rate "glow longer" than those recorded with a higher heating rate. Another influence is thermal quenching which reduces the luminescence signal with increasing temperature. Only empirical data can show what effect will dominate in the end. The crucial quantity is the signal-to-noise ratio (SNR), providing a measure of the uncertainty due to counting statistics. RTL measurements on flint sample M27 using different heating rates suggest that the SNR is better for lower heating rates

(Fig. B.5). While thermal quenching does not appear to significantly affect glow curve areas obtained with varying heating rates, the increasing thermal background with temperature is the main cause of higher SNR's at lower heating rates.

RTL measurements were conducted according to the protocol suggested by Richter & Krbetschek (2006), however once with and once without test dose monitoring. The results of the DRT indicate that the use of a test dose to correct for sensitivity changes helps to improve the accuracy of measured D_e's. Furthermore, the failure of the bracketing condition leads to exclusion of a substantial part of the measured aliquots. The method of linear interpolation between the regeneration points as suggested by Richter & Krbetschek (2006) is, however, not applicable if the bracketing condition is not fulfilled. Increasing the distance of the bracketing points in relation to the expected natural TL enhances the chance to meet the quoted condition, but also lowers the accuracy of the data. Since the results here indicate that test dose correction appears to work well, an alternative is to construct a dose response curve with more than two regeneration points and to fit this curve, as is usually done in OSL SAR dating. This method was applied in the course of the dating studies of Chapter 7.

Table B.5: Results of the DRT using the red TL emission. A γ-dose of 142.4 or 71.2 Gy served as recovery dose in this experiment. The measurement protocol comprised only two regeneration points which bracket the natural TL (NTL) signal, according to Richter & Krbetschek (2006). Regeneration doses were 128 and 157 Gy for the high recovery dose and 60 and 80 Gy for the lower recovery dose. Both uncorrected and sensitivity-corrected results are given; in the latter case a test dose of 71.2 Gy was administered after each regeneration dose and the dose response curve normalized for D_e determination. In the event that the NTL was not bracketed by regenerated signals and for a recycling ratio outside the range 0.90–1.10, aliquots were rejected and not considered for calculation of mean values (as shown in Fig. B.6). All measurements were performed in a N_2 atmosphere with a heating rate of $2\,K\,s^{-1}$ up to 450 °C. For sample M27, no repeat point was measured so that no recycling ratio can be quoted. Aliquots marked with an asterisk (*) were not bracketed by regeneration points.

		Uncorrected			Sensitivity-corrected		
Sample	Given dose [Gy]	Aliquot	Recovered dose [Gy]	Recycling ratio	Aliquot	Recovered dose [Gy]	Recycling ratio
M3	142.4	1	177.5 ± 2.0	0.84	6	133.9 ± 6.0	0.97
	142.4	2*	178.1 ± 1.6	0.84	7*	166.5 ± 6.2	1.02
	142.4	3	195.3 ± 2.3	0.88	8	156.3 ± 6.8	0.99
	142.4	4	170.8 ± 2.0	0.85	9*	157.6 ± 6.5	0.98
	142.4	5	170.8 ± 1.8	0.95	10*	160.1 ± 4.7	0.96
M20	142.4	1	153.0 ± 1.9	0.97	6	132.5 ± 6.5	0.97
	142.4	2*	129.5 ± 1.8	0.87	7*	169.5 ± 9.3	0.92
	142.4	3	146.9 ± 2.3	0.93	8	149.1 ± 7.6	0.91
	142.4	4	140.4 ± 2.4	0.92	9	156.2 ± 5.0	0.99
	142.4	5	147.2 ± 1.9	0.93	10	153.1 ± 3.0	1.04
M27	71.2	1	64.4 ± 1.9	–	6	70.5 ± 1.0	1.06
	71.2	2	61.3 ± 1.5	–	7	76.2 ± 1.1	1.08
	71.2	3*	47.3 ± 4.4	–	8	69.6 ± 1.2	0.99
	71.2	4	67.8 ± 1.5	–	9	71.9 ± 1.5	0.92
	71.2	5*	56.9 ± 1.5	–	10	71.8 ± 1.2	1.00

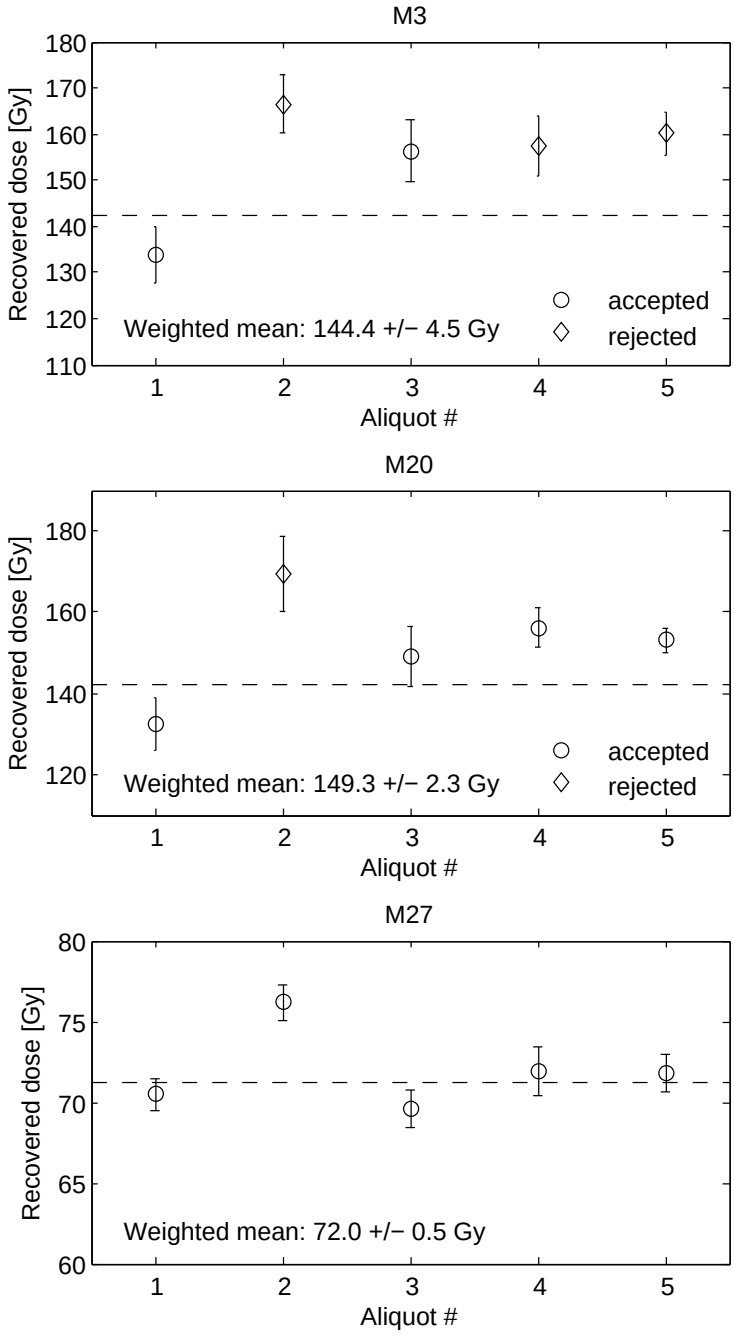

Figure B.6: Plot of the results of RTL dose revovery tests. Both accepted and rejected aliquots of sensitivity-corrected data are shown. Rejection criteria are the value of the recycling ratio and the bracketing condition, as explained in the main text. Weighted mean values were calculated using only accepted aliquots. The dashed lines respresent the recovery doses.

C Supplementary measurement data of dated silex samples

C.1 Vale Boi

C.1.1 Plateau tests

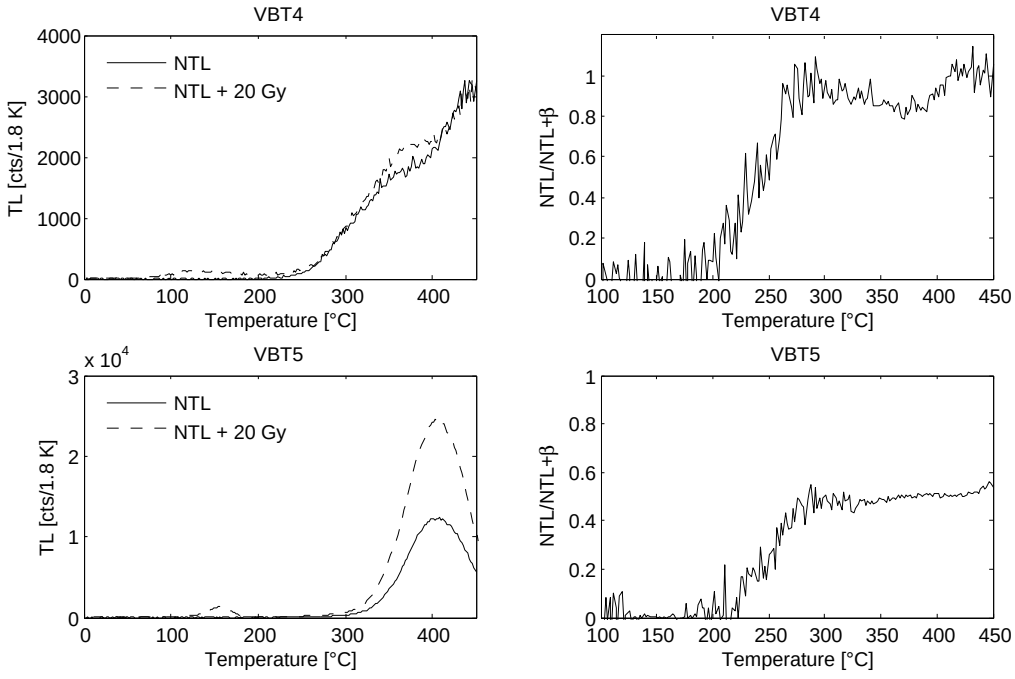

Figure C.1: Heating plateau tests of Vale Boi (VBT) samples. The plots in the left column show the glow curves of natural (NTL) and additively dosed (NTL + β) aliquots; the right column shows the ratio NTL/NTL + β. All curves are normalized (second glow).

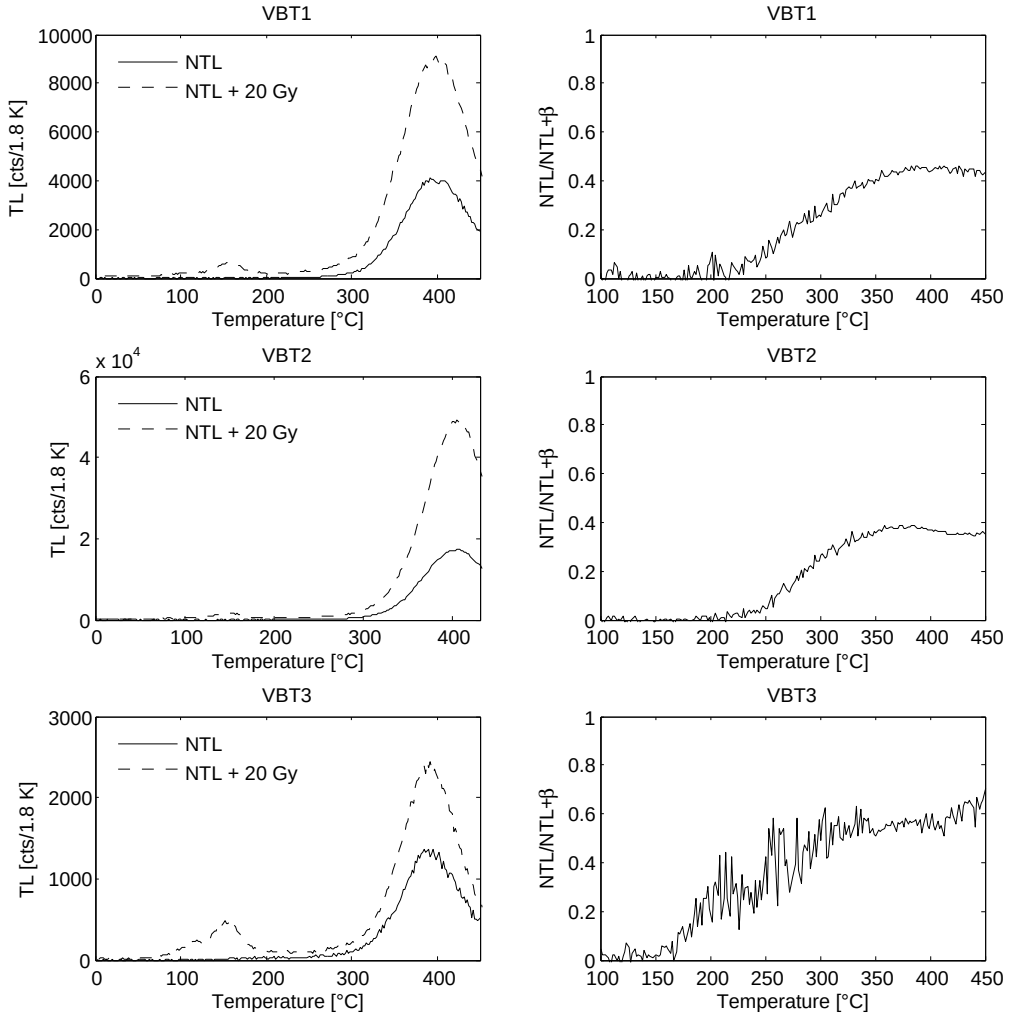

Figure C.2: Heating plateau tests of Vale Boi (VBT) samples. The plots in the left column show the glow curves of natural (NTL) and additively dosed (NTL + β) aliquots; the right column shows the ratio NTL/NTL + β. All curves are normalized (second glow).

C.1.2 Dose recovery tests

Archeological samples from the Gravettian site Vale Boi (Portugal) were subjected to a SAR DRT (blue TL emission) after thermal removal of the paleodose. In order to study potential effects of the duration of heating on the subsequently determined dose, one set of three aliquots was heated to 500 °C (cutheat) prior to artificial dosing and measurement, the other set heated in the muffle oven at 400 °C for 1 h. The results are given in Table C.1 and Fig. C.3, along with the measurement conditions. To illustrate the relatively small impact of sensitivity changes on the resulting dose (in contrast to samples M3 and M7, see Chapter B), the D_e values are quoted once without and once with sensitivity correction.

Table C.1: Results of the DRT of samples from Vale Boi (VBT). The initial doses were adjusted to the expected archeological doses of the samples, and regeneration doses were 7, 16, 24, 32, 16, 0 Gy and 12, 24, 36, 48, 24, 0 Gy, respectively. Integration limits were 370–410 °C for sample VBT1 and 350–410 °C for sample VBT2 and VBT3; a quadratic function was used to fit the dose response curves (supralinear growth). Equivalent doses are given once without and once with correction of sensitivity changes by test dose monitoring.

				Uncorrected		Sensitivity-corrected	
Sample	Aliquot	Annealing	Given dose [Gy]	Recovered dose [Gy]	Recycling ratio	Recovered dose [Gy]	Recycling ratio
VBT1	1	500 °C cutheat	20.0	19.4 ± 1.1	0.97	19.9 ± 1.0	1.01
	2	500 °C cutheat	20.0	19.6 ± 1.0	0.98	19.9 ± 1.0	1.01
	3	500 °C cutheat	20.0	19.8 ± 1.1	0.97	20.1 ± 1.0	0.98
	4	400 °C for 1 h	20.0	18.4 ± 1.0	0.97	18.2 ± 1.0	0.99
	5	400 °C for 1 h	20.0	19.5 ± 1.0	1.01	20.5 ± 1.0	0.99
	6	400 °C for 1 h	20.0	20.8 ± 1.1	0.94	20.6 ± 1.1	1.01
VBT2	1	500 °C cutheat	20.0	21.2 ± 1.2	0.94	20.6 ± 1.1	0.96
	2	500 °C cutheat	20.0	20.2 ± 1.1	1.00	20.2 ± 1.1	0.99
	3	500 °C cutheat	20.0	20.2 ± 1.1	0.93	19.8 ± 1.1	1.00
	4	400 °C for 1 h	20.0	18.9 ± 1.0	0.97	20.0 ± 1.0	0.99
	5	400 °C for 1 h	20.0	21.5 ± 1.2	0.93	21.5 ± 1.2	0.97
	6	400 °C for 1 h	20.0	22.3 ± 1.3	0.94	21.8 ± 1.2	0.99
VBT3	1	500 °C cutheat	30.0	29.3 ± 1.6	0.99	30.4 ± 1.6	0.97
	2	500 °C cutheat	30.0	28.5 ± 1.6	1.01	29.9 ± 1.5	1.01
	3	500 °C cutheat	30.0	29.1 ± 1.5	0.99	29.8 ± 1.5	0.99

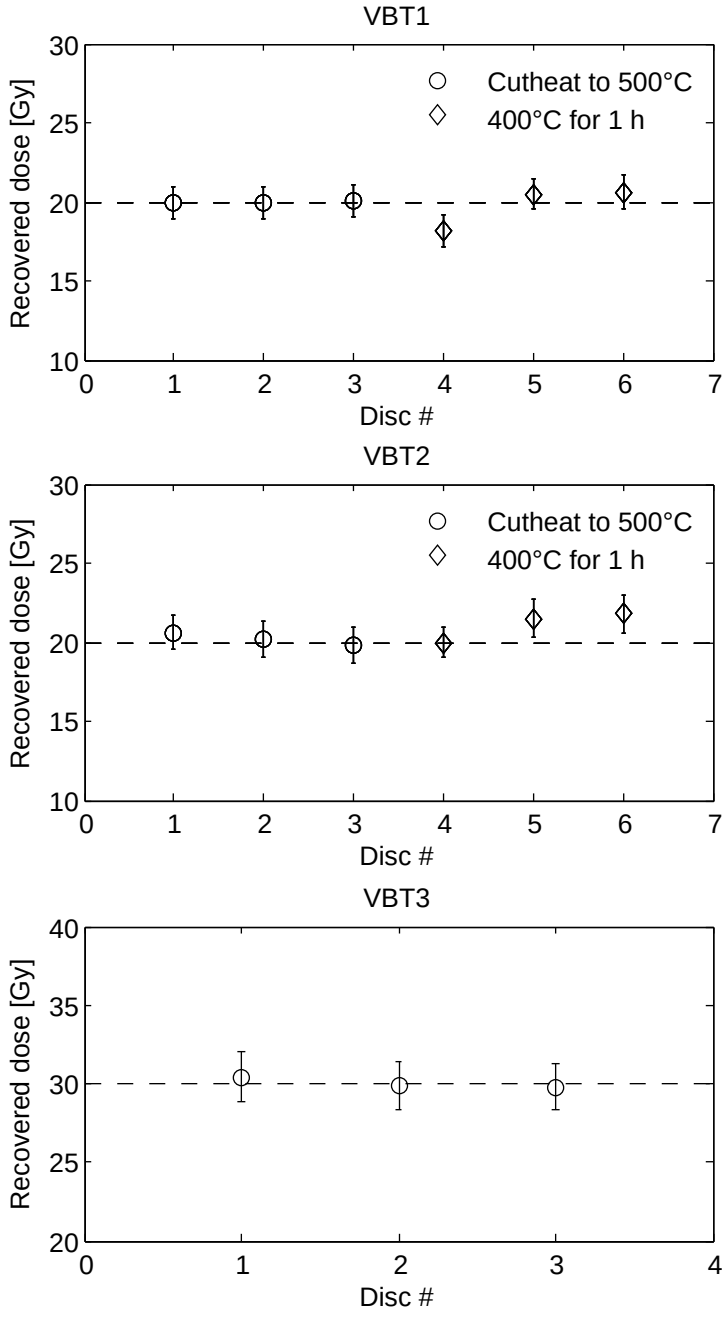

Figure C.3: Plot of DRT results of VBT samples. Due to scarcity of sample material, only one annealing treatment could be tested in case of sample VBT3. The dashed lines represent the given doses.

C.1.3 Plots of equivalent dose versus corrected natural signal

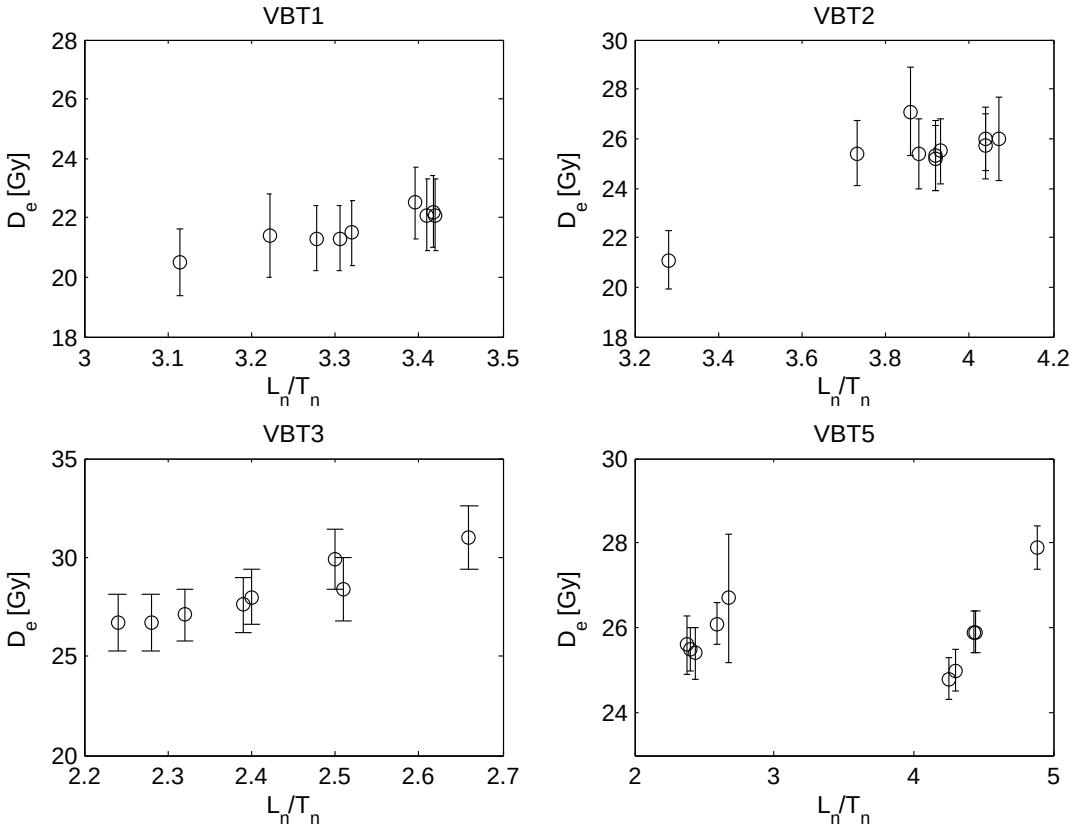

Figure C.4: Plots of D_e versus sensitivity corrected natural signal (L_n/T_n) for VBT samples.

C.2 Sodmein Cave

C.2.1 Plateau tests

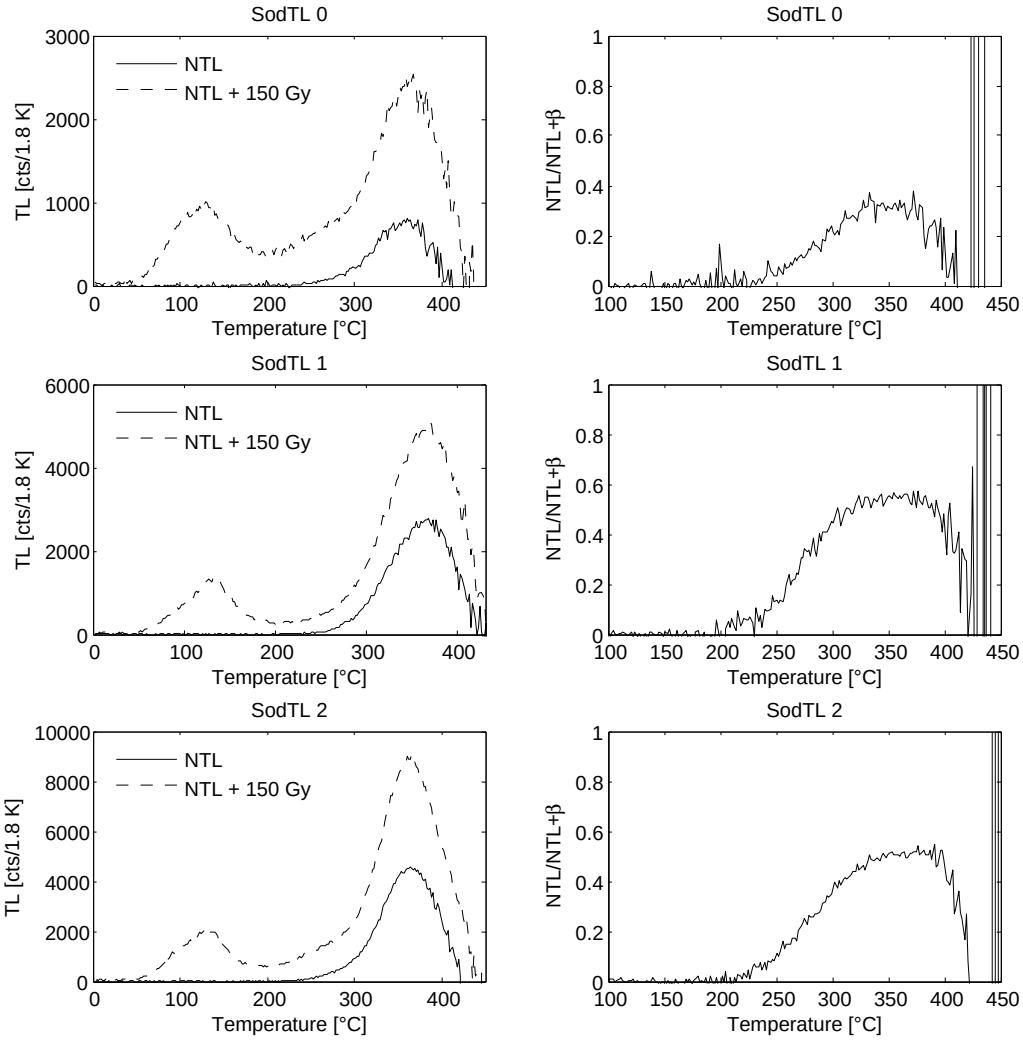

Figure C.5: Heating plateau tests of Sodmein Cave (SodTL) samples. The plots in the left column show the glow curves of natural (NTL) and additively dosed (NTL + β) aliquots; the right column shows the ratio NTL/NTL + β. All curves are normalized (second glow).

C.2.2 Dose recovery tests

Two different TL emissions (blue and red) were measured and DRT's carried out. Measurement parameters were as given in Section 7.1; the recovery dose of 150 Gy was chosen to approximately match the expected equivalent dose.

Table C.2: Results of the DRT of samples from Sodmein Cave (SodTL). The recovery doses of 150 Gy were adjusted to the expected archeological doses of the samples. Integration limits for RTL evaluation were narrowed compared to the plateau region (Fig C.5) due to background subtraction problems at higher temperatures; a single saturating exponential function was used to fit the dose response curves.

blue TL

SodTL0				SodTL1				SodTL2			
Aliquot	Temp. [°C]	D_e [Gy]	Rec. ratio	Aliquot	Temp. [°C]	D_e [Gy]	Rec. ratio	Aliquot	Temp. [°C]	D_e [Gy]	Rec. ratio
1	350–400	161.2 ± 9.8	0.98	1	350–410	161.4 ± 9.1	0.99	1	350-400	168.1 ± 8.8	0.93
2	350–400	165.7 ± 10.0	0.97	2	350–410	159.4 ± 8.9	0.96	2	350-400	170.5 ± 9.2	0.95
3	350–400	166.1 ± 9.9	0.97	3	350–410	162.4 ± 9.1	0.98	3	350-400	166.8 ± 8.8	0.94
4	350–400	–	–	4	350–410	164.3 ± 8.6	0.99	4	350-400	174.0 ± 9.4	0.95
5	350–400	161.4 ± 9.9	0.95	5	350–410	163.7 ± 8.7	0.96	5	350-400	173.9 ± 9.3	0.96
weighted mean		**163.6 ± 4.9**				**162.3 ± 4.0**				**170.6 ± 4.1**	

red TL

SodTL0				SodTL1				SodTL2			
Aliquot	Temp. [°C]	D_e [Gy]	Rec. ratio	Aliquot	Temp. [°C]	D_e [Gy]	Rec. ratio	Aliquot	Temp. [°C]	D_e [Gy]	Rec. ratio
1	340–370	–	–	1	350–390	144.3 ± 13.9	1.10	1	340–370	175.8 ± 12.8	0.89
2	340–370	166.5 ± 8.7	0.99	2	350–390	152.4 ± 10.9	1.08	2	340–370	180.6 ± 13.0	0.86
3	340–370	177.7 ± 13.4	0.83	3	350–390	156.5 ± 12.5	1.03	3	340–370	176.1 ± 12.1	0.85
4	340–370	139.4 ± 12.5	1.14	4	350–390	165.8 ± 9.6	0.90	4	340–370	171.1 ± 12.8	0.91
5	340–370	152.8 ± 9.0	0.94	5	350–390	138.5 ± 15.9	1.21	5	340–370	180.8 ± 12.9	0.82
weighted mean		**159.8 ± 6.3**				**155.7 ± 5.7**				**171.1 ± 12.8**	

C.2.3 Plots of equivalent dose versus corrected natural signal

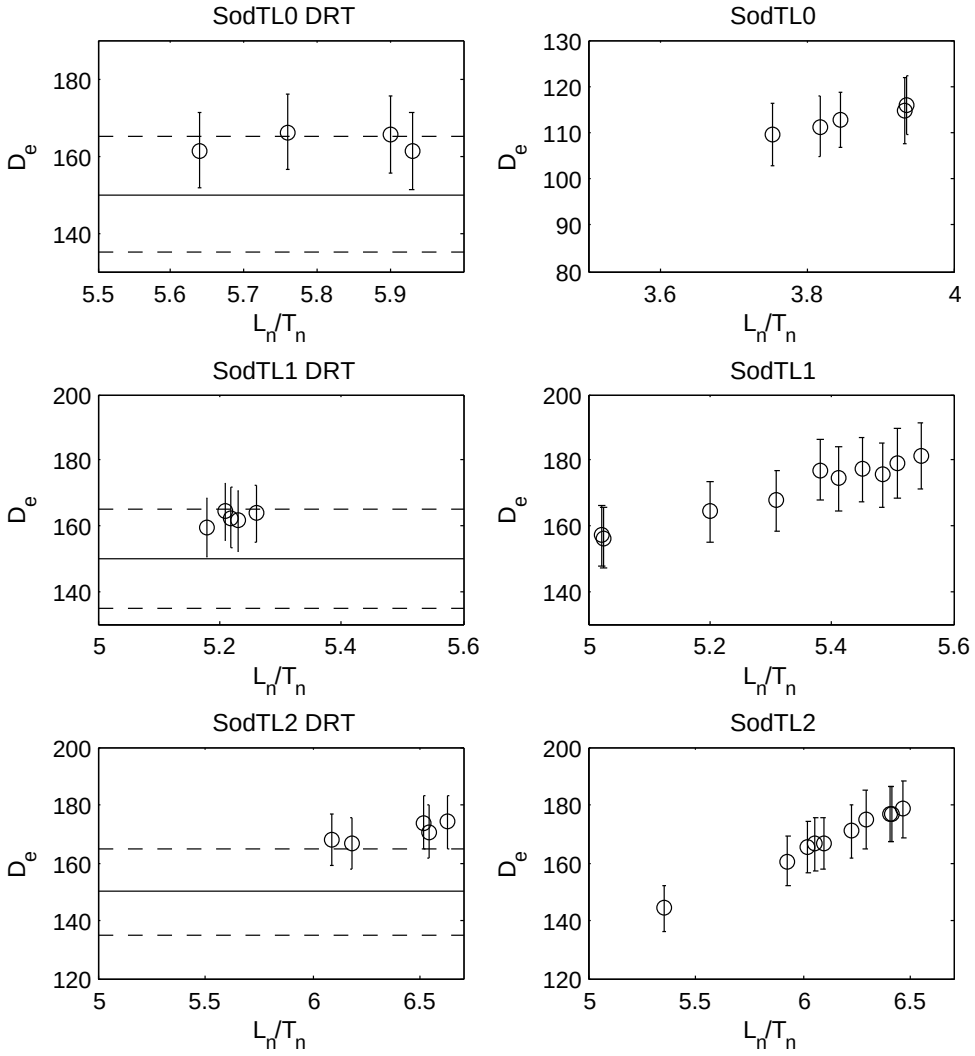

Figure C.6: Plots of D_e versus sensitivity corrected natural signal (L_n/T_n) for DRT's and natural dose measurements of Sodmein TL samples. The solid line indicates the given laboratory dose, dashed lines the 10 % error bounds. Although the spread in D_e's is only slightly larger for natural dose measurements (compared to DRT's), the range of L_n/T_n values is smaller for DRT's (except for SodTL0). For further information and interpretation, see main text (Sections 7.1 and 7.3.4).

C.3 Las Palomas

C.3.1 Plateau tests

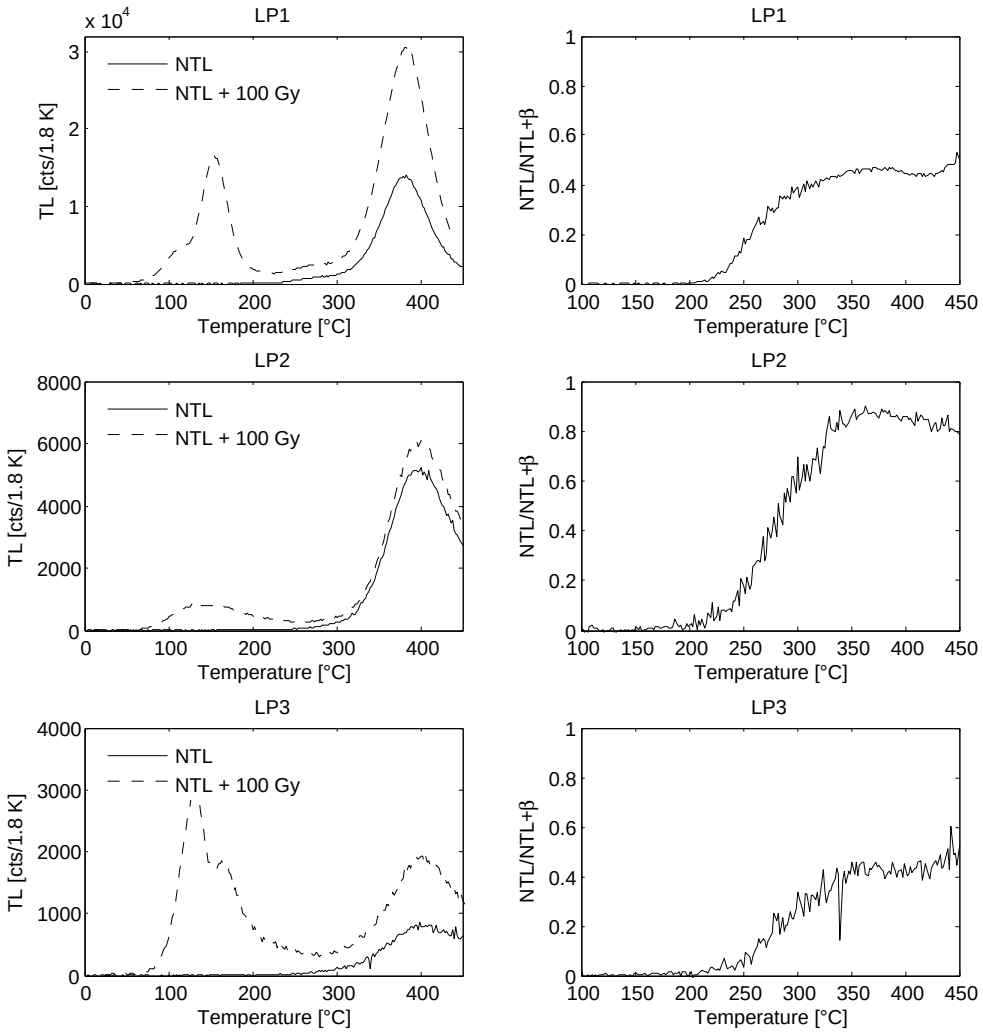

Figure C.7: Heating plateau tests of Las Palomas (LP) samples LP1, LP2 and LP3. The plots in the left column show the glow curves of natural (NTL) and additively dosed (NTL + β) aliquots; the right column shows the ratio NTL/NTL + β. All curves are normalized (second glow).

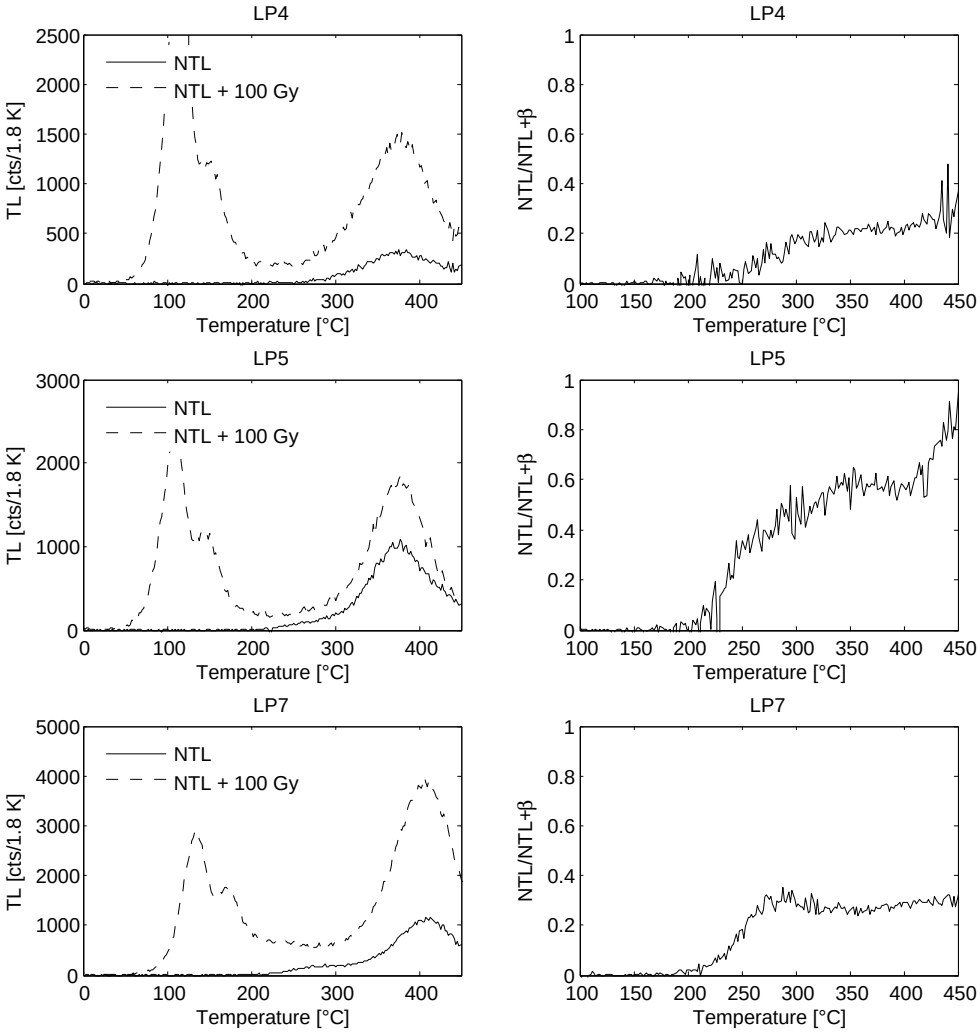

Figure C.8: Heating plateau tests of Las Palomas (LP) samples LP4, LP5 and LP7. The plots in the left column show the glow curves of natural (NTL) and additively dosed (NTL + β) aliquots; the right column shows the ratio NTL/NTL + β. All curves are normalized (second glow).

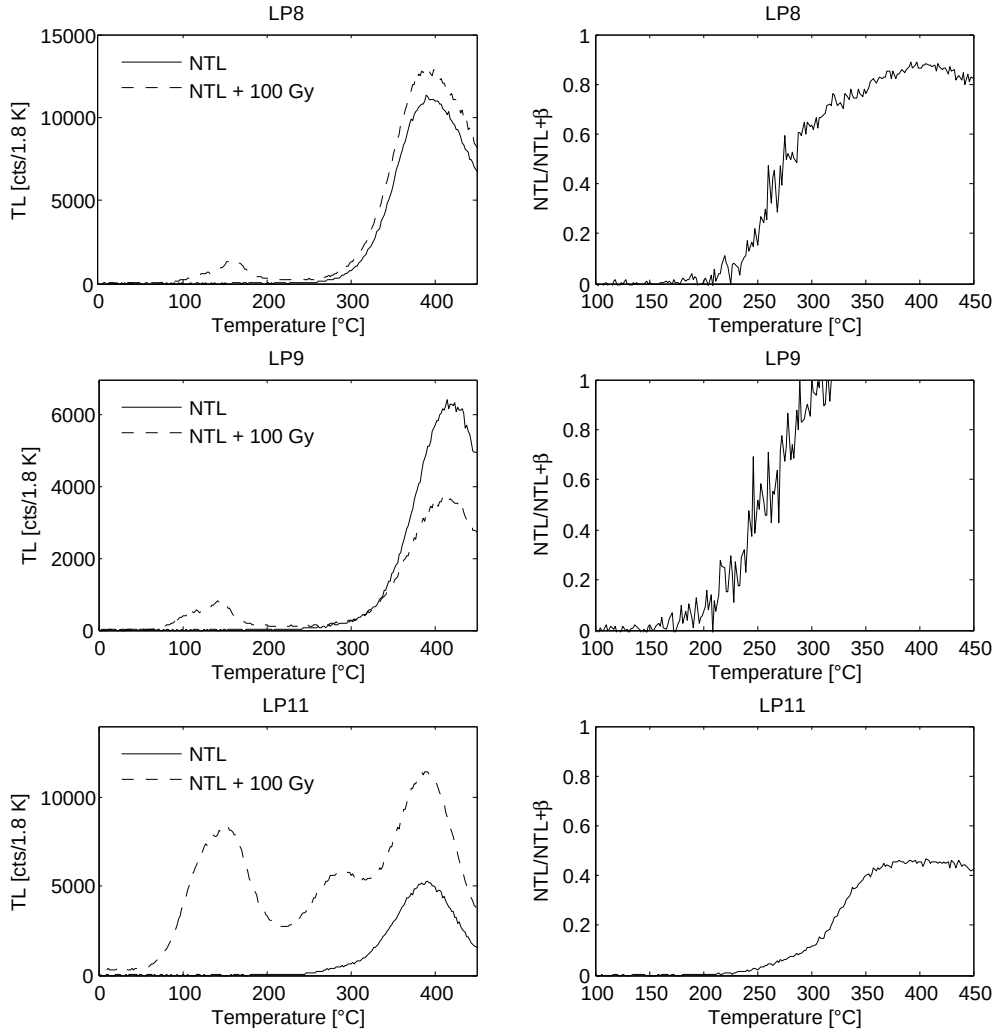

Figure C.9: Heating plateau tests of Las Palomas (LP) samples LP8, LP9 and LP11. The plots in the left column show the glow curves of natural (NTL) and additively dosed (NTL + β) aliquots; the right column shows the ratio NTL/NTL + β. All curves are normalized (second glow).

C.3.2 Plots of equivalent dose versus corrected natural signal

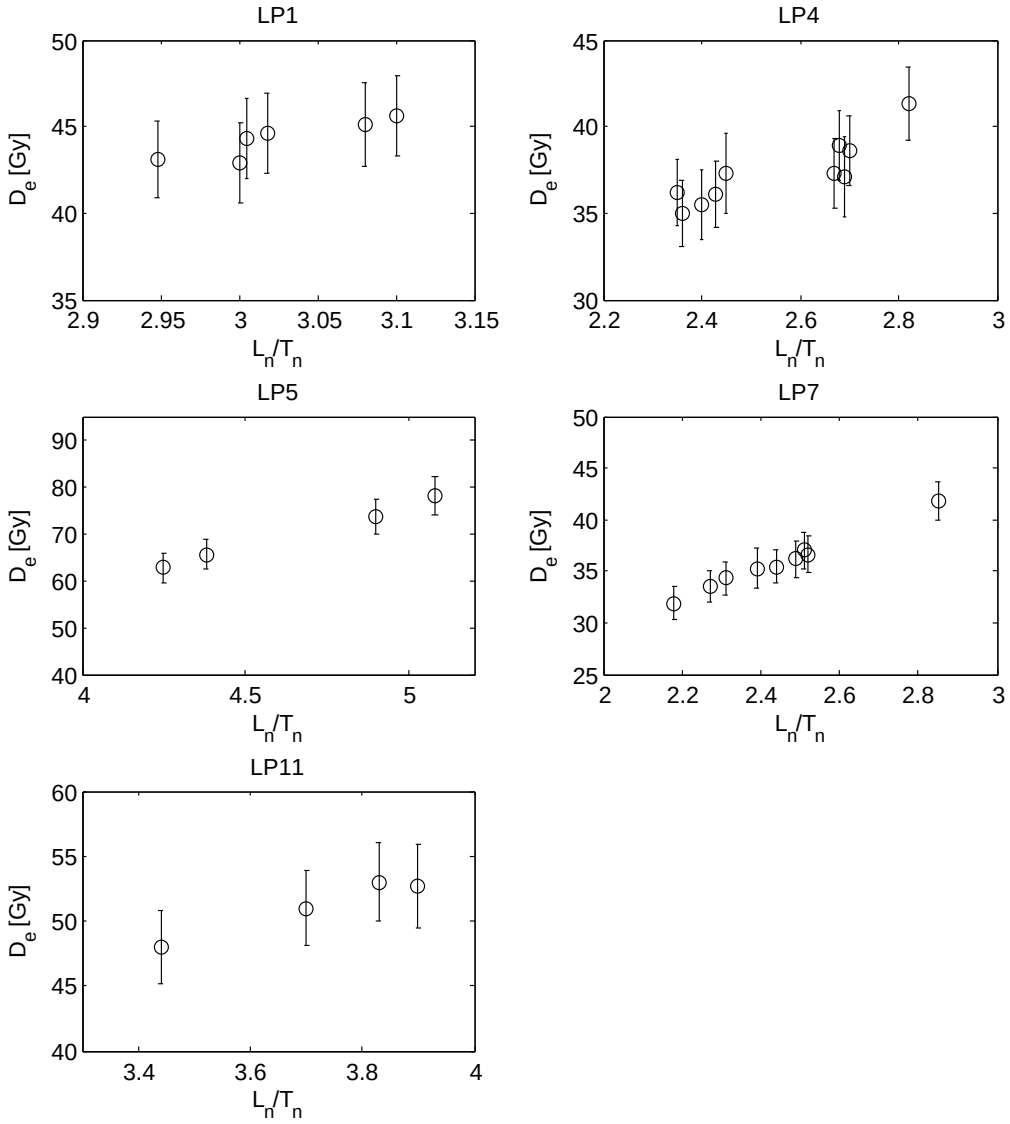

Figure C.10: Plots of D_e versus sensitivity corrected natural signal (L_n/T_n) for LP samples.

D Contribution to the manuscripts

This thesis includes five manuscripts that were submitted or accepted for publication. In the following, my contributions to these studies are assessed, while the quoted values comprise an estimated uncertainty of ± 10 %.

Chapter 2

Laboratory work	50 %
Measurements	70 %
Interpretation of results	60 %
Manuscript preparation	70 %

Chapter 3

Laboratory work	60 %
Measurements	50 %
Interpretation of results	90 %
Manuscript preparation	95 %

Chapter 4

Laboratory work	0 %
Measurements	50 %
Interpretation of results	70 %
Manuscript preparation	80 %

Chapter 5

Laboratory work	50 %
Measurements	95 %
Interpretation of results	95 %
Manuscript preparation	95 %

Chapter 6

Laboratory work	50 %
Measurements	90 %
Interpretation of results	50 %
Manuscript preparation	60 %

Acknowledgments

Die vorliegende Arbeit entstand im Rahmen des Sonderforschungsbereiches (SFB) 806 „Our Way To Europe – Culture-Environment Interaction and Human Mobility in the Late Quaternary“. Die hierdurch ermöglichten Arbeitsbedingungen und die zur Verfügung gestellte Infrastruktur trugen maßgeblich zur termingerechten Fertigstellung bei. Darüber hinaus war es durch die interdisziplinäre Struktur des Projektes möglich, einen Blick über den geographisch-physikalischen Tellerrand hinaus zu werfen und die Arbeits- und Denkweisen geisteswissenschaftlicher Fächer, wie der Archäologie und der Ethnologie, zu bestaunen. In diesem Zusammenhang sei auch die Graduiertenschule des SFB erwähnt, die einem nicht nur die „Last“ aufbürdete, in regelmäßigen Abständen den Schreibtisch zu verlassen, sondern dem Kreis der Doktoranden mit einem vielfältigen und ansprechenden Veranstaltungs- und Kursangebot zur Erweiterung der Sozialkompetenz („soft skills“) aufwartete. Auf diesem Wege möchte ich ein kollektives Dankeschön loswerden für die gute Zusammenarbeit innerhalb des SFB.

Ferner sei Prof. Dr. Ulrich Radtke für die Betreuung der Arbeit gedankt. Das Co-Referat übernahm dankenswerterweise Prof. Dr. Ludwig Zöller; er war es auch, der mich mit der Lumineszenzdatierung in Berührung brachte, mich auf die Stelle in Köln aufmerksam machte und somit meine berufliche Entwicklung mit beeinflusste (aber ich bereue nichts). Hoch anrechnen muss ich die fortwährende und engagierte fachliche Betreuung durch Dr. Alexandra Hilgers, die immer ein offenes Ohr für auftretende Probleme hatte, nächtliche Korrekturlesungen durchführte und meine Arbeiten durch wertvolle Hinweise und Diskussionen begleitete. Bedanken möchte ich mich bei ihr auch für die mir gewährten experimentellen und gestalterischen Freiheiten, die es ermöglichten auch einfach mal allein den Forscherdrang zu befriedigen, ohne stetig auf Messzeit und Probendurchsatz achten zu müssen. Unschätzbare Hilfe in fachlicher und technischer Hinsicht leistete auch Dr. Anja Zander. Immer wenn ein Gerät aufmuckte, war sie zur Stelle, hat geduldig justiert, kalibriert und repariert und alle meine „unkonventionellen“ Herangehensweisen unterstützt. Vielen Dank für die stete Hilfsbereitschaft, auch nach Feierabend. Fruchtbare Zusammenarbeit im Labor wie auch im Gelände erlebte ich mit Dr. Nicole Klasen. Herzlichen Dank möchte ich auch dem Rest der Arbeitsgruppe Geochronologie für die gute Arbeitsatmosphäre aussprechen. Dr. Daniela Hülle hat mich in vielen Fragen, v.a. aber bezüglich der Dissertation, beratschlagt, und Stefan Weiß, Christoph Burow und Melanie Bartz ließen mir Unterstützung bei Laborarbeiten zukommen.

Mit Dr. Sebastian Kreutzer habe ich während der letzten Jahre unzählige Telefonate geführt; aus diesem wertvollen Gedankenaustausch heraus konnten viele Probleme gelöst

werden (obwohl sich zuweilen auch neue, noch weitaus ausuferndere Fragen auftaten). Zudem war es uns vergönnt, gemeinsam viermal die Lumineszenzdatierungsgruppe um Dr. Richard Bailey an der Universität Oxford zu besuchen. Diese Aufenthalte waren für mich sehr fruchtbar und lehrreich, und nicht zuletzt humorvoll. Vielen Dank für die kontinuierliche Bereitschaft zum kritischen und objektiven Dialog! At this stage, I would like to thank the members of the Oxford luminescence group – Dr. Richard Bailey, Dr. Jean-Luc Schwenninger and Dr. Morteza Fattahi – for the warm welcome, the instructive time during our visits and the patient introduction to the fundamentals of luminescence dating.

Im Laufe der vergangenen drei Jahre durfte ich an einigen Geländekampagnen in Rumänien, Jordanien und Portugal teilnehmen. Für die gute Aufnahme des „TL-Menschen“ und die angenehme, lehrreiche und lustige Zeit im Feld möchte ich allen involvierten Personen der Teilprojekte B1 und C1 danken, im Besonderen Dr. Holger Kels, Dr. Valery Sitlivy, Manuel Bertrams, Dr. Daniel Schyle, PD Dr. Martin Kehl und Prof. Dr. Gerd-Christian Weniger.

Für die gute wissenschaftliche Zusammenarbeit bei den Untersuchungen zur Radionuklidverteilung in Silex möchte ich Dr. Daniel Rufer, Prof. Dr. Frank Preusser und Prof. Dr. Thomas Pettke von der Universität Bern danken. Zuverlässige und gen Ende meiner Bearbeitungszeit auch rasch gemessene ICP-MS-Daten der Silex-Proben stellte mir dankenswerterweise Dr. Haino Uwe Kasper zur Verfügung. Dank geschuldet bin ich auch Dr. Annette Kadereit und Felicitas Wolf von der Universität Heidelberg für unkomplizierte Kooperation und die Bestrahlung der Feinkornproben für die Kalibration der Kölner α-Quelle. Dr. Matthias Krbetschek war in der Anfangszeit meiner Promotion ein hilfreicher und erfahrener Ratgeber, nicht nur in Sachen Autoradiographie. Seine Art, Probleme unkonventionell und aus anderem Blickwinkel anzugehen, hat meine Arbeitsweise ein Stück weit geprägt. In Sachen Silex-Datierung war mir auch PD Dr. Daniel Richter eine große Hilfe, v.a. bei der Einarbeitung in grundlegende Techniken und die α-Bestrahlung und α-Effektivität. Bei der typographischen Gestaltung dieser Arbeit und der fortwährenden Auseinandersetzung mit LaTeX haben Sebastian Brocks und Christian Willmes von der Arbeitsgruppe GIS & Fernerkundung wertvolle Hilfe geleistet und alle Fehlermeldungen eliminieren können. Unabdingbar bei Datenauswertung und Schriftsatz waren auch zahlreiche Beiträge in goLaTeX und goMatlab sowie vergleichbaren Foren.

Für regen fernschriftlichen Austausch während der letzten Jahre sowie Beistand in „lumineszenzfernen“ Belangen und einen lustigen und gedanklich befreienden Monat in den Anden möchte ich Andreas Raithel danken.

Last but not least bin ich meiner gesamten Familie großem Dank verpflichtet. Meine Eltern haben mich Zeit meines Lebens nach besten Möglichkeiten unterstützt und mir Vertrauen gegeben, vor allem auch in den bewegten Zeiten der letzten Monate.

Vielen Dank Euch allen!

Erklärung gem. § 4, Abs. 1 Punkt 9 der Promotionsordnung

Ich versichere, dass ich die von mir vorgelegte Dissertation selbstständig angefertigt, die benutzten Quellen und Hilfsmittel vollständig angegeben und die Stellen der Arbeit – einschließlich Tabellen, Karten und Abbildungen –, die anderen Werken im Wortlaut oder dem Sinn nach entnommen sind, in jedem Einzelfall als Entlehnung kenntlich gemacht habe; dass diese Dissertation noch keiner anderen Fakultät oder Universität zur Prüfung vorgelegen hat; dass sie – abgesehen von unten angegebenen Teilpublikationen – noch nicht veröffentlicht worden ist sowie, dass ich eine solche Veröffentlichung vor Abschluss des Promotionsverfahrens nicht vornehmen werde. Die Bestimmungen dieser Promotionsordnung sind mir bekannt. Die von mir vorgelegte Dissertation ist von Univ.-Prof. Dr. U. Radtke betreut worden.

Christoph Schmidt

Teilpublikationen

Schmidt, C., Kreutzer, S., Fattahi, M., Bailey, R., Zander, A., Zöller, L., 2011. On the luminescence signal of empty sample carriers. Ancient TL 29, 65–74.

Schmidt, C., Rufer, D., Preusser, F., Krbetschek, M., Hilgers, A., 2013. Assessment of radionuclide distribution in silex by autoradiography in the context of dose rate determination for thermoluminescence dating. Archaeometry 55, 407–422.

Schmidt, C., Pettke, T., Preusser, F., Rufer, D., Kasper, H.U., Hilgers, A., 2012. Quantification and spatial distribution of dose rate relevant elements in silex used for luminescence dating. Quaternary Geochronology 12, 65–73.

Schmidt, C., Kreutzer, S., 2013. Optically stimulated luminescence of amorphous/microcrystalline SiO_2 (silex): Basic investigations and potential in archeological dosimetry. Quaternary Geochronology 15, 1–10.

Schmidt, C., Sitlivy, V., Anghelinu, M., Chabai, V., Kels, H., Uthmeier, T., Hauck, T., Băltean, I., Hilgers, A., Richter, J., Radtke, U., accepted for publication. First chronometric dates (TL and OSL) for the Aurignacian open-air site of Româneşti-Dumbrăviţa I, Romania. Journal of Archaeological Science.

Sitlivy, V., Chabai, V., Anghelinu, M., Uthmeier, T., Kels, H., Hilgers, A., **Schmidt, C.**, Niţă, L., Băltean, I., Veselsky, A., Hauck, T., 2012. The earliest Aurignacian in Romania: New investigations at the open air site of Româneşti-Dumbrăviţa I (Banat). Quartär 59, 85–130.